Advanced Software and Hardware Control Methods for Improved Static and Dynamic B_0 Shimming in Magnetic Resonance Imaging

Von der Fakultät für Mathematik, Informatik und Naturwissenschaften der RWTH Aachen University
zur Erlangung des akademischen Grades eines Doktors der Naturwissenschaften
genehmigte Dissertation

vorgelegt von

Michael Schwerter, M.Sc.

aus
Herdecke

Berichter: Prof. Dr. N. Jon Shah
Prof. Dr. Achim Stahl

Tag der mündlichen Prüfung: 17.12.2019

Declaration of Authorship

I, Michael Schwerter,

declare that this thesis and the work presented in it are my own and has been generated by me as the result of my own original research.

I do solemnly swear that:

1. This work was done wholly or mainly while in candidature for the doctoral degree at this faculty and university;
2. Where any part of this thesis has previously been submitted for a degree or any other qualification at this university or any other institution, this has been clearly stated;
3. Where I have consulted the published work of others or myself, this is always clearly attributed;
4. Where I have quoted from the work of others or myself, the source is always given. This thesis is entirely my own work, with the exception of such quotations;
5. I have acknowledged all major sources of assistance;
6. Where the thesis is based on work done by myself jointly with others, I have made clear exactly what was done by others and what I have contributed myself;
7. Parts of this work have been published before as
   - M. Schwerter, C. H. Moon, H. P. Hetherington, J. W. Pan, L. Tellmann, J. Felder, and N. J. Shah, "Interslice current constrained B0 shim optimization for high order dynamic shim updating with strongly reduced eddy currents," in *Proc. Intl. Soc. Mag. Reson. Med.*, p. 836, 2018
   - M. Schwerter, H. P. Hetherington, C. H. Moon, J. W. Pan, J. Felder, L. Tellmann, and N. J. Shah, "Interslice current change constrained B0 shim optimization for accurate high-order dynamic shim updating with strongly reduced eddy currents," *Magnetic Resonance in Medicine*, vol. 82, no. 1, pp. 263–275, 2019
   - M. Schwerter, M. Zimmermann, and N. J. Shah, "Fast 4d model based eddy current characterization for shim pre-emphasis calibrations," in *Proc. Intl. Soc. Mag. Reson. Med.*, p. 444, 2019

   and are planned to be published as
   - M. Schwerter, M. Zimmermann, and N. J. Shah, "2d image-based eddy current characterization using a model-based pre-emphasis parameter estimation." In preparation
   - M. Schwerter, M. Zimmermann, and N. J. Shah, "Generalized dynamic shim optimization for optimal B0 homogeneity at low current amplitudes." In preparation

Jülich, January 20, 2020, ...
Michael Schwerter

Abstract

Magnetic resonance imaging (MRI) is a non-invasive tomographic imaging technique and a powerful tool applied in many fields of medicine and research. Methodological developments have vastly broadened the spectrum of possible applications and turned the classical MR scanner into an inherently multi-modal imaging device. Simultaneous hardware advancements have been striving for obtaining better data quality at reduced acquisition times. Here, a central role is taken by the improvement of the MRI magnets, which are required to generate a strong, homogeneous and temporally stable static magnetic field. Any perfectly homogeneous magnetic field, however, is inevitably distorted by the unique magnetic susceptibility distribution of an examination subject. Thus, subject-specific magnetic field *shimming* technology, which homogenizes the magnetic field, is indispensable and still forms an integral part of current MR research. However, this is non-trivial, because human MR acquisitions are faced with complex distortion field patterns and, thus, many of today's applications still suffer from strong uncompensated inhomogeneities. Consequently, it was the purpose of this work to identify and overcome existing challenges in subject-specific static magnetic field shimming with a focus on human brain acquisitions.

Conventional shim approaches are typically based on 2^{nd} order spherical harmonic shim coils, whose driving currents are adjusted so as to correct for previously measured field inhomogeneities. To gain full control over this process, a comprehensive field mapping and shim current optimization framework was implemented. Accurate shim field characterizations were performed and included into custom-written software. Conducted simulations as well as phantom and in vivo measurements showed, that the shimming framework reaches optimal field homogeneity over user-defined volumes within one minute and without the need for iterations. This way, an average whole-brain field homogeneity of 18.4 ± 2.5 Hz was achieved at a main field strength of 3 T.

The shim quality was further improved via the application of a shim coil insert, which can generate very high-order spherical harmonic shim fields. Means of communication with its shim controller were implemented and integrated into the shimming software. Simulations, indicating an improve in whole-brain field homogeneity to 15.1 ± 3.8 Hz, were confirmed in experiments. This residual inhomogeneity was identified as being beyond the correction capabilities even of the high-order shim set and indicates the feasible limit of static spherical harmonic shimming.

In contrast, *dynamic* shim updates during data acquisition can further improve the achievable B_0 homogeneity. However, rapid shim changes evoke eddy current-induced distortion fields and, thus, require pre-emphasis corrections. For this, an image-based measurement scheme was developed, which is applicable to capture full 4D eddy current field evolutions. Requiring 10 min of acquisition time, a six-fold acceleration compared to an existing alternative was achieved. Combined with a novel model-based pre-emphasis reconstruction, the shim-induced eddy currents were effectively suppressed and enabled a dynamic operation of the shim hardware.

Based on this, a key finding of this work is that the dynamic shim currents and their temporal variation can be strongly constrained while negligibly compromising achievable field homogeneity. Incorporation of these constraints into the shim optimization led to a 23-fold reduction of average maximum and an 18-fold reduction of the average mean inter-slice current changes. Nonetheless, a whole-brain field homogeneity of 8.76 ± 0.32 Hz was achieved, as compared to 8.10 ± 0.31 Hz for the unconstrained case. The associated benefits are manifold, including an intrinsic eddy current reduction, decreased power supply demands and more accurate shim simulations.

In conclusion, novel and efficient means to increase the magnetic field homogeneity in MRI measurements were developed within the scope of this work. Especially the methods to measure and reduce shim-induced eddy currents improve dynamic shimming implementations significantly.

Kurzfassung

Die Magnetresonanztomographie (MRT) ist eine nicht-invasive tomografische Bildgebungstechnik und ein mächtiges Instrument in Medizin und Forschung. Methodische Weiterentwicklungen haben das Spektrum möglicher Anwendungen erheblich erweitert und den klassischen MR-Scanner zu einem inhärent multimodalen Bildgebungsgerät gemacht. Dies ging mit Optimierungen der Hardware einher, die eine höhere Datenqualität bei verkürzten Messzeiten erzielten. Eine wichtige Rolle spielt dabei seit jeher die Verbesserung der MRT Magnete, welche zur Erzeugung eines starken, homogenen und zeitlich stabilen statischen Magnetfeldes benötigt werden. Selbst ein vollkommen homogenes Magnetfeld wird jedoch unvermeidlich durch die magnetische Suszeptibilität eines Untersuchungsobjektes verzerrt. Effektive Methoden das Magnetfeld zu *shimmen* sind daher unverzichtbar und noch immer wesentlicher Bestandteil der Forschung. Dies ist jedoch nicht trivial, da bei humanen MR Anwendungen komplexe Verzerrungsmustern entstehen. Die Qualität vieler heutiger MR Anwendungen ist daher noch immer durch starke unkompensierte Inhomogenitäten beeinträchtigt. Ziel dieser Arbeit war es daher, bestehende Probleme des Shimmings des statischen Magnetfeldes zu identifizieren und Lösungstrategien zu entwickeln.
Konventionelle Shimming Ansätze basieren auf Spulen, die Felder entsprechend der Kugelflächenfunktionen 2. Ordnung erzeugen und deren Ströme so angepasst werden, dass zuvor gemessene Inhomogenitäten kompensiert werden. Die dafür erforderlichen Methoden zur Magnetfeldmessung und Shimoptimierung wurden im Rahmen dieser Arbeit entwickelt und implementiert. Präzise Charakterisierungen des Shimsystems wurden durchgeführt und in die Software integriert. Simulationen und Messungen zeigten, dass die Methode eine optimale Homogenität innerhalb von einer Minute und ohne Iterationen über benutzerdefinierte Volumina erreicht. So wurde bei einer Feldstärke von 3 T über das gesamte Gehirn eine Feldhomogenität von $18{,}4 \pm 2{,}5$ Hz erzielt.
Die Shimqualität wurde durch die Verwendung zusätzlicher Shimspulen, welche Kugelflächenfunktionen sehr hoher Ordnung erzeugen, weiter verbessert. Ansteuerungsmöglichkeiten des Shim-Controllers wurden implementiert und in die Software integriert. Simulationen, die eine Verbesserung der Homogenität über das gesamte Gehirn auf $15{,}1 \pm 3{,}8$ Hz zeigten, wurden durch Messungen bestätigt. Die verbleibenden Inhomogenitäten übersteigen das Korrekturpotenzial selbst der Shimspulen hoher Ordnung und weisen die Grenzen des statischen Shimmings auf.
Dynamische Shim-Updates während der Datenerfassung können die erreichbarer Feldhomogenität jedoch weiter verbessern. Schnelle Shim-Änderungen rufen allerdings wirbelstrominduzierte Verzerrungsfelder hervor und erfordern sogenannte *pre-emphasis* Korrekturen. Daher wurde eine Messmethode entwickelt, die den vollständigen Verlauf von 4D-Wirbelstromfeldern erfassen kann. Mit einer Messzeit von 10 Min. wurde eine sechsfache Beschleunigung im Vergleich zu einer vorhandenen Alternative erzielt. In Kombination mit einer modell-basierten *pre-emphasis* Rekonstruktion konnte gezeigt werden, dass alle Wirbelströme effektiv kompensiert wurden.
Eine zentrale Erkenntnis dieser Arbeit ist, dass die dynamischen Shimströme und deren zeitliche Änderung stark limitiert werden können, ohne die erreichbare Homogenität signifikant zu beeinträchtigen. So konnte eine 23-fache Verringerung der durchschnittlichen maximalen und eine 18-fache Verringerung der durchschnittlichen mittleren Shimstrom-Änderungen erzielt werden. Dabei wurde trotzdem eine Homogenität von $8{,}76 \pm 0{,}32$ Hz erreicht, verglichen mit $8{,}10 \pm 0{,}31$ Hz für den nicht-limitierten Fall. Die damit einhergehenden Vorteile umfassen eine intrinsische Wirbelstromreduzierung, geringere Hardwareanforderungen und genauerere Simulationen.
Zusammengefasst wurden im Rahmen dieser Arbeit neue und effiziente Techniken zur Erhöhung der MRT Magnetfeldhomogenität entwickelt. Insbesondere die Methoden zum Messen und Reduzieren der Wirbelströme verbessern die Andwendbarkeit des dynamischen Shimmings erheblich.

Contents

1 Introduction

Nuclear magnetic resonance (NMR) is a physical phenomenon, which can be exploited to examine the magnetic properties and the chemical environment of certain isotopes within an examination object. It has found its way into many technologies, amongst which magnetic resonance imaging (MRI) and spectroscopy (MRS) have emerged to become powerful tools in medicine and research. The technique is based on exposing a sample to both a static magnetic field and an oscillating radio-frequency pulse, which enables the subsequent detection of a resultant signal that is emitted from the sample. It was initially discovered in the late 1930s, when Isidor Rabi detected NMR in a molecular beam [6]. Edward Purcell and Felix Bloch extended the method in the mid-1940s to study the NMR properties of solids and liquids [7, 8]. Ten years later, Erik Odeblad investigated the varying NMR signal characteristics of different biological tissues [9]. This is the fundamental concept used to generate contrast in MRI, which was invented in the following. Even though Raymond Damadian filed a patent in 1972 on a point-by-point scanner [10], it was in 1973, when the imaging concept of today's scanners was developed. Paul Lauterbur used magnetic field gradients to spatially encode the NMR signal and reconstructed tomographic images using a back-projection technique [11]. Only shortly after, with the application of a Fourier-reconstruction [12] and further MR methodology advancements [13], many of the imaging principles that are still widely used today had already been developed by the end of the 1970s.
These days, MR techniques are not only applied for qualitative imaging, but have emerged to become versatile tools for the in vivo assessment of functional, metabolic, structural, spectroscopic and a variety of other quantitative information. However, the significant broadening of the spectrum of possible MR acquisitions has been accompanied by an increase in hardware demands. Here, one major challenge is related to the homogenization of the static magnetic field, commonly denoted as B_0. Since MR techniques rely on the application of well-defined magnetic fields, non-uniformities can lead to significant artifacts in the reconstructed data. While being problematic already at lower field strengths, the vulnerability to inhomogeneities scales with B_0 and counteracts the trend towards ultra-high field systems. The process of homogenizing the magnetic field is referred to as B_0 *shimming* and is an important step during the pre-scan adjustment procedure. A core problem is that the spatial distribution of the inhomogeneities is highly subject-dependent and renders their compensation challenging. Moreover, the B_0 shimming hardware has not advanced over the past decades and still relies on the application of a few low-order correction fields. As a result, the capabilities of conventional B_0 shim approaches are limited in their performance and do not match the demands of many MR applications. Therefore, the work of this dissertation addresses challenges pertinent to the homogenization of the static magnetic field in an MR scanner and explores novel concepts in order to improve B_0 shimming efficiency.

At the very outset of this thesis, a brief introduction into the principles of MRI will be given. Therefore, **Chapter 2** covers the fundamental concepts of NMR and how they are applied in MRI to acquire tomographic images of an examination object. It provides the theoretical basis, which is required to understand the results that were produced within the scope of this work.

Being the core topic of this thesis, **Chapter 3** reviews currently available B_0 shimming techniques. The spherical harmonic model, which is a key concept in this context, will be treated in greater detail. Moreover, the origins and the impact of uncompensated field distortions will be explained and motivate the need for an efficient B_0 shim technology. The largest part of this chapter reviews different methods for B_0 field measurements and shimming. The focus is on spherical harmonic approaches, but emerging alternatives are covered likewise. Thus, it forms a comprehensive summary of current state-of-the-art B_0 shimming techniques.

The following chapters build upon these concepts and treat four projects that were covered within the scope of this work. At the outset of each chapter, its content is put into context with other parts of this thesis.

In **Chapter 4**, the work that was performed in order to re-implement current state-of-the-art B_0 shim techniques is described. The B_0 shim system calibration procedure is introduced, which forms the basis for accurate shim simulations and correct shim adjustments. An improved shim performance is demonstrated using vendor-supplied shim hardware and the concept is extended to increase the achievable homogeneity via inclusion of non-standard hardware. Consequently, this chapter forms the basis for the advanced shim approaches that are introduced in the following.

Chapter 5 treats challenges that arise when shim currents are varied rapidly during the MR acquisition. It covers the origins of shim-induced eddy currents, describes how they are commonly modeled and presents a novel method to accurately measure them. Introducing a model-based fitting algorithm, it is demonstrated that eddy current model parameters can be reconstructed robustly from the data. By applying these parameters to calibrate appropriate shim correction signals, a fast and robust dynamic shim operation without eddy current generation is shown.

Based on this work, it is demonstrated in **Chapter 6** how a dynamic update of the shim settings can improve the B_0 homogeneity over the static shimming case. A novel optimization technique is proposed, which improves existing techniques by limiting the maximum permitted shim currents and their temporal variation. This way, shim-induced eddy currents are intrinsically reduced without significantly compromising the achievable B_0 homogeneity. Other advantages include more accurate shim simulations and decreased hardware demands, thus facilitating dynamic shimming implementations. Together with the eddy current measurement and compensation framework, the methods and results presented in this chapter form the core of this dissertation.

Ultimately, in **Chapter 7** the idea of limiting the dynamic shim-variations is being generalized and formulated as a dedicated minimization problem. An iterative optimization technique is applied to directly minimize inter-slice shim current changes. It is demonstrated in simulations that the algorithm can reduce the shim current variations most effectively.

All findings that were developed in the scope of this thesis are finally summarized in **Chapter 8** and put into context of today's state-of-the-art of B_0 shimming techniques. Possible future directions in B_0 shimming are extrapolated from these insights and conclude this work.

2

Magnetic resonance imaging

Magnetic resonance imaging (MRI) is a non-invasive imaging technique and can be used to generate tomographic images of an examination object. It is based on a strong static magnetic field, which is applied in combination with superimposing magnetic gradient and radio-frequency fields in order to trigger, encode and receive signals from an examination object. Specific sequences of these gradient and radio-frequency pulses and a concomitant recording of the resultant MR signals enables a subsequent reconstruction of a full image of the object.

The technology and methodology behind MRI is complex and a comprehensive understanding requires knowledge from various disciplines including physics, mathematics and engineering. Numerous text books have been written and give a comprehensive treatise of the theory [14] or detailed explanations of individual topics such as the physical background [15], the required hardware [16] or its control [17]. A comprehensive treatment of the theory of MRI and all its potential applications is beyond the scope of this thesis.

Instead, this chapter is intended to introduce the basic principles that are required to understand the theory, methods and results presented in this work and is adapted from the literature given above. Consequently, the origin of the MR signal is first explained and described mathematically. Based on this, the fundamental signal encoding strategy is derived and exemplified using a simple MRI acquisition scheme. The signal reception is outlined and the most common data precessing steps required for image reconstructions are explained. The main system components of an MR scanner, which are required for these processes, are briefly explained in the last section and lead over to the ensuing chapter.

2.1 Nuclear magnetic resonance

Nuclear magnetic resonance (NMR) is a physical phenomenon, which describes the processes of the absorption and emission of energy of certain atomic nuclei under exposure to a constant static magnetic field and a temporally varying radio-frequency field. By carefully controlling and monitoring these processes, insights into the properties and composition of a sample can be gained and, thus, NMR finds application in multiple scientific disciplines. For instance, it forms the basis for magnetic resonance imaging – a technique in which the principles of NMR are combined with signal encoding strategies in order to acquire tomographic images of an examination object. Because of a high abundance in biological tissues and a resultant relatively strong NMR signal, the Hydrogen nucleus is probed in the vast majority of medical MRI examinations. Therefore, the following analysis is concerned with the NMR properties of this nucleus and provides the foundation for the subsequent introduction to MRI.

2.1.1 Quantum mechanics

Being based on the concept of nuclear spin and its associated properties, the underlying principles of NMR can only fully be described by quantum mechanics [15]. However, many phenomena encountered in MRI, in which a large population of nuclei is observed simultaneously, can accurately be explained using a classical description [18]. Thus, this section introduces the quantum mechanical basics of the origins of an NMR signal and bridges the gap to a classical description of the principles applied in MRI.

The Hydrogen nucleus in an external magnetic field

The nucleus of a Hydrogen atom consists of a single proton, which has a non-zero spin with spin quantum number $s = 1/2$. Associated with it, is a spin angular momentum, $\mathbf{S} = (S_x, S_y, S_z)$, which gives rise to a nuclear magnetic dipole moment, $\boldsymbol{\mu} = (\mu_x, \mu_y, \mu_z)$, given by

$$\boldsymbol{\mu} = \gamma \mathbf{S}. \tag{2.1}$$

The gyromagnetic ratio, γ, denotes a nucleus-specific proportionality constant with a value of $\gamma = 267.52 \cdot 10^6\,\mathrm{rad\,s^{-1}\,T^{-1}}$ for the Hydrogen nucleus.
When being exposed to an external, static magnetic field, $\mathbf{B}_0$, which may without loss of generality be aligned with the z-axis of a 3D Cartesian coordinate system, i.e. $\mathbf{B}_0 = (0, 0, B_z)$, the magnetic moment is associated with quantized energy levels. They follow from

$$E = -\boldsymbol{\mu} \cdot \mathbf{B}_0 = -\mu_z B_z = -\gamma m \hbar B_z, \tag{2.2}$$

with $\hbar$ being the reduced Planck constant and m denoting the magnetic quantum number, which can take the values of $m \in \{-s, -s+1, \ldots, s-1, s\}$. Thus, in an external magnetic field, there exist $2s+1$ discrete energy levels, which are associated with the z-component of $\boldsymbol{\mu}$.
The occupation of these discrete energy levels is termed *Zeeman splitting* and is illustrated in Fig. 2.1 A for the particular case of a spin-1/2 nucleus. The lower energy level is also referred to as a *spin-up* and the higher energy level as a *spin-down* state and both follow from

$$E = \begin{cases} -\frac{1}{2}\gamma\hbar B_0, & \text{spin-up} \\ +\frac{1}{2}\gamma\hbar B_0, & \text{spin-down.} \end{cases} \tag{2.3}$$

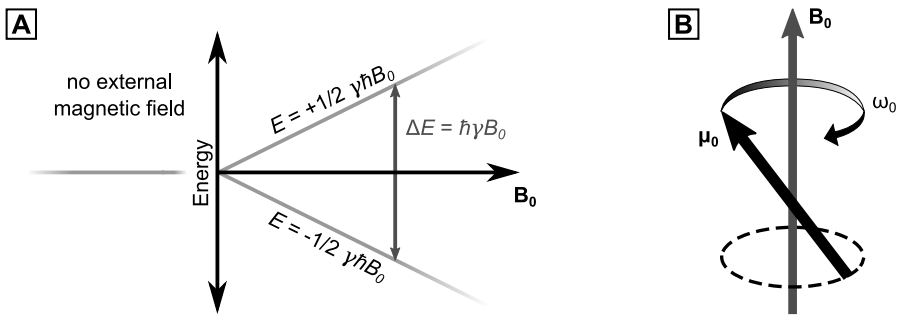

Figure 2.1: Spins in a magnetic field. **(A)** *Zeeman* splitting of a spin-$^1/_2$ particle. The nuclear magnetic dipole moment associated with the spin angular momentum of a nucleus interacts with an external magnetic field, B_0. This gives rise to two discrete energy levels with an energy difference, ΔE, which is proportional to the strength of the magnetic field. **(B)** Spin precession around $\mathbf{B}_0$. The external magnetic field exerts a force on the nuclear magnetic moment, which causes a precessional motion around the axis of the field.

The energy difference between these discrete energy levels can be determined from Eq. 2.2 and is given by

$$\Delta E = \hbar\gamma B_0 = \hbar\omega_0. \tag{2.4}$$

Besides a splitting into the different energy levels, the external magnetic field causes a precessional motion of the nuclear magnetic moments around the axis of the field. This is schematically illustrated in Fig. 2.1 B. The angular frequency of the precession is given by $\omega_0 = \gamma B_0$, which is known as the *Larmor equation*.
Irradiation of the sample with an electromagnetic pulse at this frequency can induce transitions between the discrete energy levels. After the pulse, when the spins *relax* back into the equilibrium state, the excess energy is released and becomes detectable. Since the time-course of these excitation and relaxation phenomena depends on the molecular environment of the spins, it yields information about the properties and the chemical composition of the sample. However, as will be shown in the following, in MR applications not a single spin is observed, but an ensemble consisting of a large number of nuclei.

Formation of a net magnetization

Under exposure to the external magnetic field and at a temperature of 0 K, all spins within an NMR sample would occupy the *spin-up* state, which is associated with a lower energy. At room temperature and physically feasible magnetic field strengths, however, the thermal energy associated with the thermal agitation of the particles exceeds the nuclear magnetic energy by several orders of magnitude.
The thermodynamic equilibrium of a spin ensemble in a magnetic field merely experiences a small bias towards the lower energy state of the nuclear magnetic energy. This causes an anisotropic distribution of spins, with a slight excess in the *spin-up* state. The ratio between the number of spins in the lower and the higher energy state follows a Boltzmann distribution and is given by

$$\frac{N_\uparrow}{N_\downarrow} = \exp\left(\frac{\Delta E}{k_B T}\right), \tag{2.5}$$

with k_B being the Boltzmann constant and T the absolute temperature of the sample consisting of $N = N_\uparrow + N_\downarrow$ spins in the respective spin states. At body temperature and realizable magnetic field strengths, this amounts to a spin excess of only a few *parts per million* in the spin-up state.

However, due to the large number of Hydrogen atoms in the human body, this population difference gives rise to a macroscopic net magnetization, $\mathbf{M}_0$, which has at equilibrium a magnitude of [19]

$$M_0 = \frac{N\gamma^2\hbar^2 B_0}{4k_B T}. \tag{2.6}$$

The net magnetization vector is a result of a summation over the expectation values of the nuclear magnetic moments of all spins. Even though on a microscopic scale they have non-zero magnetic moment components in directions perpendicular to $\mathbf{B}_0$, their random phases during the precession result in a net cancellation on a macroscopic scale. As a result, the magnetization at equilibrium only has a component along the direction of the external magnetic field.
This simultaneous observation of a large population of nuclei enables the transition from a quantum mechanical treatment of the nuclear magnetic dipole moment, $\boldsymbol{\mu}$, of each individual spin to a classical treatment of the net magnetization vector, $\mathbf{M}_0$, of the entire sample.

2.1.2 Bloch equations

As will be shown further below, the NMR measurement principle requires the magnetization vector to be tipped out of its equilibrium state so as to generate magnetization components in the transverse plane. Subsequently, the magnetization will return to its equilibrium state following a time course which is governed by the composition of the sample. These processes are called *excitation* and *relaxation* and their effects on the temporal evolution of the net magnetization vector are described by the *Bloch equations*. Assuming ideal experimental conditions, the equation of motion of the net magnetization is given by

$$\frac{\mathrm{d}\mathbf{M}}{\mathrm{d}t} = \underbrace{\gamma\mathbf{M}\times\mathbf{B}}_{\text{Precession}} - \underbrace{\frac{M_x\mathbf{e}_x + M_y\mathbf{e}_y}{T_2}}_{\text{T2 relaxation}} - \underbrace{\frac{(M_z - M_0)\mathbf{e}_z}{T_1}}_{\text{T1 relaxation}}. \tag{2.7}$$

The cross-product describes a torque, which acts on the magnetization vector and causes a precessional motion around the effectively applied external magnetic field. This can be a superposition of the static magnetic field, which is used for spin polarization, and further field components, which are required to excite the sample or to encode the signal. The relaxation terms describe the return of an excited spin ensemble to its equilibrium. It is characterized by a decay of the transverse and a saturation of the longitudinal magnetization components, which is governed by the tissue-specific time constants T_1 and T_2. Examples of representative excitation and relaxation trajectories are illustrated in Fig. 2.2 and further explained in the following. For these analyses, a homogeneous sample in a static and homogeneous external magnetic field is assumed and two coordinate systems are used.
The *stationary* reference frame is spanned by the orthogonal unit vectors $\mathbf{e}_x$, $\mathbf{e}_y$ and $\mathbf{e}_z$ and the z-axis is defined as being parallel to $\mathbf{B}_0$. Vector components along z are referred to as *longitudinal* and those in the xy-plane as *transverse* components. In the *rotating* reference frame, $\mathbf{e}'_z$ is pointing in the same direction as $\mathbf{e}_z$ and $\mathbf{e}'_x$ and $\mathbf{e}'_y$ are rotating at an angular frequency, ω, around the z-axis. Expressing the transverse magnetization components jointly in complex notation, conversion between both coordinate systems is denoted by $\overset{\circlearrowleft}{\rightarrow}$ and calculated as [19]

$$M_{xy} = M_x + i \cdot M_y \tag{2.8}$$

$$M'_{xy} = M_{xy} \cdot \exp(i\omega t) \tag{2.9}$$

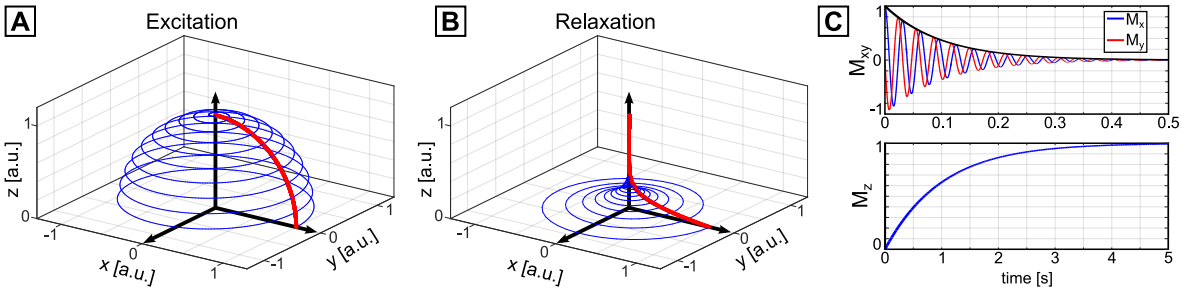

Figure 2.2: Temporal evolution of the net magnetization during excitation and relaxation. **(A)** The effectively applied magnetic field during excitation exerts a force on the magnetization, which causes a simultaneous precession about the axes of the static background and the oscillating excitation field (blue). In a frame of reference rotating at the Larmor frequency, the magnetization appears to be rotating merely about the axis of the excitation field (red). **(B)** After excitation, the magnetization relaxes back to its equilibrium state. **(C)** The relaxation can be decomposed into a vanishing transverse component and a saturation of the longitudinal component.

Excitation

Excitation describes the process of tipping the magnetization out of its equilibrium state and is achieved by irradiating the sample with a short-lived, oscillating electro-magnetic field, $\mathbf{B}_1(t)$. The direction of the field must be chosen perpendicular to the static magnetic field and can be expressed as $\mathbf{B}_1(t) = B_1 \cdot (\cos\omega t\ \mathbf{e}_x - \sin\omega t\ \mathbf{e}_y)$. Thus, in a reference frame that rotates at the same frequency as the RF pulse, the oscillating field appears stationary along one of the rotating coordinate axes. In order to efficiently excite the sample, the carrier frequency of the pulse must match the Larmor frequency of the spins, which is known as the *resonance* condition. Since for Hydrogen atoms and medical MRI magnetic field strengths this frequency typically lies in the range of a couple of hundred megahertz, the excitation pulse is also referred to as a *radio-frequency*, or *RF pulse*.
The excitation process usually takes only a few milliseconds, which is much shorter than typical values for the T_1 and T_2 constants in human tissues. As a result, the relaxation terms in Eq. 2.7 can be neglected. Denoting $\mathbf{B} = \mathbf{B}_0 + \mathbf{B}_1$ and assuming the initial condition $\mathbf{M}(0) = M_0\mathbf{e}_z$, the solution to the Bloch equations during excitation is given in the stationary and rotating frames of reference by

$$M_x(t) = \quad M_0 \cdot \sin\omega_1 t \cdot \cos\omega_0 t \quad \xrightarrow{\circlearrowleft} \quad M'_x(t) = 0 \tag{2.10}$$

$$M_y(t) = -M_0 \cdot \sin\omega_1 t \cdot \sin\omega_0 t \quad \xrightarrow{\circlearrowleft} \quad M'_y(t) = M_0 \cdot \sin\omega_1 t \tag{2.11}$$

$$M_z(t) = \quad M_0 \cdot \cos\omega_1 t \quad \xrightarrow{\circlearrowleft} \quad M'_z(t) = M_0 \cdot \cos\omega_1 t, \tag{2.12}$$

for which it is assumed that the RF pulse is applied along the $\mathbf{e}'_x$-direction. The superposition of the static background field and the oscillating excitation field exerts a force on the magnetization vector, which causes a simultaneous rotation about the axes of both fields. As can be seen in Fig. 2.2 A, in the stationary frame of reference the motion of $\mathbf{M}$ describes a downwards spiraling trajectory on the surface of a sphere with radius M_0. In the rotating frame of reference, the magnetization vector describes a *forced* precession about the direction of the excitation field with an angular frequency of $\omega_1 = \gamma B_1$. In the illustrated example, the pulse amplitude and its duration was chosen so as to flip the magnetization entirely into the transverse plane, leaving no component along the z-axis. This is called a 90°-pulse, but excitation pulses can generally be chosen to induce any desired *flip angle*.

Relaxation

After the excitation pulse is turned off, the spin system seeks to return to its thermodynamic equilibrium state. On a microscopic scale, this is governed by two separate relaxation processes. Energy, which had been absorbed by the spin system during excitation, is transferred to the surrounding tissue. It is therefore also called *spin-lattice* relaxation and responsible for re-establishing the equilibrium Boltzmann distribution, thus explains the recurring longitudinal magnetization. Moreover, microscopic field fluctuations lead to slight position-dependent precession frequency differences, which causes a loss of phase coherence between the individual spins. This is called *spin-spin* relaxation and is a stochastic, irreversible process. Since the net magnetization is a result of a summation over the expectation values of the nuclear magnetic moments of all spins, it explains the vanishing transverse magnetization.
On a macroscopic scale, relaxation leads to an exponential decay of the transverse and an exponential regrowth of the longitudinal net magnetization components. The longitudinal relaxation is characterized by the time constant T_1 and the transverse relaxation by T_2. The motion of the net magnetization vector during relaxation follows from solving Eq. 2.7 and is given by

$$M_x(t) = \quad M_\perp \cdot \exp(-t/T_2) \cdot \cos\omega_0 t \quad \xrightarrow{\circlearrowleft} \quad M'_x(t) = 0 \tag{2.13}$$

$$M_y(t) = -M_\perp \cdot \exp(-t/T_2) \cdot \sin\omega_0 t \quad \xrightarrow{\circlearrowleft} \quad M'_y(t) = M_\perp \cdot \exp(-t/T_2) \tag{2.14}$$

$$M_z(t) = M_0 - (M_0 - M_\parallel) \cdot \exp(-t/T_1) \quad \xrightarrow{\circlearrowleft} \quad M'_z(t) = M_0 - (M_0 - M_\parallel) \cdot \exp(-t/T_1), \tag{2.15}$$

with $M_\perp$ and $M_\parallel$ being the magnitudes of the transverse and longitudinal magnetization components immediately after excitation. Fig. 2.2 B illustrates the temporal evolution of the magnetization during relaxation. It demonstrates the effect of a shorter T_2 than T_1 time constant, which is typical for most biological tissues, and which results into a vanished transverse magnetization long before the longitudinal magnetization has reached its equilibrium state.
As will be shown in Section 3.2.2, the effective transverse relaxation is even shorter, which is due to macro- and mesoscopic field inhomogeneities which induce a further spin dephasing [20]. These B_0 inhomogeneities are attributed to external sources, so that the reduction in transverse magnetization is characterized by a so called T_2^*-relaxation. It follows from $1/T_2^* = 1/T_2 + 1/T_2'$, with T_2' being the time-constant which characterizes the relaxation due to external field inhomogeneities.

Signal reception

The time course of the magnetization during the relaxation period can be observed by placing *receiver-coils* close to the sample. According to *Faraday's Law of Induction*, the rotating transverse magnetization leads to a changing magnetic flux seen by the coil, which in turn induces an electromotive force in the coil windings. The resultant alternating voltage is proportional to the transverse magnetization and, therefore, a measure of the sample magnetization and its relaxation rate.
In Fig. 2.2 C, the relaxation time course of the net magnetization is decomposed and plotted individually for each vector component. In the stationary frame of reference, the x- and y-components oscillate at the Larmor frequency while decaying exponentially in magnitude. This corresponds to the signal seen by the receiver coil and is known as a *free induction decay* (FID). To exploit this technique for imaging applications, it is necessary to spatially encode the signal originating from different locations within the sample, which is explained in the following section.

2.2 MR image encoding

The origin of the MR signal has been derived and its detection principle has been described. Without any encoding strategies, however, the recorded FIDs correspond to the volume integral of the signals received from the entire sample. Thus, imaging applications require a form of spatial signal encoding, which is achieved by superimposing magnetic field gradients to the sample. As will be shown in the following, these encoding fields cause position dependent variations of local spin precession frequencies, which enables the attribution of individual signal contributions to distinct positions within the sample.

2.2.1 Signal localization

In this analysis, only the detectable transverse magnetization, given by Eqs. 2.13 and 2.14, is considered and expressed in complex notation described by Eq. 2.8. MR images are treated as voxelized representations of continuous, but non-uniform objects, with corresponding discrete voxel positions $\mathbf{r} = (x, y, z)$. Depending on the tissue within a given voxel, the relaxation constants, $T_1(\mathbf{r})$ and $T_2(\mathbf{r})$, become functions of space. Moreover, as described by Eq. 2.6, the equilibrium magnetization becomes a function of position and *spin density* within a given voxel. The associated transverse magnetization immediately after excitation is defined as $M_{xy}(\mathbf{r}, 0) = M_0(\mathbf{r}) \cdot \mathrm{f}(\alpha(\mathbf{r}), TR)$. It depends on the effectively applied flip angle, $\alpha(\mathbf{r})$, and an acquisition timing parameter, TR, which will be introduced further below. Lastly, the contribution of the magnetization in each voxel to the detected signal is weighted by a function, $s(\mathbf{r})$, which is associated with the sensitivity of the receiver coil with respect to the voxel positions.

Application of the Bloch equations for the MR signal description

The solutions of the Bloch equations during the relaxation period can be extended by an additional phase factor, $\exp(-i\phi(\mathbf{r}, t))$, which accounts for field components other than the applied static magnetic field. It originates from variations of local precession frequencies, $\Delta\omega(\mathbf{r}, t)$, which can be attributed to unwanted B_0 field inhomogeneities or purposefully applied encoding fields.

$$\Delta\omega(\mathbf{r}, t) = \gamma \Delta B_z(\mathbf{r}, t) \quad \longrightarrow \quad \phi(\mathbf{r}, t) = \int_0^t \Delta\omega(\mathbf{r}, \tau) d\tau \tag{2.16}$$

Including this term into the Bloch equations and using the aforementioned definitions, the induced signal in the receiver coil is then given by [19]

$$\begin{aligned} u(t) &= -\int_V s(\mathbf{r}) \frac{\partial}{\partial t} \left[M_{xy}(\mathbf{r}, t) \right] d\mathbf{r} \\ &= -\int_V s(\mathbf{r}) \frac{\partial}{\partial t} \left[M_{xy}(\mathbf{r}, 0) \exp\left(-i\omega_0 t - \frac{t}{T_2(\mathbf{r})} - i\phi(\mathbf{r}, t) \right) \right] d\mathbf{r}. \end{aligned} \tag{2.17}$$

The MR signal oscillates at a carrier frequency, ω_0, and the spatially depended T_2-relaxation leads to an overall decrease in signal amplitude. Depending on the strength of the added field components, the received signal will be further modulated by the effect of the local phase offsets. In the following section it is demonstrated how these properties can be exploited in order to reconstruct an image of the transverse magnetization distribution from the acquired MR signals.

The k-space formalism and its application to MR imaging

To further simplify the MR signal equation, it is assumed that the readout period is short compared to the relaxation time constants. Denoting the time of the signal acquisition as the *echo time*, TE, the T_2-decay then leads to a tissue-dependent modulation of the apparent transverse magnetization as a function of its position. This induces a contrast weighting, which can be approximated by $c(\mathbf{r}) = \exp(-TE/T_2(\mathbf{r}))$. Ideal experimental conditions are still assumed for this analysis, thus the effective transverse relaxation according to T_2^* is ignored. Consequently, it is assumed that no B_0 field variations other than those generated by the encoding gradients are present. Using the definitions of the orthogonal gradient encoding fields given by

$$G_x = \frac{dB_z}{dx}, \quad G_y = \frac{dB_z}{dy} \quad \text{and} \quad G_z = \frac{dB_z}{dz}, \tag{2.18}$$

the added phase factor can be described entirely by the position within the object and the applied encoding gradient *waveforms*. Thus, Eq. 2.16 can be written as

$$\phi(\mathbf{r}, t) = \gamma \int_0^t \mathbf{r} \cdot \mathbf{G}\, d\tau. \tag{2.19}$$

To simplify the notation, a new set of coordinates is introduced, which defines the gradient-integrals in terms of so called *k-space* coordinates [21] according to

$$k_x(t) = \gamma \int_0^t G_x(\tau) d\tau, \quad k_y(t) = \gamma \int_0^t G_y(\tau) d\tau \quad \text{and} \quad k_z(t) = \gamma \int_0^t G_z(\tau) d\tau. \tag{2.20}$$

Moreover, evaluating the time-derivative, ignoring constant factors and demodulating the receiver signal through multiplication with $\exp(i\omega_0 t)$ to form a baseband signal [22], Eq. 2.17 can be re-written to yield the comprehensive *MR signal equation*. It is given by

$$u(t) \approx \int_V \underbrace{s(\mathbf{r})\, c(\mathbf{r})\, M_{xy}(\mathbf{r}, 0)}_{\text{Image}} \cdot \exp(-i(k_x(t)x + k_y(t)y + k_z(t)z)) d\mathbf{r}. \tag{2.21}$$

It shows that the acquired MR data corresponds to a multi-dimensional Fourier transform of the transverse magnetization, weighted by the coil sensitivity and the local relaxation rate. A full image of the object can be reconstructed by sufficiently sampling the k-space domain and by applying an inverse Fourier transformation to the acquired dataset. In the following section, it is demonstrated how this is achieved by sequentially applying different gradient encodings and by reading and storing the resultant varying MR signals.

2.2.2 Pulse sequences

The previous analyses have shown that a spin system and the temporal evolution of its associated net magnetization can be manipulated via *sequences* of applied RF and gradient pulses. Many techniques have been developed, which exploit these methods in various ways in order to acquire MR images with different contrasts or even entirely different information content. One possible acquisition strategy is schematically illustrated in Fig. 2.3 and further explained in the following. It is a 2D imaging technique, in which the MR signal is received only from a thin slice through the imaging volume. Thus, the aforementioned gradient encoding techniques merely need to be applied in the remaining two dimensions.

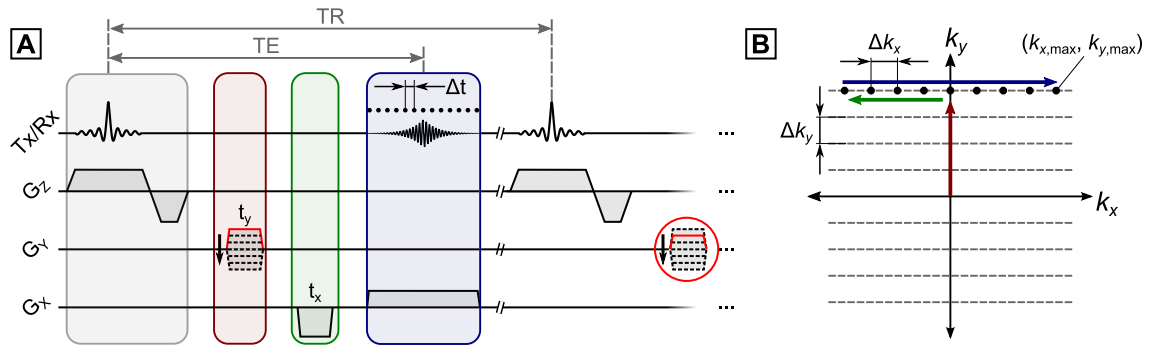

Figure 2.3: Example of a basic MR image acquisition scheme. **(A)** The gray-shaded area depicts the slice selection. A gradient applied along the z-direction introduces a linear variation of local precession frequencies. Excitation with an RF pulse of a certain bandwidth excites only spins in a 2D plane, in which the resonance condition is met. The color-coded areas show how the spatially encoding gradient pulses are used to impose the previously introduced phases to the signal originating from the excited 2D plane (see text for details). **(B)** Through the application of G_y (red), the MR signal gets modulated and, consequently, k-space is traversed along the corresponding k_y-direction. The same holds true for the subsequent application of G_x (green). By recording the MR signal while applying a constant $+x$-gradient, the k-space dataset can be filled sequentially. The sequence timing parameters TE and TR influence the magnetization evolution and, hence, the contrast of the final MR image.

Slice selection

Non-selective RF pulses, transmitted at the Larmor frequency in the absence of any other magnetic encoding fields, would excite the entire sample. The introduced gradient encoding process, therefore, would need to encode the signal in three dimensions in order to reconstruct the MR image. Even though this *3D imaging* technique is a commonly applied acquisition scheme, a concept known as *slice selective excitation* can already restrict the signal to be originating solely from a thin slice through the volume. Consequently, the required encoding processes are reduced to the remaining two dimensions within the imaging plane.
The gray-shaded area in Fig. 2.3 A highlights the RF and gradient pulses that are required for this process. The application of a gradient field along the z-axis introduces a variation of local precession frequencies along that direction. Excitation with an RF pulse of a certain finite bandwidth, $\Delta\omega$, generates transverse magnetization components only in those regions, in which the resonance condition is met and all other regions remain ideally unaffected. Thus, by carefully choosing the frequency content of the RF pulse, as well as the strength and orientation of the slice selection gradient, an arbitrarily oriented slice with desired thickness can be excited.
It is to be noted, that the slice selection gradient causes a position-dependent phase accrual of the net magnetization components in through-slice direction. An additional gradient pulse can *re-phase* these transverse magnetization components. It is applied immediately after excitation and with the same direction and amplitude, but opposite polarity and half the duration. Subsequently, the transverse magnetization is in phase and evolves merely under the influence of the static magnetic field and intrinsic relaxation effects.

Image encoding

The MR signal encoding process is highlighted in color in Fig. 2.3 A. Following Eq. 2.19, the application of the illustrated encoding gradients induces local phase variations across the object. Their underlying gradient waveforms are associated with certain k-space coordinates, which can be calculated from Eq. 2.20. These coordinates depend on the gradient direction, amplitude and

duration, and can be sampled individually by varying these parameters. For each coordinate, the associated MR signal is recorded and written into the k-space dataset, which is sequentially filled before being Fourier transformed to yield the final MR image. The order of the encoding process and its effect on the MR signal is best understood, when analyzing the individual encoding periods in the associated sequence diagram.
The red-shaded area after the slice-selection depicts a y-gradient with a certain positive amplitude, which is applied for a time t_y, and which results in a certain $+k_y$-coordinate. Likewise, highlighted by the green-shaded area, the subsequent application of an x-gradient with a given duration t_x and a certain negative amplitude results in a certain $-k_x$-coordinate. Thus, the phase factor in the MR signal equation is at this time uniquely defined by the amplitudes and durations of the applied in-plane gradients and associated with a distinct k-space position.
The blue-shaded area highlights the subsequently performed MR signal readout period. Under the constant application of a positive x-gradient, the k_x-coordinate evolves linearly as a function of the chosen gradient amplitude and its duration from $-k_x$ to $+k_x$. Discretization of the readout period into an equidistantly spaced set of N sampling points, each of which separated by the dwell time, Δt, results in an incremental change in the k_x-position. Since in the meantime no gradient is applied in the y-direction, the k_y-coordinate remains unchanged. Thus, by simultaneously recording the MR signal, which is at each time defined by Eq. 2.21, the associated *line* of the k-space is filled. The time, at which the area under the positive *readout* gradient equals that of the previously applied *pre-phasing* gradient, is termed *echo time* (TE) and maximizes the amplitude of the received MR signal for the current k-space line. All three gradient encoding steps and their effects on the k-space traversal are shown in Fig. 2.3 B.
The final MR image can be reconstructed artifact-free, only if the entire k-space has been sampled before the inverse Fourier transform is being applied. Thus, in the given example, after having acquired the first line at a given k_y-value, all remaining lines must be recorded subsequently. This is achieved by repeating the aforementioned processes, from the slice selection to the readout period, and by incrementally reducing the G_y amplitude in each step so as to sample each line from $+k_y$ to $-k_y$. The time between two slice-selective sample excitations is termed *repetition time*, TR. The sampling density in the k-space domain, given by the incremental changes Δk_x and Δk_y, as well as the absolute maximum k-coordinates, $k_{x,\max}$ and $k_{y,\max}$, are dictated by the desired spatial resolution of the MR image and its *field-of-view*. This type of MR imaging technique is termed a *gradient echo sequence* and is one of many acquisition variants.

Image contrast

If the coil sensitivity and the flip angle is assumed to be homogeneous, the image contrast depends on three parameters. These include the spin density at a given voxel position and the tissue-specific T_1 and T_2 relaxation times. A relative weighting with respect to one of these parameters can be generated through choice of the values for TE and TR, respectively. The TR-interval denotes the time during which the longitudinal magnetization can relax back to equilibrium before being tipped back into the transverse plane. During the TE-interval, the transverse net magnetization components dephase and its duration dictates the amount of residual transverse magnetization at the time of the signal readout.
For the analyses so far, only the net magnetization magnitude has been considered. However, the Fourier transformed MR images are complex-valued and, thus, have an additional phase associated with the transverse magnetization at each spatio-temporal sampling point. This can be regarded as another source of MR image contrast and will be treated in Section 3.3.2.

2.3 MR hardware

The NMR phenomenon finds application in multiple scientific areas, each of which with its specific demands in terms of the strength of the magnetic field, the size of the system, required additional components and other design criteria. This section gives a brief overview of the hardware of a medical MR scanner, which is typically used for whole-body applications.

2.3.1 MR system components

The previously introduced principle of NMR and its usage in MRI demands the application of three types of magnetic fields. A strong static magnetic field is required to generate a sufficiently strong sample magnetization. Moreover, three orthogonal dynamic field components, with temporal variations in the kilohertz-range, are needed for the image encoding process. Lastly, an excitation field, applied perpendicular to the static field and oscillating in the megahertz-range, must be applied for the excitation of the spin system. All three types of fields are generated via dedicated coil assemblies. These main components must be constructed as compact as possible, but with the demand of providing sufficient space to enclose a human subject. Thus, as schematically illustrated in Fig. 2.4, most MR systems have a cylindrical geometry. The most common design approaches are briefly discussed in the following.

The magnet

Typical magnets for in vivo MR applications must adhere to several challenging requirements in their design and construction process. Reasoned by the Boltzmann distribution and as described by Eq. 2.6, the magnetic field strength needs to be high, so as to induce a strong sample magnetization and provide for an associated high *signal-to-noise ratio* (SNR). Moreover, as will be explained in Section 3.2.2, most MR measurements require the magnetic field to vary by only a few parts per million or less from the specified field strength at a simultaneously very high temporal stability. All of these demands have to be combined in a system that is large enough for human whole-body applications.
MR scanners that are used in research and clinical routine typically employ magnets that operate at field strengths of 1.5 or 3.0 T. In an attempt to further increase the SNR, there is a trend towards *ultra-high field* systems with even higher field strengths of as much as 7.0 T and above. Most commonly, superconducting solenoids, wound on the surface of a cylinder, are employed in order to generate these static magnetic fields. To keep the superconducting wires below their critical temperature, the magnets are cooled down to $\sim$4 K and are enclosed in a vessel containing liquid helium.
The ideal NMR magnet is a perfectly wound solenoid with infinite length, which would theoretically generate an absolutely homogeneous magnetic field. However, any practically realized truncated version necessarily has a slightly non-homogeneous field distribution. Thus, modern magnets make use of a sectioned coil design [23] or employ a compensated solenoid [24] to homogenize the target field inside the scanner within a spherical volume of a given diameter.

The gradient system

The gradient system is used to perform the signal manipulations that are required for the image encoding process described in Section 2.2.1. The required linear variations of the z-component of

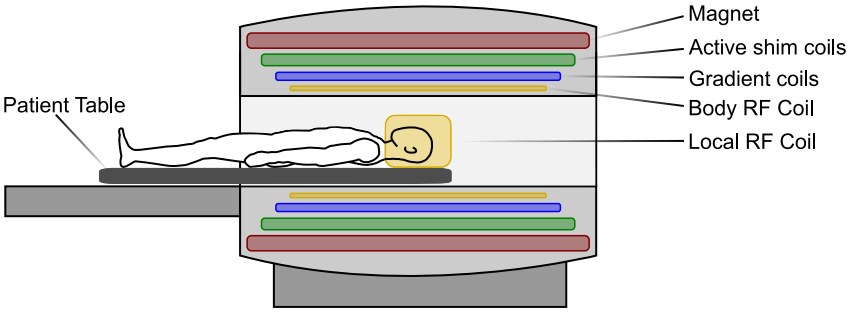

Figure 2.4: Schematic of an MR Scanner. The static magnetic field is typically generated by a solenoid made from superconducting wires enclosed in a liquid helium containing vessel. Additional active shim coils are employed in order to correct for magnetic field distortions. The gradient coil assembly can be inserted into the magnet bore and often houses trays for additional passive shim elements. Sample excitation and signal reception can be performed using a large body coil or smaller local coils.

the magnetic field along one of the three main axes can already be generated by relatively simple coil geometries. A *Maxwell* coil can generate a z-gradient and a pair of *Golay* coils, rotated by 90° towards each other, can generate the transverse x- and y-gradients, respectively.
However, besides generating the desired linear field variations, modern gradient systems must fulfill further requirements, which turned the associated coil design into a scientific discipline of its own. Targeting high gradient amplitudes and low rise times to enable fast imaging, led to high-performance gradient systems with complicated wire patterns [25]. Other design criteria led to the development of a more efficient temperature-handling [26] or a reduced risk of gradient-induced peripheral nerve stimulations [27]. The associated numerical gradient coil optimizations are often formulated such as to search for a current path, which generates the targeted field pattern, while adhering to side conditions imposed by the desired gradient coil properties.
The final wire patterns are usually enclosed in epoxy resin, which structurally fixates the coils in order to withstand the mechanical forces that they are exposed to. These assemblies usually contain additional trays, which can accommodate passive B_0 *shim* elements. They are used to compensate for static B_0 field inhomogeneities which originate from magnet imperfections or other constant field distortions. The use of these elements is further detailed in Section 3.2.1.

The radio frequency system

The RF system is required for the sample excitation and the signal reception. The applied RF coils can be implemented as dedicated transmitters or receivers, or as combined *transceiver* coils, which rapidly switch between both modes. They are typically optimized for their area of application and differ in complexity and size. They can either be incorporated as full body coils into the magnet assembly or realized as smaller local coils, which can be brought closer to the object in order to increase efficiency and sensitivity [28]. Arrays of multiple small-diameter coils with different sensitivities across the imaging object can be used to improve performance [29]. *Parallel imaging* methods make use of this property and and include it as a degree of freedom into the signal encoding and image reconstruction processes [30].
The operating frequency of the RF coils scales with the magnetic field strengths and the associated wavelength approaches the size of the imaged body parts for *ultra-high field* scanners. This can lead to constructive and destructive interferences, which impairs the image quality and can even impose a safety hazard when generating *hot-spots*. Thus, optimizations concerned with the excitation and reception process are focused on an improved hardware and its optimal control.

The shim system

Due to fabrication tolerances and other sources of magnetic field distortions, non-uniformities in the static magnetic field of an MR system are generally inevitable. However, since any unintended field distortion induces additional local precession frequency variations, attempts are made to mitigate these by means of B_0 *shim* systems. Besides field homogeneity adjustments based on passive shim elements, some MR scanners are equipped with additional superconducting shim coils. They are designed to generate well-defined spherical harmonic correction fields and their driving currents are adjusted during the magnet installation. Subsequently, the currents remain constant, unless the MR system is modified in a way which causes changes in the static magnetic field distribution. This way, the magnetic field homogeneity of an empty scanner, measured as the peak-to-peak deviation within a spherical volume with diameter of as much as 45 cm, can be shimmed to 1-2 parts per million [31].
However, when placing an examination subject into the scanner, the associated unique distribution of tissues with varying magnetic susceptibilities distorts the initial field homogeneity. This causes strong and localized B_0 offsets and necessitates individual pre-scan shim adjustments. MR systems, therefore, contain user-controllable sets of room-temperature shim coils, which are most commonly designed such as to produce spherical harmonic field distributions up to 2^{nd} and sometimes 3^{rd} order. The required wire patterns can be determined analytically, which leads to relatively simple current paths. Alternatively, numerical optimization algorithms can be employed to find current paths which generate the desired target field while simultaneously meeting additional performance specifications [32]. The choice of spherical harmonics as a basis for the generation of the correction fields stems from the early days in NMR [33, 34] and a comprehensive treatise of this topic has been provided by Roméo and Hoult [35]. Field patterns other than spherical harmonics are also used for B_0 shimming, but rather applied in research and have not yet made their way into clinical routine [36]. Being the central topic of this work, more information on B_0 shimming will be given in the following literature review.

3

Review of B_0 shimming techniques

B_0 shimming refers to the process of homogenizing the static magnetic field of an MR system. It is an integral part of both the magnet installation procedure when siting the system, as well as the repeatedly performed subject-specific pre-scan adjustments. A good B_0 field homogeneity is critical, since it has significant impact on the data quality of the subsequently performed MR measurements.

Upon installation, mainly due to fabrication tolerances and magnetic forces that act on the coil windings, the bare magnet will have a field homogeneity which is insufficient for most MR applications. Therefore, magnetizable material is added to specific locations in the magnet bore, such that apparent inhomogeneity terms are canceled. The term *shimming* stems from this procedure and, figuratively speaking, refers to the process which was conducted when permanent magnets were homogenized by adding small ferro-magnetic wedges to the assembly. It is sometimes also used in the context of optimizing the homogeneity of the RF transmit field, but will in the remainder of this work always refer to the homogenization of the static magnetic field of the MR system.

For the work conducted in the scope of this thesis, the compensation of susceptibility-induced B_0 field inhomogeneities is of greater relevance than those of magnet imperfections. These highly subject-dependent field distortions are typically canceled by means of active shim coils, which are predominantly designed such as to generate spherical harmonic magnetic shim fields. Therefore, the following chapter discusses the origins and nature of B_0 inhomogeneities and gives a thorough literature review about available methods that are employed to compensate for them. Mainly shim approaches for MR applications in the human brain are considered in this state-of-the-art summary. The interested reader is also referred to review articles, which give an excellent introduction into this topic [37, 38, 39, 40] and which are complemented by the book chapters in [41] and [42].

In recent times, non-spherical harmonic shim approaches have emerged with the goal of addressing the remaining challenges in B_0 shimming. These techniques, as well as a brief presentation of possible retrospective B_0 distortion correction alternatives, are summarized in the end of this chapter.

3.1 Basic principles

The fundamental concepts, which form the basis for conventional B_0 shim approaches, are explained in this section. Since the most widespread form of shimming is based on spherical harmonic functions, their mathematical description as well as their relevant properties with respect to B_0 shimming are introduced. Moreover, common definitions of magnetic field homogeneity and the associated quantification of an obtainable B_0 shim quality are given.

3.1.1 Spherical harmonics

The magnetic field inside the empty bore of an MRI scanner obeys Laplace's equation, which is given by $\nabla^2 \mathbf{B}_0 = 0$. Its solution can be expressed as a linear expansion of real regular solid spherical harmonic functions (shortly termed spherical harmonics in the following), which makes them a natural choice for the target field in shim coil design. Their properties are described in the following and the first six orders of the spherical harmonic functions are illustrated in Fig. 3.1.

Mathematical description

Given a certain radius, r, and the polar and azimuthal angles, θ and ϕ, respectively, the spherical harmonics are conveniently expressed in polar coordinates and characterized via their order, n, and degree, m. The associated approximation of the distortion field, ΔB_0, follows from [43]

$$\Delta B_0(r, \theta, \phi) = \sum_{n=0}^{\infty} \sum_{m=-n}^{n} c_{n,m}\, r^n\, P_{n,m}(\cos\theta) \cos(m\phi - \phi_m). \tag{3.1}$$

The functions given by $P_{n,m}(\cos\theta)$ are the associated Legendre polynomials, $c_{n,m}$ is a constant and $\phi_m = \pi/2$ for $m < 0$ and $\phi_m = 0$ for $m \geq 0$. The zeroth order term corresponds to a global field offset, the first order terms are field gradients along all three spatial directions and all higher order terms are functions with increasing spatial variations. Functions for which $m = 0$ are rotationally invariant about the z-axis and are referred to as the *zonal* harmonics. Functions for which $m = n$ are termed sectoral harmonics and all other functions are called *tesseral* harmonics. Both oscillate around the z-axis with a spatial frequency that depends on m.

Spherical harmonic shim coils

Under the assumptions that the magnetic field inside the MR scanner can accurately be described via a spherical harmonic expansion, it is a natural choice that shim coils are designed such as to produce ideally pure spherical harmonic field distributions. A variation of the shim coil currents then corresponds to an adjustment of the coefficients of a suitable compensation field expansion. However, the fact that the ideal functional forms can only be generated up to a certain accuracy using realistically manufactured shim coils, leads to inevitable shim *impurities*. These have to be considered when adjusting the shim currents, which will be further detailed in Section 4.2.2. Moreover, due to space limitations in the bore of an MR scanner, the spherical harmonic expansion is truncated and limited to typically the 2^{nd} order, thus leading to merely nine shim terms. Mostly non-standard hardware setups currently include higher order terms. A shim coil insert applied in this work comprises up to the full 4^{th} order and four 5^{th} and two 6^{th} order terms, which correspond to the currently highest order terms used in human MR applications.

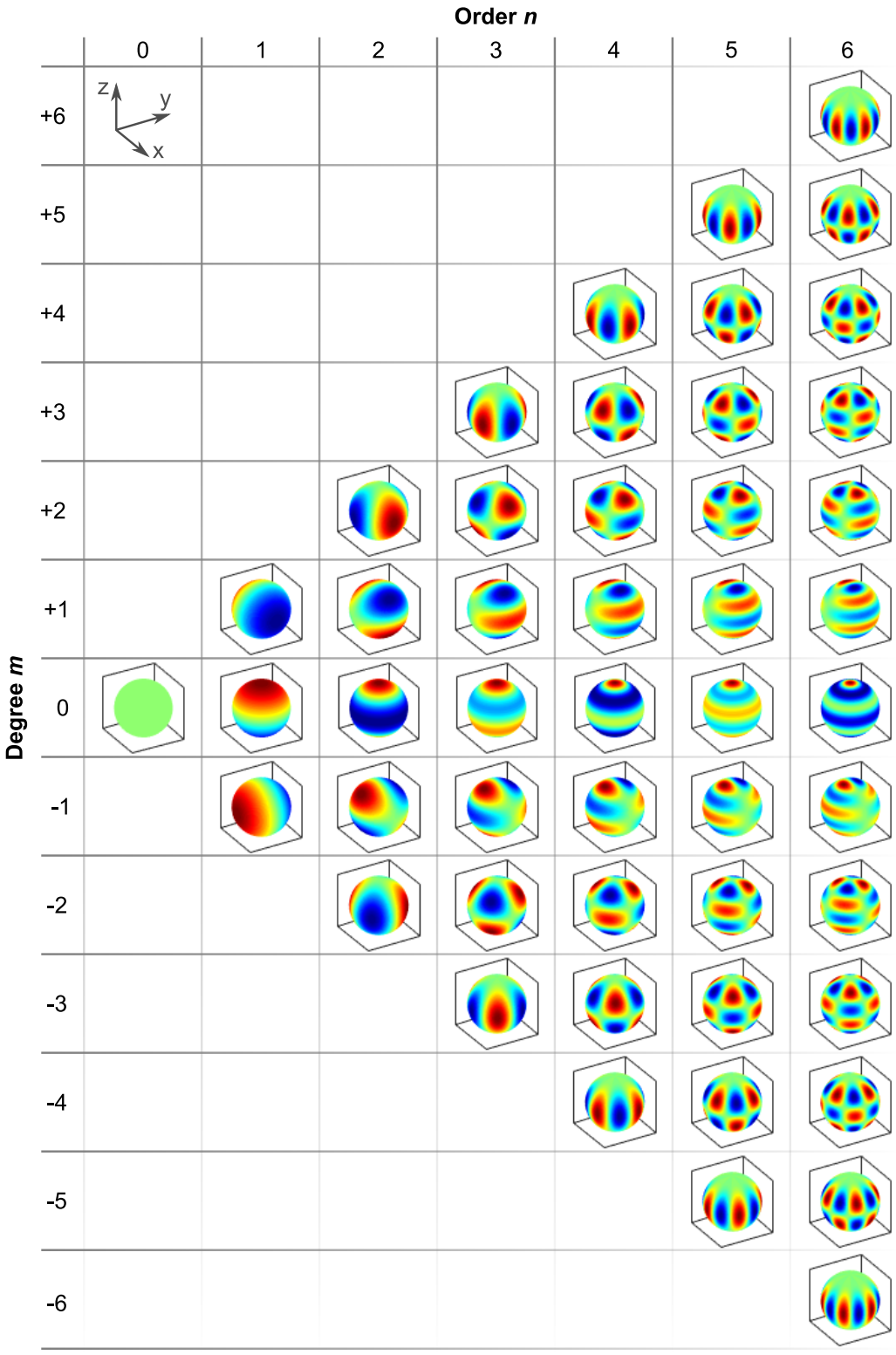

Figure 3.1: Spherical harmonic functions plotted on the surface of a sphere. B_0 shim systems of conventional MR scanners typically have a set of shim coils, which generate magnetic fields up to and including the 2^{nd} order. A very high order shim insert employed in the scope of this thesis is capable of generating all spherical harmonics up to and including the full 4^{th} order, except for the linear 1^{st} order terms. Additionally, four 5^{th} order terms with $m \in \{-5, -4, +4, +5\}$ and two 6^{th} order terms with $m \in \{-5, +5\}$ can be generated.

Properties of spherical harmonics

The spherical harmonic functions are orthogonal over spherical volumes located in the iso-center of the shim system. In terms of the shimming process, this implicates that each shim coil current can individually be optimized such as to cancel the associated inhomogeneity term. For a long time, this formed the basis for manual shim adjustments which will be detailed in Section 3.3.1. For non-centered volumes, however, this property is no longer given and different spherical harmonics can *degenerate* to have the same functional form. Manual shim adjustments then become cumbersome or even impossible [44]. Moreover, it also poses a challenge to automated shim calculations based on numerical optimizations, because it leads to an ill-conditioning of the problem and can result into excessive shim currents.

3.1.2 Homogeneity criteria and field measurement units

A given magnetic field homogeneity is always associated with a certain volume-of-interest over which the field was optimized and is, therefore, dependent upon the underlying MR acquisition. For human brain applications, this volume is typically a single voxel, a single slice, a slab of slices, the entire brain or individual anatomical structures and the achievable B_0 homogeneity is generally better for smaller volumes.
To quantify the B_0 shim quality, it is common to determine the standard deviation of the residual field offsets in the entire region-of-interest. Instead of absolute field offsets in units of *Tesla*, the homogeneity is typically given in units of *Hertz*. Realistic values after 2^{nd} order whole-brain shimming are in the order of ~ 20 Hz at 3 T and, correspondingly, ~ 47 Hz at 7 T. Thus, the induced field offsets scale linearly with B_0 and the achievable homogeneity is dependent on the main field strength. In order to compare B_0 homogeneity across multiple field strengths, it is possible to express it in *parts-per-million* (ppm). This implies that the aforementioned whole-brain homogeneity after 2^{nd} order shimming can be quantified as ~ 0.16 ppm.
When applied to non-Gaussian frequency distributions, the standard deviation as a measure for the actual B_0 homogeneity can be misleading. Alternatively, percentile ranges can be determined, which indicate the fraction of voxels that is within a specified frequency range.

3.2 | B_0 inhomogeneities in MR systems

This section introduces the origins of the B_0 field inhomogeneities and the impact that they can have on different MR applications. It motivates the need for the application of the B_0 shimming techniques, which will be introduced thereafter.

3.2.1 Sources of B_0 inhomogeneities

Inhomogeneities in the static magnetic field can be classified according to their scale and, thus, grouped into micro-, meso- and macroscopic contributions [20]. Microscopic inhomogeneities cause spin relaxation, whereas mesoscopic inhomogeneities can contribute to contrasts used to monitor physiological parameters [37]. The extent of macroscopic inhomogeneities, however, spans over multiple voxels and provides no access to information of anatomical or physiological interest. Hence, they are sought to be minimized in the shimming process.

System imperfections

Upon installation, the homogeneity of the bare magnet is usually insufficient for MR applications. This is due to the fact that finite-length solenoids necessarily compromise achievable field homogeneity for compactness. Magnet design optimization can alleviate this problem, e.g. by using additional compensation coils or by sub-dividing the solenoid into multiple discrete parts with individual current densities [24]. However, fabrication tolerances and forces that act on the coil windings also lead to deviations of the real from the ideal current density distribution and introduce further inhomogeneities. The strength of these inhomogeneities are typically significant and can be on the order of tens or hundreds of ppm. Dedicated adjustment processes, which are performed during the magnet installation procedure, reduce this inhomogeneity to around 1-2 ppm peak-to-peak [41]. This is explained in further detail in Section 3.4.1.

Sample-induced B_0 inhomogeneities

In a vacuum, the magnetic field strength, $\mathbf{H}$, is related to the magnetic flux density, $\mathbf{B}$, via the vacuum permeability, μ_0, according to $\mathbf{B} = \mu_0\mathbf{H}$. In the presence of a linear medium, this relation changes to $\mathbf{B} = \mu_0(\mathbf{H} + \mathbf{M})$, where $\mathbf{M}$ is the magnetization of the material. The strength of the magnetization is governed by the relative magnetic permeability of the material, μ_r. Introducing the material magnetic susceptibility, given by $\chi = \mu_\mathrm{r} - 1$, it can be calculated as $\mathbf{M} = \chi\mathbf{H}$. For non-magnetic materials, $\chi = 0$ and materials with a slightly positive or negative susceptibility are referred to as being *para-* or *diamagnetic*, respectively. Materials that reveal *ferromagnetism* have $\chi \gg 1$ and are MR-incompatible. Typical values of magnetic susceptibilities encountered in human MR applications are $\chi_\mathrm{air} = 0.3$ ppm, $\chi_\mathrm{bone} = -11.3$ ppm and $\chi_\mathrm{water} = -9.2$ ppm [37]. Inhomogeneities in the magnetic flux density, which is often loosely referred to as the *magnetic field*, arise at boundaries between materials with susceptibility differences. The resultant strength depends on the susceptibility difference and the geometry of the individual objects. Thus, the magnetic field homogeneity is being distorted as a function of the susceptibility gradients and the geometrical shapes of all involved objects. In the human brain, the most prominent field offsets arise at the boundaries between brain tissue and air-filled cavities. The frontal lobe, for example, is affected by the susceptibility gradient between the brain tissue and the air within the nasal cavities and, likewise, the temporal lobes are affected by the interface to the auditory canals.

These field inhomogeneities are spatially varying, but constant over time. Nonetheless, inducing field offsets up to ~ 5 ppm, their impact on the MR measurement can be significant. In addition to that dynamic changes in the magnetic field can occur. For example, besides motion artifacts, any intra-acquisition subject movement results in a change of the susceptibility distribution relative to B_0, which then leads to field perturbations [45]. Whereas the former can be addressed via prospective [46] or retrospective [47] motion correction techniques, the latter needs additional means in order to measure and correct for the B_0 changes. Breathing, the beating heart or any other change of the position of the susceptibility distribution outside the imaging volume can also distort the field inside the region-of-interest [48]. Even though the magnitude of these inhomogeneities is rather small and typically in the order of ~ 0.1 ppm, they can pose a problem to some sensitive applications.

3.2.2 Impact of static B_0 inhomogeneities

Inhomogeneities in the static magnetic field lead to variations of the local precession frequency and a concomitant shortening of the transverse relaxation. Depending on the type of MR application, this has various effects on the acquired data. One of which is a loss of signal due to canceling components of the magnetization vector. Depending on the chosen echo time, this can ultimately result into a complete dephasing of the signal in highly inhomogeneous regions. Since the slice-thickness in MR imaging applications is typically larger than the in-plane resolution, the corresponding largest amount of dephasing occurs in through-slice direction. Thus, the choice of a smaller slice thickness reduces the signal loss, but has implications on the measurement time, signal-to-noise ratio, volume coverage, etc.
Because MRI uses well-defined magnetic fields in order to encode the signal, field distortions can also lead to voxel mis-registrations. It is a major source of artifact and especially prominent in *echo-planar imaging* (EPI). It is a single-shot imaging technique, in which the entire *k*-space is traversed in a *zig-zag*-trajectory following a single excitation. As a result, the *dwell time* between the acquisition of consecutive *k*-space points in the frequency-encoding direction is much shorter than the *echo-spacing*, which is the time between adjacent samples in the phase encoding direction. Thus, with a given *receiver bandwidth* (rBW), which denotes the frequency spread induced by the imaging gradients, the voxel-shift δv in frequency and phase encoding direction can be calculated according to [37]

$$\delta v_{\text{freq}} = \frac{\gamma \Delta \mathrm{B}_0(\mathbf{r}) N}{\text{rBW}} \quad \text{and} \quad \delta v_{\text{phase}} = \frac{\gamma \Delta \mathrm{B}_0(\mathbf{r}) N M}{\text{rBW}}. \tag{3.2}$$

With N and M denoting the number of sampled points in the frequency and phase encoding direction, respectively, it can readily be seen that the phase-encoding direction suffers from larger voxel displacements. For typical acquisition conditions, these can be as high as several voxels, which leads to strong image distortions. Besides an improved B_0 shimming, also undersampling strategies in phase encoding direction can be employed to reduce these artifacts.
Spectroscopic applications suffer from B_0-induced *line-broadening*, which is due to the fact that the spectral line-width is proportional to $1/T_2^*$. It complicates a correct metabolite quantification and renders spectroscopic acquisitions over extended volumes challenging. Off-resonances also affect other MR acquisition components, including excitation or selective signal suppression. Overall, the ongoing trend towards MR systems with higher magnetic field strengths complicates their effective cancellation, because the susceptibility-induced offsets scale with B_0. Consequently, efficient shimming strategies become even more important at these field strengths.

3.3 Measurement of B_0 inhomogeneities

In order to find an appropriate shim setting during the pre-scan adjustment process, it is essential to first quantitatively assess the apparent B_0 inhomogeneities. Moreover, because their characteristics are governed by the susceptibility distribution of the sample itself, it is required to be able to measure them on a per-subject basis. This demand is further complicated by the fact, that the magnetic field needs to be probed with high precision within the sample, which precludes the use of conventional field sensing devices. Instead, exploiting the dependency between magnetic field strength and resultant spin precession frequency, the NMR signal from the sample itself is most commonly used for B_0 field characterizations.
The Larmor equation relates precession frequency, ω, and nominal magnetic field strength, B_0, via the nucleus-specific gyromagnetic ratio, γ. It follows, that an additional spatially varying static magnetic field offset term, $\Delta B_0(\mathbf{r})$, introduces a position-dependent variation of local precession frequencies, $\omega(\mathbf{r})$, which in turn causes a position- and time-dependent phase accrual, $\phi(\mathbf{r}, t)$, which is described by

$$\omega(\mathbf{r}) = \gamma \cdot (B_0 + \Delta B_0(\mathbf{r})) \quad \Longleftrightarrow \quad \phi(\mathbf{r}, t) = \gamma \cdot (B_0 + \Delta B_0(\mathbf{r})) \cdot t. \tag{3.3}$$

A number of different frequency- or phase-based field mapping approaches exist, which utilize either of these relationships to draw inferences from the acquired data about the underlying magnetic field distribution. The fundamental idea, which is schematically illustrated in Fig. 3.2, is to acquire spatially-resolved samples of frequency- or phase-measurements from within the object and to solve Eq. 3.3 for the spatially varying magnetic field offset term.
The B_0 measurement approaches differ in the way how the B_0 inhomogeneities are sampled in space and time, with each technique having its unique strengths and limitations in terms of acquisition speed, measurement accuracy, hardware complexity or spatial and temporal resolution. The applied sampling scheme is chosen such as to be optimal for the shimming target of the planned measurement and forms the basis for accurate shim adjustments. This section reviews magnetic field mapping techniques that have been published and used in B_0 shimming applications for MR imaging or spectroscopy.

3.3.1 FID-based field assessment

The simplest field characterization techniques analyze the FID signal from the sample, which is subjected to the magnetic field to be measured. Macroscopic inhomogeneities lead to a spread of local precession frequencies in the excited volume and, hence, contribute to a stronger spin dephasing. This causes a faster T_2^*-decay of the time-domain signal and a concomitant broadening of the spectral line widths in the frequency-domain. Using the FID as a quality measure, the amplitudes of the magnetic correction fields can be varied sequentially such as to maximize the T_2^*-decay rate or to minimize the spectral line width. This is schematically illustrated in Fig. 3.2 A.
Time- or frequency-domain shape-optimization of the FID signal has already been used early on for global shim optimizations [49]. However, because the FID is the volume integral of the NMR signal received from the entire excited volume, the spatial distribution of the B_0 inhomogeneities cannot be resolved. Thus, even though the shimming process can be guided by following specific procedures [50] and despite characteristic FID patterns can give some indication of present inhomogeneity terms [44], finding the optimal shim setting remains challenging and time-

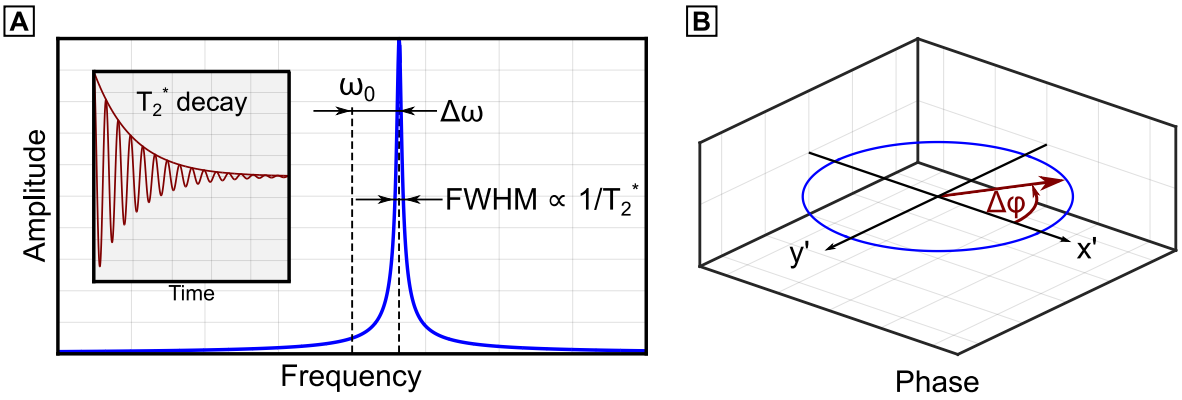

Figure 3.2: Fundamental principles of FID-based and spatially-resolved frequency- or phase-based B_0 characterization techniques. **A)** Variations in the static magnetic field lead to local shifts of the Larmor frequency, which results in a corresponding faster T_2^* decay of the signal received from the entire excited volume. B_0 shimming can be performed by maximizing the energy of the FID, or minimizing of the *full-width-at-half-maximum* (FWHM) of its corresponding frequency spectrum. Alternatively, if spatially-resolved spectra are acquired, the local magnetic field offsets can be calculated from the difference of the frequency component with highest amplitude to the nominal center frequency, ω_0, and yield quantitative B_0 maps. **B)** Static magnetic field inhomogeneities, and their corresponding spatial variation of local resonance frequencies, introduce a phase accrual of the magnetization vector in the rotating frame of reference. Phase-sensitive detection of the MR signal and exact knowledge of the phase evolution time enables an accurate calculation of the underlying B_0 offset.

consuming. In addition to that, shim coil impurities and optimizations over off-center positioned volumes can cause the shim functions to become non-orthogonal and interacting, which introduces local minima to the shimming process [51]. Attempts to automate the optimization removed any operator bias [52], but could not ensure finding the optimal shim setting either. Moreover, because of the development of more powerful techniques, FID-based field characterizations are generally not used for shim optimizations anymore. However, because of its low technological and methodological requirements, the FID-optimization has been used for a long time for B_0 shimming in MR applications.

3.3.2 Image-based field mapping

As indicated by Eq. 3.3, the apparent B_0 inhomogeneities in the sample modulate the acquired MR signal. Image-based field mapping techniques apply conventional gradient encoding strategies to spatially resolve them such that the resultant images are voxel-wise representations of the spatially varying B_0 field offset. As shown in Fig. 3.3 A, this allows the field mapping volume to be chosen such as to optimally comply with the shimming volume. Due to their versatile applicability, image-based field mapping techniques constitute the most prevalent form of B_0 field characterization for B_0 shimming purposes.

Frequency-based approaches

Combining MR spectroscopy and imaging, *chemical shift imaging* is a technique used to acquire full NMR spectra at distinct voxel positions. Originally developed for quantitative metabolite mapping [53], the same principle has been suggested to be applied also for field mapping [54]. Following spin excitation, only phase encoding gradients are used for spatial encoding. Thus, the signal evolves under the influence of the magnetic field inhomogeneities and is acquired in

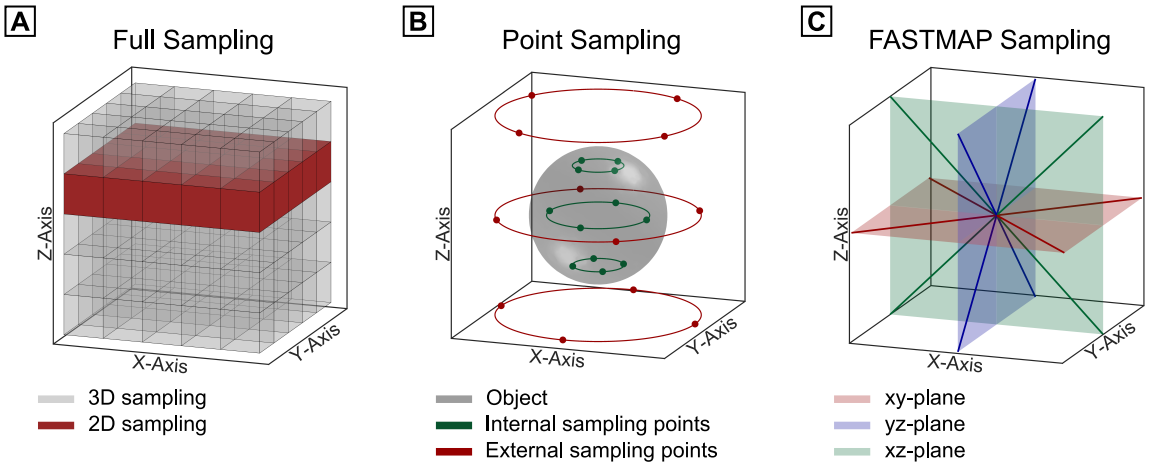

Figure 3.3: Sampling strategies for B_0 mapping. **A)** Samples of the local magnetic field offset can be acquired on regular, discretized 2D or 3D image grids, with the advantage of being able to optimally adapt the field mapping geometry to the volume of the planned measurement. **B)** Using localized MR spectroscopy techniques, samples of the magnetic field offset can be recorded at distinct locations within the object (green points). Using additional field probing hardware, it is possible to also monitor the magnetic field changes outside of the sample during the actual MR measurements (red points) and to approximate the resultant field changes inside the object. **C)** The coefficients of a 2^{nd} order spherical harmonic expansions of the magnetic field in the volume-of-interest can be calculated from six columnar 1D field measurements along the displayed directions within the object.

the absence of any readout gradients. A Fourier transformation of the acquired dataset yields a spatially resolved frequency spectrum at each sampled point in space. As illustrated in Fig. 3.2 A and using Eq. 3.3, the magnetic field offset can then be calculated voxel-wise from the difference of the frequency component with highest amplitude to the nominal center frequency. It has been shown, that this technique is applicable to precisely measure purposefully induced magnetic field offset terms in phantoms [55] and has also been used to asses and correct for B_0 inhomogeneities in human in vivo acquisitions [56]. Moreover, because regular image encoding methods are used, shimming can be carried out over arbitrarily positioned and sized 2D or 3D volumes [57].
The drawback of frequency-based field mapping is the substantial acquisition time, which is needed to acquire an entire spectrum at each sampled point in space, even though only a single scalar value is needed for the field characterization. To alleviate this problem, a spatial undersampling strategy has been suggested. It is based on the concept that it is not necessary to acquire fully sampled field maps, but that a limited number of sampling points is sufficient for a low-order spherical harmonic field approximation. This can be achieved by acquiring stimulated echoes from the overlapping region of three selectively excited, orthogonal slices [58] and by converting the recorded spectrum of each resultant voxel into magnetic field values as described above. It has been shown, that when appropriately distributing these single-point measurements in the sample, a number of low-order spherical harmonic components can unambiguously be determined [59]. Unlike regular image sampling schemes, the voxels are not ordered in image matrices, but distributed in space such as to fulfill minimum spatial sampling requirements. This is schematically illustrated in Fig. 3.3 B.

Phase-based approaches

As illustrated in Fig. 3.2 B, phase-based field mapping approaches employ an evolution time, τ, during which the magnetization vector accrues a phase, ϕ_τ, which is proportional to the local

magnetic field offset. Assuming ideal experimental conditions, i.e. the absence of eddy currents, an on-resonant detection of the MR signal in the rotating frame of reference and neglecting initial phases, the magnetic field offset can be calculated from the phase data following

$$\Delta B_0(\mathbf{r}) = \frac{\phi_\tau(\mathbf{r})}{\gamma \cdot \tau}. \tag{3.4}$$

Since it is no longer needed to acquire a spectrum at each sampling point, this type of measurement is faster than frequency-based approaches. Moreover, different sequence types are applicable for the phase data acquisition, which renders this approach to be very versatile.
Initially, a spin echo sequence was suggested for the acquisition of the phase image [60]. In this approach, the interval between the 90° excitation and the 180° inversion pulse is chosen such as to differ by a value of τ from the interval between the inversion pulse and the spin echo, which leads to an inhomogeneity-induced phase accrual. Its combination with automated calculations of optimal shim currents enabled a rapid and non-iterative shim optimization [61]. Due to its efficacy, this still forms the basis for conventional static shim optimizations today, but several enhancements to the phase-based field mapping sequences were developed.
Based on the phase difference between images acquired at two different echo times and their relative echo time difference, *gradient echo* imaging became a rapid alternative to spin echo based approaches [62]. Moreover, by choosing the echo times of both images such, that the signal from water and fat is in phase at each time of echo formation, chemical shift artifacts from the most abundant proton species after water can be avoided. Also the use of spectral-spatial pulses, which selectively excite only the water protons of the sample, was suggested for this purpose [63]. Further speed improvements were introduced by using multi-echo gradient echo sequences [64] or echo-planar readouts [65] for the acquisition of the phase images. Moreover, if more than two such phase-images are acquired, the application of a linear regression of the phase versus the echo times has shown to improve the robustness against phase noise and yields more accurate field maps [66]. To render the fast gradient echo sequences to be also more robust against gradient delays and eddy currents, acquisition schemes with inherent compensation of hardware imperfections were suggested for field mapping [67]. These developments illustrate, how phase-based field mapping sequences were tailored for an improved accuracy of the volumetric magnetic field information at reduced scanning times and reason their wide usage in B_0 shimming.

3.3.3 Projection-based field mapping

Projection-based field mapping techniques were developed to further accelerate the B_0 field characterization. These approaches approximate low-order components of the B_0 inhomogeneities from data acquired along 1D profiles through the sample. For static shim optimizations, methods based on the *fast automatic shimming technique by mapping along projections*, commonly abbreviated as *FASTMAP*, became a rapid B_0 mapping alternative. Dynamic variation of the B_0 field can be assessed during the actual MR measurements using so called navigator techniques.

Static approaches

Projection-based techniques are based on the concept, that the maximum achievable complexity of any applied shim field is dictated by the available shim system. Since this is usually limited to a full set of 2^{nd} order spherical harmonics, a spatial field sampling which enables an unambiguous calculation of the first nine coefficients of a spherical harmonic expansion suffices for field mapping

for the purposes of B_0 shimming. It has been shown, that these coefficients can be determined analytically, when sampling the field along six 1D profiles through the sample [68]. This requires the projections to be placed along the directions of the side-diagonals of a cubic volume, which can be achieved by selectively exciting bar-shaped profiles. The acquisition scheme is illustrated in Fig. 3.3 C. The B_0 information is encoded in the phase difference between the profiles acquired at two different echo times. The approach has proven to be a rapid shimming method for in vivo single voxel spectroscopy [69] and still is a widely applied technique in that area.
Due to its acquisition time efficiency and its convenient applicability to spherical harmonic shimming, multiple variants of the *FASTMAP* sampling scheme were developed. Using a more efficient excitation scheme and a weighted polynomial regression for the calculation of optimal coefficients, *FASTERMAP* was proposed as a first advancement [70]. It provides an improved signal-to-noise ratio of the acquired projection data and opens up the possibility to use the projection-based sampling not only for shimming over small voxels, but also over larger volumes encountered in imaging applications. Similar to the idea behind multi-echo imaging, the *FASTESTMAP* acquisition scheme was developed to sample multiple echoes of each projection at different echo times following a single excitation. The omission of a no longer required reference scan for the phase subtraction provided further acquisition time reductions [71]. Moreover, an optimization of the excitation pulses to be more SAR-efficient enabled a transfer of this technique to ultra-high field acquisitions [72].
It is to be noted, that the original *FASTMAP*-based field sampling along projections assumes a smooth B_0 field variation. This is a valid assumption for small voxels, but becomes increasingly less appropriate for larger volumes, such as slabs or slices, where strong susceptibility-induced field gradients may be encountered. However, by varying the number and orientation of the projections, it has been shown that the sampling scheme can also be adjusted to be more suitable for shimming over straight transversal, sagittal and coronal slice volumes [73] as well as over arbitrarily rotated oblique slices [74]. Placing a pair of four projections into two parallel slices can even enable an accurate spherical harmonic shim optimization up to 3^{rd} order for slab-like volumes, which makes it suited also for global shimming in imaging applications [75].

Dynamic approaches

Conventional static B_0 shimming is concerned with canceling magnetic field inhomogeneities that arise from susceptibility differences within the object. However, as discussed in Section 3.2.1, several sources exist that can induce a dynamic variation of the B_0 field. Hence, for a retrospective correction of the acquired data or a prospective re-adjustment of the shim currents, strategies for a concurrent assessment of the dynamic B_0 inhomogeneities during the MR data acquisition are of great interest. Due to the stringent requirement of not interfering with the MR measurement and the necessity to provide for a certain spatial sampling which enables a B_0 field characterization, this is a challenging task.
Because of their rapid acquisition times, projection-based techniques that can be interleaved with the actual MR measurement sequence are suited for this purpose. In contrast to the *FASTMAP* projections, these so-called navigator techniques typically acquire the central k-space line of an entire excited slice in the presence of a readout gradient. Thus, the excited volume is projected onto one of the principal gradient axes and a comparison of the phase of the acquired data to a reference condition enables a tracking of the frequency and 1^{st} order B_0 variations relative to an initial state [76]. An example of a representative navigator acquisition scheme and a qualitative sketch of a resultant field estimation along a given direction is illustrated in Fig. 3.4.

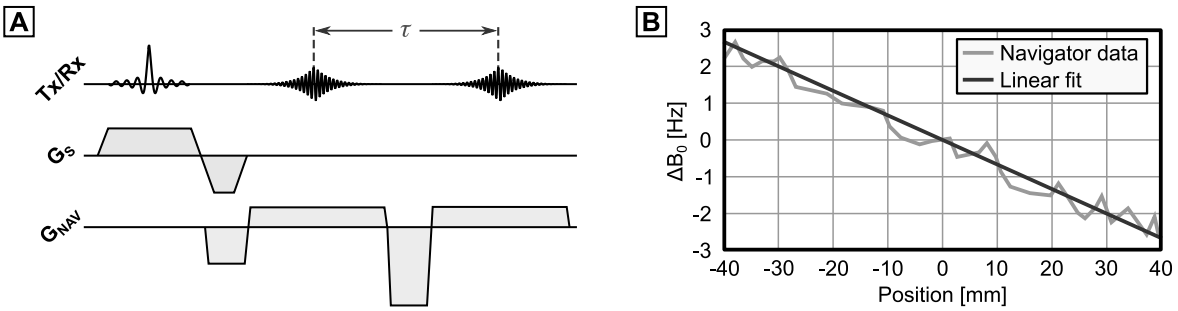

Figure 3.4: Navigator acquisition scheme to assess B_0 information for real-time shimming. **(A)** Following slice selection, the entire excited volume is projected onto a given axis, which is defined by the navigator readout gradient. Acquisition of two such profiles, separated by the evolution time, τ, enables the calculation of a phase difference between both navigators. **(B)** The slope and intercept of a linear fit of the phase difference data yields the frequency and linear field offset along that direction. Figure adapted from [77]

3.3.4 Fieldprobe-based field mapping

The previously discussed B_0 mapping techniques all had in common, that the magnetic field data is acquired in a dedicated acquisition, but using the same standard MR hardware which is also used for the actual MR measurement. An interference-free integration of the B_0 mapping into the MR acquisition is, therefore, impractical for most approaches and complicates the acquisition of dynamic field evolutions. This motivated the development of B_0 field monitoring techniques that rely on additional hardware, which can provide fast and accurate updates of the temporal evolution of the magnetic field independent from the MR scanner.
By using small samples of NMR-active nuclei, which can be excited using a separate spectrometer, it is possible to acquire field measurements at discrete probe positions. By appropriately sampling the magnetic field inside the scanner, this enables an approximation of the volumetric B_0 field distribution in a volume-of-interest encompassed by the probes. Besides for concurrent field monitoring, this type of B_0 field measurement is also used for the magnet shimming process during system installation.

Field plotting for magnet shimming

MR sequence-based field mapping techniques are based on the assumption that they are executed on a properly calibrated MR scanner. However, this is not the case at the time of the magnet installation, during which substantial B_0 inhomogeneities due to fabrication tolerances may be present, and which precludes a regular system operation. In an initial magnet shimming process, these inhomogeneities are being corrected, for which it is essential to be able to precisely measure them independently from the MR scanner hardware. This is typically done by mounting a field probe on a positioning device, which can accurately move the sample to desired measurement locations within the magnetic field. By appropriately sampling multiple coordinates, a magnetic field plot can be generated, which enables a high-order spherical harmonic field expansion of the magnetic field inhomogeneities [35]. A Fourier analysis of the azimuthal field plots might as well be used to determine its spherical harmonic coefficients [78]. This type of B_0 field measurement is exceptional in that it is usually only performed once during magnet installation, upon which the discussed MR sequence-based field mapping techniques can be employed.

Concurrent field monitoring

The application of a single-probe field monitoring system as a device to track the center frequency of the magnet has been applied early on as a *field frequency lock* in NMR spectroscopy applications to measure field deviations caused by magnet drifts during long measurements [79]. When wanting to also resolve higher-order field dynamics, it is required to use an array of multiple probes. They have to be arranged such as to fulfill a certain spatial sampling requirement in order to unambiguously determine a desired number of spherical harmonic components of the magnetic field distribution. This is schematically illustrated in Fig. 3.3 B.
A probe design optimization, with the goal of miniaturizing the setup while maintaining a high signal-to-noise ratio [80], enabled 1^{st} order field monitoring measurements with a setup of four simultaneously operating field probes [81]. These initial systems were receive-only and required the probe excitation to be delivered by the host MR system, which causes potential perturbations of the actual MR measurement during probe excitation and vice versa. This problem was resolved by isolating the host and the monitoring MR system with dedicated transmit-receive NMR probes [82]. Operating the field monitoring system with NMR-active nuclei other than protons additionally provided a spectral decoupling [83].
It is to be noted that this setup is inherently limited in the effect that it cannot directly assess the magnetic field evolution that originates inside the sample. Hence, any field evolution data based on this type of measurement is only an approximation of the inner-volume field evolution based on magnetic field samples taken on the outside. It is, therefore, important to appropriately choose the number and the position of the field probes. Based on that, the spherical harmonic order, up to which the magnetic field offset terms can be approximated reliably, needs to be critically evaluated [84]. In general, however, a good measurement accuracy has been reported, for example for subject-motion induced B_0 fluctuations that are typically encountered during in vivo MR measurements [85].

3.4 Spherical Harmonic B_0 Shimming

It is the key task of the B_0 shimming routine to decompose the acquired field map data into correctable field correction terms. In principle, any set of basis functions can be chosen for the purposes of shimming, but most commonly a spherical harmonic model is chosen. The advantage pertaining to this model is, that it provides a complete set of orthogonal basis functions, whose lower order terms can be generated from relatively simple current paths.
Historically, the orthogonality of the shim functions was desirable for the FID-based shim approaches, because it enables a shim adjustment of individual coils which does not interact with the remaining terms. The development of B_0 mapping techniques as well as automated numerical shim optimization algorithms, however, facilitated the implementation of shim hardware which generates field functions other than spherical harmonics. Nonetheless, spherical harmonic coils still constitute the most prevalent form of shim systems and are also employed within the scope of this work. In the following, shim optimizations based on this principle are, hence, explained in greater detail and current non-spherical harmonic approaches are briefly reviewed thereafter.

3.4.1 Magnet shimming

As explained in Section 3.2.1, upon installation, the bare magnet has a homogeneity which is insufficient for most MR applications. Hence, as part of the magnet installation, the magnetic field is subjected to a fine-adjustment procedure, during which it is homogenized over a spherical volume of a certain diameter. Since the magnet bore is a current-free region, any spatial field deviation must necessarily stem from outside this volume. Thus, following the reasoning given in Section 3.1.1, the application of Laplace's equation is perfectly valid and an expansion in spherical harmonics can approximate the magnetic field to a very high degree. The magnet shimming procedure consists of determining the spherical harmonic coefficients of the apparent inhomogeneity terms from magnetic field plots and canceling them by superimposing appropriate fields with opposite polarity. Generation of the correction fields is accomplished actively or passively and on modern MR scanners, typically a combination of both is employed.
Active magnet shim processes employ shim coils, which are designed such as to annul the measured inhomogeneities. The amplitudes of these coils are adjusted during the magnet calibration and remain unchanged, unless the magnet requires a re-adjustment. In contrast, passive shim approaches add materials to certain locations within the the scanner bore, which are then magnetized by the main magnetic field and, thus, generate field components which superimpose to the main field. The magnetic field produced by small passive shim elements can be determined analytically. Moreover, building blocks that consist of multiple such elements can be derived from simple symmetry considerations [35]. The rationale of the passive shimming process is to place multiple of these elements or building blocks such as to produce a certain pure spherical harmonic shim term [86]. This type of field correction is time-consuming, but well-suited to compensate for most system-specific inhomogeneity terms. It can even correct for very strong inhomogeneities by increasing the size of the passive shim elements [87].
Even though the basic principle is unchanged, passive shim settings are nowadays determined automatically by numerical optimization. The required passive shim elements are fitted into dedicated shim trays, which are typically located in the gradient coil insert. Additional cooling mechanisms can even maintain a stable temperature of the passive shims, thus preventing temperature-induced susceptibility changes.

3.4.2 Sample specific shimming

Sample-specific B_0 shimming targets the compensation of static magnetic field deviations that are induced by the susceptibility distribution of the sample itself. Different approaches exist for this purpose, which can be distinguished by their temporal shim update rate. In *static shimming*, a field map is acquired before the actual MR measurement and the entire volume is decomposed into its spherical harmonic components. The resultant coefficients are converted to shim currents, which are sent to the shim power supplies and kept constant throughout the subsequent acquisitions. For *dynamic shimming*, the shim region is partitioned into multiple sub-volumes and an optimal shim setting is calculated for each of it. The shim settings are loaded into shim buffers and applied immediately prior to the acquisition of the corresponding sub-volume. Both concepts are visualized in Fig. 3.5 and illustrate the increase in overall field shaping capability, when approximating the measured B_0 distribution over smaller volumes.
Even though the temporal shim update rates differ in static and dynamic shimming, both have in common, that optimal shim currents are determined from measured data that was collected prior to the actual scan. Any subsequently introduced B_0 field perturbation remains, therefore, undetected and cannot be compensated. *Real-time* shim approaches address this issue by acquiring intra-acquisition information about apparent B_0 changes and re-adjust the shim setting accordingly. For these approaches, however, it is very challenging to acquire spatially resolved B_0 field information from the sample without interfering with the actual MR measurement.

Static shimming

Static shimming describes the process of calculating and setting a single shim solution for a particular volume-of-interest, and keeping the shim currents constant throughout the following measurement. Static *local* shimming refers to homogenizing the magnetic field over a region of limited extend, e.g. over small cuboidal volumes for single-voxel spectroscopy acquisitions or over single slices for spectroscopic imaging. Most often, however, a static *global* shim setting is required, which homogenizes the magnetic field over an extended volume. Of particular interest in many MR applications, as well as in this work, is a static global B_0 homogenization over the volume encompassing the entire human brain.
The various B_0 field mapping techniques have unique strengths and limitations and differ in their suitability for static global shim approaches. Most commonly, multi-echo gradient echo phase image-based approaches are employed, due to their short acquisition times and high volume coverage. Let $\mathbf{b} \in \mathbb{R}^{m\times 1}$ denote the residual B_0 inhomogeneities measured with any applicable field mapping technique and which contains m elements corresponding to the mask voxels in the volume-of-interest. Furthermore, let $\mathbf{A} \in \mathbb{R}^{m\times n}$ denote the system matrix of n spherical harmonic shim functions, evaluated at the coordinates of the sampled inhomogeneities. The shimming process can then be formulated as a least-squares optimization problem, with the target of finding a solution, $\mathbf{x} \in \mathbb{R}^{n\times 1}$, which corresponds to the set of shim currents that minimizes

$$\min_x \|\mathbf{Ax} - \mathbf{b}\|_2^2 \quad \text{s.t.} \quad \mathbf{lb} \leq \mathbf{x} \leq \mathbf{ub}. \tag{3.5}$$

A simple least-squares solution can be found via pseudo-inversion of the system matrix. However, depending on the purity of the shim fields and the positioning of the shimming volume, the problem can become ill-conditioned. As a result, pseudo-inversion is prone to producing unstable solutions, which are caused by an amplification of noise in the input data. It can also cause infeasible solutions, when individual shim currents exceed the power supply limits.

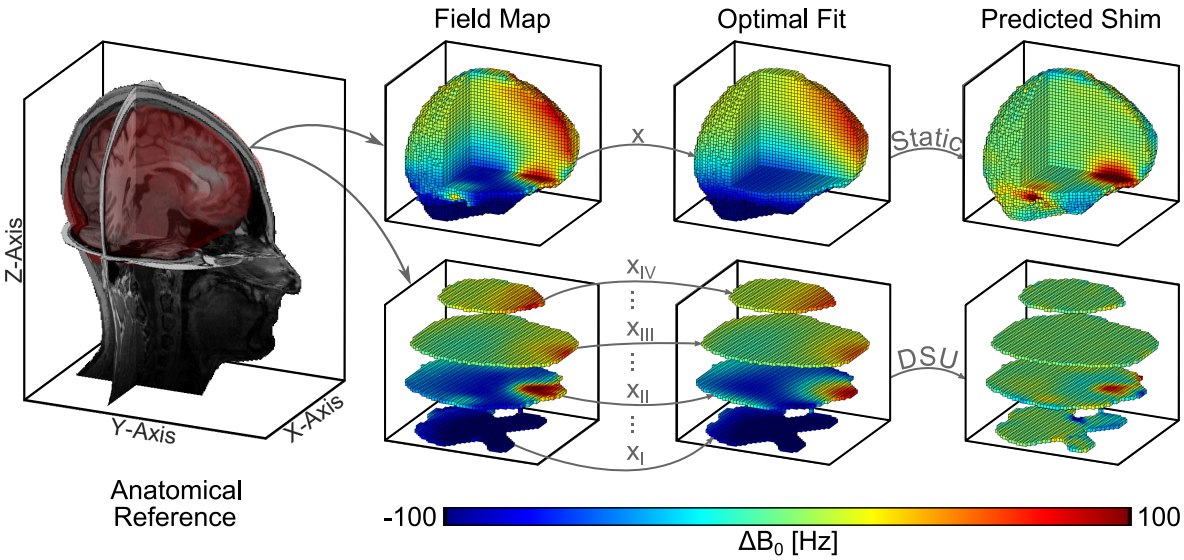

Figure 3.5: Concepts of sample-specific static and dynamic shim approaches. The magnitude data of an anatomical reference dataset is typically used to define a volume-of-interest for B_0 shimming. After the field map acquisition, the shim currents are calculated so as to optimally cancel the the measured inhomogeneities. In static shim approaches, a single set of shim currents, $\mathbf{x}$, is determined, which is optimal for homogenizing B_0 over the entire volume. Dynamic shim updating (DSU) approaches calculate a set of optimal shim currents, $\mathbf{x}_i$, for each of multiple sub-volumes and readjust the shim setting immediately prior to the associated acquisition. Static shimming is easier to implement, but dynamic shimming can significantly improve the achievable B_0 homogeneity.

It has been shown, that a simple truncation of the excessive shim currents results in sub-optimal solutions, but that an incorporation of the lower and upper shim power supply limits into the optimization, via the hard bounds $\mathbf{lb}, \mathbf{ub} \in \mathbb{R}^{n\times 1}$, can solve this issue [88]. Due to the inclusion of the box constraints, the problem described by Eq. 3.5 can no longer be solved by pseudo-inversion, but requires the application of numerical optimization algorithms. This also facilitates the inclusion of further shim constraints into the optimization and enables the development of dedicated shim software, that is optimally adapted to the available shim hardware. For instance, it has been shown, that a regularization of the optimization problem, by penalizing high solution norms, is well-suited for reducing the overall current demands and has negligible impact on the achievable shimming performance [89].
Further developments tailored the optimization function such as to be better suited for dedicated types of applications. For instance, certain acquisitions are prone to excessively high B_0 offsets, but can tolerate moderate B_0 deviations. For these measurements, a minimization of the maximum off-resonance frequency, at the cost of a less optimal shim in a least-squares sense, has shown to improve acquisition conditions. It was achieved by replacing the ℓ^2-norm minimization in Eq. 3.5 by a *minimiax*-optimization [90]. Furthermore, spectroscopic measurements are vulnerable to be confounded by spurious signals in cases where off-resonances outside the volume-of-interest exceed a certain threshold. In these cases, the cost function can be extended such as to minimize the ℓ^2-norm within the region of interest, while simultaneously setting user-defined constraints to the maximum tolerable field offset outside of it [91]. Similarly, a region-of-less-interest was suggested to be included in the shim optimization, which can additionally be defined and weighted against the actual region-of-interest [92].
For static shimming in applications that investigate localized structures, advanced volume-of-interest selections were employed. A data registration to pre-parcellated atlases was suggested

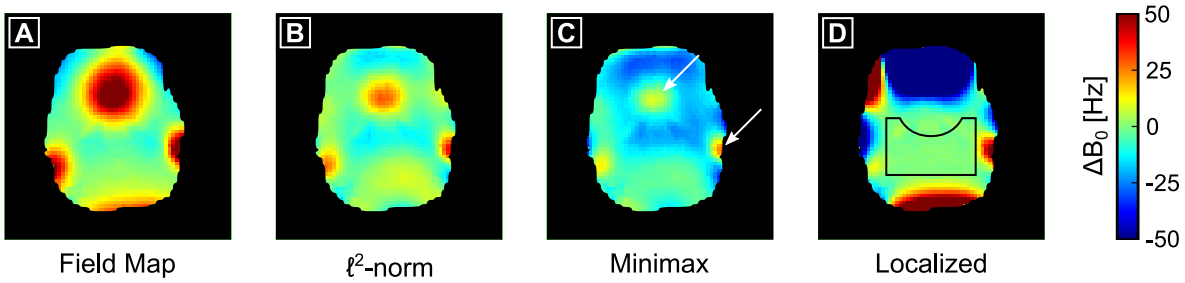

Figure 3.6: Examples of dedicated static shimming routines. **A)** Transversal slice of a field map after 2nd order global shimming. **B)** A regular ℓ^2-norm minimization of the inhomogeneities in the given slice is equivalent to minimizing the standard deviation of the B_0 offsets. **C)** Application of a *minimax*-optimization reduces the maximum occurring absolute field offset at the cost of moderately worse field homogeneity in other regions. **D)** Excluding highly inhomogeneous regions from the optimization by dedicated region selections can significantly improve the achievable homogeneity locally, but may result in excessive offsets in remote regions.

to optimize the shimming specifically for certain anatomical structures in the human brain [93]. Moreover, field map guided manual selections of volumes-of-interest, so as to exclude very high-order spatial B_0 variations, has shown to be well-suited for focussing the shim corrections to certain areas without diminishing the achievable B_0 homogeneity by terms that are incorrectable to the shim hardware. This approach was successfully used in a spectroscopic imaging study, in which the hippocampus was investigated and its shim region was chosen such as to exclude the high spatial B_0 variations induced by the proximal air-filled auditory canals [94]. Selected examples of these modified static shim approaches are schematically illustrated in Fig. 3.6.
The effect of using different optimization algorithms to solve Eq. 3.5 was analyzed for global shimming as well as for local shimming of small cuboidal and single-slice volumes [95]. It was found, that strong variations in shimming performance, algorithm runtime and robustness against starting values exist between the different solvers. For optimal shim quality in a given application, the respectively applied shim algorithm needs to be chosen with caution.
In conclusion, static global B_0 homogenization is the most frequently applied form of B_0 shimming. Through hardware and software advances, these shim routines have evolved from a rather heuristic FID-based field optimization to a quantitative and versatile pre-scan adjustment step. The inclusion of additional constraints, which can reflect the technical limitations of the hardware, or a certain desired form of the targeted shim field, enables the shim algorithm to be specifically tailored for the planned measurements.

Dynamic shimming

The efficiency of spherical harmonic static B_0 shimming over extended volumes is inherently limited in the sense that it constitutes a compromise of optimal inhomogeneity cancellation between regions that pose very different shim challenges. For example in the human brain, the optimal shim settings for the inferior temporal lobes, the pre-frontal cortex or the brain stem would differ, if calculated individually for each particular area. A least-squares fit of the available low-order shim functions to the entirety of the measured B_0 field distribution does not contain sufficiently high spatial variation for a complete inhomogeneity compensation. Hence, it corresponds merely to the best possible approximation of an ideal global shim field.
Dynamic shimming, also termed *dynamic shim updating* (DSU), is a B_0 shim approach that was developed to make a more efficient use of an available shim set. As can be seen in Fig. 3.5, it exploits the fact that B_0 inhomogeneities can be better approximated when being analyzed over

smaller volumes. Thus, optimal shim settings are calculated for multiple sub-volumes and the corresponding shim coil currents are loaded and updated during the subsequent acquisition. It is applicable to a multitude of applications encountered in MRI and MRS, for which the data acquisition is inherently separated in space and time. For example, optimal shim settings can be calculated for individual slices for multi-slice imaging, or individual voxels for multi-voxel spectroscopy. The benefits of an improved shim performance have been shown in simulations, demonstrating signal intensity gains and geometric distortion reductions [96].
For dynamic shimming, the optimization function needs to be modified such that a set of optimal shim values is calculated individually for each sub-volume, k, and can be formulated as

$$\min_{x_k} \|\mathbf{A}_k\mathbf{x}_k - \mathbf{b}_k\|_2^2 \quad \text{s.t.} \quad \mathbf{lb} \leq \mathbf{x}_k \leq \mathbf{ub}. \tag{3.6}$$

The associated temporal variation of $\mathbf{x}_k$, however, poses a challenge to the required temporal stability of the calculated shim fields. Governed by the inductance of a shim coil, the shim field settling that follows upon a rapid change in shim current might not occur instantaneously. Moreover, as illustrated in Fig. 3.7, intra-acquisition shim current changes can induce eddy currents, which in turn generate time-varying magnetic perturbation fields. Both effects can cause deviations from the target field with temporal decay constants that exceed the subsequent acquisition period and, hence, lead to suboptimal data quality. Additionally, as explained in Section 3.1.1, the spherical harmonic shim functions can become degenerate, when being analyzed over small volumes. Consequently, the shim functions included in the optimization can become linearly dependent, which renders the problem described by Eq. 3.6 ill-conditioned and can result in excessively high shim currents for individual channels. Developments in dynamic shimming applications were, consequently, concerned with calculating feasible shim currents for localized volumes and handling the issues related to rapid shim field stabilization.
The initial dynamic shimming implementations, however, were faced with challenges pertaining to the realization of its associated technological demands. The conventional MR hardware needs to be extended such as to provide the possibility to store pre-calculated sets of shim values in rapidly accessible shim buffers, so that shim currents can be updated during the acquisition in near real-time. The first realization of such a dynamic shimming interface provided the option of updating the 1^{st} order terms for a set of four slices [97]. This setup was soon extended to also include center frequency adjustments and could be scaled to any desired number of slices [98]. These early dynamic shimming implementations could still avoid the problems of shim degeneracies and temporal shim instabilities by limiting the dynamically updated terms to the actively shielded linear components only. However, since this equally limits the B_0 shim efficiency, solutions for rapid high-order shim updates are desirable.
The first 2^{nd} order multi-slice dynamic shimming experiments were conducted on a small-bore animal scanner, for which the previously described shim settling and eddy current issues were reportedly limited to the Z2-shim only. By implementing an eddy current compensation circuitry, which superimposed exponentially decaying correction currents to the shim outputs, the temporal interactions of the Z2-shim to a global B_0 component could be reduced to an acceptable level [99]. This type of *pre-emphasis* correction for self- and cross-term eddy currents is known from fine-adjustments of the imaging gradients [100] and could successfully be translated to the shim coils for dynamic shimming applications. A full 2^{nd} order dynamic shimming pre-emphasis implementation has been implemented on a human MR system and shown to be applicable for a temporally stable dynamic B_0 field homogenization [101]. Significant B_0 homogeneity improvements were demonstrated for human brain acquisitions and problems related to shim

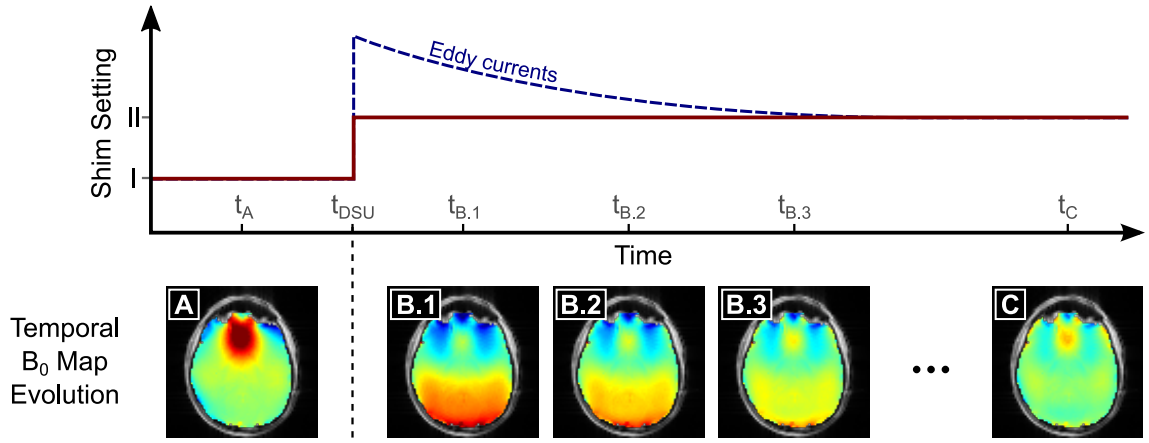

Figure 3.7: Illustration of the achievable shim quality for static versus dynamic shimming and the effect of rapid shim changes on the temporal shim field fidelity. **A)** When applying a global shim setting I, significant inhomogeneities remain uncorrected to the available set of shim coils. **B)** When rapidly switching the shims to a slice-optimized setting II, eddy currents are induced and generate perturbation fields that superimpose to the shim field. **C)** Only after the eddy current fields have decayed, the improve in shim quality provided by the slice-optimized shim can be obtained. Eddy current compensation techniques aim to reduce the interval between t_{DSU} and t_C.
It should be noted that during dynamic shimming, currents are not switched between global and slice-wise shim settings, but between optimal settings for adjacent slices. The eddy current issue, however, is the same and the given depiction was merely chosen to additionally illustrate the shim quality difference that is achievable with dynamic as compared to static shimming.

degeneracies were handled by excluding linearly dependent terms. This, however, requires the shim functions to be analyzed for degeneracies in dependence upon the slicing geometry.
Increased shimming demands at ultra-high fields render the application of dynamic shimming at systems operating at 7 T and above very promising. Thus, a dynamic shimming setup for human brain imaging was implemented at 7 T using a partially shielded 2^{nd} order shim set [102]. However, since in this work no additional eddy current pre-emphasis corrections were implemented, it required the un-shielded channels to be switched at relatively slow update rates. The concomitant MR acquisition delays render this approach infeasible for application in most MR studies. In contrast to that, the acquisition delays were effectively removed via an implementation of a fully pre-emphasized 3^{rd} order dynamic shimming system at 7 T [103]. The demonstrated homogeneity gains proved that the potentials of the 3^{rd} order shim set were fully exploited at negligible acquisition time prolongations. However, in this study it was already stated, that the number of potential eddy current terms scales with the order of included spherical harmonic shim coils and, likewise, the associated pre-emphasis calibration overhead. In combination with a decrease in shim efficiency for spherical harmonic shim coils of higher orders, the usefulness of extending dynamic shimming to above 3^{rd} order was critically discussed.
Besides a slice-wise B_0 field homogenization, dynamic shimming introduces a new flexibility in terms of separating regions with different shimming demands. In a simulation study, it has been shown, that when parcellating the volume-of-interest into rectangular volumes of various sizes, regions of similar B_0 non-uniformity can be optimized individually, and macroscopic B_0 inhomogeneities can almost entirely be removed [104]. With currently available volume selection methods, however, the acquisition requirements associated with the parcellated dynamic shim settings are infeasible. Nonetheless, the gains in overall B_0 homogeneity, provided by the methodological developments in dynamic shimming, have successfully been translated to numerous in vivo applications. So have dynamically shimmed volumes been used and shown to improve

results in a multi-slice spectroscopic imaging study [105] and an EPI-based functional imaging study [106]. Moreover, an improved B_0 homogeneity has been demonstrated in dynamically shimmed multi-voxel spectroscopy acquisitions [107].
In conclusion, the major challenge for a successful dynamic shimming implementation is the setup of a well-calibrated shim pre-emphasis correction circuitry in order to suppress shim-induced eddy currents. Even tough software-based approaches were suggested for this purpose [108], these methods have so far failed in proving to be a robust alternative to hardware-based pre-emphasis implementations. Moreover, numerical optimization strategies need to be employed, in order to solve shim degeneracy issues which inherently arise when reducing the shimming volume. However, if implemented properly, dynamic shimming can improve the overall achievable B_0 homogeneity and optimally exploits the field shaping capabilities of an available shim set.

Real-time shimming

In contrast to static or dynamic shimming, real-time shim approaches target intra-acquisition deviations of the magnetic field from a given reference state. The B_0 information is assessed during the actual MR scan, processed and translated into appropriate shim corrections, which are immediately effectuated. The main challenge is to quantitatively determine the spatial distribution and the amplitudes of the field deviation terms without interfering with the actual MR measurement and ideally without prolonging its acquisition time.
As described in Section 3.2.1, dynamic field perturbations are usually of lower amplitudes than those of susceptibility-induced static B_0 inhomogeneities. Moreover, because many field fluctuations originate from remote regions, for example breathing-induced field changes in the human brain, the spatial pattern can often be approximated with sufficient accuracy by low-order spherical harmonics. Real-time shim approaches are, therefore, usually concerned with temporally sampling the B_0 field fluctuation such as to be able to reconstruct the low-order spherical harmonic coefficients that are associated with an available shim set.
Navigator approaches, introduced in Section 3.3.3, are well-suited candidates for real-time B_0 field assessments. So called *shim navigators*, which measure the central k-space lines after slice excitation at two different echo times, were suggested for this purpose [77]. A comparison of the phase-difference data to that of a set of reference navigators can be used to track the changes in center frequency and 1^{st} order field offset terms across the sample. Its applicability to correct for motion-induced field fluctuations in real-time has been demonstrated in EPI acquisitions. A similar readout was suggested to be used in a combined motion- and shim-correction navigator scheme, but in which the linear shim changes were estimated from the time-domain signal of the central k-space line [109]. In this approach, linear field changes across the sample can be measured as shifts of the echo peaks and shim corrections can be calculated from a comparison to an initial reference state. Both sampling schemes are described by the sequence diagram shown in Figure 3.4 and differ merely in the respective data processing. Frequency and linear shim updates were also implemented and used for single voxel spectroscopy applications, employing a navigator scheme that measures the field offsets across the voxel [110]. Very low resolution dual-echo 3D multi-shot EPIs were likewise suggested as volumetric navigators for frequency and 1^{st} order shim updates [111]. Reported acquisition times of 928 ms per navigator are an exclusion criterion for its utilization in many other MR applications, but the possibility of using regular image acquisition and processing schemes facilitates its implementation.
However, acquisition time penalties and potential RF- or gradient-pulse interferences still pose an impediment for the application of navigators in many MR applications. Thus, a decoupling of

the real-time B_0 field assessment from the simultaneously running MR acquisition is desirable. An indirect approach to counteract breathing-induced field fluctuations was developed for this purpose, which utilizes a breathing belt to monitor the chest motion of a subject [112]. For this, previously acquired brain field maps, associated with and linked to different chest poses during the breathing cycle, are acquired in an initial calibration scan. They are then used during the actual MR acquisition, to extrapolate in real-time from the breathing belt readings to the consequent dynamic field fluctuations. In contrast to navigators, the fully sampled field maps enable the detection of higher order field dynamics. Using the breathing-belt for 2^{nd} order real-time shim updates, the original study has shown a better phase stability for EPI data and demonstrated an improve in image quality for multi-shot gradient-echo images at 7 T.
Despite its advantages, the breathing-belt based B_0 fluctuation monitoring requires a subject-specific calibration, is limited to reproducible chest-motion induced field changes and relies on a robust and correct correlation of the breathing-belt signal to the actual field fluctuations. Hence, this type of indirect field assessment is prone to false B_0 estimation and a direct field measurement is generally more preferable. This can be achieved by NMR field probe-based B_0 monitoring systems and their commercialization has led to a more wide-spread utilization in different real-time shim scenarios. Using field probes, not only to monitor and correct for system-dependent frequency drifts, but also for motion-induced center frequency changes, has shown to improve the spectral quality in MR spectroscopy applications in the human breast using a single-probe system [113]. This approach has been extended to a real-time feedback control system, which is based on concurrent field monitoring using 16 field probes, thus enabling full 3^{rd} order B_0 shim updates [114]. Field-probe based monitoring of spherical harmonic B_0 field deviations that originate from outside the volume-of-interest forms the current gold standard for real-time shim feedback systems. It has enabled the successful application of real-time shim feedback loops for spectroscopy [115], T_2^*-weighted imaging [116] and T_2^*-mapping [117] as well as quantitative susceptibility mapping [118].

3.4.3 Strengths and limitations of spherical harmonic B_0 shimming

The aforementioned examples prove the general applicability of spherical harmonics for static, dynamic and real-time B_0 shimming. From a theoretical perspective, however, it can be argued that Laplace's equation is only valid for source-free regions, which is not true in cases where a subject is in the scanner [119]. Consequently, in contrast to the magnet shimming procedure, the rationale for the application of spherical harmonics is inconsistent for subject-specific shimming. Thus, this approach has a natural limitation in the sense that it can only approximate high-order inhomogeneity terms with lower-order functions. Therefore, even though being exceptionally well-suited for shimming the bare magnet, even very high-order spherical harmonic shim fields cannot fully describe the complex inhomogeneity patterns induced by a human subject.
Appreciating the fact that a perfect cancellation of the B_0 inhomogeneities cannot be achieved with present technologies, several investigations were, therefore, concerned with determining the feasible limits of the spherical harmonic shim approach. In general, the benefit of implementing more and more high-order shim coils is counteracted by space limitations inside the MR scanner. In addition to that, shim coil complexity and required shim currents scale with the spherical harmonic order. Hence, one possible way of quantifying the cost-benefit ratio of higher-order spherical harmonic shim coils, is to address the question as to how much homogeneity improvement can realistically be obtained when including more terms into the B_0 shim optimization.
Initial simulated and experimental results demonstrated the benefits of 2^{nd} order shimming over

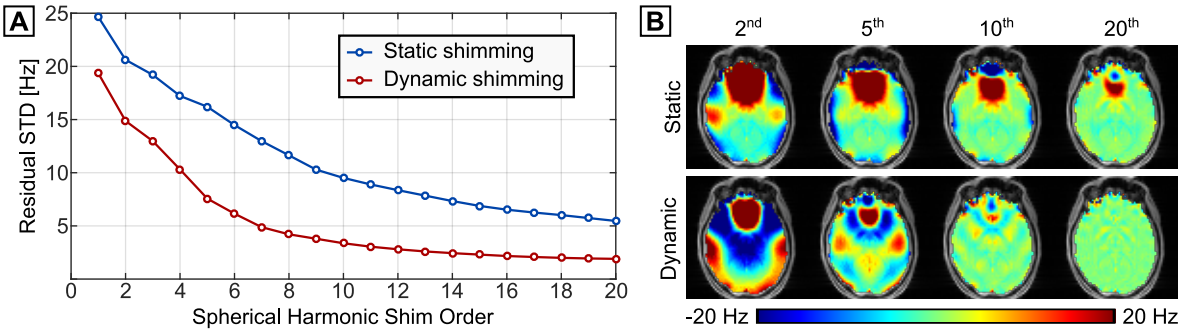

Figure 3.8: Impact of high-order spherical harmonic shimming on the achievable B_0 homogeneity. **(A)** An increase in the applied spherical harmonic shim order improves the achievable B_0 homogeneity for both, static and dynamic shimming. Dynamic shimming approaches the intrinsic limit of the achievable B_0 homogeneity, which is given by the susceptibility differences of the brain tissues, much faster than static shimming. However, due to space restrictions, this limit cannot realistically be reached. **(B)** The example of a representative field map slice illustrates the gradual improvement when including higher shim orders into either static or dynamic shim optimizations. Both rows show the same, central transverse slice.

adjusting merely the center frequency and the linear terms [120]. It was found, that a 2^{nd} order shim set yields B_0 homogeneity improvements, particularly in regions close to large susceptibility gradients. Consequently, the brain volume that could be shimmed to below a given homogeneity threshold for MR spectroscopy increased by 30%. The analysis was extended to the full 4^{th} and partial 5^{th} and 6^{th} order using experimental data and up to the 15^{th} order using simulated data [121]. By separately analyzing the homogeneity gains over an entire slab and over individual 1 cm^3 voxels within that slab, the role of very high-order shimming was investigated with a focus on spectroscopic imaging. In contrast to the widely held opinion of a diminishing efficacy of higher-order shim terms at realizable current demands, a significant improvement provided by the very high-order spherical harmonic shim terms was demonstrated. Moreover, when optimizing field homogeneity over individual slices, the simulated data showed an asymptotic behavior towards a residual inhomogeneity level evoked by the intrinsic susceptibility differences between gray and white matter. This was identified as the upper limit for any shim approach, and can approximately be reached when dynamically shimming up to the 7^{th} spherical harmonic order. Naturally, this can merely be considered as a theoretical value, because space limitations and excessive shim currents were excluded from the analysis.

Furthermore, as shown in Fig. 3.8, targeting an equal shim performance for a global whole-brain field homogenization necessitates the utilization of even higher-order terms. Since this is clearly beyond the physically feasible limit, any realistic high-order shim optimization cannot fully correct for all inhomogeneities, but merely is a best possible fit of an available set of shim functions to a measured field distribution. Moreover, including more shim terms into the optimization yields an overall homogeneity improvement in large parts of the volume, but might even come at the expense of stronger offsets in other parts [122]. The usage of higher-order shim coils, which provide shim fields with stronger spatial variations, thus requires a careful and application-specific examination of the resultant field maps.

In summary, the application of very high-order spherical harmonic shim fields is challenging in the sense that it requires more sophisticated hardware. Moreover, while competing with other hardware components for the available bore space, the applied shim order needs to be critically reviewed with respect to the expectable homogeneity gains. This can be inferred from simulations or extrapolated from the aforementioned experimental studies.

3.5 Non-spherical harmonic B_0 shim approaches

As a consequence of the limited correction capabilities of spherical harmonic shim fields, several alternatives based on different technologies have been developed. With the aim of generating more localized correction field patterns, these approaches specifically target the highly inhomogeneous brain regions close to strong susceptibility gradients. According to their correction field generation principle, they can be divided into passive and active shim approaches. Published examples of both shimming techniques are briefly reviewed in the following.

3.5.1 Sample specific passive shim approaches

Similar to correcting for system imperfections during the magnet installation procedure, various methods have been suggested to apply passive shim approaches for a subject-specific static B_0 field homogenization. The idea is that the susceptibility of the applied material as well as its dedicated geometry and position relative to the object can additionally distort the magnetic field in a way that the subject-specific B_0 inhomogeneities are canceled.
The implementation of subject-specific arrangements of ferromagnetic materials into an RF birdcage coil assembly was suggested for this purpose [123]. Based on a target shim field, the position of the shim material was optimized on a cylindrical surface surrounding the RF coil in order to achieve a best possible inhomogeneity correction. A similar approach extended this technique by using combinations of dia- and paramagnetic substances, which increases the field shaping capabilities due to the opposing signs of the susceptibility [124]. Moreover, a passive shim assembly was developed, which facilitates the positioning of the shim materials [125].
In an attempt to bring the passive shim elements closer to the origin of the B_0 inhomogeneities, the application of shims which are inserted into the mouth, or placed close to the ears was suggested [126]. Using strongly diamagnetic materials and targeting the strongest inhomogeneities in the inferior frontal cortex and the inferior temporal cortices, significant signal recovery was demonstrated in EPI images. The method has been extended to enable a subject-specific optimization of the size and shape of the applied shim elements [127]. Moreover, simulations have shown an improved signal stability in EPI time-series [128] and functional MRI measurements revealed an increased sensitivity to functional activation in the inferior frontal cortex as a result of the applied mouth shims [129].
Despite the reported increase in signal recovery and functional activation sensitivity, intra-oral passive shim elements have not achieved widespread adoption. Patient discomfort considerations as well as the evocation of physical reactions to the shim elements, including head motion and frequent swallowing, have led to the recommendation to use this shim approach only for dedicated measurements targeting the orbitofrontal cortex [130].

3.5.2 Non-spherical harmonic shim coils

A drawback of subject-specific passive shim approaches is the inter-subject variability of the susceptibility-induced B_0 inhomogeneity and the consequent difficult and time-consuming adaption of the shim materials. Therefore, targeting similar shim field patterns as the intra-oral passive shim approach, the application of small active intra-oral shim coils was suggested and has shown to similarly recover the functional MRI signal in acquired in vivo brain images [131]. The advantage of this technique over the passive shim elements is that the amplitude of the shim field can be scaled subject-specifically by the amount of current through the shim coil.

However, because the placement of electrical coils into the subject's mouth is a risk of hazard and increases discomfort, it was proposed to move the local shim coils to the periphery. In a pilot study, a small number of local shim coils were placed in a position anterior to the subject's face and arranged such that their cumulative field generated a desired shim correction in the prefrontal cortex [132]. By optimizing the position of a main loop and few additional balancing coils, a very localized field shape could be generated, which was appropriate for homogenizing the magnetic field across multiple subjects. Fig. 3.9 displays a single shim-loop setup and illustrates the idea of employing small coils to generate a simple but localized field.
The idea of using small and localized shim coils arranged in an array in order to generate complex field distributions has subsequently been generalized. As has initially been suggested similarly in abstract-form [133] a multi-coil array with 24 shim loops, regularly distributed over a cylindrical surface and close-fitting to the volume of interest, was developed [36]. It was extended to include 48 shim loops, and versatile field shaping capabilities were demonstrated in simulations and phantom experiments [134]. The results could successfully be transferred to mouse [135], rat [136] and human brain [137] acquisitions. An improved shim quality over 2^{nd} order spherical harmonic shimming was demonstrated in EPI and T_2^*-mapping applications [138].
To increase the efficiency of the local shim loops and to make a better use of the limited available bore space, the distance of the shim coils to the subject was further reduced by integrating them into the RF elements of a receiver-array. A proof-of-concept has been delivered by demonstrating results from a phantom measurement using a two-coil setup [139]. This could successfully be scaled to a more effective 32-channel setup and translated to human applications [140]. It has been shown that the local shim fields can improve the B_0 homogeneity over static 2^{nd} order spherical harmonic shimming and reduce EPI distortions [141]. Further improvements of these $\Delta B_0/R_x$-arrays were developed, which targeted increases in shim field shaping flexibility. This was implemented by dividing the direct current B_0 shim part of the assembly into multiple smaller shim loops. Each sub-element can be controlled by individual power supplies [142] or by using a switch matrix to distribute the shim currents from a single power supply to the individual shim paths [143].
For most of these techniques, however, it was exploited that the greater distance of the multi-coil arrays to the large conducting surfaces of the MR scanner leads to considerably weaker eddy currents when switching the shims rapidly. Similar to the principle of spherical harmonic dynamic shimming, this allowed a dynamic adjustment of the shim currents for multi-slice acquisitions, however, without the need for an eddy current compensation. Hence, the experimental studies have shown an improved shim performance for dynamically shimmed multi-slice acquisitions, but their effectiveness for shimming extended volumes for 3D or multi-band measurements has yet to be shown more extensively.
Alternatively, a combined usage of multi-coil and spherical harmonic shim approaches is conceivable and as been realized in a few initial implementations. For instance, a unified shim coil assembly, which can generate both, low-order spherical harmonic shim functions, as well as a certain number of localized field patterns, has been designed [144]. Furthermore, a spatially separated solution was suggested, which divides the spherical harmonic and the multi-coil wire patterns into two distinct surfaces [145]. Through application of an RF shield, both shim systems are electrically isolated from the RF coil array and can be driven individually so as to provide for the best possible field homogeneity.
Other approaches have investigated the applicability of generating dedicated wire patterns, which are optimized so as to generate exactly the field that is required to compensate for a certain subject-specific B_0 inhomogeneity distribution. For instance, field maps were analyzed via a

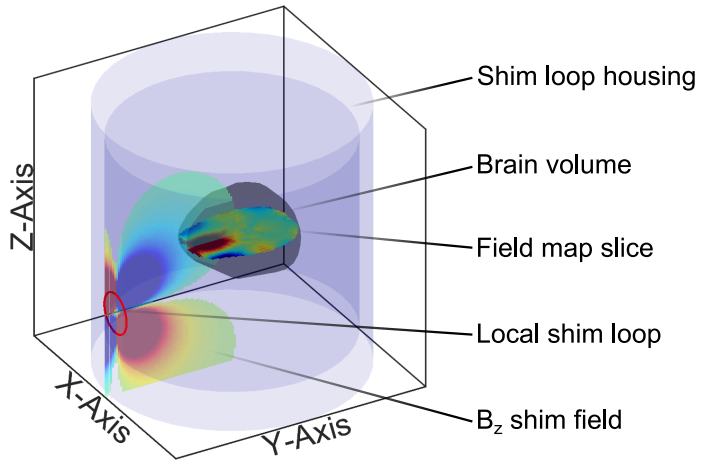

Figure 3.9: Basic principle of using small current loops to generate localized B_0 shim fields. The displayed transverse field map slice shows the typical residual B_0 inhomogeneity in the prefrontal cortex area. A loop coil, positioned in the indicated location, can be driven such as to generate a z-component of a resultant magnetic field, which is suitable to cancel large parts of the subject-specific B_0 inhomogeneities. For an efficient B_0 inhomogeneity cancellation, the number and the position of the applied shim loops are typically optimized, but the key concept remains the same.[1]

singular value decomposition and the basis functions corresponding to the largest singular values were suggested to be the optimal set of basis functions for human in vivo shimming [146]. While it is impractical to build the resultant wire paths in conventional manufacturing processes for immediate in vivo application, the implementation of an adaptive current network was suggested to be applicable for this purpose [147]. It can control the flow of current over a given surface by means of actively controlled solid-state switches. However, being conceptionally well-suited for generating the exact required magnetic fields, this approach is technologically difficult to realize using currently available technology.
In contrast to the pure spherical harmonic shim approach, for which each shim field can be described analytically, the multi-coil approaches do not adhere to any given model which could define the shim fields. The wire patterns do not necessarily have to follow simple loop geometries, but can follow any desired path which is experimentally realizable [148]. While this increases the flexibility in terms of shim field generation, it also complicates a comparison between different multi-coil shim configurations. It was, therefore, suggested to publish the applied wire pattern alongside with the reported improvements of a given setup [149].
In summary, non-spherical harmonic active shim approaches are an interesting alternative or addition to conventional shim techniques. A growing number of concepts is being developed and previously presented studies have reported significant gains in achievable B_0 homogeneity. However, being a relatively new technique, its robustness against inter-subject variability and its suitability for global whole-brain shimming still needs to be proven more extensively.

3.5.3 Acquisition strategies and post-processing techniques

The aforementioned B_0 shimming techniques have in common, that they cannot fully compensate for the high-order B_0 inhomogeneities. Therefore, several techniques have been developed, which try reduce the impact on the resultant MR images and spectra. This can be done by optimizing

[1] The Biot-Savart simulations were conducted using a Matlab tool provided by [150], as described in [140].

the variable sequence parameters, such that the influence of the B_0 inhomogeneities is minimized. Alternatively, after having acquired the MR data, post-processing techniques can be employed to retrospectively subtract out the inhomogeneity effects. Not necessarily being a form of active B_0 shimming, thus being beyond the scope of this work, these approaches are merely briefly discussed for reasons of completeness.

Z-shimming

The spatial resolution in MR images is often chosen such that the slice thickness exceeds the in-plane voxel size. Signal loss in MR images due to magnetic field variations over the dimension of the voxel can, therefore, in large parts be attributed to spin dephasing in through-slice direction. For slice thicknesses typically encountered in MR imaging, the through-slice variation of ΔB_0 can in good approximation be described by a linear term. Thus, by applying a gradient pulse in the slice-direction, the spin system can be pre-phased before the data readout, such that the through-slice gradient is compensated at the time of the echo formation [151]. Since MR images are often acquired in a transverse orientation, meaning that the z-gradient is used for slice selection, this method became known as *z-shimming*.
The through-slice gradient strengths vary across the object, and for an optimal compensation, multiple images with different z-shim gradient pulse strengths must be acquired. A composite image, consisting of one regular and multiple z-shimmed acquisitions, can then be formed by means of a maximum-intensity-projection, a sum-of-squares reconstruction [152] or a Fourier reconstruction [153]. It has been demonstrated, that an effective signal restoration can be obtained in highly inhomogeneous regions, for instance by acquiring multiple EPI images with different z-shim pulses [154] or by employing a multi-echo sequence with z-shim pulses prior to each individual echo readout [155]. The drawback of any z-shimmed acquisition is the intrinsic measurement time prolongation, which is needed to acquire the additional images.

Sequence parameter optimization

After having optimized the B_0 shim setting, a number of sequence parameters can be tuned such as to minimize the effects of magnetic field inhomogeneities. Spin-echo sequences are intrinsically less prone to inhomogeneity effects than gradient-echo based techniques, however the associated prolongated acquisition time often precludes their application. As has been discussed in the previous section, gradient-echo based acquisition strategies often suffer from signal loss due to spin dephasing in through-slice direction. Hence, decreasing the slice thickness can equally decrease the signal dropout, but comes at the expense of a lower signal-to-noise ratio and a reduced volume coverage. Alternatively, a decrease in echo time grants the spin system a shorter period over which the dephasing may occur and can similarly be used to reduce the signal dropout. However, this has an impact on the tissue contrast and can even be infeasible, for instance when a fixed echo time must be chosen to be sensitive to certain physiological parameters. In-plane acquisition acceleration by means of parallel imaging can also be applied to reduce geometric distortions. Skipping k-space lines in the phase-encoding direction reduces the effective echo-spacing an can, therefore, reduce the voxel shifts in that direction. Besides introducing a certain robustness against B_0 inhomogeneities, all of the aforementioned acquisition strategies have a more or less severe impact on the acquired images. Therefore, they cannot be regarded as a universal form of B_0 shimming, but can help when highly inhomogeneous regions are targeted and the conventional active shim approaches are insufficient.

Distortion correction

Image distortions induced by B_0 inhomogeneities can retrospectively be corrected using dedicated post-processing routines. When knowing the ramp- and dwell-times of the imaging gradients, an acquired field map can be converted to a voxel shift map. This map, which indicates the voxel shift in the phase encoding direction, can then be used to shift back the voxels of an acquired distorted EPI image [156]. Alternatively, two EPI datasets, acquired with opposing phase-encoding directions, were suggested to yield sufficient information about the voxel shifts in order to perform a distortion correction. The direction of the voxel shifts in the images depends on the applied phase encoding direction. Thus, an algorithm is used to estimate a distortion field, which maximizes the similarity between the two image datasets after correction [157].
However, retrospective corrections cannot perfectly restore a distorted image and cannot recover the information loss due to dephased signal. Similar as for the sequence parameters optimization, prospective active B_0 shim approaches are, therefore, always preferable, but distortion corrections can additionally be applied.

4

Spherical harmonic shim system calibration and static B_0 shimming

The origins of B_0 field distortions, caused by system imperfections and individual magnetic susceptibility distributions, have been introduced in Section 3.2.1. The necessity to cancel them in a pre-scan adjustment process, to minimize artifacts in MR imaging and spectroscopy applications, has been motivated in Section 3.2.2. Quantitative image-based field mapping techniques have been summarized in Section 3.3.2 and form the basis for the majority of automated B_0 shim routines used to compensate for these inhomogeneities. The most commonly employed hardware for the B_0 field homogenization are spherical harmonic shim coils, and methodologies to correctly control this type of shim system have been reviewed in Section 3.4.

In order to efficiently correct for B_0 inhomogeneities by means of accurate shim adjustments, it is indispensable to initially measure the apparent field distribution with high precision. Sequences for B_0 mapping must fulfill certain requirements with respect to spatial sampling density, acquisition time and measurement accuracy. Subsequently, the collected B_0 field information need to be correctly decomposed into their spherical harmonic components. During this shim optimization process, realistic and accurate modeling of the real spherical harmonic correction fields is of critical importance, since many shim fields deviate to a greater or lesser extent from their ideal functions. Both of these subjects will be discussed in the following.

To meet the requirement of precise field assessments, a B_0 mapping sequence and its required processing routines are described here and applied throughout this work in the context of B_0 shimming. Moreover, for a realistic shim field modeling, the shim calibration process and its results are shown for conventional 2^{nd} order spherical harmonic shim systems. Likewise, results from a very high-order shim insert with full 4^{th} and partial 5^{th} and 6^{th} order shims are shown. The integration of the B_0 mapping and the shim calibration into a custom-written, versatile B_0 shim program is used to ultimately demonstrate the applicability of this framework for effective and non-iterative static B_0 shim optimizations in phantom and in vivo measurements.

The work presented here can, therefore, be regarded as a combination of a re-implementation of current state-of-the-art B_0 shim methodologies and further developments, forming a fast and non-iterative B_0 shim routine. The strengths and limitations of conventional and very high-order static spherical harmonic B_0 shimming are demonstrated towards the end of this chapter and motivate the need for the development of more efficient shim techniques. Chapters 5 and 6, therefore, build upon these results and explore the performance gains of spherical harmonic shim systems when they are exploited to their full potential in dynamic operation.

4.1 Introduction

The concept of B_0 shimming based on spherical harmonic resistive shim coils is the most widespread form of magnetic field homogenization in MR applications. Since shim settings can conveniently be updated by changing the individual shim currents, it is a rapid and efficient method used for static, dynamic and real-time shim adjustments. Based on subject-specific B_0 maps, optimal shim currents for each available shim coil are typically calculated in a dedicated adjustment process via a least-squares fit of the associated spherical harmonic shim functions to the measured field data. However, direct application of the ideal functional forms typically leads to an erroneous or, at best, sub-optimal correction of the measured B_0 inhomogeneities. This is due to the fact that system specific shim coil efficiencies as well as shim coil impurities are not considered in the ideal model, but can have a significant impact on the quality of the calculated shim solution. The former is a measure of the shim field amplitude as a function of the input shim coil current and the latter describes spatial deviations of the generated shim fields from the ideal spherical harmonic functions. As a consequence of these coil properties, the optimal B_0 homogeneity might not be reached when using the ideal functions, or settles only after several B_0 shim iterations. Hence, the B_0 shim process can degenerate into a very time-consuming pre-scan adjustment procedure or even fail completely in meeting the demands of the subsequent MR measurements.
It is the purpose of the shim calibration process to calculate the system-specific efficiency of each shim coil and to quantitatively determine its impurity characteristics. The information thus gained is used to correct the ideal spherical harmonic system matrix such as to optimally describe the real behavior of the given shim system. This enables a very accurate prediction of the applied shim correction field and, thus, forms the basis for efficient and non-iterative shim adjustments. The data which is required for this purpose is most commonly obtained from acquiring *shim offset maps* of spherical phantoms, which are positioned in the iso-center of the scanner such as to cover the volume of interest. The maps are acquired while offsetting a given shim channel by a known input current and, thus, allowing the shim current through a shim coil to be related to the resulting shim field offset. Early works in automated B_0 shimming used this offset data directly in the shimming process by calculating a linear combination of the maps, which would optimally cancel the measured B_0 inhomogeneities in the object [61]. Despite having formed the basis even for most recent shim optimization frameworks, this method is prone to introducing potential errors from the initial shim map acquisition into each following shim optimization. Furthermore, it is inflexible when shimming over regions that differ in volume or image matrix size from those of the shim offset maps.
As a consequence, a model-based shim calibration, which enables a more accurate and very versatile approximation of the spatial field response of a shim coil to a known input current, became the method of choice [41]. It is commonly implemented by mapping all impurity terms of each shim coil and by subsequently approximating them using a very high-order spherical harmonic expansion. Using this information, alongside with the simultaneously gained shim coil efficiencies, the response of a shim coil to a given input current can conveniently be modeled, by assuming a linear relationship between applied shim current and resultant shim- and impurity-fields. This procedure has been demonstrated to be more robust against systematic errors and enables the inclusion of the shim efficiency and impurity information into the spherical harmonic system matrix [158]. By evaluating the ideal spherical harmonic functions at each desired location and by correcting the resultant field functions using the shim calibration results, B_0 shimming can, therefore, be carried out very accurately over arbitrarily sized and positioned shim volumes. As a

result, the shimming process is no more limited to the acquisition geometry of the acquired shim offset maps.
In summary, the inclusion of the comprehensive shim calibration results into the subject-specific shim optimization process intrinsically converts the associated fit coefficients into the correct hardware units. This is a direct consequence of using the correct shim coil efficiencies during the shim calculation. Simultaneously, it accounts for deviations of the real shim fields from the ideal spherical harmonic model, which enables an accurate and non-iterative shim adjustment procedure. This is achieved by also including the shim impurity information. It follows, that accurate B_0 mapping plays a key role, not only during the conventional subject-specific shim optimization process, but also during the shim calibration procedure, when collecting the individual shim offset maps. Thus, this chapter introduces the B_0 mapping sequence and the associated processing steps, which are applied for field mapping purposes throughout this work. Moreover, the model-based shim calibration steps are outlined and detailed results are presented for all systems that were employed in this work. Ultimately, the applicability of the calculated B_0 shim system calibration matrices are demonstrated using a custom-written, static, non-iterative B_0 shimming routine.

4.2 Theory

The core principle of the B_0 shimming process involves a linear least-squares fit of a certain set of basis functions to a measured field distribution. In this context, the sampled B_0 field can be expressed as a vector of observed values and the set of shim functions as a system matrix which describes the linear system. The optimal shim values, consequently, correspond to the elements of the parameter vector which best possible fit the functions to the measured data. Mathematically, this is described by the optimization problem given by Eq. 3.5 in the previous chapter. Thus, three processes are required in order to be able to robustly calculate optimal shim currents on a subject-specific basis. They are detailed in the following and include the theoretical background of how to correctly measure the B_0 inhomogeneities, characterize the shim system and, ultimately, use both information to calculate a set of optimal shim values.

4.2.1 Field mapping

As discussed in Section 3.3, the first step towards a precise correction of B_0 inhomogeneities, is to quantitatively measure them. Due to their short acquisition times, phase-based methods are well-suited for field assessments and are commonly combined with image encoding techniques to provide for volumetric B_0 field maps. Based on the measured phase values and the associated phase evolution time, these B_0 field information are calculated from Eq. 3.4. Accurate MR phase-image based field mapping is, however, more complex than it was outlined in the literature review given in the previous chapter. As shown in the following, the main challenges pertaining to this technique include multi-dimensional phase wrapping in regions of high B_0 heterogeneity, the presence of initial and dynamic phase offsets in the measured data and the requirement to balance phase contrast and signal-to-noise ratio.

Phase wrapping

Phase *wrapping* is a phenomenon which is related to the periodicity of the MR signal phase and occurs, because the measured phase values are restricted to a limited circular range within $(-\pi, \pi]$. Therefore, following the pictorial representation of the phase angle given in Fig. 3.2 B, phase values that are evoked by magnetic field inhomogeneities which exceed a certain threshold, will wrap back into that range after a certain phase evolution time.
Given π and t_{TE}, corresponding to the absolute value of the limit of the phase range and the echo time at which the MR signal is recorded, the wrap threshold can be converted to a maximum absolute precession frequency offset, ω_{max}. Beyond this threshold, the magnetic field offset cannot be resolved unambiguously from the phase data anymore. It follows from

$$\pi = \omega_{\mathrm{max}} \cdot t_{\mathrm{TE}} \quad \Longrightarrow \quad \omega_{\mathrm{max}} = \frac{\pi}{t_{\mathrm{TE}}}, \tag{4.1}$$

and, hence, provides a direct link to the adjustable sequence parameters. Thus, based on the frequency offset induced by the susceptibility distribution of the subject and without the application of further processing techniques, the echo time must be decreased such that the above requirement is fulfilled in order to avoid phase wrapping. This is demonstrated in Fig. 4.1 A for a series of phase images sampled at different echo times using a gradient echo sequence. The first sampled echo is largely unaffected by phase wrapping, thus adhering to the aforementioned requirement, but the wrap count increases severely with the chosen echo time. Fig. 4.1 B

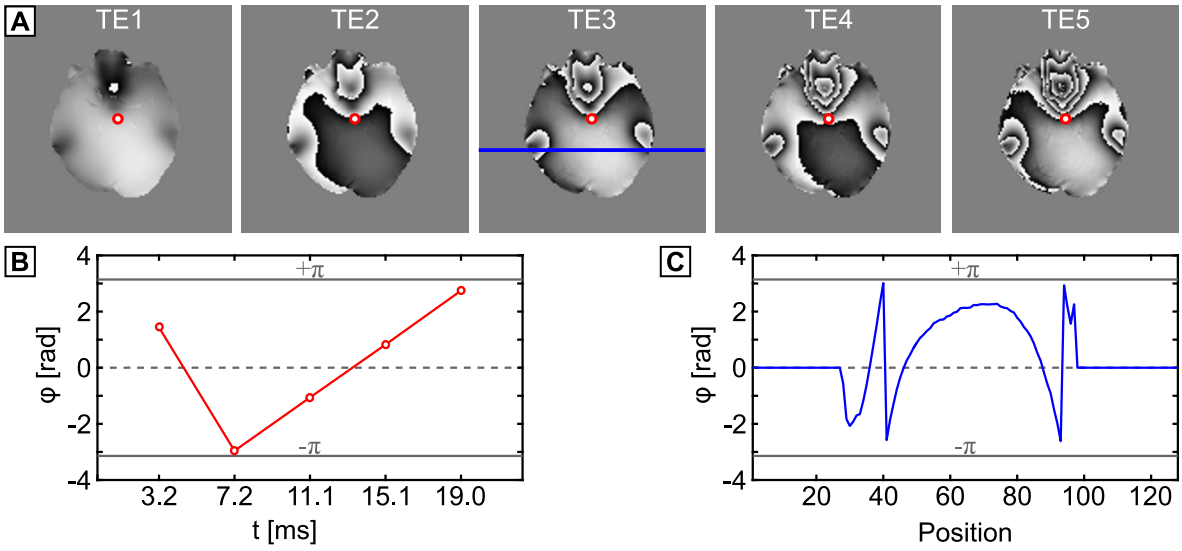

Figure 4.1: Phase data after brain-masking, acquired with a multi-echo gradient echo sequence. **(A)** The individual echoes are separated by 4 ms and demonstrate the increase in phase wrap count as a function of the echo time. It can be seen that the first echo is largely unaffected, merely with small phase wrapping effects in the pre-frontal cortex area. The later echoes reveal significant phase wrap effects. **(B)** Temporal phase wrapping is shown for the voxel indicated by the red circle in each phase image. **(C)** The 1D profile along the blue line illustrated in the phase image of the third echo and reveals spatial phase wraps that are evoked by the air-filled auditory canals.

illustrates the effect of phase wraps that occur at a given voxel location within the indicated evolution period. Moreover, because the phase evolution of every voxel is governed by the highly position-dependent B_0 field shifts, this phase wrapping occurs at different time-points within the sample. As can be seen in the phase images and in Fig. 4.1 C, this leads to complicated phase wraps in the spatial domain and renders a direct application of phase data of late echoes impractical for quantitative field mapping. The impact of this phenomenon can more conveniently be quantified when converting the aforementioned threshold values to the associated frequency and magnetic field offsets, which follow from

$$f_{\text{max}} = \frac{1}{2 \cdot t_{\text{TE}}} \quad \text{and} \quad \Delta B_{0,\text{max}} = \frac{\pi}{\gamma \cdot t_{\text{TE}}}. \tag{4.2}$$

It implies that a phase evolution time of 4 ms results into a maximum tolerable signed field offset of only ± 125 Hz or ± 2.9 μT, respectively. Depending on the applied static magnetic field strength and as was shown in Section 3.2.1, the frequency variation in the human brain may exceed this threshold in large parts already at this relatively short phase evolution time. However, for reasons detailed later in this section, longer phase evolution times and multiple sampled echoes are desirable for accurate B_0 field mapping. Hence, in order to extend the applicable phase evolution period, phase *unwrapping* techniques were developed, which can be divided into temporal and spatial domain algorithms.

The *temporal* phase unwrapping algorithms analyze the local phase evolution at each voxel location over multiple sampled echoes, independently from the spatially neighboring samples. Starting at the first echo, each subsequently sampled phase value is analyzed and compared to the previous sample. In cases where the difference between both values exceeds $\pm\pi$, integer multiples of 2π are added to the current phase value such that the result falls within the expected range. This is illustrated in Fig. 4.2 A. For this method to work robustly, the first phase evolution

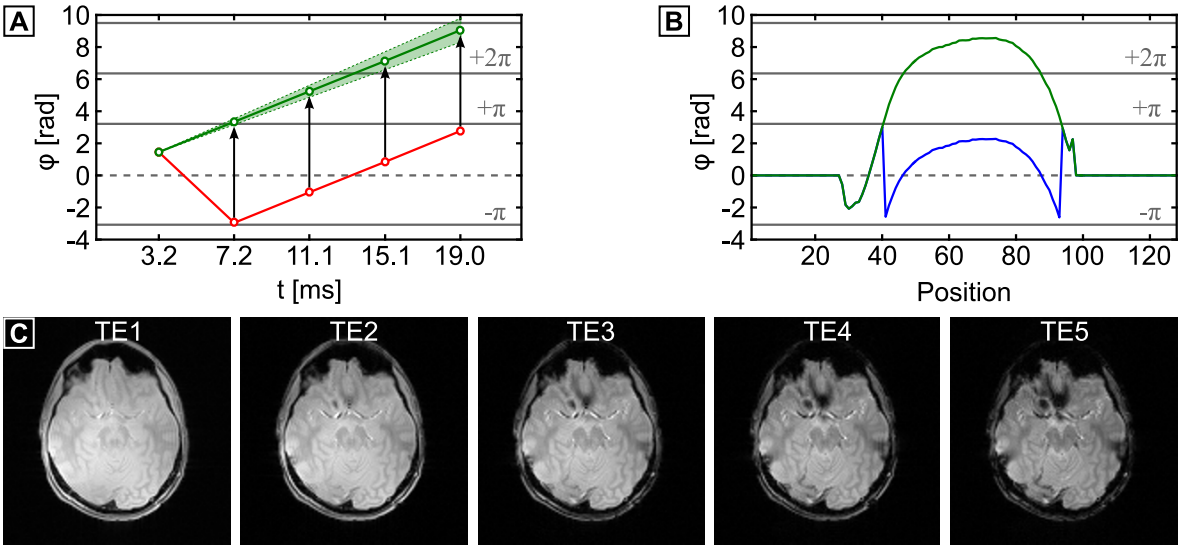

Figure 4.2: Phase unwrapping principles and signal-to-noise considerations for field mapping. The plots show the same phase evolutions as Fig. 4.1. **(A)** In this example, the phase evolution at the distinct voxel position has induced wraps, occurring at the second and all subsequent echoes. Addition of $+2\pi$ during the temporal unwrapping process shifts all phase values back into the expected range. **(B)** Similarly, spatial unwrapping removes the phase discontinuities along the 1D profile. Extensions to higher dimensions, however, must address phase wraps that are potentially occurring between multiple adjacent voxels. **(C)** As can be seen from the magnitude images, spin dephasing reduces the signal-to-noise ratio of later echoes. This also leads to uncertainties in the phase measurement, which is qualitatively indicated by the green error band in the temporal phase evolution plot.

time must be chosen short enough such as to induce no phase wraps and, furthermore, certain demands with respect to phase noise of all acquired echoes must be fulfilled.
In contrast to this 1D phase analysis, *spatial* unwrapping algorithms analyze the phase images separately for each acquired echo, but along all sampled spatial directions. Because susceptibility-induced B_0 distortions have a rather smooth spatial variation, it is assumed that the phase differences between voxels are comparably small, unless the signal has wrapped. Following this, an unwrapping operation is performed in cases where neighboring voxels exhibit absolute phase difference values greater than π. This unwrapping process is schematically illustrated in Fig. 4.2 B for a single line along the horizontal direction. The challenge, however, lies in the demand of unwrapping the phase along all spatial directions without causing any ambiguity between neighboring voxels. Since this is a difficult task, spatial unwrapping algorithms are typically more complicated and require longer processing times, but can yield superior results. Moreover, because spatial unwrapping is performed individually for each echo, temporal phase wraps may still occur between the images acquired at different echo times. Therefore, as illustrated in Fig. 4.3, the unwrapped phase images must be re-ordered in a final temporal unwrapping step. For reasons detailed in the following, instead of regular phase images, the depicted slices show the phase differences between the first and all subsequently acquired echoes of a multi-echo sequence.

Initial and dynamic phase offsets

In addition to a phase accrual induced by static B_0 inhomogeneities, MR images can have an additional initial phase offset, induced by a non-zero phase term immediately after sample excitation at $t = 0$. This offset is constant over time, but can be spatially varying and demands

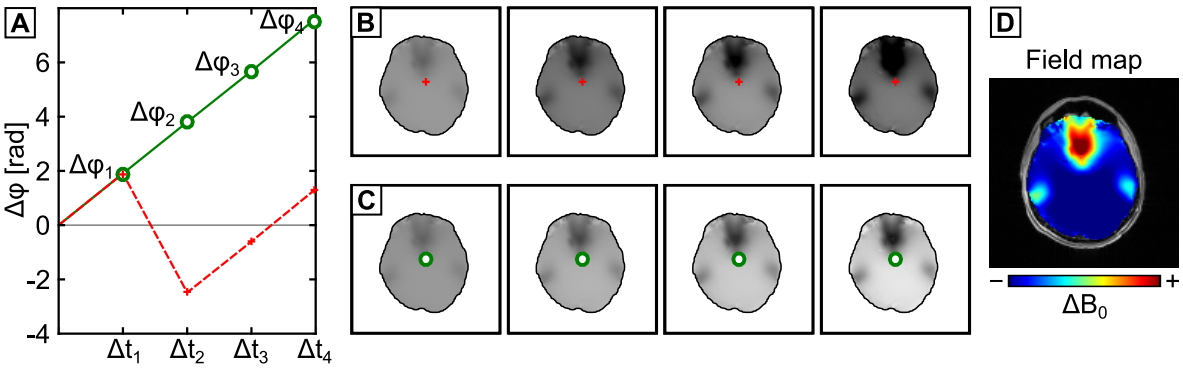

Figure 4.3: Spatial unwrapping and temporal echo re-ordering for a robust field map reconstruction. **(A)** Plot of the phase evolution of the central voxel, marked in the slices of the spatially unwrapped phase difference images shown in **(B)** and the additionally temporally re-ordered images shown in **(C)**. The phase difference follows from subtracting the phase of the first echo from all subsequent echoes and, likewise, the resultant phase evolution times follow from subtracting the first echo time from the later echo times. The phase offset added to the temporally re-ordered slices is calculated from the temporally unwrapped vector shown in the plot. **(D)** The final field map is calculated via linear regression applied to the unwrapped phase images.

the incorporation of an additional static phase offset term, $\phi_0(\mathbf{r}) \neq 0$, into the phase equation. When using multi-channel receiver arrays, this static phase offset can even vary among the individual coil elements and renders the channel combination during the reconstruction more challenging [159]. Moreover, dynamic field terms of uncompensated eddy currents induced by the imaging gradients or field fluctuations induced by the the subject itself can cause additional temporally and spatially varying phases, $\phi_{Dyn}(\mathbf{r}, t)$ [81]. Signal contributions from chemical shift species, such as the proton signal from lipids, can also alter the phase, but are typically neglected in the human brain due to their low abundance. Nonetheless, the phase equation contains unwanted static and dynamic terms according to

$$\phi(\mathbf{r}, t) = \gamma \cdot \Delta B_0(\mathbf{r}) \cdot t + \phi_0(\mathbf{r}) + \phi_{\mathrm{Dyn}}(\mathbf{r}, t) \tag{4.3}$$

and direct application of Eq. 3.4 using a single phase image can result into an incorrect estimation of the underlying static magnetic field offset.
For the reconstructions of B_0 field maps, however, it is not required to measure the exact phase that has accumulated since sample excitation, but instead it is sufficient to monitor the phase evolution during any fixed evolution period. This can be done by acquiring phase images at different echo times, $\phi_{\mathrm{TE}_i}(\mathbf{r})$, and by calculating the phase difference between them. The constant phase offsets are subtracted out by this operation, leaving only the phase that has accumulated within the period between both echo times. Due to the subtraction process, it follows that the effective phase evolution time then corresponds to the echo time difference between both images and, hence, the magnetic field information follow from

$$\Delta B_0(\mathbf{r}) = \frac{\phi_{\mathrm{TE}_2}(\mathbf{r}) - \phi_{\mathrm{TE}_1}(\mathbf{r})}{\gamma \cdot (t_{\mathrm{TE}_2} - t_{\mathrm{TE}_1})}. \tag{4.4}$$

The time-dependent dynamic phase offsets are more difficult to deal with, since several sources affect the sampled echoes differently and, thus, cannot be entirely subtracted out. One of the major contributions, however, stems from eddy currents induced by the readout gradients. Therefore, in this particular case a remedy can be provided, when choosing a mono-polar readout

mode, i.e. when sampling even and odd echoes along the same direction in k-space. Based on the premise that all readout gradients are prepared with equal amplitudes and durations, each image will be affected equally by the readout gradient induced eddy currents. Consequently, their eddy current contributions are equal and, thus, the dynamic phase effects can be reduced when applying the aforementioned phase subtraction operation.

Phase signal optimization

In the previous section, the benefits of B_0 mapping based on phase difference images were detailed and the general framework for field map calculations based on this data was established. This principle can be further generalized, because the number of acquired echoes does not have to be limited to two, i.e. a single phase difference image. Considering measurement noise, the acquisition of multiple echoes in combination with a linear regression analysis on the acquired data is even beneficial for a robust estimation of the true linear phase evolution.
As illustrated in Fig. 4.3 A, if multiple unwrapped phase measurements are available, the regression coefficients for the linear phase evolution can be calculated and turned into magnetic field values. Consequently, with Δt_i and $\Delta\phi_i$ being the echo time and the unwrapped phase difference between the first and later sampled echoes, respectively, and with $\overline{\Delta t}$ and $\overline{\Delta\phi}$ denoting the mean echo time and mean phase difference, the magnetic field offset can be calculated from [160]

$$\Delta B_0(\mathbf{r}) = \frac{\sum_{i=1}^{N}(\Delta t_i - \overline{\Delta t}) \cdot (\Delta\phi_i(\mathbf{r}) - \overline{\Delta\phi}(\mathbf{r}))}{\gamma \cdot \sum_{i=1}^{N}(\Delta t_i - \overline{\Delta t})^2}. \tag{4.5}$$

Results for a field map reconstruction based on acquired phase images are displayed in Fig. 4.3 D. However, as can be seen from the magnitude images shown in Fig. 4.2 C, the decrease in signal-to-noise ratio as a function of the applied echo time introduces uncertainties, which can falsify the B_0 maps. Hence, the number of acquired phase images as well as their individual echo times must be carefully chosen such as to balance signal-to-noise ratio, phase contrast and acquisition time.

4.2.2 Shim coil characterization

As was introduced above, when wanting to accurately control the shim system via adjusting the coil currents, it is essential to characterize the response behavior of each individual shim coil to a given input current. This section focuses explicitly on the static shim coil behavior, for which a sufficiently long settling time between the change in coil current and the analysis of the associated shim field is assumed. In contrast to that, Chapter 5 will treat the dynamic response of a shim coil shortly after a rapid change in shim current.

Shim coil efficiency

The *shim coil efficiency* describes the relationship between an electrical current being passed through a shim coil and the strength of the targeted spherical harmonic shim field generated by that coil and current. It is a scalar-valued characteristic of each coil and commonly expressed in units of $\mathrm{Hz}/(\mathrm{cm}^n \cdot \mathrm{A})$, where n refers to the order of the shim coil. Fig. 4.4 shows acquired shim offset maps, which illustrate the varying shim efficiencies of different shim coils energized by equal input currents. The shim efficiency can also be regarded as a constant scaling factor, which converts between the amplitude of a calculated ideal spherical harmonic basis function

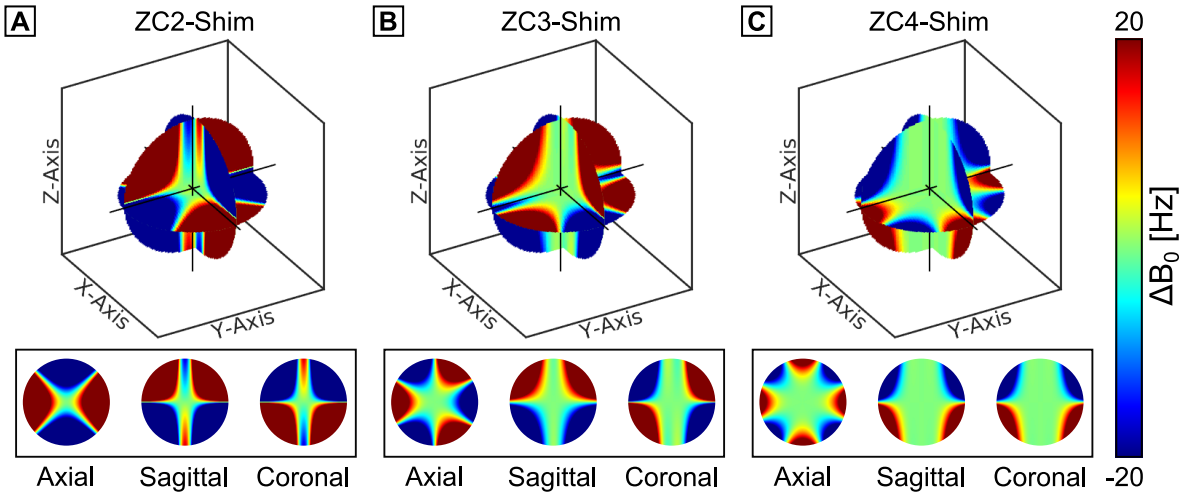

Figure 4.4: 3D shim field distributions generated by a 1 A shim current applied to different shim coils. The induced field offset measured over the entire volume is highest for the 3rd order shim coil shown in **(A)** and decreases for the 4th and 5th order shims shown in **(B)** and **(C)**, respectively. Naturally, this effect applies equally to any other lower or higher order shim coil not shown in this illustration. The images show, that the shim efficiency decreases especially in more iso-centered regions. Due to a zero-crossing of the shim fields in the iso-center, the illustrated slices are located 1 cm off-center.

and the effectively generated field amplitude, when passing a current of 1 A through the coil. Exact knowledge of the efficiencies of each available shim coil enables a correct scaling of the spherical harmonic coefficients that are calculated in the shim optimization. Therefore, its precise determination is of critical importance during the shim calibration procedure.
The shim coil efficiency varies with $r^{-(n+1)}$ [161], where r refers to the radius of the spherical harmonic shim coil of order n. It follows that higher order shim coils either require higher shim currents, or need to be constructed with smaller radii, in order to generate shim field amplitudes comparable to those of lower order coils. The reason for that lies in a self-canceling behavior of the coil for winding patterns that are used to create higher-order field functions [88]. This effect can also be seen from the maps shown in Fig. 4.4 for the shim fields of a 3rd, 4th and 5th order shim coil generated by a 1 A input current.

Shim coil impurities

Besides the targeted ideal spherical harmonic field function, realistically built shim coils generate additional and unwanted static field terms, which are spatially varying deviations of the real shim field from the targeted ideal spherical harmonic function. These *shim coil impurities* can originate from coil manufacturing tolerances or inaccuracies or a misplacement of the coil with respect to the iso-center of the magnet and the gradient set [63]. If not considered in the optimization process, the shim adjustment of a shim coil will, depending on the magnitudes of its impurities, introduce additional, unwanted magnetic field terms, which are scaled by the amplitude of the applied shim current. In extreme cases, the magnitude of the unwanted cross-terms can even exceed that of the desired self-term. Hence, ignoring shim coil impurities renders the shim optimization inaccurate, because it leads to deviations of the predicted from the effectively applied shim field.
The impurity characteristics of a 3rd order shim coil used in this work are illustrated in Fig. 4.5. Although at first glance the coil appears to be producing a very pure Z2S term, a comparison to

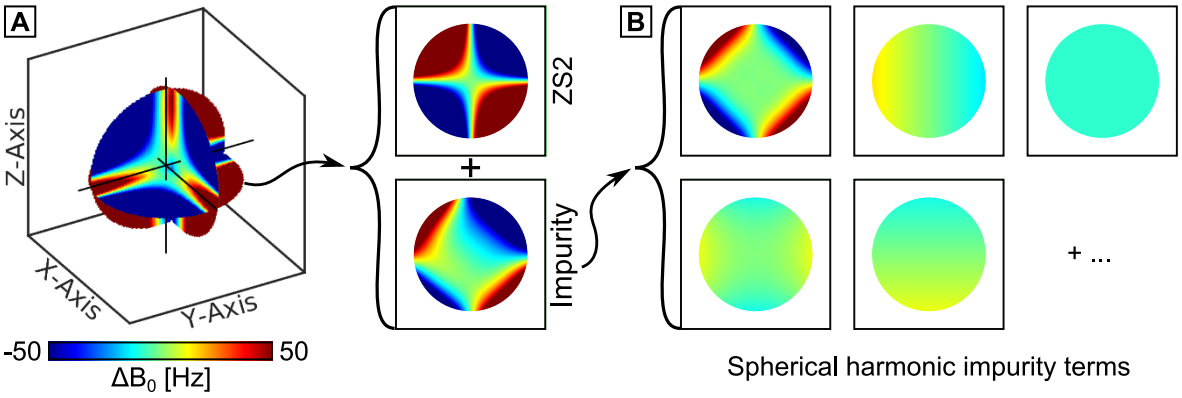

Figure 4.5: Illustration of shim coil impurities of a 3rd order ZS2-term. **(A)** 2 cm off-center positioned slices through a 3D field map volume illustrate the real shim field function generated by a 1 A current through the associated shim coil. As shown for the transverse slice, the map can be decomposed into an ideal ZS2-shim contribution and a superimposing shim impurity field. **(B)** The residual impurity field itself can be approximated by a high-order spherical harmonic expansion. Thus, even highly impure shim fields can be described by a spherical harmonic model using the coefficient of the self-term as well as those of the most prominent cross-terms.

the ideal function and a subsequent spherical harmonic decomposition of the residual impurity map reveals non-negligible cross-terms. A characterization of the impurities of each shim coil, and inclusion of this knowledge into the shim optimization, allows for a more accurate modeling of the shim fields and, thus, forms the basis for non-iterative shim adjustments.

Shim calibration procedure

The aforementioned coil properties can be determined in a single calibration procedure, which is schematically illustrated in Fig. 4.6 for a C2 shim coil. Shim offset maps of a typically spherical water phantom are successively acquired for each shim coil at multiple current offsets. The applied shim offsets must be chosen carefully such as to cause no artifacts induced by the resultant shim field. The acquired maps can then additionally be corrected by subtracting a reference map, which is acquired in the absence of any shim offsets, and which leaves a *difference* field map, affected merely by the impact of the applied shim field. Ideal spherical harmonic functions are then evaluated up to a maximum order, n_{max}, which determines the accuracy of the subsequently performed high-order spherical harmonic shim field approximation. The 3D coordinates at which the functions are being evaluated correspond to the field map voxel locations within the scanner. For each available shim offset map, the entire set of $N = (n_{\text{max}} + 1)^2$ functions is fitted to the data, leading to $2n + 1$ coefficients per order, n.
For each spherical harmonic field term, linear regression is then used to model the relationship between the applied shim offset current and the associated fit coefficients. The fit statistics can be used to identify terms, whose spherical harmonic coefficients have a linear dependence on the applied shim current. The slopes of these lines are in units of $\text{Hz}/(\text{cm}^n \cdot \text{A})$ and correspond to the coefficients of the linear approximation of the given shim term. The slope of the self-term corresponds to the shim coil efficiency and the linear combination of all cross-terms describes the shim coil impurity.
The results of the regression analysis are stored in shim calibration vectors $\mathbf{v} \in \mathbb{R}^{N\times 1}$. In combination with the ideal spherical harmonic field functions, which can be evaluated at any point within a volume of interest, this vector holds all significant coefficients for the linear

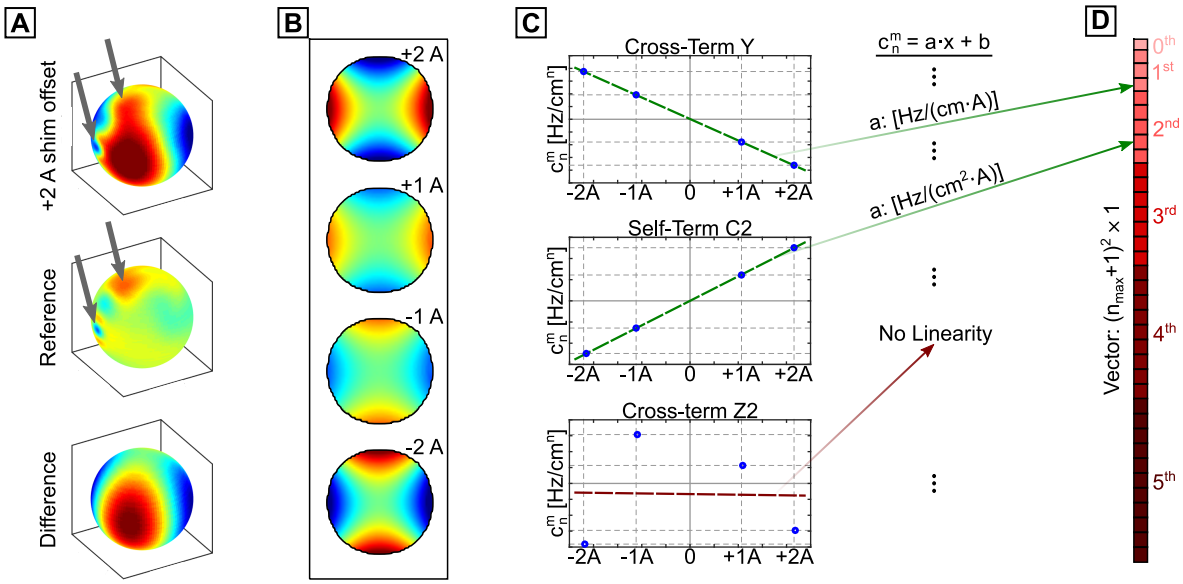

Figure 4.6: Schematic of the shim coil characterization procedure of a C2 shim coil. **(A)** Shim offset maps are acquired for multiple shim current offsets and can individually be corrected by a reference map to account for baseline B_0 field inhomogeneities. The volume shown here was acquired in the presence of a +2 A current offset. **(B)** Transverse slices of shim offset maps acquired at four current offset values, indicating the linear dependence of the dominant self-term on the applied current. **(C)** Each shim offset volume is decomposed into $(n_{\max}+1)^2$ spherical harmonic components. A linear regression is applied to the resultant coefficients to discriminate between linear and non-linear terms. The slope of the line of the self-term corresponds to the shim coil efficiency and the slopes of all relevant cross-terms characterize the shim coil impurity. **(D)** The values of the slopes of all spherical harmonic terms that reveal a linear dependence on the applied current offset are stored in a calibration vector, all other entries are zero-filled. In this example, the shim coil was approximated by a 5^{th} order linear spherical harmonic expansion ($n_{\max} = 5$).

approximation of the spherical harmonic shim term and comprehensively describes the static behavior of each shim coil analyzed in this way.

4.2.3 Shim optimization

The field mapping is performed on a subject-specific basis and repeated whenever a certain volume is chosen over which a dedicated shim optimization is required. The shim calibration, on the other hand, is performed subject-independently and only once. It merely needs to be repeated in cases of MR system modifications that affect the shim set. During the shim optimization, both information need to be combined in order to be able to realistically model the shim correction fields while searching for the set of optimal subject-specific shim currents.

Integration of the shim calibration

The calibration results of each shim coil can be combined and written into a single matrix, thus, collectively describing the static behavior of the entire shim system. Let M be the number of coils of a given shim system and let $N = (n_{\max}+1)^2$ denote the number of spherical harmonics used to characterize each coil up to order $n_{\max}$. The resultant individual shim calibration vectors $\{\mathbf{v}_i \in \mathbb{R}^{N\times 1}, i = 1,\ldots,M\}$ define the calibration matrix $\mathbf{C} = [\mathbf{v}_1,\ldots,\mathbf{v}_M] \in \mathbb{R}^{N\times M}$. Its main diagonal elements correspond to the shim coil efficiencies and all non-zero off-center

elements indicate a non-negligible cross-term to other spherical harmonics. Furthermore, let $\{\mathbf{r}_\ell \in \mathbb{R}^{3\times1}, \ell = 1, \ldots, L\}$ denote the 3D Cartesian coordinates of each of the L discretely sampled voxels of an acquired field map. The ideal spherical harmonic functions, $\mathrm{f}_{n,m}(\mathbf{r}_\ell)$, of order n and degree m can be evaluated at all sampling positions up to order n_{max} and stored column-wise in the spherical harmonic matrix $\mathbf{H} \in \mathbb{R}^{L\times N}$. The system matrix, $\mathbf{A}$, follows from $\mathbf{A} = \mathbf{H} \cdot \mathbf{C}$ and is an accurate approximation of the real spherical harmonic shim fields as they are generated by the given shim coils at the individual voxel positions.
Since the calibration matrix is position-independent and the spherical harmonics can be evaluated at any feasible location within the active MR volume, this approach can be used to shim over arbitrarily positioned volumes. It entails that, as long as the shimming volume does not exceed the calibration volume, the volume-of-interest can be chosen independently from the acquisition geometry of the shim calibration data. To a certain extent, this also applies to volumes that exceed the calibration volume. However, in these cases, the shim accuracy must be critically evaluated and it must be ensured that the target volume over which the shim coils were designed is not exceeded. Importantly, since any measurement or data processing errors during the calibration procedure consequently translate into all subsequent MR measurements, an accurate shim calibration is critical.

Calculation of optimal shim currents

The optimal shim currents follow from a least-squares minimization of the differences between the measured B_0 inhomogeneities and a linear combination of the real spherical harmonic shim fields described by the columns in the system matrix. In the previous two sections, the details on how to correctly measure the apparent B_0 field distortions, $\mathbf{b}$, and set up the system matrix, $\mathbf{A}$, have been given. In principle, the shim calculation can then most simply be carried out via a pseudo-inversion of the system matrix, which provides the desired minimum-norm solution, $\mathbf{x}$, for the least-squares optimization problem.
However, a simple matrix inversion cannot account for hardware limitations and is prone to measurement noise and poorly conditioned system matrices. Hence, more adept technique were developed which aim at incorporating additional constraints into the optimization process [95]. Besides hardware limitations, the applied constraints can also take a form that introduces certain desired properties to the resultant shim solutions. For example, the shim may be optimized such as to keep the currents of certain sets of coils low or to limit the maximum field offsets in distinct regions outside of the adjustment volume [91]. Within this confined search space, numerical optimization algorithms are typically employed in order to find the parameter vector which best possible cancels the measured B_0 inhomogeneities while complying with all side conditions.

4.3 Methods

The methods described in detail in the following build upon the theory explained in the previous section and include the field map data acquisition and processing as well as the shim coil characterization. Moreover, the techniques employed to obtain optimal shim currents and the way they are effectuated are outlined. Being explained here for conventional static shimming, these methods are in large parts equally applicable to the more advanced techniques treated in the subsequent chapters.

4.3.1 Hardware

Two types of spherical harmonic shim systems were used within the scope of this work for magnetic field homogenization. Conventional vendor supplied systems were used, which are incorporated in the MR scanner hardware and designed such as to generate the three 1^{st} order spherical harmonic terms via the gradient coils and the five 2^{nd} order terms via dedicated shim coils. This type of shim system is the industrial standard and has been detailed in Section 2.3.1. Additionally, a dedicated very high order spherical harmonic shim insert was employed, which hosts 28 small-diameter spherical harmonic shim coils and can be inserted into the bore of whole-body MR scanners to extend their built-in shim systems. This non-standard hardware is explained in greater detail below.

Very high order spherical harmonic shim system

The very high order shim (VHOS) system is a portable shim unit, designed for correcting high-degree and high-order spherical harmonic B_0 field inhomogeneities. It is a standalone, modular unit, consisting of three subcomponents. The entire system as well as its integration into the MR scanner is illustrated in Fig. 4.7. All subcomponents were manufactured and provided by *Resonance Research, Inc.* (Billerica, MA, USA).
A cylindrical in-bore shim insert with an inner/outer diameter of 381/465 mm and a length of 707 mm houses 28 resistive shim coils and forms the core of the unit. Each of the shim coils is individually designed to produce a spherical harmonic magnetic field distribution of given order and degree over a 220 mm diameter spherical volume. Except for the linear 1^{st} order terms, it can generate all spherical harmonics up to full 4^{th} order, as well as four 5^{th} and two 6^{th} order terms. The field patterns of all included shim terms are shown in the field plots in Fig. 3.1. Electrical isolation and mechanical robustness is achieved through an extensive housing which additionally provides water ports for active cooling of the shim coils. Functionality of the water cooling is provided by a water chiller and monitored via a PT-100 temperature sensor embedded in the coil assembly.
The shim insert is driven by a multi-channel power supply system, which is self-contained and has an integrated digital control and communication system used to adjust the output currents. Communication with the power supply for setting specific shim values is performed digitally via a serial RS-232 port. The transmitted commands are interpreted and checked for feasibility, validity and safe operation by internal low-level proprietary software, which in turn executes the setting of the demanded current values. The power supply is configured in sets of four amplifier banks, each of which supplying seven individually controllable output channels, which are connected to the insert shims. It can deliver up to ± 5 A per channel at a cumulative maximum current output of ± 10 A per bank resulting into a cumulative absolute maximum current output of 20 A per

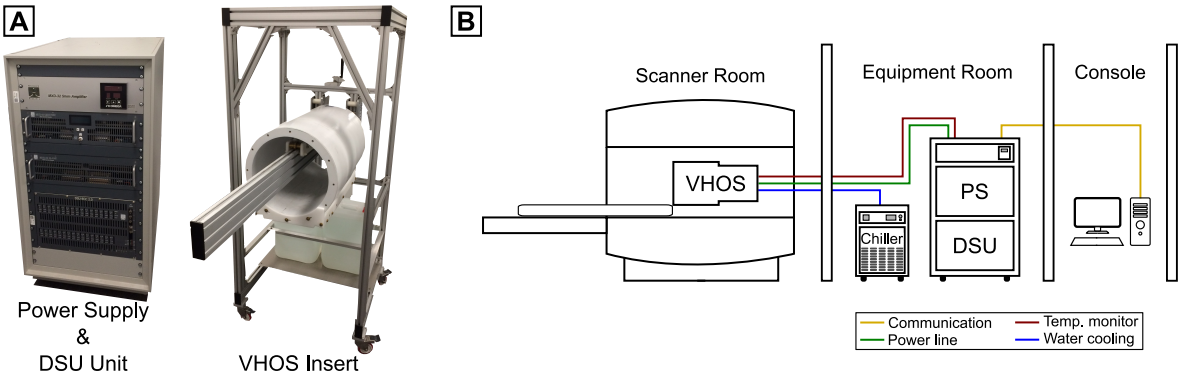

Figure 4.7: Very high-order spherical harmonic B_0 shim system. **(A)** Photographs of the individual sub-components, which form the entire shim system. The power supply (PS) and a dynamic shim updating unit (DSU) are stored in a mobile casing. The ver high-order shim coil insert (VHOS) can be moved on a trolly to the back-end of an MR scanner, from where it can be inserted into the bore and moved to the iso-center. **(B)** The insert is installed in the MR scanner, the power electronics and the water chiller are installed in the equipment room and the shim computer is controlled from the console room. Adapted from schematic provided by *Resonance Research, Inc.*

amplifier bank. The specific bank and channel configurations of the shim insert coils are given in Table 4.1 at the end of Section 4.4. In combination with their shim coil efficiencies and the maximum channel current output limits, these parameters define the correction capabilities of the provided high-order spherical harmonic field functions.
A dynamic shimming unit, capable of storing and updating specific shim settings rapidly during MR acquisitions, can be interfaced to the power supply and used when aiming at synchronizing B_0 homogenization with the MR scanner's pulse sequence. This device is optional and only used in the work presented in Chapters 5 and 6 and, therefore, excluded during static operation.
The shim insert is mounted onto a rail system, which enables a positioning of the shim coils around the iso-center of the magnet and gradient system. Due to a concomitant reduction in the usable diameter of the MR scanner, the RF system of the host MR scanner needs to be specially adapted. In the particular setup used in this work, a solid framework, which can accommodate the RF coil, is fixedly attached to the head-end of the patient table. Using the electrically controllable table feed, the RF coil can then be moved to the joint iso-center of the MR and shim system. In this work, all MR measurements with the high-order shim insert were performed using a dedicated 1Tx/8Rx-channel RF coil (Siemens Healthineers, Erlangen, Germany). For this purpose, an additional, slotted RF shield was placed into the available space between RF coil and the inner wall of the shim insert and completed the entire setup.

Implementation and usage of the shim insert

Means of communication with the controller of the shim power supply were implemented via the available serial port using custom-written software (MATLAB, The MathWorks, Natick, MA, USA) and made accessible via a graphical user interface on a dedicated shim calculation PC. Safe operation of the power supply within the hardware specifications was implemented using an object-oriented approach. Within this framework, an instance of the implemented power supply class corresponds to a software mapping of the functionality of the hardware via dedicated member functions and properties. Upon initialization, it starts the communication with the power supply and provides all means for executing the commands that are pre-implemented in the firmware of the power supply. Moreover, it simultaneously keeps track of the state and condition

of the power supply, thus monitoring its safe operation while rejecting infeasible commands. The shim insert was certified as an in-house product according to §12 of the German Act on Medical Devices. As such, it may be used on a 3T TRIO MR system (Siemens Healthineers, Erlangen, Germany), which was specifically adapted such as to provide for the aforementioned table modifications.

4.3.2 Data acquisition and processing

The applied B_0 field map acquisition and reconstruction steps are outlined in the following and were identical, irrespective of their application for shim coil calibration or shim optimization purposes. Merely the variable sequence parameter adjustments and the mask selection differed between phantom and in vivo measurements. Using the resultant field map data, the subsequent processing steps for the shim calibration or shim optimization varied and were implemented as explained below.

Field mapping

B_0 field mapping for the calibration and all in vivo shim data acquisitions was performed as described in Section 4.2.1 using a multi-echo gradient-echo sequence with mono-polar readouts. During measurements for which the total acquisition time was to be kept short, a conventional gradient echo scheme was employed, acquiring multiple echoes following a single excitation as illustrated in Fig. 4.8 A. In cases where a very high accuracy of the B_0 maps was required, the sequence shown in Fig. 4.8 B was used [94]. Its gradient switching scheme is more benign in terms of eddy current generation, because the altered looping structure does not require the application of any read-rephasing gradients and sets the relative timing of the phase encoding gradient equal for all acquired echoes. Thus the phase subtraction process during the field map reconstruction can more effectively eliminate potential dynamic phase offsets induced by eddy currents (cf. Section 4.2.1).
Due to varying object sizes and acquisition time demands, the sequence parameters varied slightly between different acquisitions. Typical values for 2D B_0 field map acquisitions based on the multi-echo gradient-echo sequence shown in Fig. 4.8 B, were TR $=$ 540 ms, TE $=$ $[4, 5, 6, 8, 12]$ ms, BW $=$ 500 Hz/px and $\alpha = 20°$. Using a matrix size of $[64 \times 64 \times 33]$ and covering a field-of-view of $[192 \times 192 \times 99]$ mm^3 in a 3 mm isotropic resolution without slice gaps, the total acquisition time amounts to 3:40 Min. With equal image resolution and field-of-view size, the acquisition time could be reduced to well below one minute when using the conventional multi-echo acquisition scheme shown in Fig. 4.8 A.
Upon acquisition, the data were Fourier transformed and the first echo phase was subtracted as outlined in Section 4.2.1. The individual channels were recombined using a weighted summation based on coil sensitivities estimated from the magnitude data of each channel. The phase was determined from the combined complex images within a defined mask volume. For human head imaging, the mask was confined to the brain tissue, which was segmented from the magnitude image of the first echo using FSL *BET* [162]. For other acquisitions, the mask was generated by thresholding the magnitude image of the first echo. The phase data of the individual echoes was spatially unwrapped using FSL *PRELUDE* [163] and subsequently re-ordered in time using a 1D temporal unwrap operation based on the phase evolution of the central voxel within the object. The final field map data was calculated by linear regression applied to the resultant unwrapped phase difference data and the associated echo time differences.

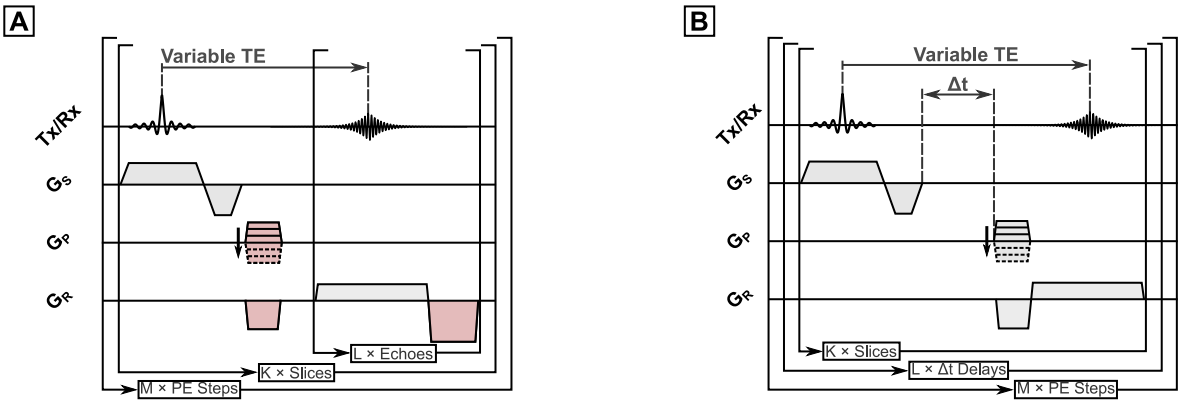

Figure 4.8: Multi-echo gradient echo sequences used for B_0 mapping. **(A)** Conventional acquisition scheme with multiple mono-polar echo readouts following a single excitation. Potential eddy currents from the gradients displayed in red can have a different impact on the signals acquired at different echo times. **(B)** At the cost of a slightly prolonged acquisition time, the acquisition order of the echoes can be modified, such that the effect of the aforementioned gradients is canceled by the phase subtraction process during field map reconstruction.[1]

Data processing for shim calibrations

For shim calibration purposes, a spherical water phantom with a diameter of 140 mm was used and positioned in the iso-center of the system such as to optimally comply with the active MR volume of the magnet, gradient and shim system. The shim calibration was performed as explained in Section 4.2.2. Two B_0 field maps with positive and two with negative current offsets were acquired for each shim coil, thus balancing acquisition time and fit accuracy.
The amplitudes of the applied shim offsets define the shim current range, over which the shim calibration is valid. Any subsequent shim optimizations during which shim currents are calculated which exceed these maximum offsets are, therefore, based on the assumption that the shim system behaves linear. Only in that case, the linear extrapolation to regions outside of the shim calibration current range would be applicable and lead to correct shim correction currents. On the other hand, excessively high shim currents offsets induce aliasing artifacts in the acquired field maps, hence the applied shim current offsets cannot be chosen arbitrarily high. Therefore, the offsets were applied within a range such that the resultant standard deviation, measured over all voxels in the shim offset field map, did not exceed a value of ~ 100 Hz.
Each shim offset map was reconstructed and processed as described in the previous section and a full set of 10^{th} order spherical harmonic functions was iteratively fitted to the resultant data. For this purpose, an unconstrained linear least-squares solver was used and, starting with the 1^{st} order terms, in each iteration all terms of the next higher order were included into the fit. Using the results of each preceding iteration as the starting values for the current iteration, this approach provides modest means of a regularization. Each set of four fit coefficients of each of the 121 spherical harmonic terms was then subjected to a linear regression against the respectively applied shim offset currents. Each term, for which the linear fit revealed a p-value of $p < 0.05$ was deemed significant and its slope was included in the final shim calibration vector. Once the maps of all shim coils were processed, the full calibration matrix was assembled from the individual shim coil calibration results and stored for application within the actual B_0 shim optimization framework.

[1] This sequence was kindly provided by Dr. Hoby Hetherington, UPMC, MRRC, Pittsburgh, PA, USA.

Data processing for shim optimizations

Besides calculating a solution which optimizes the B_0 homogeneity, the shim optimization must also ensure compliance with the hardware limitations. These limits typically include channel-wise lower and upper current constraints. Moreover, as explained in Section 4.3.1, the shim currents applied to the very high-order shim insert additionally need to comply with the amplifier bank limitations.

Suppose that n shim coils are driven by one common amplifier bank and their shim currents are written in the vector $\tilde{\mathbf{x}} \in \mathbb{R}^{n\times 1}$, which is a subset of the full shim current vector $\mathbf{x}$. Furthermore, let the current output be constrained, such that the signed cumulative current output per amplifier bank may not exceed $\pm I_S$ and the absolute cumulative current output may not exceed I_A. A simple summation over all elements in $\tilde{\mathbf{x}}$ in order to determine the cumulative current output is infeasible, because the variable elements are signed and their individual contributions to the current sum may cancel. Instead, it is possible to determine all possible combinations of the elements in $\tilde{\mathbf{x}}$ by sequentially varying their sign. The absolute cumulative current output then follows from determining the highest sum amongst all combinations. The signed cumulative current outputs can be calculated similarly and examples of both calculations are given in the following.

For the sake of simplicity, and without loss of generality, in the following example it is assumed, that a pair of two shims is supplied by one amplifier bank ($n = 2$). Using the matrices

$$\mathbf{C}_A = \begin{bmatrix} 1 & 1 \\ 1 & -1 \\ -1 & 1 \\ -1 & -1 \end{bmatrix}, \quad \mathbf{C}_+ = \begin{bmatrix} 1 & 1 \\ 1 & 0 \\ 0 & 1 \\ 0 & 0 \end{bmatrix} \quad \text{and} \quad \mathbf{C}_- = \begin{bmatrix} -1 & -1 \\ -1 & 0 \\ 0 & -1 \\ 0 & 0 \end{bmatrix}, \tag{4.6}$$

the aforementioned combinations of the shim coil currents can be computed efficiently via matrix-vector multiplications. Using the vectors $\mathbf{d}_A = [I_A; I_A; I_A; I_A]$ and $\mathbf{d}_S = [I_S; I_S; I_S; I_S]$, the desired constraints can then be enforced during the shim optimization by linear inequality constraints. Consequently, conformity with the absolute cumulative current constraint is implemented via $\mathbf{C}_A \cdot \tilde{\mathbf{x}} < \mathbf{d}_A$ and, similarly, via $\mathbf{C}_+ \cdot \tilde{\mathbf{x}} < \mathbf{d}_S$ and $\mathbf{C}_- \cdot \tilde{\mathbf{x}} < \mathbf{d}_S$ for the signed cumulative current constraints. An extension of this approach to including more shim terms per amplifier bank, e.g. with $n = 7$ for the particular case of the very high-order shim system used in this work, is straightforward and simply increases the matrix sizes due to an increase in the number of possible combinations.

Using $\mathbf{C}_\Sigma = [\mathbf{C}_A; \mathbf{C}_+; \mathbf{C}_-]$ and $\mathbf{d}_\Sigma = [\mathbf{d}_A; \mathbf{d}_S; \mathbf{d}_S]$, the individual constraints can collectively be enforced via $\mathbf{C}_\Sigma \cdot \tilde{\mathbf{x}} < \mathbf{d}_\Sigma$. Moreover, if multiple banks are present, each of which with the demand to conform to the above constraints, multiple copies of the summation matrices and constraint vectors can be grouped into $\mathbf{C}$ and $\mathbf{d}$, respectively, such that the hardware limits are imposed to the full parameter vector $\mathbf{x}$. Including the channel-wise lower and upper current constraints, $\mathbf{lb}, \mathbf{ub} \in \mathbb{R}^{N\times 1}$, the entire B_0 shim optimization problem, which optimizes the shim currents for all N shim coils within the confined search space, is given by

$$\min_{\mathbf{x}} \quad \|\mathbf{Ax} - \mathbf{b}\|^2 \qquad \text{s.t.} \qquad \begin{cases} \mathbf{lb} \leq \mathbf{x} \leq \mathbf{ub} \\ \mathbf{C} \cdot \mathbf{x} < \mathbf{d}. \end{cases} \tag{4.7}$$

Minimization of Eq. 4.7 was performed within this work using the MATLAB built-in *fmincon* solver with a *sequential quadratic programming* algorithm.

4.4 Results

The aforementioned shim calibration and optimization methods were applied to various shim systems on different MR scanners. These include regular vendor-supplied shim systems incorporated into either large-diameter whole-body human systems or small-bore animal systems. Moreover, the previously introduced very high-order shim coil insert was calibrated and employed likewise. In the following, the results for the shim calibration processes as well as their application in conventional static shim optimizations are shown.

4.4.1 Shim system calibrations

The shim coil characterization processes, explained in Section 4.2.2, were performed successively for each available shim system. The results of all analyzed coils of a given shim system were collectively stored in system-specific shim calibration matrices as outlined in Section 4.2.3. Once calibrated, the B_0 shim algorithm detailed in Section 4.3.2 could then be applied to subject-specifically optimize the individual shim coil currents over user-defined regions-of-interest using the custom-written B_0 shim software via its dedicated graphical user interface.

Shim calibration validation

With the shim offset data acquired and used during the shim calibration process, the correct functionality of the B_0 shim optimization was subsequently probed in a first test. Since the shim setting of each offset map was purposefully mis-adjusted by off-setting one particular channel from the best possible shimmed state, the shim optimization algorithm should ideally reconstruct the respectively applied current offset from the given data. Fig. 4.9 A displays the collective results, derived from applying this procedure individually to each acquired shim offset map. The data is shown for six shim systems that were calibrated within the scope of this work and illustrated as a plot of the known input current versus the fitted correction current.
The graph demonstrates that the known offset currents were accurately determined by using the calibration results during the shim optimization. It also proves the robustness of the implemented shim calibration when being applied to different types of spherical harmonic shim systems. With a deviation of $8 \cdot 10^{-4}$ from the ideal slope of $m = 1$, the linear fit applied to the known input and calculated output currents indicates a correct and accurate application of the gained calibration information.

Shim efficiency analysis

Further analysis of the determined coil properties of each calibrated shim system helps in interpreting calculated shim currents that are based on the individual calibration matrices. For instance, high current values may be explained by low shim efficiencies or the presence of strong cross-terms. As shown in Fig. 4.9 B, an expected decrease in shim coil efficiency with r^{-n+1}, where r refers to the coil radius and n to the spherical harmonic order, was observed for all analyzed shim systems. The illustrated results demonstrate this effect for one conventional large-diameter vendor-supplied shim system and the very high-order shim insert of smaller diameter. The displayed values are in accordance with those of the other calibrated shim systems and with efficiency values published in the literature [158].
For the displayed graph, the shim efficiencies were averaged over all available shim terms of a

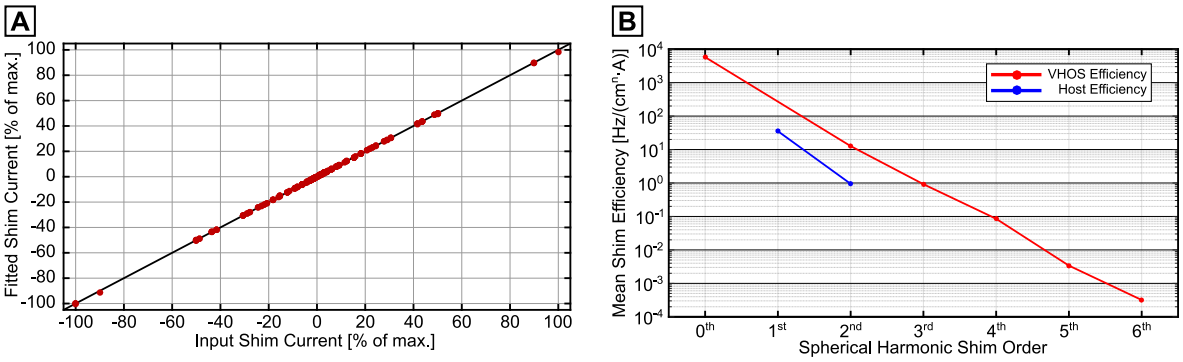

Figure 4.9: Shim coil calibration results. **(A)** After having characterized the shim coils of all available shim systems, the underlying shim offset data was subjected to the custom-written B_0 shim software. The plot shows the resultant fitted shim coil currents of each shim offset map as a function of the known input current. It reveals a direct mapping of the input- and output-currents, thus conforming the validity of the calculated shim calibration matrices and their correct application in the B_0 shimming framework. **(B)** The self-term efficiencies of all shim coils of a common spherical harmonic order were averaged and are shown here for two selected shim systems used in this work. Both differ in shim coil radius and maximum shim coil order, thus demonstrating the dependency of the shim efficiency on both parameters.

common spherical harmonic order. A clear dependency of the coil efficiency on the radius and the spherical harmonic order can be seen when comparing the lower-order large-diameter scanner shims to the small-diameter higher-order coils of the shim insert. Table 4.1, which is appended to this section, provides a list of the efficiencies of the shim systems that were used most frequently within the scope of this work.

Shim impurity analysis

In combination with the shim efficiency, it is essential to also quantify the impurity characteristics of each shim coil in order to accurately describe its overall performance. However, since they are very unique to each shim coil and each shim system, a general statement on their appearance, like the shim efficiency decrease for increasing shim orders, cannot be given similarly for the impurities. Still it can be stated that lower-order shim coils often produce a very pure self-term over the volume for which they were designed and generate negligible cross-terms. Higher-order terms are more challenging to generate and require more difficult wire patterns, such as to produce the targeted spherical harmonic field while simultaneously canceling the higher and lower order cross-terms.

Extreme shim coil impurity characteristics, which correspond to the entries in the coil-specific shim calibration vector introduced in Section 4.2.2, are illustrated in Fig. 4.10 A for two coils. For each of the 121 spherical harmonic terms that were included in the 10^{th} order shim calibration, the maximum field offset within a spherical volume of 140 mm diameter was calculated for the self- and each of the non-negligible cross-terms. The volume was chosen such as to approximately comply with the volume of a human brain and resultant maximum field offsets were set relative to that of the self-term. Within this analysis, the self-terms should produce an amplitude of 100% and all cross-terms should ideally be close to zero.

The bar plots in Fig. 4.10 A illustrate strong deviations of this ideal shim coil performance. A 3^{rd} order Z2Y-shim with a dominant cross-term to Y is shown, for which the maximum self-term field amplitude is exceeded by that of the cross-term by a factor of $\sim\times 4$. Moreover, results of a 4^{th} order Z2S2-shim are shown, whose performance can only accurately be described, when

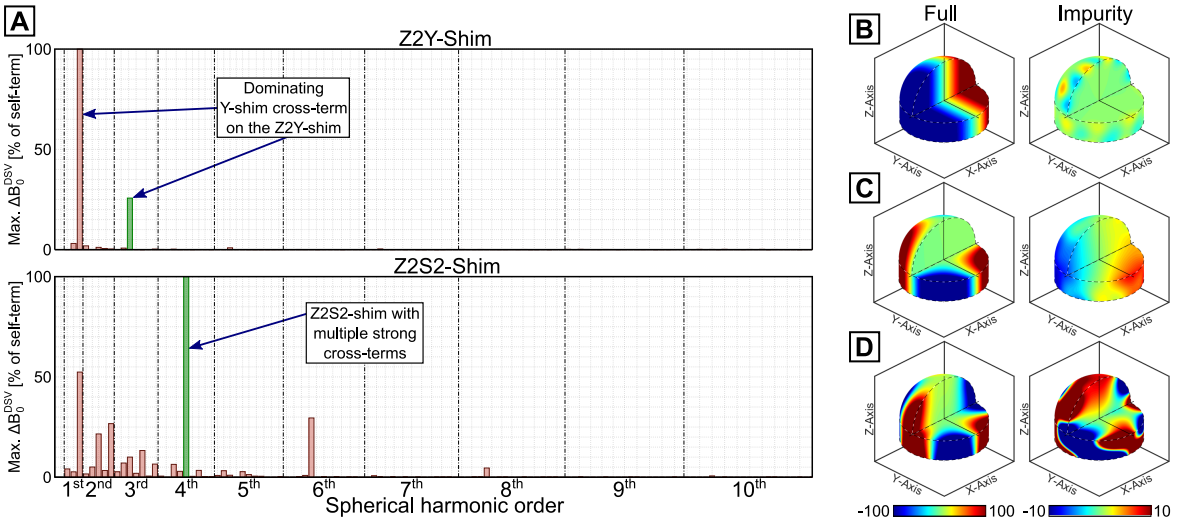

Figure 4.10: Shim impurity results. **(A)** Calibration results of a Z2Y- and a Z2S2-shim with noticeable differences from the ideal performance. The former has a cross-term to the Y-shim, which significantly exceeds the amplitude of the self-term. The latter has a multitude of non-negligible cross-terms to lower and higher orders. The amplitudes were determined as the maximum B_0 field offset, induced in a 140 mm diameter, iso-centered sphere, and set relative to that of the self-term. The plots in **(B)** - **(D)** show the real shim fields of an X-, S2- and C3-shim, each with a different degree of impurity. The full plots were simulated for an approximation of the coil performance using the self- and all cross-terms. The impurity fields were calculated using the cross-terms coefficients only. For visualization purposes, the color scale of the impurity fields was scaled by a factor of $\times 10$.

including multiple non-negligible lower- and higher-order cross-terms in its spherical harmonic field approximation.

The geometries illustrated in Fig. 4.10 B are used to demonstrate the effects of varying impurity characteristics on the generated magnetic field distribution. Shim fields from three coils were simulated over spherical, cylindrical and planar surfaces to illustrate their spatial field pattern. When using the entire set of approximation coefficients, each of the three terms seems to be generating the targeted spherical harmonic shim field with a very high accuracy. However, using only the non-negligible cross-terms, the superimposing impurity fields can be visualized and the performance of the individual coils in suppressing the unwanted terms can be revealed. The importance of including the shim impurity information, especially for the higher-order coils, can readily be seen from these plots. Even though some shim coils deviate strongly from the targeted ideal spherical harmonic shim functions, their real performance can still accurately be described using the linear combination of very high-order spherical harmonic functions.

4.4.2 Static shimming

An accurate calibration of the shim set is imperative for meaningful B_0 shim simulations and forms the basis for non-iterative B_0 shim updates. Thus, the previously presented calibration results were used in static shim optimizations in different scenarios. Conventional 2^{nd} order shim optimizations were performed, aiming at gaining full control over the B_0 field homogenization capabilities provided by the host MR system. Moreover, this process was extended in dedicated acquisitions to also include the shim insert hardware in order to implement very high-order B_0 shim corrections.

Conventional 2nd order shimming

Reaching an optimal shim quality within a short adjustment time is desirable for an efficient workflow during an MR exam. Thus, the convergence rate of the implemented B_0 shimming framework and the quality of the calculated shim solutions were analyzed quantitatively. For this purpose, in vivo whole-brain B_0 field map data were acquired and processed using the gradient echo sequence and the shim optimization framework described in Section 4.3.2. A number of $N = 16$ datasets were acquired in an initial *unshimmed* state on a 3T TIM TRIO scanner using its default shim setting. Depending on the anatomy and the associated susceptibility distribution of the subject, this initial shim state was characterized by a residual whole-brain standard deviation of $\sigma = 51 \pm 19$ Hz. The reconstructed field maps were decomposed into a 2nd order static shim solution and a predicted *shimmed* state was simulated from the resultant coefficients. The scanner shims were updated accordingly and a further field map was acquired with equal acquisition parameters, which was then analyzed in two ways. The acquired and reconstructed maps were compared to their respective predicted solutions in terms of the achieved residual whole-brain standard deviation. Furthermore, the *shimmed* field map data was again processed in the shim optimization framework to check for residual shim terms, which had not been corrected during the first pass. Thus, both analyses give insight into whether or not the best-possible B_0 homogeneity provided by the given shim set has been reached without the need for any optimization iterations.
The results of this analysis are summarized in the graph shown in Fig. 4.11 A. The large variation of the initial shim quality demonstrates the requirement for the shim optimization to be capable of handling different shim conditions. A stronger B_0 non-uniformity typically evokes higher changes in shim currents and, therefore, requires a better accuracy of the shim calibration. In all analyzed cases, the predicted and the acquired B_0 homogeneity after one iteration of the shim optimization matched very well. On average, the residual whole-brain standard deviation between the predicted and the acquired solution differed by only 0.09 Hz. Furthermore, a second shim optimization based on the shimmed field maps revealed that no correctable shim terms of relevant amplitude were present in the data after the first iteration. On average, the gain in whole-brain standard deviation, if the second shim setting was applied, was 0.12 Hz, as compared to 32.79 Hz for the first shim iteration.
Fig. 4.11 B illustrates an example of a sub-optimal initial shim setting and how the superimposed shim correction field is used to compensate for large parts of the B_0 inhomogeneity. The dominant quadratic form of the applied shim field and how it is shaped to approximate the measured B_0 inhomogeneity is apparent. However, the mid-sagittal view clearly reveals the residual B_0 inhomogeneity after shimming, which is predominantly visible in the pre-frontal cortex area. The residual whole-brain B_0 homogeneity after 2nd order shimming was on average 18.43 ± 2.47 Hz, which is consistent with values published in the literature [40]. The previous analyses show, that the residual B_0 offsets are un-correctable to the given 2nd order shim set and, therefore, require the application of more efficient shim techniques.

Very high-order shimming

The limits of the conventional spherical harmonic shim approaches have theoretically been deduced in Section 3.4.3 and practically validated in the previous section. The gradual improvement of the B_0 uniformity, when including higher orders into the static shim optimization, has been explained in the literature review given in Chapter 3 and shown in simulations in Fig. 3.8. Using the very high-order shim insert, these improvements were implemented on a 3T MR system to

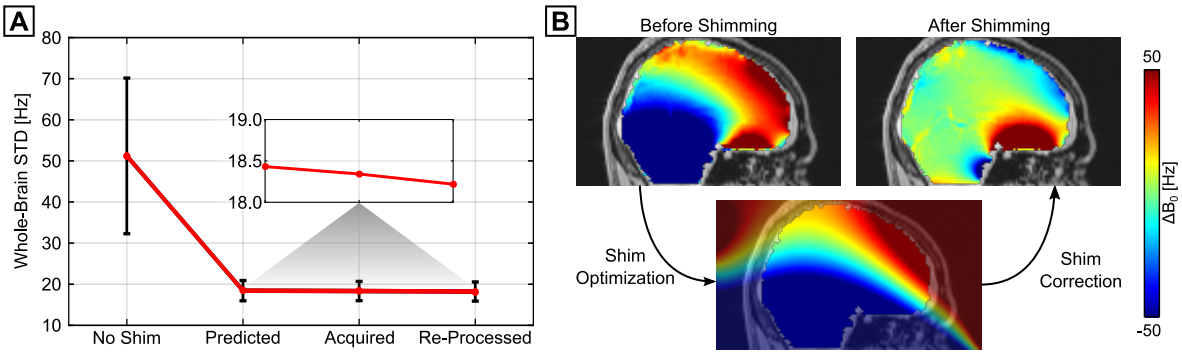

Figure 4.11: Static 2nd order shimming results. **(A)** Shim convergence plot for 16 analyzed field map datasets. Each dataset was acquired in an sub-optimal, default shim state and processed in the implemented B_0 shimming framework. The resultant shim coefficients were applied and a second field map was acquired. A comparison between the predicted and the acquired field map, as well as the negligible homogeneity improvement when performing a second iteration of the shim optimization demonstrate the accuracy of the shim calibration. **(B)** A mid-sagittal slice of an unshimmed and a shimmed field map demonstrate the improvements provided by the 2nd order shim field. It can also be seen that the dominant quadratic nature of the shim field cannot compensate for the higher-order field inhomogeneity terms.

extend the vendor-supplied B_0 shim performance. During these measurements, all 1st and 2nd order corrections were effectuated via the host shims and all available higher order terms via the shim insert. A joint calibration matrix, composed of the individual shim calibration vectors of each employed shim coil, was used to collectively optimize all included shim terms.

The shim calibration procedure for the shim insert has been carried out as was previously shown for conventional 2nd order shim systems. Phantom and in vivo B_0 shim measurements were performed and the convergence rate of the B_0 shimming framework, when including the higher-order shims, was found to be equal, thus did not require any optimization iterations. Fig. 4.12 A illustrates the residual B_0 field inhomogeneity distribution of an in vivo whole-brain field map of a volunteer, acquired after one iteration of conventional 2nd order and very high-order shimming, respectively. For this dataset, the whole-brain standard deviation improved from 19.51 Hz for the 2nd order case, to 13.89 Hz after shimming with the full set of 4th and partial 5th and 6th order shims. Moreover, the number of voxels with excessively high field offsets decreased significantly. Using the high-order shims, 90% of the field map voxels were within a range of 34 Hz around the center frequency, as opposed to 52 Hz for the 2nd order case.

The associated field map slices from four different brain regions, shown in Fig. 4.12 B, demonstrate which regions in the human brain benefit from the more versatile field shaping capabilities. However, likewise it can be seen that the very localized B_0 inhomogeneities, which are present in multiple parts within the brain, are merely reduced, but not eliminated. Being mainly caused by the air-tissue interfaces around the brain, which differ amongst subjects in their exact shape, but typically follow the same rough structure, these findings apply to a greater or lesser extent to all in vivo acquisitions of the human brain.

Similar analyses can be carried out for more localized acquisition geometries, e.g. as encountered in single-voxel-spectroscopy measurements. The challenge is to focus the shim optimization capabilities to smaller and arbitrarily positioned volumes. In order to to compare 2nd and higher order shim performances for these acquisitions, a phantom measurement was performed. After 2nd order static shimming over the entire spherical volume, a cubic shim optimization volume with an edge length of 35 mm and a resultant size of 42.88 cm^3 was placed into a region, which was affected by high-order residual inhomogeneities. A 2nd and a 4th order shim setting was calculated,

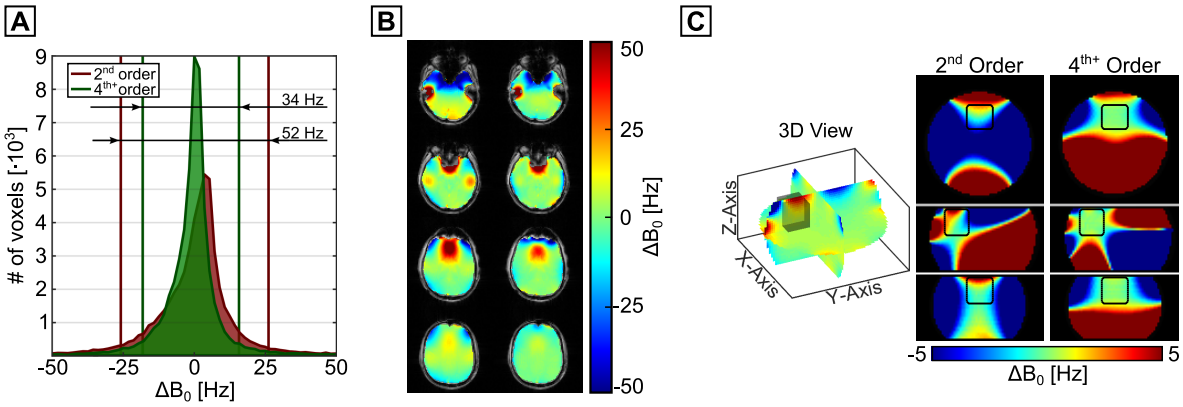

Figure 4.12: Examples of very high-order static shimming results. **(A)** Histograms of the field map data acquired after static 2nd and very high-order shimming demonstrate the homogeneity gains provided by the employed shim insert. The whole-brain standard deviation decreased from 19.51 Hz to 13.89 Hz and the 90th-percentile range decreased from 52 Hz to 34 Hz. **(B)** The regions of B_0 homogeneity improvements can be seen in the four selected in vivo field map slices. At the same time, these B_0 maps indicate the limits of the high-order shim set in terms of compensating for high-amplitude and very localized B_0 non-uniformities. **(C)** The single voxel shimming experiment, conducted in a phantom, demonstrates the versatile field shaping capabilities of the high-order shim insert. The shim optimization over the cubic adjustment volume, outlined in black, is much more effective using the high-order shims.

such as to best possible homogenize the voxel volume. The settings were individually applied and field maps were acquired to assess the resultant field distributions. The acquisition geometries and the acquired field map data is illustrated in Fig. 4.12 C. The inclusion of additional higher order terms clearly compensates for residual localized field offsets, which are still present after 2nd order shimming. It is to be noted, that the achievable shim quality is highly dependent on the object and the region-of-interest, thus differences in B_0 homogenization performances between different shim orders will be more or less pronounced. Yet, this acquisition demonstrates that the control over the coils provided by the high-order shim insert works correctly and is applicable to localize the shimming target to structures other than conventional whole-brain acquisitions. The benefits when translating these methods to actual in vivo single-voxel-spectroscopy measurements have been demonstrated in [39].

Spherical Harmonic Shim Functions								
Spherical Harmonic Properties				Shim Coil Efficiency [$\mathbf{Hz/(cm^n \cdot A)}$]				RRI
idx	(n/m)	Name	Function[†]	TRIO	MR/PET	Animal	VHOS	(B/C)
1	(0/ 0)	B0	1	-	-	-	$5.77 \cdot 10^{+3}$	(1/6)
2	(1/ 0)	Z	z	$3.87 \cdot 10^{+1}$	$3.87 \cdot 10^{+1}$	$1.03 \cdot 10^{+2}$	-	-
3	(1/ 1)	X	x	$3.39 \cdot 10^{+1}$	$3.37 \cdot 10^{+1}$	$1.10 \cdot 10^{+2}$	-	-
4	(1/-1)	Y	y	$3.37 \cdot 10^{+1}$	$3.37 \cdot 10^{+1}$	$1.09 \cdot 10^{+2}$	-	-
5	(2/ 0)	Z2	$z^2 - 1/2 \cdot \rho^2$	$1.14 \cdot 10^{+0}$	$1.13 \cdot 10^{+0}$	$1.55 \cdot 10^{+1}$	$6.98 \cdot 10^{+0}$	(1/1)
6	(2/ 1)	ZX	zx	$1.22 \cdot 10^{+0}$	$1.22 \cdot 10^{+0}$	$2.05 \cdot 10^{+1}$	$2.47 \cdot 10^{+1}$	(1/2)
7	(2/-1)	ZY	zy	$1.21 \cdot 10^{+0}$	$1.20 \cdot 10^{+0}$	$2.06 \cdot 10^{+1}$	$2.44 \cdot 10^{+1}$	(1/3)
8	(2/ 2)	C2	$x^2 - y^2$	$5.82 \cdot 10^{-1}$	$5.79 \cdot 10^{-1}$	$6.44 \cdot 10^{+0}$	$3.65 \cdot 10^{+0}$	(1/4)
9	(2/-2)	S2	xy	$5.88 \cdot 10^{-1}$	$5.84 \cdot 10^{-1}$	$6.78 \cdot 10^{+0}$	$3.61 \cdot 10^{+0}$	(1/5)
10	(3/ 0)	Z3	$z(z^2 - 3/2 \cdot \rho^2)$	-	-	-	$5.08 \cdot 10^{-1}$	(1/7)
11	(3/ 1)	Z2X	$x(z^2 - 1/4 \cdot \rho^2)$	-	-	-	$1.00 \cdot 10^{+0}$	(2/2)
12	(3/-1)	Z2Y	$y(z^2 - 1/4 \cdot \rho^2)$	-	-	-	$1.00 \cdot 10^{+0}$	(2/3)
13	(3/ 2)	ZC2	$z(x^2 - y^2)$	-	-	-	$1.80 \cdot 10^{+0}$	(2/4)
14	(3/-2)	ZS2	zxy	-	-	-	$1.75 \cdot 10^{+0}$	(2/5)
15	(3/ 3)	C3	$x(x^2 - 3y^2)$	-	-	-	$1.94 \cdot 10^{-1}$	(2/6)
16	(3/-3)	S3	$y(3x^2 - y^2)$	-	-	-	$1.90 \cdot 10^{-1}$	(2/7)
17	(4/ 0)	Z4	$z^4 - 3z^2 \cdot \rho^2 + 3/8 \cdot \rho^4$	-	-	-	$4.38 \cdot 10^{-2}$	(2/1)
18	(4/ 1)	Z3X	$zx(z^2 - 3/4 \cdot \rho^2)$	-	-	-	$1.26 \cdot 10^{-1}$	(3/4)
19	(4/-1)	Z3Y	$zy(z^2 - 3/4 \cdot \rho^2)$	-	-	-	$1.22 \cdot 10^{-1}$	(3/5)
20	(4/ 2)	Z2C2	$(x^2 - y^2)(z^2 - 1/6 \cdot \rho^2)$	-	-	-	$0.96 \cdot 10^{-1}$	(3/2)
21	(4/-2)	Z2S2	$xy(z^2 - 1/6 \cdot \rho^2)$	-	-	-	$0.92 \cdot 10^{-1}$	(3/3)
22	(4/ 3)	ZC3	$zx(x^2 - 3y^2)$	-	-	-	$1.26 \cdot 10^{-1}$	(4/2)
23	(4/-3)	ZS3	$zx(3x^2 - y^2)$	-	-	-	$1.23 \cdot 10^{-1}$	(4/3)
24	(4/ 4)	C4	$x^4 - 6x^2y^2 + y^4$	-	-	-	$1.91 \cdot 10^{-2}$	(3/6)
25	(4/-4)	S4	$xy(x^2 - y^2)$	-	-	-	$1.90 \cdot 10^{-2}$	(3/7)
33	(5/ 4)	ZC4	$z(x^4 - 6x^2y^2 + y^4)$	-	-	-	$5.82 \cdot 10^{-3}$	(3/1)
34	(5/-4)	ZS4	$zxy(x^2 - y^2)$	-	-	-	$5.76 \cdot 10^{-3}$	(4/1)
35	(5/ 5)	C5	$x(x^4 - 10x^2y^2 + 5y^4)$	-	-	-	$1.00 \cdot 10^{-3}$	(4/4)
36	(5/-5)	S5	$y(y^4 - 10x^2y^2 + 5x^4)$	-	-	-	$0.99 \cdot 10^{-3}$	(4/6)
46	(6/ 5)	ZC5	$zx(x^4 - 10x^2y^2 + 5y^4)$	-	-	-	$3.26 \cdot 10^{-4}$	(4/5)
47	(6/-5)	ZS5	$zy(y^4 - 10x^2y^2 + 5x^4)$	-	-	-	$3.11 \cdot 10^{-4}$	(4/7)

Table 4.1: Shim coil efficiencies of the shim systems used in this work. The linear index, the order and degree, the common name and the Cartesian functions are given for all available spherical harmonics. The calibrated shim efficiencies are given and for the high-order shim insert, the amplifier bank and channel indices are given.

[†]Note that $\rho^2 = x^2 + y^2$ and that constant factors have been removed from the Cartesian functions.

4.5 Discussion and conclusions

The fundamental requirements for non-iterative B_0 shim optimizations were motivated, the associated shim routines were implemented and the results were presented in this chapter. The involved data acquisition and processing steps reduce to three major parts. These include the B_0 field map acquisition, its decomposition into individual spherical harmonic correction fields as well as the calculation and application of the shim calibration matrix, which links both aforementioned processes.

Being flexible in terms of the field-of-view and image matrix sizes of the acquisition volume, the applied image-based field assessments, on the basis of a gradient-echo sequence, have proven to be well-suited for B_0 shimming purposes. Even though the acquisition time is longer than for projection-based field measurements using the *FASTMAP*-sampling scheme, the resultant volumetric data is applicable to also determine spherical harmonic components of orders higher than two, which is required for acquisitions that make use of the shim insert. The actual shim optimization process has proven to robustly reconstruct optimal shim currents while adhering to the specific hardware constraints which limit the search space of the algorithm. In this work it has been shown, that further shim iterations are not required, since near-optimal shim conditions are typically reached in a first pass. This is in large parts due to an accurate modeling of the real shim behavior and its incorporation into the system matrix using the results of the shim calibration procedure. The applied 10^{th} order spherical harmonic approximation of the real shim behavior can accurately describe the impurity characteristics of each term.

Using this optimization framework for 2^{nd} order shim updates gives full control over the conventional B_0 shimming process and leaves the user independent from the vendor-supplied shimming methods implemented on the MR systems. As such, it is an implementation of state-of-the-art B_0 shimming procedures, with a proven record of finding the best-possible shim condition with a very high reliability. Moreover, its convergence to the predicted shim state can be monitored, thus reassures the user of having optimal shim conditions for the subsequent MR measurements. Due to the shallowness of the available spherical harmonic correction fields, the rather coarse spatial sampling density of the field maps was considered sufficient for the purposes of B_0 shimming. Thus, the entire process was balanced in terms of its acquisition and processing time and the accuracy of the shim field approximation.

An extension of the 2^{nd} order shimming framework to also include all higher order terms provided by the shim coil insert has been implemented and the associated advantages have been demonstrated. The choice of an object-oriented approach to control the shim power supply has proven to be well-suited to effectuate the desired shim commands and to monitor the state of the power supply. Moreover, due to its intrinsic feasibility check of the incoming commands, it renders the communication with the power supply immune to infeasible shim adjustments. The applied high-order shim field corrections improve the B_0 homogeneity over the 2^{nd} order case within the realms of possibility. These limits are always dictated by the natural limitations of a truncated spherical harmonic expansion of a given maximum order. Thus, it has been shown that for whole-brain static shimming, the higher-order shim set provides some improvement, but cannot fully compensate for all susceptibility induced field offsets.

The software for the B_0 shimming routine is modular and can be controlled via a dedicated graphical-user-interface. Its modularity enables a simple extension of the functionality to include more features or to replaces certain modules. For instance, several algorithms for MR phase unrwapping exist [164] and the spectrum of available implementations can easily be extended and presented to the end-user. Likewise, as shown in Fig. 3.6, the applied shim optimization

algorithm can be extended to include several target functions in order to provide means for B_0 field homogenization capabilities that are tailored for specific applications. The graphical user interface provides a simple and efficient control of the program, with which the desired implementations and all required parameters can be selected. Thus, the integration of the shim optimization into the entire MR measurement is streamlined.
The accuracy of the shim calibration and the proven close match between predicted and acquired field maps during the shimming process is highly important for the validity of all shim simulations that are based on realistic current values. In Chapter 6 a novel shim optimization algorithm for dynamic shimming applications is presented, which is critically dependent on this assumption. Therefore, the methods and results presented in this chapter not only reproduce the state-of-the-art B_0 shim methodologies, but also pave the way for more advanced shimming strategies. Due to the limitations of static B_0 shimming with current technology, these methods are very important for the improvements in achievable B_0 shim quality.

5

Fast model-based eddy current characterization

Static spherical harmonic B_0 shimming was introduced in Section 3.4 and its practical implementation within the scope of this work was described in Chapter 4. The employed spherical harmonic shim systems were shown to be able to improve the B_0 homogeneity in large parts of the human brain via static shimming, but fail in approximating the higher order inhomogeneities encountered in certain localized regions. Dynamic shimming, makes a more efficient use of a given shim system by changing the shim setting during the acquisition and, thus, provides a potential remedy to this issue. However, for this method to work without acquisition time penalties, eddy currents induced by rapid shim switching must be addressed.

The most commonly applied method to compensate for shim-induced eddy currents is a *pre-emphasis* implementation, which superimposes correction currents to the shim outputs such as to counteract the dynamic effects of the eddy currents. For this purpose, it is required to accurately measure the amplitudes and the temporal evolution of the eddy current-induced distortion fields. However, since the time course of these eddy currents can reach up to several seconds, their comprehensive 4D characterization measurements are in general very time-consuming or require the application of additional hardware.

In this chapter a novel method to measure shim induced eddy currents is being presented. It utilizes only regular MR hardware and aims at reducing the measurement time while simultaneously increasing the robustness of the subsequent eddy current parameter reconstruction. For this purpose, an efficient 2D image-based eddy current sampling scheme is proposed. It is combined with a model-based eddy current fitting routine, which incorporates the most commonly applied physical eddy current model at an earlier processing stage than it is usually done.

The validity of this approach is demonstrated on the basis of simulations using realistic eddy current parameters and experimental data is shown for measured and characterized shim-induced eddy currents. The presented framework facilitates the successful implementation of dynamic shimming and was, therefore, an integral part of the work presented in Chapter 6.

Parts of this work were published in:

M. Schwerter, M. Zimmermann, and N. J. Shah, "Fast 4d model based eddy current characterization for shim pre-emphasis calibrations," in *Proc. Intl. Soc. Mag. Reson. Med.*, p. 444, 2019

5.1 Introduction

As was shown in Section 3.2.2, the homogeneity of the static magnetic field is a crucial parameter for obtaining high-quality data in MR applications. However, in Chapter 4 it was demonstrated, that the subject-specific susceptibility distribution associated with human in vivo measurements induces complex B_0 inhomogeneity patterns. These are beyond the correction capabilities of conventional static spherical harmonic shimming and necessitate the development of more effective shim techniques. Besides recent multi-coil shim approaches, reviewed in Section 3.5.2, the application of spherical harmonic dynamic shim updating has proven to enhance the B_0 homogeneity while having the advantage of not requiring an additional shim system. It is based on the fact that high-order inhomogeneities can be better approximated by lower-order spherical harmonic shim functions when being analyzed over smaller volumes. Thus, an improved B_0 homogeneity is established by making a more efficient use of the available shim coils.
However, implementing dynamic shimming is challenging and although being available for more than two decades [97, 98], it is not yet routine. The most commonly reported complication pertaining to this technique is the generation of eddy currents, which can be caused by rapid intra-acquisition shim current changes. Associated with these eddy currents are time-varying perturbation fields, which temporally degrade the B_0 homogeneity. To address this problem, eddy current compensations are commonly implemented by shim *pre-emphasis* [100, 165]. This technique superimposes time-dependent correction currents to the shim outputs, such as to counteract the eddy current effects. For a precise adjustment of the pre-emphasis correction signals, however, a preceding eddy current characterization is indispensable. This is non-trivial, because it requires an accurate and quantitative spatio-temporal sampling of the eddy current perturbation fields. Moreover, the acquired data needs to be decomposed into the spherical harmonic field components that are correctable to the available shim set and their individual decay rates must be determined. Exacerbated by the fact that pre-emphasis adjustments can be iterative, it follows that a comprehensive eddy current compensation can be difficult and its implementation time-consuming. This motivates the need for an efficient eddy current characterization framework.
Providing precise measurements at a very high temporal resolution, eddy current characterizations based on field probes [81] form the current gold standard for pre-emphasis calibrations [166]. On the downside, this approach requires additional hardware, and cost and complexity scale with the order of the included spherical harmonic field terms. MR sequence-based techniques, on the other side, offer a lower temporal resolution and sensitivity, but generally do not require additional hardware. Commonly applied methods make use of the *FASTMAP* [69] sampling scheme, which can be adapted to assess eddy current information [167]. However, since in this approach eddy currents are mapped along 1D projections, the spatial dimension is undersampled. An unambiguous determination of all eddy current terms, therefore, requires the acquisition of multiple profiles along different directions. The number of required directions scales with the spherical harmonic order of the eddy current terms and renders its application to higher order shim systems increasingly less efficient. To overcome this issue, an eddy current characterization technique was proposed, in which full 3D eddy current maps are acquired at multiple sampled points in time [168]. While providing full 4D information about the eddy current evolution, this approach requires substantial acquisition times of up to one hour per shim.
In this work, a novel eddy current characterization framework is presented, which introduces two innovations to the existing techniques [3]. It adapts the idea of the image-based approach, but instead of 3D volumes, only three 2D slices are acquired per time point. The acquisition scheme

is based on the idea, that an orthogonal and off-center placement of these slices introduces sufficient spatial dependency to the data to unambiguously determine all spherical harmonic eddy current terms. As a result, the acquisition time is shortened by a factor of six when considering equal image resolutions. Moreover, a model-based fitting approach is presented, which robustly reconstructs the spherical harmonic eddy current coefficients from the acquired data. Fitting noise is considerably reduced through inclusion of prior knowledge about the temporal evolution of the eddy current terms. Following a brief explanation of the underlying eddy current model, the proposed sampling scheme, as well as the model-based eddy current fitting routine, are explained in detail in this chapter. The accompanying advantages are shown in simulations and measurements and demonstrate the applicability of the proposed technique.

5.2 Theory

In this section, the most commonly applied model used to characterize eddy currents in MR systems is revisited. Moreover, the conventional application of this model in order to fit optimal pre-emphasis correction parameters is briefly explained. The limitations of this strategy are outlined and motivate the applicability of the proposed eddy current fitting, which will be introduced in the ensuing section.

5.2.1 Eddy current model

When changing the current through a shim coil, the resultant changing magnetic field induces eddy currents in nearby conducting surfaces, which in turn generate a time-varying magnetic perturbation field, $\Delta B_0(\mathbf{r}, t)$. This field can be modelled at position $\mathbf{r}$ and time t using a linear spherical harmonic expansion to describe its spatial characteristics and a multi-exponential decay to describe the temporal evolution. It is given by

$$\Delta B_0(\mathbf{r}, t) = \underbrace{\sum_{n=0}^{\infty} \sum_{m=-n}^{n} f_{n,m}(\mathbf{r})}_{\text{Spatial Term}} \cdot \underbrace{\sum_{i=1}^{\infty} a_{n,m}^{(i)} \cdot \exp\left(-\frac{t}{\tau_{n,m}^{(i)}}\right)}_{\text{Temporal Evolution}}, \tag{5.1}$$

with $f_{n,m}(\cdot)$ denoting the spherical harmonic function of order n and degree m and $a_{n,m}^{(i)}$ and $\tau_{n,m}^{(i)}$ being the amplitude and the time constant of the modulating exponential function with index i. It is the objective of the eddy current characterization to find for each coil all non-negligible spherical harmonic self- and cross-terms and to determine the amplitudes and time constants of their decay rate. This is schematically illustrated in Fig. 5.1. The choice of the spherical harmonic spatial term in Eq. 5.1 follows from the fact that the magnetic field inside an MR scanner can be described by Laplace's equation [35]. The solution of which can be expressed as an infinite series of spherical harmonics and, thus, serves for the purpose of approximating the eddy current fields. The temporal evolution follows from a circuit analysis of the shim- and eddy current-loops via the Laplace transform. As was shown in [165], this analysis reveals that a step change in shim current results into a sum of exponentially decaying eddy current terms.
While this gives a theoretical validation of the applicability of the given model, its utilization is also reasonable from a hardware perspective: The correction field shaping capabilities of standard MR systems are limited to those provided by the set of available shim coils. These coils are specifically designed to generate ideally pure spherical harmonic fields, thus emphasizing the applicability of the chosen spatial model. Moreover, the time-course of the shim updates is commonly modulated using high-pass filters to provide for the required correction currents. These systems generate exponentially decaying correction signals and, therefore, emphasize the applicability of the applied temporal model. It follows that any spatial or temporal eddy current component that is not described by this model, can also not be compensated with the standard hardware.

5.2.2 Conventional application of the eddy current model

Independent of the acquisition scheme that is used to collect the eddy current data, the model described by Eq. 5.1 needs to be applied to fit appropriate eddy current compensation parameters. During this process, conventional eddy current characterization techniques regard the spatial

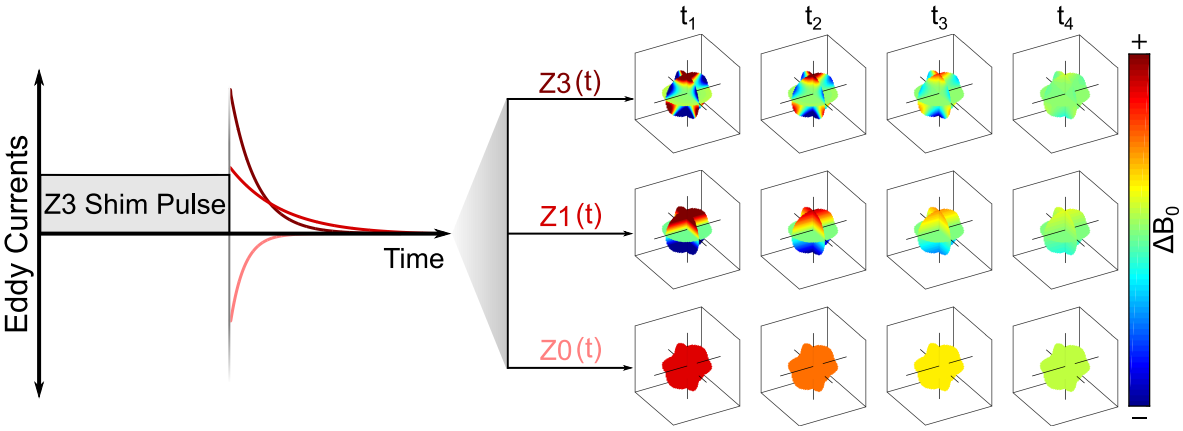

Figure 5.1: Qualitative depiction of an eddy current decay following a Z3 shim pulse with one self- (Z3) and two cross-term components (Z1 and Z0). The total eddy current field is a superposition of the perturbation fields generated by each eddy current loop at each sampled time point and needs to be decomposed into the individual terms before estimating their decay rates.

and the temporal component of the measured eddy current fields independently. That is to say, after the acquisition, the data at each time point is decomposed individually into its spherical harmonic components, regardless of the sampled data in the temporal vicinity. Hence, the expected exponential time-course of the spherical harmonic coefficients is not acknowledged at this stage. It is only after having processed all sampled time points, that the exponential model is fitted to each of the resulting time-series of spherical harmonic coefficients in order to determine the amplitudes and time constants of each non-negligible eddy current term. The time-course of each reconstructed spherical harmonic term, however, does not necessarily reveal exponential decay characteristics. This is due to the fact that the reconstruction of the spherical harmonic coefficients is an ill-conditioned, inverse problem and, therefore, prone to introducing fitting noise. Consequently, it can have a significant impact on the accuracy and the precision of the subsequently performed exponential fit and its resulting eddy current compensation parameters. In the worst-case scenario, apparent eddy current terms might be missed in the reconstruction or false positive terms might be detected.

An approach in which the spatial and the temporal model are applied simultaneously, has not yet been reported. Thus, due to the aforementioned drawbacks that arise when separating both parts of the model, in this work it is proposed to include the exponential decay already into the spherical harmonic decomposition and to solve the unified problem by numerical optimization. The central motive is to approximate the true eddy current time-course for each spherical harmonic term as good as possible with as few exponential terms as necessary. This approach reduces fitting noise and renders the subsequent calculation of optimal eddy current correction amplitudes and time constants more accurate.

5.3 Methods

Two novel concepts for characterizing shim-induced eddy currents are described in this section. A 2D image-based acquisition scheme is proposed, which sufficiently samples the spatial domain, while significantly reducing acquisition times compared to equivalent 3D approaches. Moreover, a model-based fitting routine is presented, which can be applied to the acquired data in order to robustly reconstruct optimal pre-emphasis parameters contained therein. Lastly, the hardware used to prove the applicability of the proposed techniques is briefly described.

5.3.1 Proposed eddy current data acquisition scheme

Provided that the spatio-temporal sampling is sufficiently high, the application of the eddy current model to the acquired data is generally not dependent on the underlying measurement technique. The routine presented in this work is based on measuring time-dependent phase offsets that are induced in 2D gradient echo images, which are acquired at different time-points during the eddy current decay. The sequence diagram and the sampling scheme are illustrated in Fig. 5.2.
A spherical water phantom is placed into the iso-center of the magnet and a conventional static B_0 shim is performed. From the shimmed state, a current offset is applied to the coil to be characterized and a sufficiently long time, TS, is waited, for all eddy currents generated by the leading edge of the pulse to decay. The shim current is then set back and a 2D slice is excited, in which the eddy currents generated by the falling edge of the shim pulse induce a phase offset in the image data. During the time-course of one eddy current decay, the same slice is then repeatedly excited N_T times and each time, the same line in k-space is recorded. This process is successively repeated for each out of M phase encoding steps, leading to a full 2D image at each sampled point in time on the eddy current decay curve. The first sampling point is given by the delay between the shim pulse and the center of the RF pulse plus the value of the echo time, TE. The sampling rate is dictated by value of the repetition time, TR.
Additionally, a reference scan is acquired using the same acquisition scheme, but without application of the eddy current generating shim pulse. Phase subtraction of the reference data from the eddy current data eliminates phase offsets from sources other than the eddy currents, e.g. the imaging gradients. The eddy current information is then encoded in the phase evolution of the resultant difference data.
Since different spherical harmonic terms can have the same functional form, when being analyzed over 2D slices [74], the acquisition of only one eddy current encoded slice typically does not suffice to unambiguously determine its spherical harmonic components. Moreover, the shim functions can have a zero-crossing in the iso-center of the scanner, which means that iso-centered slices provide little or no information about eddy current terms that have certain spatial dependencies. Therefore, the introduced acquisition scheme is applied in order to acquire three off-center slices that are oriented orthogonally towards each other. Thus, eddy current information is sampled in all spatial directions and shim degeneracy problems are bypassed.

5.3.2 Model-based fitting of spherical harmonic coefficients

Equation 5.1, which comprehensively describes the eddy current decay, can be simplified and re-written in matrix-vector-notation. Subsequently, it can be cast into a minimization problem and efficiently solved by numerical optimization. As will be shown in the following, this allows for the inclusion of prior knowledge and enables the joint application of the spatio-temporal model.

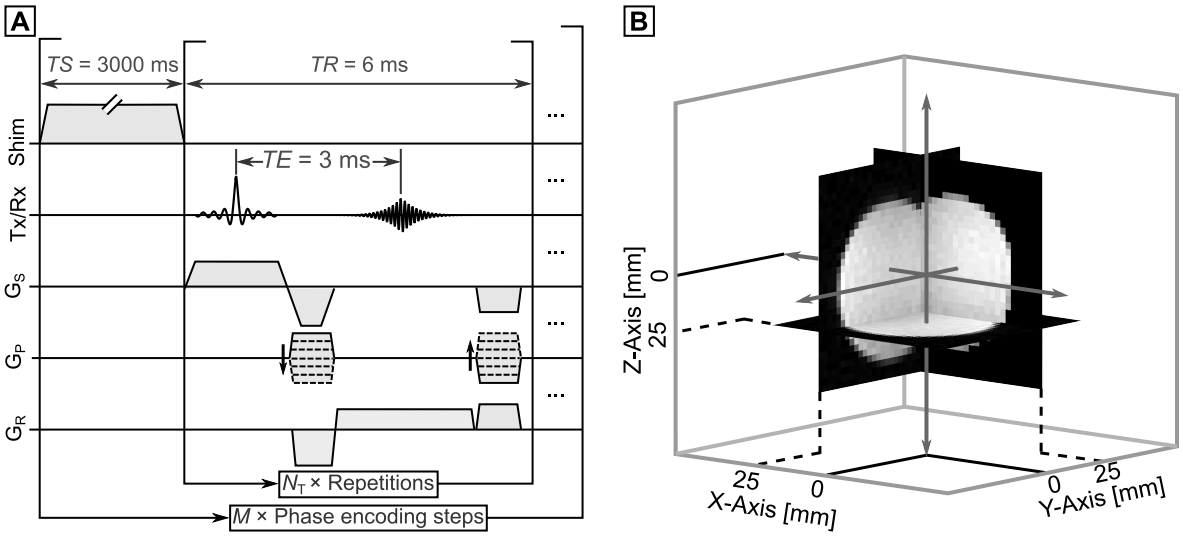

Figure 5.2: Sequence diagram and spatial sampling scheme of the proposed eddy current measurement approach. **(A)** A total number of N_T 2D gradient echo images are acquired during the time-course of the eddy current decay. The eddy current information, induced by the shim pulse, is encoded in the phase evolution of the image data. **(B)** Three orthogonal and off-center placed slices are acquired to resolve the spatial dependencies of the eddy current data. The displayed magnitude images illustrate the slice orientation and the off-center positioning.

Problem re-formulation

Because spherical harmonic terms of orders higher than that of the evoking shim coil have not been observed in reality [103], the full eddy current model can be simplified. Considering a maximum spherical harmonic order, n_max, the associated maximum number of potential spherical harmonic eddy current terms follows from $N_\mathsf{SH} = (n_\mathsf{max} + 1)^2$. Moreover, let N_R be the number of spatial eddy current sampling points in all three slices and let $\mathbf{r}_j \in \mathbb{R}^{3\times 1}$ denote their discrete voxel positions. The real spherical harmonic functions can then be described by the system matrix $\mathbf{A} \in \mathbb{R}^{N_\mathsf{R}\times N_\mathsf{SH}}$, which follows from evaluating $\mathsf{f}_{n,m}(\mathbf{r}_j)$ up to order n_max for all $j \in \{1, \ldots, N_\mathsf{R}\}$ and correcting the resultant ideal spherical harmonic functions by a system-specific calibration matrix. This correction step is detailed in Section 4.2.3. It accounts for deviations of the real spherical harmonic shim fields from the ideal functions and converts any spherical harmonic fit coefficient, which is calculated based on this matrix, into hardware units.
Furthermore, with N_T being the number of temporal eddy current sampling points, the total eddy current field, measured at all spatial and temporal sampling points, can be re-written as a vector $\mathbf{b} \in \mathbb{R}^{N_\mathsf{R}\cdot N_\mathsf{T}\times 1}$. Writing the eddy current amplitudes of all spherical harmonic terms at each sampled time-point into the concatenated vector $\mathbf{x} \in \mathbb{R}^{N_\mathsf{SH}\cdot N_\mathsf{T}\times 1}$ and using a block-diagonal matrix populated with N_T copies of the system matrix, $\bar{\mathbf{A}} = \mathrm{diag}(\mathbf{A}, \cdots, \mathbf{A})$, the model described by Eq. 5.1 can be re-written as $\bar{\mathbf{A}}\mathbf{x} = \mathbf{b}$. It comprehensively relates the discretely, spatio-temporally sampled eddy current field, $\mathbf{b}$, to the system described by $\mathbf{A}$ in matrix-vector-notation. The purpose of each eddy current fitting routine is to optimize the model parameters, $\mathbf{x}$, such as to best possible describe the measured data.

Joint application of the spatio-temporal eddy current model

As described in Section 5.2.2, conventional eddy current fitting techniques solve the problem given by $\bar{\mathbf{A}}\mathbf{x} = \mathbf{b}$ directly for $\mathbf{x}$ through numerical optimization or matrix inversion. This approach

treats the elements in $\mathbf{x}$ independently along the temporal dimension, which ignores the underlying time-course. However, the matrix-vector-notation enables the inclusion of this prior knowledge when extending the optimization problem. This was achieved in the proposed approach by re-formulating the objective function, such as to impose the expected exponential decay on the model parameters.
Introducing a linear operator $\mathcal{H}(\cdot)$, which acts on $\mathbf{x}$, the time-course of the amplitudes of all spherical harmonic eddy current terms can be re-written as a stack of *Hankel matrices*. It can be shown, that the rank of each of these matrices equals the number of exponentials used to describe the corresponding time-course. The application of a numerical optimization framework which enforces a rank-minimization of the Hankel matrices, therefore, minimizes the number of exponentials with which the underlying signal is approximated. Unfortunately, rank-minimization is NP-hard and cannot be solved efficiently. Under suitable conditions, however, it can be replaced by minimizing the nuclear norm, which then leads to the exact same unique solution [169]. Thus, in this work it is proposed to solve the problem described by

$$\min_{\mathbf{x}} \quad \|\mathcal{H}(\mathbf{x})\|_{*,1} \qquad \text{s.t.} \qquad \|\bar{\mathbf{A}}\mathbf{x} - \mathbf{b}\|_2^2 \leq \epsilon^2, \tag{5.2}$$

where the minimization of the mixed norm, $\|(\cdot)\|_{*,1}$, is equal to minimizing the sum over the nuclear norms of the Hankel matrices. The approximation of the measured eddy current field is simultaneously established by enforcing data consistency in a side condition, in which the choice of ϵ controls the desired accuracy.
To solve Eq. 5.2, an iterative optimization based on Bregman's method [170] and ADMM-updates (*alternating direction method of multipliers*) [171] was employed. In the implementation of this optimization strategy that was used in this work, three optimization variables can be adjusted in order to efficiently minimize the objective function. A weighting factor, λ, is internally used to balance the Hankel- versus the data-term. It is initially chosen high enough so as to overemphasize the Hankel-term, thus violating the side condition. An outer loop is then used to iteratively increase the impact of the data term, either until the side condition is met, or until a number of maximum iterations, N_{outer}, is reached. After each such Bregman-update, the ADMM-algorithm optimizes the parameter vector in an inner loop using a number of N_{inner} iterations.
The use of ADMM-updates for the rank-minimization of Hankel matrices was initially suggested in [172]. This type of optimization has already been combined with Bregman-updates and used in MR applications in the context of quantitative relaxation parameter mapping in the work implemented by Zimmermann *et al.* as described in [173]. Based on this implementation, the optimization algorithm used in this work was adapted to solve the eddy current fitting problem jointly by the author of this thesis and Zimmermann. The contributions to the algorithm of the work presented in this thesis include the conceptualization of using the spatial spherical harmonic model for the temporal eddy current fit stabilization. Moreover, the algorithm was tailored and the optimization parameters were tuned in simulations in order to appropriately handle the eddy current data. For this, rather than optimizing ϵ, the property of the Bregman method to provide for a monotonic decrease of the data residual during each iteration was exploited. Consequently, as will be shown in Section 5.4.2, an optimal combination of the optimization variables λ, N_{outer} and N_{inner} was determined.

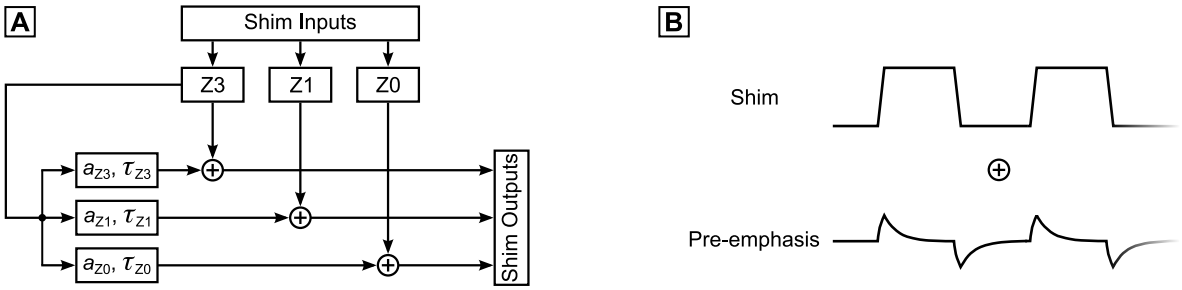

Figure 5.3: Eddy current compensation hardware. **(A)** Eddy current compensation interconnection scheme for the hypothetical eddy current evolution, previously illustrated in Fig. 5.1. A change in the input current to the Z3 self-term triggers the generation of a correction signal in a dedicated compensation module. The resultant correction current is superimposed to the shim current output. Likewise, interconnections to potential eddy current cross-terms can be made and the decay rates of their correction currents can be individually adjusted in the respective compensation modules. **(B)** The effective temporal variation of the shim current outputs is a superposition of the actual shim currents and the pre-emphasis correction currents, which are fed in by potentially multiple connected compensation modules.

5.3.3 Hardware and Acquisition

All eddy current measurements were performed on a 3T Tim Trio system using a 1Tx/8Rx-channel RF coil (Siemens Healthineers, Erlangen, Germany). Rapid shim changes were effectuated via a small-diameter 28-channel spherical harmonic shim coil insert detailed in Section 4.3.1. The insert was driven by a power supply with ± 5 A output current per channel and a dynamic shimming unit with eddy current compensation capabilities (Resonance Research Inc., Billerica, MA, USA). An internal matrix interconnection switch enables a free assignment of the correction signal generating pre-emphasis modules to any available output channel. This is illustrated in Fig. 5.3 A for an example of a representative pre-emphasis interconnection scheme. The time-course of a potential rapid shim current switching scheme and the associated response of the pre-emphasis correction circuitry is illustrated in Fig. 5.3 B.
Eddy currents which can be induced by the large-diameter shim system of the host MR scanner were not characterized in this work. The 1^{st} order gradients are actively shielded and fine-tuned via an internal, vendor-supplied eddy current compensation circuitry. Hence, they can be driven dynamically while generating only negligible eddy currents. The 2^{nd} order shim coils of the host MR scanner are supplied by a power supply which lacks the option of changing shim currents dynamically and does not have any eddy current compensation capabilities.
The acquisition of the eddy current encoded 2D images was performed using a matrix size of $[32 \times 32]$ at a 3 mm isotropic resolution. The sampling scheme illustrated in Fig. 5.2 was used to sample 3000 ms of the eddy current decay at 500 time points with a sampling interval of 6 ms. This resulted in an acquisition time of 3:12 min per image and a total scan time of 9:36 min per shim coil.

5.4 Results

The proposed 4D eddy current characterization framework was tested in multiple scenarios. Initially, to verify a correct implementation of the sampling scheme and the processing pipelines, artificially generated eddy currents with known decay characteristics were sampled, analyzed and compared to the input values. Moreover, to test the applicability of the slice-based sampling scheme for the reconstruction of high-order eddy current terms, extensive simulations with varying eddy current signal and noise characteristics were conducted. In this context, the proposed model-based analysis of the eddy current data was compared to the conventional approach. Lastly, the eddy currents generated during the dynamic operation of the very high-order shim insert were probed experimentally.

5.4.1 Measurements of artificially generated eddy currents

To test the applicability and the correct functionality of the proposed eddy current measurement sequence, a proof-of-concept experiment was conducted. For this purpose, a shim coil was first determined which, when driven dynamically with rapid shim current changes, generates only negligible eddy currents itself. The pre-emphasis module of this shim channel was then purposefully mis-adjusted to generate an exponentially decaying shim field with a known amplitude and time-constant. The resultant field dynamics were sampled using the proposed measurement sequence and the subsequently reconstructed and quantified time-course was compared to the known input parameters.

Preliminary shim coil tests

The eddy current induction properties of multiple shim coils were probed by acquiring regular B_0 maps in the presence of the dynamic shim current switching scheme illustrated in Fig. 5.4 A. The input currents to a given coil were adjusted such as to vary between consecutive slices repeatedly by ± 0.5 A, each time separated by one slice for which no offset was applied. Multiple coils were analyzed this way, with the alternating shim current offset scheme being applied to one distinct shim channel at a time.
In cases of shim coils for which the rapid change in shim amplitude induces eddy currents, the resultant distortion fields superimpose to the acquired data and become apparent in the acquired B_0 maps. The residual eddy current fields are then directly visible in the zero-crossing slices. Likewise, the offset-affected slices reveal B_0 distributions which differ from the prescribed dynamic shim field. It is to be noted, that the distinctness of this effect can be reduced by a partial cancellation of mid- and long-term eddy currents due to the opposing polarities of the shim current changes. Hence, this technique does not serve as a quantitative eddy current characterization, but can be used to efficiently detect the mere presence of eddy currents.
A subsequent analysis of the zero-crossing field map slices, via a quantification of the apparent residual B_0 field offset as shown in Fig. 5.4 D, revealed that no noticeable eddy currents were induced by the C3-shim. This finding was supported by the fact that an individual shim optimization over each set of eight slices, which was affected by either the positive or the negative current offset, returned the effectively applied shim values of +0.5 A and -0.5 A, respectively. For comparison, the illustrated data of the Z2- and the Z3-shim indicates the presence of residual eddy current fields with different kinds of spatial patterns.

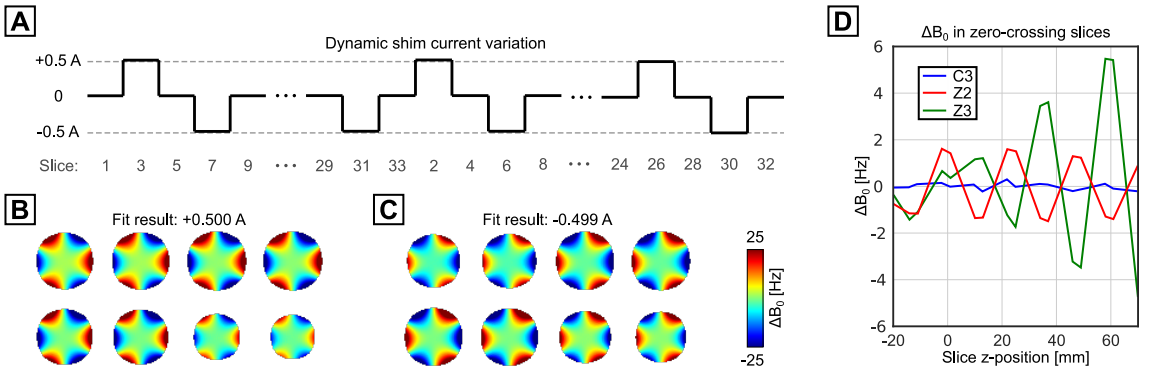

Figure 5.4: Eddy current test measurements. **(A)** Shim current switching scheme, which was applied to acquire 33 field map slices in an interleaved acquisition mode. The shim current offset was applied to one distinct shim channel at a time and varied sequentially between ±0.5 A, each time separated by one slice for which no dynamic shim offset was applied. The resultant field map slices for the C3-shim are shown in **(B)** for the positive current offset and in **(C)** for the negative current offset. Each of both sets of eight slices was then separately subjected to a shim optimization routine, which in turn re-calculated the known input values. **(D)** Plots of the B_0 field offset in the zero-crossing slices. The values for the C3-shim show no apparent offset, thus indicating that no residual eddy currents are present. In contrast to that, the graphs plotted for the Z2- and the Z3-shim reveal a fluctuating B_0-component (Z2) and a fluctuating Z-component (Z3), respectively.

Quantitative eddy current test measurements

An exponentially decaying shim field with an amplitude of $a = 0.2$ Hz/cm^3 and a time-constant of $\tau = 220$ ms was generated by adjusting the pre-emphasis module of the C3-shim accordingly. The resultant field dynamics were sampled for 3000 ms using the proposed measurement technique. Based on the results of the experiment described in the previous section, it follows that the B_0 field evolution stems solely from the purposefully introduced shim field modulation and not from shim-induced eddy currents. Thus, this analysis was used to test the applicability of the proposed technique to correctly reconstruct the known input parameters of the field decay.
For this, a spherical harmonic decomposition was performed at each time point and an exponential function was fitted to the resultant time-series of the C3-coefficients. This conventional application of the eddy current model was chosen to specifically analyze the proposed sampling scheme independently from the proposed model-based reconstruction. Examples of representative eddy current field maps, sampled at five different time points, are shown in Fig. 5.5 A. The spatial pattern of the spherical harmonic C3-term and its temporal decay is visible in the acquired data. Moreover, the spherical harmonic fit and its difference to the acquired slices illustrate that the data can comprehensively be described by the chosen model. The reconstructed eddy current amplitude of 0.204 Hz/cm^3 and time constant of 222 ms are in close agreement with the prescribed values. The low-amplitude fit residual, shown in Fig. 5.5 B, is fluctuating at the noise-level, thus indicating that the calculated results describe the data correctly.

5.4.2 Eddy current characterization simulations

Simulations based on eddy currents with varying spatio-temporal field patterns and different noise levels were performed to test the influence of these parameters on the accuracy of the reconstructed coefficients. The results obtained from applying the conventional fitting approach were compared to those from the model-based approach and are presented in the following.

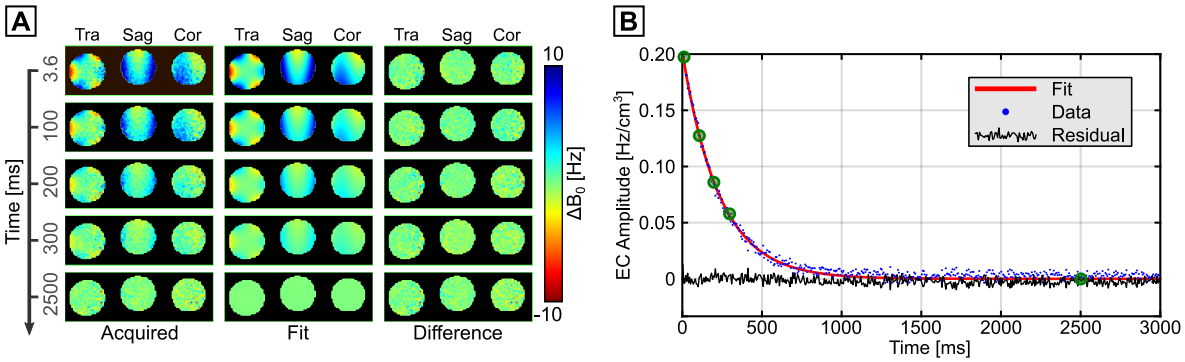

Figure 5.5: Eddy current test measurement. **(A)** An exponentially decaying shim field was generated by adjusting the pre-emphasis module of the C3-shim such as to generate an artificial eddy current field with known decay characteristics. The pre-emphasis adjustments were chosen such as to generate a mono-exponential decay with an amplitude of 0.2 Hz/cm^3 and a time-constant of 220 ms. The C3-shim was chosen, because it generates negligible eddy currents itself. The field map data, acquired at the five distinct time-points highlighted in the accompanying plot, reveals the expected and gradually decaying spatial pattern of the C3-shim term. The sets of displayed slices show, that the spherical harmonic fit can accurately describe the acquired data. **(B)** A spherical harmonic decomposition at each time-point and a mono-exponential fit to the resultant time-series of C3-coefficients was used to reconstruct the prescribed pre-emphasis parameters. The fit revealed an amplitude of 0.204 Hz/cm^3 and a time constant of 222 ms.

Conventional eddy current processing results

Various eddy current decays were simulated in order to test the proposed eddy current characterization scheme under different measurement conditions. The amplitudes and time constants for the simulated time series were either based on parameters taken from previously published dynamic shimming papers [101, 103], or randomly generated using realistic values in the same range. Based on the calculated decay rates, the associated distortion field distributions at the proposed 2D sampling slice locations were then determined. For this, a field-of-view size of [96 × 96 × 96] mm^3 and a matrix size of [32 × 32 × 32] was chosen and the eddy current fields were calculated at an isotropic spatial resolution of 3 mm within an iso-centered, spherical volume with a diameter of 90 mm. The three orthogonal sampling slices were extracted from the simulated volumes at an off-center position of 21 mm. Lastly, the eddy current fields were scaled in magnitude and confounded by additive Gaussian noise with different noise levels. Thus, as illustrated in Fig. 5.6, the simulated data covered various signal-to-noise ratios and different decay rates. A total number of 1250 dataset were generated this way.
All datasets were first processed using the conventional approach, i.e. by applying the spatial and the temporal part of the eddy current model in a decoupled and consecutive manner. Each fit was then evaluated by calculating the residual eddy current field distribution, which would result from applying the reconstructed pre-emphasis parameters. Based on this, the effectiveness of the compensation was quantified as the maximum absolute residual field offset within the spherical phantom. A summary of the results of all processed datasets is shown in Fig. 5.7 A. The error surface displays the average maximum absolute field offset, which was determined as the mean value of 50 datasets per eddy current amplitude and noise level combination.
The plot indicates that the conventional application of the eddy current model is applicable to datasets with low noise levels. An increase in the noise, however, de-stabilizes the fit and renders the reconstructed pre-emphasis parameters increasingly less accurate. For comparison, Fig. 5.7 B shows the results obtained when including only those spherical harmonic functions into the fit,

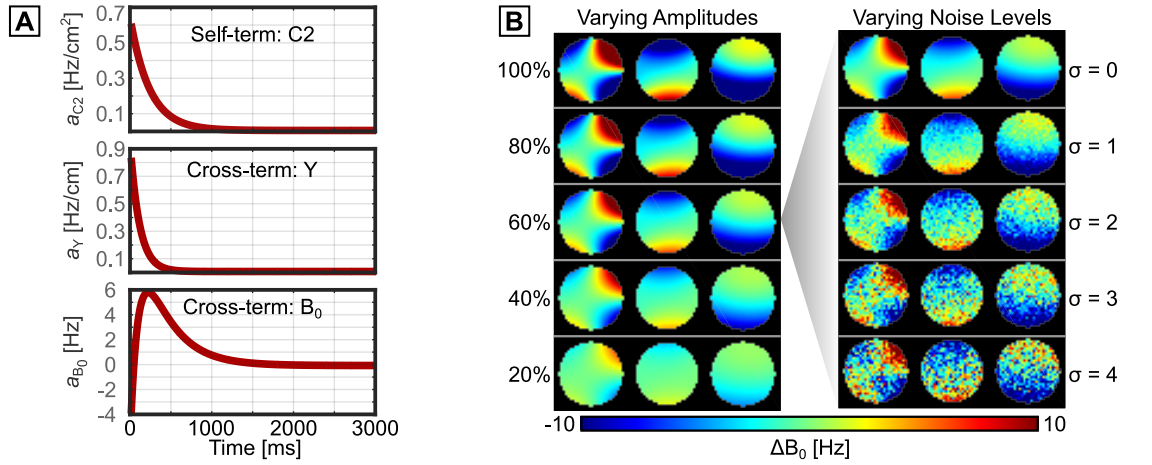

Figure 5.6: Eddy current data generation for the pre-emphasis parameter reconstruction simulations. **(A)** Realistic eddy current decay rates, published in the dynamic shimming literature [101, 103], were used to simulate the resultant distortion fields at the 2D slice locations of the proposed sampling scheme. The illustrated plots show one example of a representative dataset, which describes the time series of the eddy currents induced by rapidly switching a spherical harmonic C2-coil. The associated distortion field can be decomposed into an exponentially decaying self-term plus a Y- and a B_0-cross-term. **(B)** To extend the number of simulated datasets, further eddy current fields were simulated. Multiple randomly chosen spherical harmonic terms with arbitrary decay rates were superimposed to form base datasets. Their individual amplitudes were scaled and the data was confounded by Gaussian noise with varying noise levels in order to simulate different signal-to-noise ratios. All eddy current datasets were then subjected to the pre-emphasis parameter reconstruction routine.

that are also present in the simulated eddy current data. The resultant error in the residual data is significantly reduced, which demonstrates that when the optimization problem is well-behaved, the sampling scheme is applicable for a correct pre-emphasis parameter reconstruction. Thus, even though measurement noise and shim degeneracies can significantly impair the accuracy of the reconstructed pre-emphasis parameters, correct eddy current time-series can still be determined with a very high accuracy when handling these confounding influences. As will be shown in the following, this feature can be provided by the model-based reconstruction.

Model-based eddy current processing results

As described in Section 5.3.2, the model-based eddy current fitting algorithm can be adjusted by means of three optimization variables. These include a weighting factor (λ) as well as the number of iterations in the outer and the inner loop (N_{outer} and N_{inner}). All three variables were optimized in simulations in order to find combinations that yield accurate results while providing robustness against variations in the signal-to-noise ratio and the individual compositions of the eddy current fields. For this, 45 eddy current time-series with randomly chosen spherical harmonic components and individual decay rates were calculated and evaluated at the proposed slice-based sampling positions. The eddy current images were subsequently confounded by additive Gaussian noise with a standard deviation of $\sigma \in \{1, 2, 3\}$.
Using three different values for the weighting factor, $\lambda \in \{10, 100, 1000\}$ and four different numbers of iterations in the inner loop, $N_{\text{inner}} \in \{50, 100, 250, 500\}$, each dataset was then repetitively subjected to the model-based reconstruction. With a maximum number of iterations in the outer loop, $N_{\text{outer}} = 10$, a total number of 120 different parameter combinations per dataset were tested this way and the associated pre-emphasis parameters were determined.

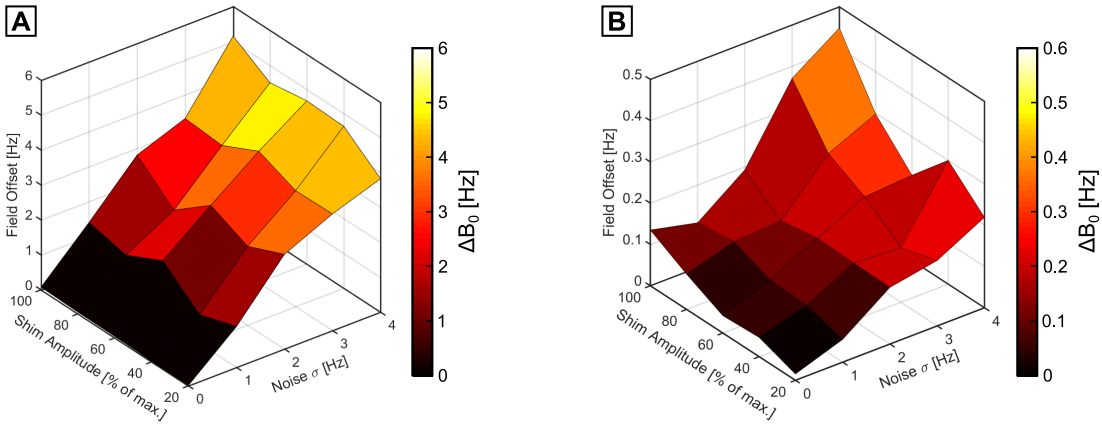

Figure 5.7: Maximum residual eddy current field offset in the pre-emphasis compensated time series, averaged over 50 datasets per eddy current amplitude and noise parameter combination (see text for details). **(A)** Accurate pre-emphasis parameters can be determined in the presence of low noise-levels. An increase in noise, however, de-stabilizes the spherical harmonic fit and leads to a sub-optimal compensation performance. **(B)** Changing the system matrix such as to include only the spherical harmonic terms that are known to be present in the simulated data, reduces the fitting error significantly to an acceptable level. This step is not applicable when using real measured data, but can similarly be achieved using the model-based reconstruction. Note the $\times 10$ lower scaling.

Like the results obtained from the conventional eddy current fitting, the effectiveness of the calculated pre-emphasis parameters was then quantified by means of the maximum absolute residual field offset in the simulated eddy current compensated data. The results of this analysis are summarized in Fig. 5.8 A. In dependence upon on the values of the optimization variables, the plot shows the maximum absolute field offset, which was averaged for each parameter setting over all 45 datasets. It indicates that a robust parameter combination is given by the values of $\lambda = 1000$ and $N_{\text{outer}} = [7 \,..\, 10]$. It can be seen that the algorithm reveals a certain robustness against variations in the number of iterations in the inner loop. Nonetheless, all subsequent analyses were performed with a value of $N_{\text{inner}} = 500$, as well as $N_{\text{outer}} = 7$ and $\lambda = 1000$.
The optimized parameters were used in the proposed model-based eddy current fitting framework to decompose the simulated datasets into their spherical harmonic components and to fit the resultant exponential decay rates of the detected non-negligible terms. The same processing steps were conducted for the conventional application of the eddy current model and the results of both techniques were compared to each other. The maximum absolute field offset, averaged over all 45 datasets, was found to be 0.51 ± 0.51 Hz for the model-based results as compared to 4.14 ± 3.60 Hz for the conventionally derived results.
An example of the data restoration capabilities of the model-based reconstruction is illustrated in Fig. 5.8 B. The results of the conventional application of the eddy current model introduces strong fitting noise in the time-course of the spherical harmonic coefficients. Even though the decay of the individual eddy current terms is clearly visible in the data, a quantitative calculation of optimal pre-emphasis parameters is biased by the noise. In contrast to that, the model-based reconstruction stabilizes the spherical harmonic fit and returns the input parameters correctly.

5.4.3 Eddy current characterization measurements

The proposed eddy current measurement and processing framework was used to characterize the individual coils of the very high-order spherical harmonic shim insert. Measurements were performed before and after adjusting the pre-emphasis modules in order to verify the validity of

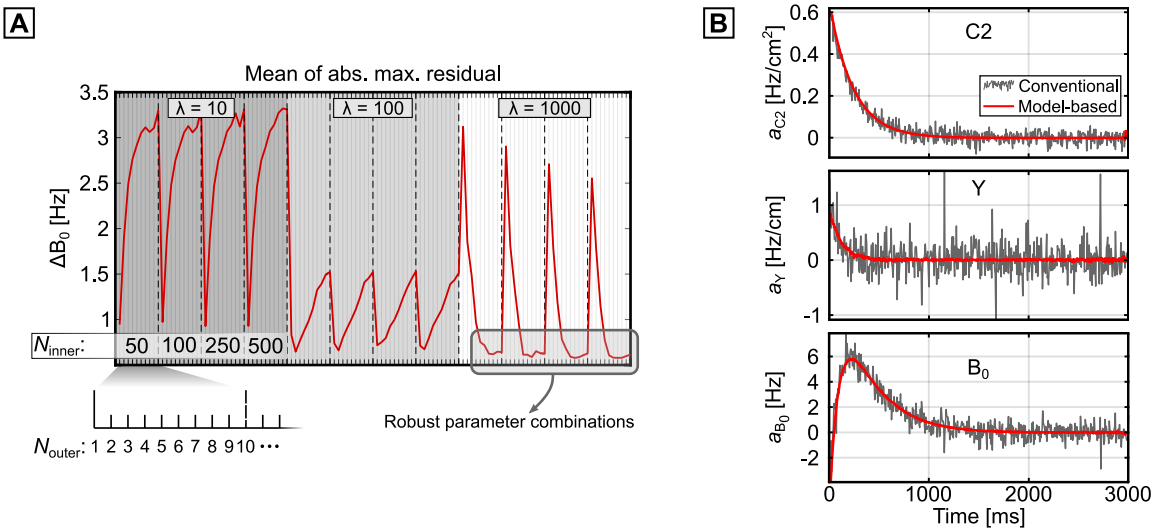

Figure 5.8: Model-based eddy current fitting results. **(A)** Optimization of the adjustable algorithm variables. For each λ-value, the indicated four different numbers of iterations in the inner loop were performed, each time for a total number of 10 iterations in the outer loop. After each iteration in the outer loop, the results were stored and used to determine the eddy current compensation performance of the associated pre-emphasis parameters (see text for details). **(B)** Example of the spherical harmonic fit stabilization capabilities of the proposed model-based algorithm as compared to results derived from the conventional approach.

the obtained correction parameters. The results for three shim coils are shown in Fig. 5.9 and illustrate examples of typical pre-emphasis adjustment challenges.

The eddy currents of the B_0-coil were measured following a +0.5 A shim pulse, which corresponds to an effective shim field of 2885 Hz. With a resultant maximum value of almost 260 Hz immediately after the shim pulse, the induced eddy current field reached an amplitude of more than 9% of the evoking shim field. Moreover, as can be seen in the zoomed view on the eddy current amplitude evolution, as well as from the plot of the predicted eddy current compensation residuals, the underlying eddy current time-course decays multi-exponentially. The associated exponential fit revealed that the eddy current evolution can only be described accurately, when using at least one short-, mid- and long-term pre-emphasis time constant, respectively. This finding was validated by re-measuring the eddy currents after having adjusted three compensation modules of the B_0-coil accordingly.

The results of the measurements of the eddy currents generated by the Z3-coil are shown in Fig. 5.9 B and indicate the presence of a rapidly decaying self-term and a slowly decaying B_0 cross-term. As can be seen in the post-compensation time-series, both eddy current terms could be suppressed by implementing the associated pre-emphasis module adjustments.

The eddy current measurement results of the ZX-shim demonstrate the strength of the model-based reconstruction scheme in detecting low-amplitude eddy currents in the presence of high noise-levels. Whereas the time-series of the ZX-coefficients derived from the conventional application of the model is dominated by fitting noise, the model-based reconstruction reveals a distinct eddy current term. As can be seen in the zoomed view, the same results can be obtained from the conventional approach when fitting only the ZX-term to the data instead of the full set of 16 3^{rd} order spherical harmonics. This finding is in accordance with the results illustrated in Fig. 5.7 and demonstrates that correct eddy current estimates can be gained from the proposed sampling scheme if the confounding noise and shim degeneracy influences are handled properly.

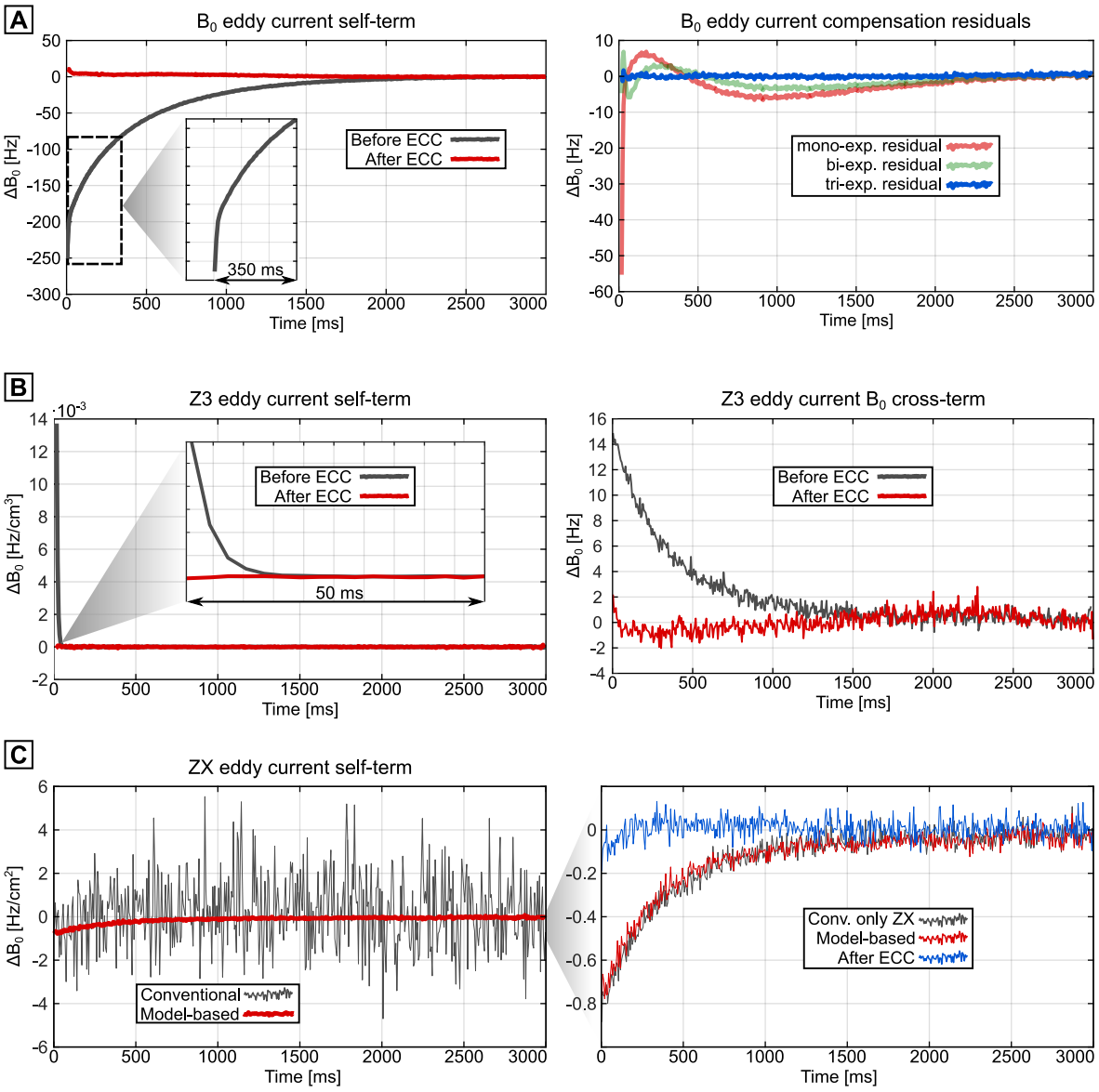

Figure 5.9: Eddy current measurement and compensation results. **(A)** The self-term eddy current evolution generated by the B_0-coil following a 0.5 A shim pulse. The zoomed view clearly reveals a rapidly and a slowly decaying component. The calculated compensation residuals, resulting from approximating the decay with one, two or three exponentials, indicate that adequate eddy current suppression levels can only be reached with at least three terms. The re-measured eddy currents, after having adjusted three pre-emphasis modules of the B_0-coil, validate the calculations. **(B)** The measured Z3-induced eddy currents can be decomposed into a rapidly decaying self-term and a slowly decaying cross-term to B_0. The re-measured eddy current decay, after having adjusted the pre-emphasis modules of both shims accordingly, shows that both terms could successfully be compensated. **(C)** The conventional application of the eddy current model fails in reconstructing an applicable time-series of the spherical harmonic ZX eddy current coefficients. The fit can significantly be improved using the model-based optimization. The zoomed view illustrates that it can similarly be stabilized in the conventional approach when fitting only the ZX self-term to the data instead of the full set of the 3rd order spherical harmonics. The post-compensation eddy current measurement results demonstrate the achieved level of suppression.

5.5 Discussion and conclusions

In this work, a 2D image-based eddy current measurement scheme has been developed and applied for a high-order spherical harmonic characterization of eddy current fields. Moreover, a model-based algorithm for an optimal pre-emphasis parameter reconstruction has been employed to improve the data fitting accuracy through inclusion of prior knowledge about the time-course of the spherical harmonic eddy current terms. The applicability of both techniques has been validated in extensive simulations as well as real eddy current measurements using a dynamically driven very high-order spherical harmonic shim coil insert. The results were used to implement an effective pre-emphasis eddy current compensation setting, which enables a rapid updating of shim currents during sequence execution and, thus, forms the basis for dynamic shimming implementations.

The utilization of image-based eddy current measurement techniques is convenient, because the acquired data is already interpretable via direct comparison to the spherical harmonic field functions. Moreover, depending on the chosen matrix and field-of-view sizes, image-based approaches typically achieve a dense sampling of the spatial domain. As such, they are well-suited for the detection and the correct characterization even of high-order eddy current terms, which is an intrinsic limitation of projection-based techniques. The associated disadvantage of a requiring prolonged acquisition times has significantly been reduced in this work by switching from a full 3D sampling [168] to a more time-efficient 2D image-based sampling. Thus, considering equal spatial resolutions of the acquired eddy current images, the acquisition time using the proposed slice-based measurement is reduced by a factor of six. Nonetheless, it has been shown that the gained information is still sufficient for the purposes of the spatial eddy current characterization using a spherical harmonic basis. However, despite the achieved acquisition time reduction, image-based measurement techniques can generally not compete with the temporal sampling capabilities of NMR fieldprobe-based measurements. Yet, additional measurement hardware is not required and, therefore, they form a convenient alternative.

Based on simulated eddy current data, evaluated at the proposed 2D slice-based sampling positions, it has been demonstrated, that the conventionally employed decoupled application of the eddy current model is highly sensitive to noise in the data. As a result, the pre-emphasis parameters obtained from realistically achievable signal-to-noise ratios of the eddy current data are often inaccurate and the resultant eddy current suppression levels are insufficient. Considering a certain maximum order of the spherical harmonics used to characterize the eddy currents, the field decomposition becomes instable when fitting the associated full set of functions to the data. The resultant fitting noise can significantly degrade the accuracy of the individual eddy current coefficient time-series, or suppresses apparent eddy current terms entirely. It has been demonstrated that the fit quality is strongly improved, when only the subset of functions is included into the fit, that is *de facto* present in the data. In that case, the simulations have shown, that the resultant eddy current suppression can be reduced to the sub-Hertz level. However, since the subset of spherical harmonic functions that are contained in the eddy current data is generally unknown, this form of improving the conditioning of the problem is not applicable to real measured data.

Alternatively, the inclusion of the prior knowledge about the exponential decay of the eddy current terms into the spherical harmonic decomposition can similarly stabilize the optimization. The implementation of this feature, via a rank-minimization of the Hankel-matrices associated with the time-course of the spherical harmonic eddy current coefficients, has proven to be well-suited for this purpose. The algorithm automatically detects all spherical harmonics that are required

to accurately approximate the measured data and simultaneously suppresses all other terms. It intrinsically avoids problems that are associated with shim degeneracies and, thus, it is a form of an optimization regularization which is informed by valid prior knowledge.
It has been found, that the measured eddy current amplitudes of the shim insert are significantly lower than those obtained for conventional spherical harmonic shims of the host scanner. This is due to a smaller diameter of the shim coils and a resultant greater distance to the conducting surfaces of the MR system. As such, the pre-emphasis calibration overhead for the very high-order shim system is smaller than it was predicted, based on a simple extrapolation from results obtained for a lower-order large-diameter shim coil characterization [103].
In conclusion, an entirely image-based very high order eddy current characterization can be performed in approximately 10 minutes using the proposed approach. The achieved eddy current suppression levels allow for a rapid updating of the shim currents during the MR sequence execution, which is required for dynamic shimming implementations. Therefore, the results of this work form in integral part of the dynamic shimming optimization which will be presented in the following chapter.

6

Inter-slice current change constrained dynamic B_0 shimming

As was introduced in Section 3.4 and presented in greater detail in Chapter 4, static spherical harmonic B_0 shimming can be used to improve the magnetic field homogeneity. This is commonly done by adjusting the shim currents on a per-subject basis prior to the actual MR acquisitions, such as to optimally cancel apparent inhomogeneity terms. However, certain anatomical structures induce B_0 inhomogeneities with complex spatial patterns and which are un-correctable to static shimming routines. Therefore, dynamic shim approaches are used to update the shim setting during the acquisition, such as to be optimal for each acquired sub-volume. Thus, B_0 homogeneity is improved simply by making a more efficient use of an available set of shim coils.

Spherical harmonic dynamic B_0 shimming, however, can be complicated by eddy currents induced by rapid shim field changes, an ill-posedness of the shim optimization problem and the need for stronger power supplies. Therefore, in this chapter a novel algorithm is presented, which aims at reducing the absolute dynamic shim current amplitudes and their temporal variation at negligible losses in achievable B_0 homogeneity. Assuming a smoothness of the B_0 inhomogeneity variation in the slice direction and being based on the fact that eddy current amplitudes are proportional to the magnitude of the shim current changes, the aforementioned problems are entirely handled on the algorithmic side, while simultaneously reducing hardware requirements.

The applicability of the proposed algorithm was validated in simulations and in phantom and in vivo measurements. While conventional 4^{th+} order dynamic shim optimizations improve the B_0 homogeneity on average by a factor of 2.1 over standard 2^{nd} order static solutions, the proposed routine reaches a factor of 2.0, while simultaneously providing a 14-fold reduction of the average maximum shim current changes. As a result, it has the potential to mitigate the remaining challenges in dynamic B_0 shimming and help in making its application more readily available.

Parts of this work were published in:

M. Schwerter, C. H. Moon, H. P. Hetherington, J. W. Pan, L. Tellmann, J. Felder, and N. J. Shah, "Interslice current constrained B0 shim optimization for high order dynamic shim updating with strongly reduced eddy currents," in *Proc. Intl. Soc. Mag. Reson. Med.*, p. 836, 2018

M. Schwerter, H. P. Hetherington, C. H. Moon, J. W. Pan, J. Felder, L. Tellmann, and N. J. Shah, "Interslice current change constrained B0 shim optimization for accurate high-order dynamic shim updating with strongly reduced eddy currents," *Magnetic Resonance in Medicine*, vol. 82, no. 1, pp. 263–275, 2019

6.1 Introduction

The homogenization of the static magnetic field is a key requirement for obtaining high-quality data in most MR applications. Although B_0 is kept well under control during the manufacturing and installation of the bare magnet [174], it was shown in Section 3.2.1, that the placement of tissues with varying magnetic susceptibilities into the magnetic field induces complex and high order, subject-specific B_0 inhomogeneities. Therefore, standard MR systems contain sets of 2^{nd} and sometimes 3^{rd} order spherical harmonic shim coils [35] which generate adjustable magnetic fields to cancel the apparent inhomogeneity terms. However, space limitations and shim coil efficiency considerations restrict the feasible number of shim coils and impose a natural limitation to this approach, leading to the inability to approximate higher order terms. It has been demonstrated in Chapter 4, that even very high-order spherical harmonic shim systems, which exhaust the physical limits dictated by the MR system, cannot fully compensate for all inhomogeneity terms in the human brain. While already being problematic at clinical field strengths of 3 T and below, this issue is exacerbated at higher field strengths and stands in contrast to the trend towards ultra-high field MR systems, since vendor-supplied means of B_0 shimming have not advanced to match demand.

This motivates the development of more effective shim techniques, and recent approaches, such as static [132] and dynamic [137] multi-coil shimming and integrated $\Delta B_0/R_x$ shim arrays [139, 140] have already demonstrated remarkable improvements, at least over standard static 2^{nd} order spherical harmonic shimming. In contrast to these techniques which employ additional shim coils, dynamic shim updating is a concept which aims at making a more efficient use of an available set of spherical harmonic shim coils. Its was already introduced in the mid-nineties [97, 98] and exploits the fact that B_0 inhomogeneities can be better approximated over smaller volumes and thus updates shim coil currents during the acquisition to be optimal for each sub-volume. The initial 1^{st} order dynamic shimming experiments have been extended to also include 2^{nd} [101] and 3^{rd} [103] orders and have proven to yield better B_0 homogeneity at ultra-high fields [102] and in both multi-voxel and multi-slice applications [107], such as spectroscopic imaging [105] and functional MRI [106]. However, despite being available for more than two decades, and notwithstanding its B_0 homogeneity improvement, dynamic shimming is not yet routine. Commonly reported complications pertaining to successfully implementing this technique are the generation of eddy currents through rapid intra-acquisition shim current changes, an ill-posedness of the numerical optimization problem, and a resulting need for stronger power supplies.

In this chapter it is shown, that these dynamic shimming-specific problems can be substantially reduced, if not eliminated, by appropriately constraining the shim current calculation and by complementing the algorithm with *a priori* information about preferred solutions. While reaching a similar B_0 homogenization performance as other state-of-the-art dynamic shimming techniques, the resulting strong shim current reduction limits potential eddy currents and addresses shim degeneracies at overall reduced hardware requirements. Following a detailed analysis of the aforementioned challenges, in this chapter the performance of the novel dynamic shim current optimization is investigated and its advantages are demonstrated in simulations and in vivo high-order dynamic shimming measurements. Parts of this work were published in [1] and [2]. Unless otherwise stated, the work presented in this chapter is the work of the author of this thesis.

6.2 Theory

In the following, a detailed analysis of current challenges for dynamic B_0 shimming is being presented alongside with the theoretical background of the proposed solution approach. Each of these challenges is effectively addressed by the proposed shim optimization algorithm, which is thoroughly explained in the subsequent section.

6.2.1 Challenges in dynamic shim updating

As was outlined in Section 3.4.2, in contrast to conventional static shimming, *dynamic shim updating* describes a method of changing shim currents during the acquisition such as to optimally cancel residual B_0 inhomogeneities in distinct sub-volumes. However, successful application of calculated dynamic shim currents may be compromised by specific problems intrinsic to this advanced B_0 shim approach. These are outlined in the following and schematically illustrated in Fig. 6.1.

(I) Rapid intra-acquisition shim current changes can induce eddy currents in nearby conducting surfaces, which in turn generate time-varying magnetic perturbation fields. Eddy current amplitudes and time constants during dynamic shimming can be high enough to make the B_0 homogeneity worse than for the equivalent static case [103].

(II) Eddy currents are commonly handled by pre-emphasis modules which superimpose correction currents to the shim outputs to cancel the eddy current fields [175]. Therefore, parts of the dynamic range of the power supply cannot be used for the purpose of shimming, and a numerical dynamic shim optimization in its standard form can run into current limitations [41].

(III) Since they require a full 4D characterization of the eddy currents generated by each shim coil [166], accurate pre-emphasis adjustments are iterative and time-consuming. Conventional MR sequence-based eddy current measurement techniques, e.g. based on multiple projections [167] or full 4D eddy current maps [168], can take up to one hour measurement time per shim channel. Slight calibration inaccuracies can already translate into long-lived and uncompensated eddy currents, with amplitudes that scale with the initial change in shim current.

(IV) The shim basis functions are not necessarily orthogonal over the dynamic shimming sub-volumes. This shim degeneracy degrades the linear independence of the system and renders the optimization problem described by Eq. 3.6 as being ill-conditioned, which can cause excessive dynamic shim currents [74].

(V) Shim optimization routines require system-specific shim calibrations, which relate the shim current through a shim coil with the magnitude of the resulting shim field [158]. Due to phase wrapping and intra-voxel dephasing artifacts induced by high shim offsets, the calibration data can often only be acquired at comparably low shim currents. Consequently, dynamic shim fields calculated from conventional optimization routines, which often employ higher shim currents [176], may be incorrectly modeled when falling into a current regime not covered in the calibration procedure. The dynamic range of shim offsets that can be sampled during the calibration data acquisition depends on the efficiency of the shim coil and is narrower for the more efficient lower order shim coils.

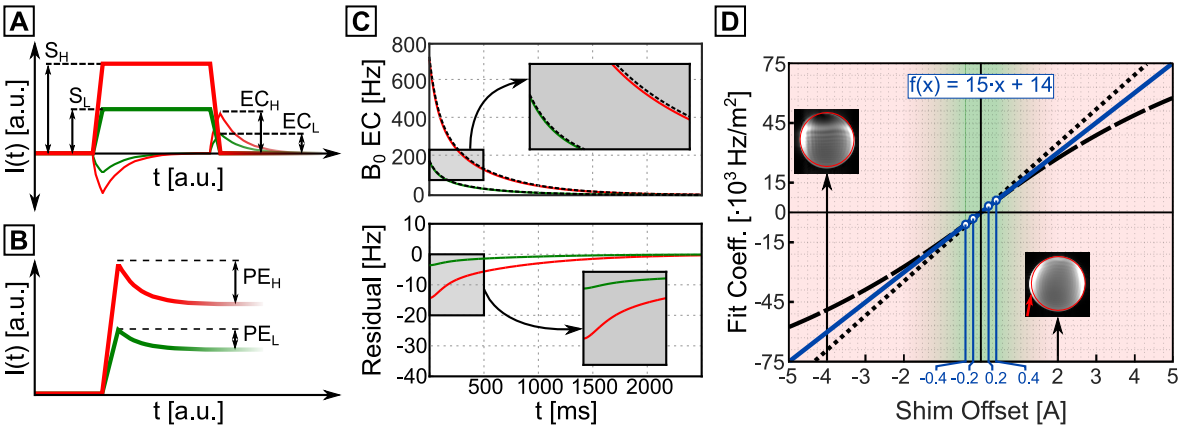

Figure 6.1: Challenges for dynamic shim updating [2]. **(A)** A rapid shim current change induces eddy currents in nearby conducting surfaces. Shim steps with high amplitudes, S_H, cause higher eddy current amplitudes, EC_H (red), than shim steps of low amplitude (green). **(B)** The amplitude of a pre-emphasis overshoot used to correct for shim-induced eddy currents is proportional to the initial change in shim current. Thus, high amplitude shim steps require higher pre-emphasis amplitudes, PE_H (red), than low amplitude shim steps, PE_L (green). **(C)** Inaccuracies in the pre-emphasis adjustment cause uncompensated eddy currents. The offset of the correction signal (black dashed lines) scales with the original shim current change and eddy currents of larger shim steps (red) will have stronger residuals than those of smaller shim steps (green). The illustrated data demonstrates the effect of a 2% error in the adjustment of the amplitudes and time constants of a three-term exponential pre-emphasis self-term correction of a B_0-coil. **(D)** Image artifacts prohibit the acquisition of high shim offset data during the calibration of a shim system (magnitude data shown). The linear fit derived from data sampled at relatively small offsets (green shaded area) might fail in modeling the shim system at high current offsets (red shaded area). Small fitting errors (dotted) or slight power supply non-linearities (dashed) can lead to erroneous shim calculations at high current values. The data shown here qualitatively demonstrates this effect for the calibration data of a spherical harmonic C2-coil of a 3T system.

6.2.2 Proposed solution approach

Being a severe source of artifacts on their own, the dynamic shimming problems given in Section 6.2.1 are coupled and can accumulate in their negative effect on the MR signal. For instance, an ill-posed shim optimization over a certain sub-volume can lead to excessive shim currents for potentially degenerate shim channels. As a result, a rapid change to these high shim values can induce strong eddy currents which, in turn, require high eddy current compensating pre-emphasis overshoots. Both effects then result into situations in which the given power supply limits can be heavily exceeded. In addition to that, inevitably occurring inaccuracies in the eddy current compensation adjustments have a significantly lager impact and can result into uncompensated field fluctuations. Lastly, the employed shim calibration matrix may be inaccurate at these high shim values, which results into a quasi-static deviation from the targeted correction field. Consequently, these problems originate from and are scaled by excessive dynamic shim currents and their temporal variation. It follows, that their effects can be minimized if the absolute current amplitudes and the change between consecutive shim currents can be reduced substantially without affecting the achievable B_0 homogeneity.

This is the central motive of the proposed solution approach. In the following it is hypothesized that for the general slice-wise dynamic shim optimization problem described by Eq. 3.6, the solution space is large enough to allow the feasible set of solutions to be strongly constrained, while negligibly affecting the achievable B_0 homogeneity. Thus, B_0 homogenization performances similar to the optimal solution are expected to be found for considerably smaller shim current

amplitudes. In addition, it is assumed that for slice thicknesses on the order of a few millimeters, the B_0 inhomogeneities vary smoothly in slice direction and hence minor changes in dynamic shim currents are sufficient to adapt to the new shim challenge as dictated by the slice acquisition order. Exploiting this knowledge by extending Eq. 3.6 to include regularization terms and additional constraints provides a means of handling the dynamic shimming problems on the algorithmic side. By doing this, the general shimming process remains unaffected, while simultaneously reducing hardware requirements.

6.3 Methods

The methods developed for this project build upon the results presented in the previous two chapters. A thorough and accurate shim calibration, presented in Chapter 4, is essential not only for calculating correct static and dynamic shim fields, but also forms the basis for meaningful shim simulations. Precise eddy current measurements, presented in Chapter 5, are indispensable for the implementation of shim pre-emphasis corrections when wanting to rapidly change the shim currents during dynamic shim updating. The results from both concepts were utilized during the implementation of the methods presented in the following.

6.3.1 The proposed dynamic shim current calculation algorithm

To minimize the effects of the problems discussed in Section 6.2.1, the aims of the shim calculation algorithm are to reduce the shim amplitudes and their temporal variation while still optimally canceling residual B_0 inhomogeneities. In the proposed algorithm this is realized by complementing Eq. 3.6 with two regularization terms as well as by tightening the constraints of the shim calculation according to

$$\begin{aligned} \min_{\mathbf{x}_k} \quad & \underbrace{\|\mathbf{A}_k\mathbf{x}_k - \mathbf{b}_k\|^2}_{\text{Data Term}} + \underbrace{\lambda \cdot \|\mathbf{x}_k\|^2}_{\text{Abs. Term}} + \underbrace{\epsilon \cdot \|\mathbf{x}_k - \mathbf{x}_{k-1}\|^2}_{\text{Diff. Term}} \\ \text{s.t.} \quad & \begin{cases} \mathbf{lb}_k \leq \mathbf{x}_k \leq \mathbf{lb}_k \\ \mathbf{C} \cdot \mathbf{x}_k < \mathbf{d}. \end{cases} \end{aligned} \tag{6.1}$$

Including the Tikhonov regularization term $\|\mathbf{x}_k\|^2$ gives preference to solutions with small absolute values of the shim amplitudes and $\|\mathbf{x}_k - \mathbf{x}_{k-1}\|^2$ reduces the difference to the previous shim values. Thus, the causes of the aforementioned problems are effectively addressed by both terms. The parameters λ and ϵ control the respective regularization weighting and can individually be tuned such as to optimally balance the shim correction and the regularization impact.
While the regularization terms drag the solution towards a preferred set of shim values, the lower and upper bounds, $\mathbf{lb}_k$ and $\mathbf{ub}_k$, are updated for every slice. This is done to additionally set an explicit limit to the maximally permitted dynamic inter-slice shim current changes, which becomes effective whenever the impact of the associated regularization term is outweighed by that of the data term. The linear inequality constraints, $\mathbf{C}$ and $\mathbf{d}$, are used to reduce the cumulative current output of a set of shims to user-selected values, which is a consequence of the hardware used in this work. The power supply is built such that a set of seven shims is supplied by a common amplifier bank, which has certain limits with respect to the maximum signed and cumulative current output. A full list of used variables can be found at the end of this section.
To address through-slice dephasing, shim values for each slice are calculated in a moving boxcar mode by including both adjacent slices into the fit. This additionally reduces shim degeneracies and establishes data-sharing between fits of consecutive slices, which is beneficial for keeping their individual dynamic shim solutions similar. Although Eq. 6.1 can be used to loop over the slices to successively calculate all shim solutions, compliance with the explicit inter-slice current limit will not be guaranteed between the last and first slice. Therefore, an initial step is introduced in which the shim calculation for the outermost slices is coupled in a joint optimization. Consequently, the entire algorithm consists of three steps, which are detailed in the following and illustrated schematically in Fig. 6.2.

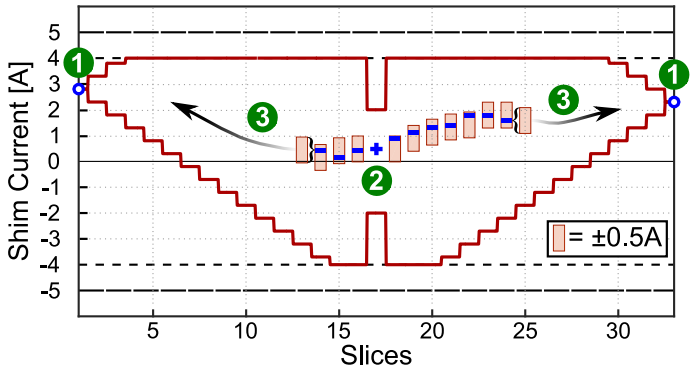

Figure 6.2: Processing steps of the dynamic shimming algorithm illustrated for 33 slices of one shim channel with $I^{(i)}_{max}$ limited to 4 A and with a maximum inter-slice shim current limit of $v^{(i)}$ = 0.5 A [2]. **(1)** Dynamic shim currents are calculated for the end-slices (blue circles) and constrained such that their difference is smaller than or equal to the chosen maximum inter-slice difference. **(2)** A shim solution is calculated for the starting slice (blue cross) with the upper and lower bounds tightened to $I^{(i)}_{max}/2$ in order to assure full flexibility for the calculation of the subsequent slices. **(3)** All other slice solutions (blue bars) are calculated successively under the guidance of the respective most stringent constraints as dictated by either the chosen inter-slice current limit, the power supply limit or the end-slice solutions. The inter-slice limits are displayed as red boxes with magnitudes of $\pm v^{(i)}$ and the solid red line illustrates how the upper and lower bounds are tightened by $lc^{(i)}_k$ and $uc^{(i)}_k$ given by Eqs. 6.7 and 6.8 in order to maintain the inter-slice limits with respect to the end-slice solutions.

Step 1: Calculation of the end-slice solutions.

Standard dynamic shim solutions, $\mathbf{x}^s_k$, for the two end-slices with indices $k \in \{1, N\}$ are calculated individually from Eq. 6.1, with the non-slice-specific power supply current limits, $\pm\mathbf{I}_{max}$, as the lower and upper bounds and by setting $\epsilon = 0$. The scalar-valued norms, S_k, of these solutions follow from

$$S_k = \|\mathbf{A}_k\mathbf{x}^s_k - \mathbf{b}_k\|^2 + \lambda \cdot \|\mathbf{x}^s_k\|^2 \tag{6.2}$$

and yield quantitative parameters as a reference for the shim performance without application of any inter-slice current constraints. Now let $\mathbf{v}$ be a vector of the explicit inter-slice shim current limits given by $v^{(i)} = p^{(i)} \cdot I^{(i)}_{max}$ with $\{p^{(i)} \in \mathbb{R} \mid 0 < p^{(i)} \leq 2\}$, i being the index of the shim channel, and let $\mathbf{M}_1, \mathbf{M}_2 \in \mathbb{R}^{n\times n}$ be the diagonal matrices

$$\mathbf{M}_1 = \begin{bmatrix} +1 & \dots & 0 \\ \vdots & \ddots & \vdots \\ 0 & \dots & +1 \end{bmatrix} \quad \text{and} \quad \mathbf{M}_2 = \begin{bmatrix} -1 & \dots & 0 \\ \vdots & \ddots & \vdots \\ 0 & \dots & -1 \end{bmatrix}. \tag{6.3}$$

Using the solution norms of the standard solutions, the shim current calculation for both slices can be coupled in a joint optimization framework according to

$$\begin{aligned} &\min_{x_k} \quad \sum_{k\in\{1,N\}} \|\mathbf{A}_k\mathbf{x}_k - \mathbf{b}_k\|^2 + \lambda \cdot \|\mathbf{x}_k\|^2 - S_k \\ &\text{s.t.} \quad \begin{cases} \mathbf{lb}_k \leq \mathbf{x}_k \leq \mathbf{lb}_k \\ \mathbf{C}\mathbf{x}_k < \mathbf{d} \\ \begin{bmatrix} \mathbf{M}_1 & \mathbf{M}_2 \\ \mathbf{M}_2 & \mathbf{M}_1 \end{bmatrix} \cdot \begin{bmatrix} \mathbf{x}_1 \\ \mathbf{x}_N \end{bmatrix} \leq \begin{bmatrix} \mathbf{v} \\ \mathbf{v} \end{bmatrix}. \end{cases} \end{aligned} \tag{6.4}$$

Minimization of Eq. 6.4 simultaneously calculates the solutions $\mathbf{x}_1$ and $\mathbf{x}_N$, which are ideally close to the B_0 shimming capabilities of the standard non-coupled solutions for these slices. The added linear inequality constraints limit the inter-slice difference between the outermost slices to be equal to or smaller than the values in $\mathbf{v}$.

Step 2: Calculation of a solution for a starting slice.

Because all slice solutions depend on the shim values of their preceding slice, it is beneficial for the first processed slice not to have a solution that is close to the power supply limits. Hence, although the processing loop can start at any slice index, the first processed slice is chosen to be the center of the stack. To further emphasize the favored condition of having low currents for the first processed slice, the upper and lower bounds are reduced to $\pm\mathbf{I}_{\text{max}}/2$, and the starting slice solution follows from solving Eq. 6.1 with a value of $\epsilon = 0$.

Step 3: Calculation of all other slices in acquisition order.

Starting with the solution of Step 2, the prior information about the shim values of every preceding slice serves as an initial guess for the current slice solution. This information is also used to update the lower and upper bounds in Eq. 6.1 so that shim current changes are limited to $\pm\mathbf{v}$. To ensure that all calculated solutions also maintain this limit with respect to the calculated end-slice solutions of Step 1, an individual set of lower and upper current constraints is introduced and calculated from integer multiple values in $\mathbf{v}$ and for all slice indices k following

$$\mathrm{lc}_k^{(i)} = \max\left(\left\{\mathrm{x}_{k-1}^{(i)} - (N-k)\cdot\mathrm{v}^{(i)}, \mathrm{x}_{k-1}^{(i)} - (k-1)\cdot\mathrm{v}^{(i)}\right\}\right) \tag{6.5}$$

and

$$\mathrm{uc}_k^{(i)} = \min\left(\left\{\mathrm{x}_{k-1}^{(i)} + (N-k)\cdot\mathrm{v}^{(i)}, \mathrm{x}_{k-1}^{(i)} + (k-1)\cdot\mathrm{v}^{(i)}\right\}\right) \tag{6.6}$$

The final lower and upper bounds are defined as the most stringent constraints and are dictated by either the inter-slice limits with respect to the preceding slice, the inter-slice limits with respect to one of the end slices, or the power supply limits. They then follow from

$$\mathrm{lb}_k^{(i)} = \max\left(\left\{\mathrm{x}_{k-1}^{(i)} - \mathrm{v}^{(i)}, \mathrm{lc}_k^{(i)}, -\mathrm{I}_{\text{max}}^{(i)}\right\}\right) \tag{6.7}$$

and

$$\mathrm{ub}_k^{(i)} = \min\left(\left\{\mathrm{x}_{k-1}^{(i)} + \mathrm{v}^{(i)}, \mathrm{uc}_k^{(i)}, \mathrm{I}_{\text{max}}^{(i)}\right\}\right) \tag{6.8}$$

and define the solutions space boundaries for the entire dataset. They correspond to a shim current constraining *envelope*, which is illustrated in Fig. 6.2 by the red solid line.

6.3.2 Hardware

All measurements were performed on a 3T Tim Trio system using a 1Tx/8Rx-channel RF coil (Siemens Healthineers, Erlangen, Germany). The 2$^{\text{nd}}$ order spherical harmonic shim system of the scanner was extended by the 28-channel spherical harmonic shim coil insert driven by a power supply with $\pm$5 A output current per channel and a dynamic shimming unit enabling rapid shim updates with eddy current compensation up to full 4$^{\text{th}}$ and partial 5$^{\text{th}}$ and 6$^{\text{th}}$ order (Resonance Research Inc., Billerica, MA, USA).
Dynamic 1$^{\text{st}}$ order shim updates were initiated from the sequence and applied through the scanner gradient system. The gradient dynamic inter-slice shim current change was limited in the algorithm to be 10% of the channel maximum output current. Dynamic shim updates for the

Z0 and all higher order terms were triggered from the sequence and applied through the shim insert. The maximum output currents of these channels were clipped to ±4 A and the channels supplied from a common power supply sub-unit (cf. Table 4.1) were additionally constrained so as not to exceed a cumulative sum of ±8 A. Their maximum inter-slice shim current change was limited to ±0.5 A ($p^{(i)} = 0.1$), which implied that only non-negligible eddy currents from shim steps up to 0.5 A required a pre-emphasis compensation. These eddy currents were mapped as explained in Chapter 5 and compensated by adjusting the pre-emphasis modules of the dynamic shimming unit accordingly. Dynamic shim currents were updated 2 ms before slice excitation using a ramp function.

6.3.3 Data acquisition and processing parameters

The imaging protocol used to assess the achievable B_0 homogeneity included the acquisition of both static and dynamic field maps using a 2D multi-echo gradient-echo sequence with TE = [4, 5, 6, 8, 12] ms and TR = 540 ms [94]. The sequence was implemented and provided by Dr. Hoby Hetherington and colleagues and is detailed in Section 4.3.2. The field-of-view and image matrix sizes were adjusted to cover the region-of-interest in 3 mm isotropic resolution. The processing software and all graphical user interfaces were written in MATLAB R2015b (The MathWorks, Inc., Natick, MA, USA) and the minimization of Eq. 6.1 was performed using the built-in fmincon solver with the *sequential quadratic programming* algorithm. Phase unwrapping for field map calculation was done with FSL PRELUDE [163] and the region-of-interest for the in vivo measurements was restricted to the brain area which was segmented using FSL BET [162]. Phantom experiments, using a water-filled sphere, were performed to set up and calibrate the dynamic shimming hardware and to test the correct functionality of the proposed algorithm. Statically shimmed in vivo field maps were acquired and used to simulate the effects of constraining the available shim current hardware. Dynamically shimmed in vivo field maps were acquired and used to evaluate the performance of the proposed algorithm and to quantify the achievable B_0 homogeneity. All in vivo measurements were approved by the local Ethics Committee and written, informed consent was obtained from the participants accordingly.

Table of Variables	
Variable	**Meaning**
$\mathbf{A}$	System matrix of spherical harmonic field functions
$\mathbf{b}$	Measured field inhomogeneities
$\mathbf{x}$	Shim current vector, optimally chosen to minimize $\|\mathbf{Ax}-\mathbf{b}\|_2^2$
$\mathbf{x}_k$	Dynamic shim current vector for slice k, calculated with the proposed algorithm
$\mathbf{x}_k^s$	Dynamic shim current vector for slice k, calculated without any inter-slice current constraints
S_k	Solution norm based on solutions of the standard optimization algorithm ($\mathbf{x}_k^s$)
k	Slice index
N	Number of slices in the dataset
$\mathbf{lb}, \mathbf{ub}$	Lower and upper bounds for the optimization
$\mathbf{l}_{\text{max}}$	Vector of max. absolute shim currents for each channel, dictated by the power supply
$\mathbf{v}$	Vector of max. permitted absolute inter-slice shim current changes, e.g. $\pm$0.5 A
$\mathbf{p}$	Percentage of the power supply dynamic range that is used for max. inter-slice current changes
$\mathbf{lc}, \mathbf{uc}$	Vectors of lower and upper constraints, dictated by the solutions for the two end-slices
λ	Regularization parameter to control reduction of absolute current amplitudes
ϵ	Regularization parameter to control reduction of inter-slice shim current changes
$\mathbf{C}$	Linear inequality constraint matrix to limit cumulative current output of sets of shims
$\mathbf{d}$	Cumulative current constraint vector, used to limit the solution following $\mathbf{Cx} \leq \mathbf{d}$

Table 6.1: List of variables used in the proposed algorithm.

6.4 Results

The results presented in this section follow a certain argumentation in order to emphasize the applicability of the proposed dynamic shim optimization. Initially, the hypotheses regarding the feasibility of employing lower shim current amplitudes and reduced shim current variations, while still reaching near-optimal B_0 homogenization performances, are being tested in simulations for their validity. Subsequently, the proposed regularization terms are analyzed with respect to their applicability to achieving that shim current reduction. Having established and proven these necessary conditions, the performance of the proposed routine is benchmarked against the outcome of a conventional shim calculation algorithm on the basis of phantom and in vivo measurements. Finally, simulated results are presented which enable a projection of the performance of the algorithm to well-established acquisition schemes other than sequential slice-wise imaging.

6.4.1 Feasibility of limiting shim amplitudes and their temporal variation

To evaluate the impact of limiting the dynamic shim current amplitudes, simulations were performed for eight 2^{nd} order statically shimmed in vivo field maps. Standard dynamic shim solutions were calculated from Eq. 3.6 with values for the upper and lower bounds ranging from 100% to 1% of the maximum available power supply current output. The result for one dataset is illustrated in Fig. 6.3 as a plot of the residual slice-wise standard deviation as a function of the applied power supply limit. A zoomed view of the slices with highest residual B_0 inhomogeneity reveals that by reducing the limits to 25% of the maximum power supply current output, the standard deviation in the given slices increases by less than 0.5 Hz. For all analyzed datasets, the average increase in slice-wise standard deviation, as induced by decreasing the power supply limits by a factor of four, is 0.1 Hz.
To evaluate the feasibility of penalizing high inter-slice shim current changes, slice-wise shim fields were simulated for all unconstrained dynamic shimming solutions. Using this data, difference maps were calculated by subtracting the simulated field in each slice from that of every subsequent slice. Fig. 6.4 illustrates the results for one dataset and depicts the magnitude of the change in the shim fields for six representative slices. This approach approximates the actual change of the dynamic shim fields and qualitatively demonstrates that the required changes in shim current amplitude are considerably lower than the absolute amplitudes required. For the eight processed datasets, the respective maximum absolute field offset in the difference maps was determined and then averaged over all datasets. This average maximum absolute field offset, which can be seen as a measure for the required maximum inter-slice shim current change, was 34 Hz.

6.4.2 Standard vs. proposed dynamic shim optimization framework

Constraining the shim optimization, as carried out in Section 6.4.1, demonstrates that solutions for the optimization problem exist that reach similar homogeneities at lower overall current demands. To investigate the extent to which preference can be given to these solutions by applying regularization terms, simulations were conducted and the performance of a standard dynamic shim optimization was compared to the proposed routine.
Fig. 6.5 shows the average power supply usage for the eight analyzed subjects. These were derived from the non-regularized routine and from the proposed routine with different regularization weightings using the parameter values $\lambda, \epsilon = [0.001, 0.005, 0.01]$. The plots show the mean

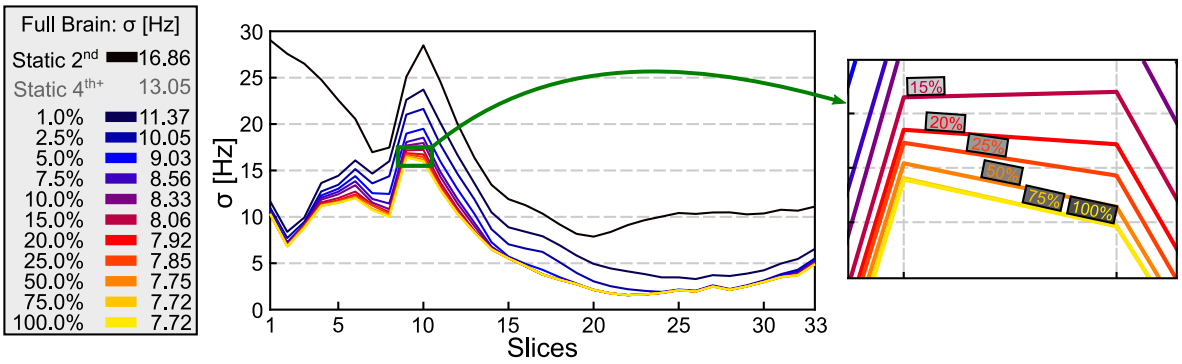

Figure 6.3: Residual slice-wise standard deviation after static shimming and after dynamic shimming with different power supply limits ranging from 100% to 1% of the channel's maximum current outputs (±5 A to ±0.05 A) [2]. It can be seen in all slices on the plot, and in the zoomed view on slices nine and ten, which reveal the highest B_0 inhomogeneity, that the standard deviation only increases slowly when cutting back large parts of the dynamic range of the power supply. It also shows, that the addition of very low-amplitude shim fields improves the B_0 homogeneity over the static case already.

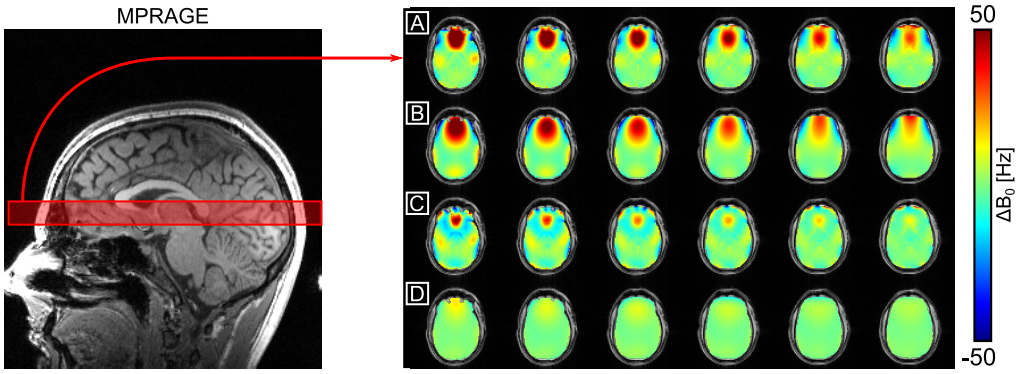

Figure 6.4: Inter-slice shim field variation illustrated for six slices through the prefrontal cortex area [2]. **(A)** The 2nd order statically shimmed field map slices show the residual B_0 inhomogeneities. **(B)** The unconstrained high-order dynamic shim fields can approximate large parts of these inhomogeneities. **(C)** The predicted shimmed slices, following from subtracting the shim fields from the field map data, show a resultant strong reduction of the residual B_0 inhomogeneities. **(D)** In contrast to the actual shim fields (2nd row), the inter-slice changes in the shim field amplitudes between consecutive slices, given by subtracting the simulated shim field in each slice from that of every subsequent slice, are low and demonstrate the applicability of inter-slice shim current constraints.

and maximum current amplitudes, as well as the mean and maximum current changes between adjacent slices for each channel of the shim insert power supply. The mean absolute current amplitudes and the mean amplitude changes were averaged for each channel over all slices and then over all datasets. The maximum absolute current amplitudes and maximum amplitude changes were determined as the respective maximum value amongst all slices. This was then averaged over all datasets. While all plots show a significant reduction for all regularization weightings, the strongest relative reduction is achieved for the maximum inter-slice current changes, which is also the dominant eddy current-generating parameter. The average whole-brain standard deviation, obtained when applying the given solutions, was determined as 8.10 Hz (unconstrained) versus 8.29 Hz ($\lambda, \epsilon = 0.001$), 8.54 Hz ($\lambda, \epsilon = 0.005$) and 8.76 Hz ($\lambda, \epsilon = 0.01$), as compared to 17.14 Hz for the static case. Depending on the chosen regularization parameter value, the slight degradation in whole-brain standard deviation for the regularized versus the standard optimization comes with the advantage of an average 6.3-, 14.2- or even 23.0-fold

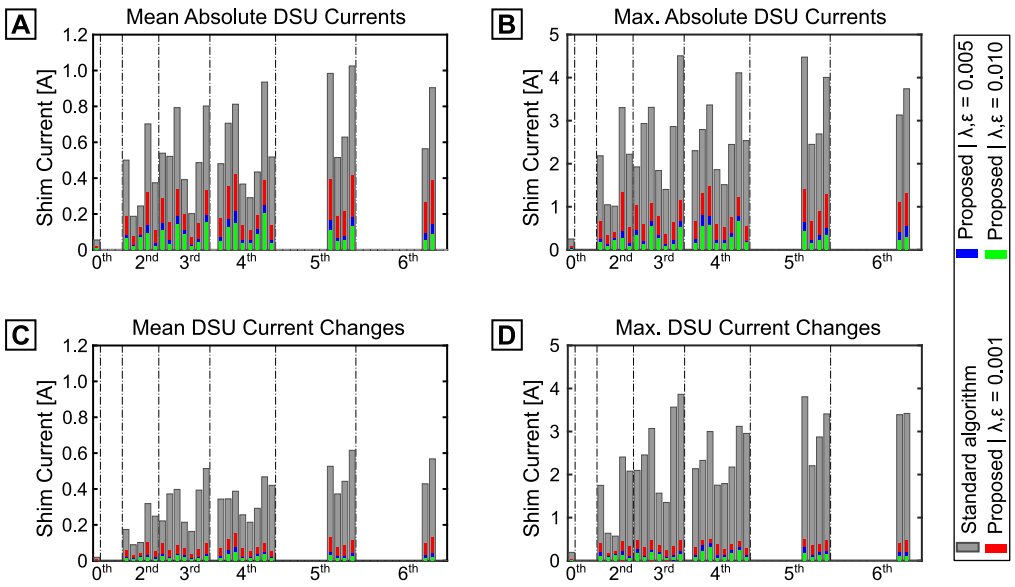

Figure 6.5: Shim current amplitude evaluation for simulated solutions obtained from and averaged over eight in vivo datasets [2]. The current values are shown for the channels of the different spherical harmonic orders of the shim insert. (**A**) Mean absolute dynamic shim current amplitude of each channel, averaged over all slices and then over all datasets. (**B**) Highest absolute dynamic shim current amplitude of each channel, calculated as the maximum absolute current amongst all slices, which was then averaged over all datasets. (**C**) Mean absolute dynamic shim current difference between adjacent slices for each channel, averaged over all slices and then over all datasets. (**D**) Highest absolute dynamic shim current difference between adjacent slices for each channel, calculated as the maximum absolute dynamic shim current difference amongst all slices, which was then averaged over all datasets.

reduction in the maximum dynamic shim current change, and a 4.2-, 11.4- or 18.2-fold reduction of the mean dynamic shim current change.
Fig. 6.6 A visualizes the difference in temporal shim current variation between the solutions derived from the standard approach versus the proposed algorithm, with a regularization weighting of $\lambda, \epsilon = 0.01$. The shim current amplitudes from the given subject are plotted for one representative term from each spherical harmonic shim order greater than $n = 1$. It can be seen that the proposed routine reduces the absolute current amplitudes and imposes a smoothness on the temporal variation, thus supporting the findings displayed in Fig. 6.5.
Additionally, Fig. 6.6 B shows simulated field maps and illustrates how the regularized solutions can be used to improve the field homogeneity over the 2nd order static case. The majority of the field homogenization capabilities and the most significant improvements over the static solution are already provided by a very stringent regularization weightings of $\lambda, \epsilon = 0.01$. Barely any difference can be seen to the unconstrained solutions.

6.4.3 Phantom experiments

A phantom experiment was performed to test the pre-emphasis adjustments and the accuracy of the applied dynamic shim fields. A 2nd order statically shimmed, in vivo field map was acquired and a high order dynamic shim solution with $\lambda, \epsilon = 0.01$ was calculated. The slice locations of the in vivo data were copied and the calculated dynamic shim currents were applied in a phantom. The subtraction of a static phantom field map from the acquired dynamic phantom field map yielded the effectively applied dynamic shim fields as determined for the in vivo shim set and

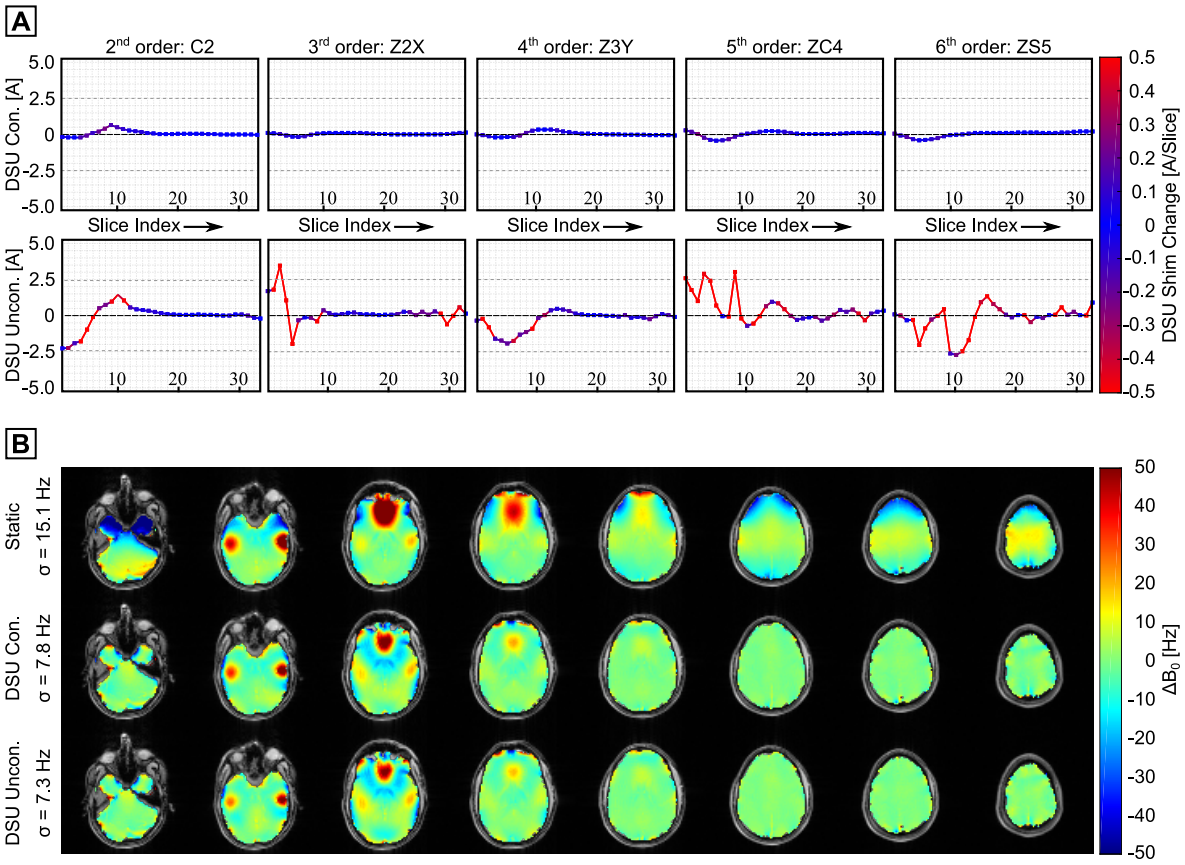

Figure 6.6: Comparison between the results obtained from a standard dynamic shim optimization versus the proposed routine with $\lambda, \epsilon = 0.01$ [2]. **(A)** Temporal shim current variation derived from the proposed routine (top row) and from the standard routine (bottom row) shown for one representative term of each spherical harmonic shim order greater than $n = 1$. The magnitude of the change in shim current is color-coded. **(B)** Acquired 2nd order static field map slices and predicted dynamically shimmed field map slices for the proposed routine and for the unconstrained case. The regularized solution shows a significant improvement over the static shim solution and only minor differences exist to the unconstrained solution. For display purposes only every fourth slice of the dataset is shown.

allowed a comparison to the predicted shim fields without any subject influences.
The results for three neighboring slices from three different brain regions are illustrated in Fig. 6.7 and demonstrate the match between the predicted and acquired shim fields. Despite the applied regularization terms and the added constraints, versatile field shaping capabilities, as provided by the shim set, can be seen from the maps.

6.4.4 In vivo experiments

Unshimmed field maps, followed by 2nd order whole-brain statically shimmed field maps, were acquired from three volunteers. These were then used in the proposed dynamic shim optimization process with $\lambda, \epsilon = 0.01$ and the results were applied to acquire dynamically shimmed field maps. The static and dynamic shim calculation was performed with the fully-automated custom shim software and the resulting field maps were acquired non-iteratively.
Fig. 6.8 illustrates the results of one dataset and shows the homogeneity gain provided by the dynamic shim. The sagittal views show the elimination of residual B_0 inhomogeneities in large

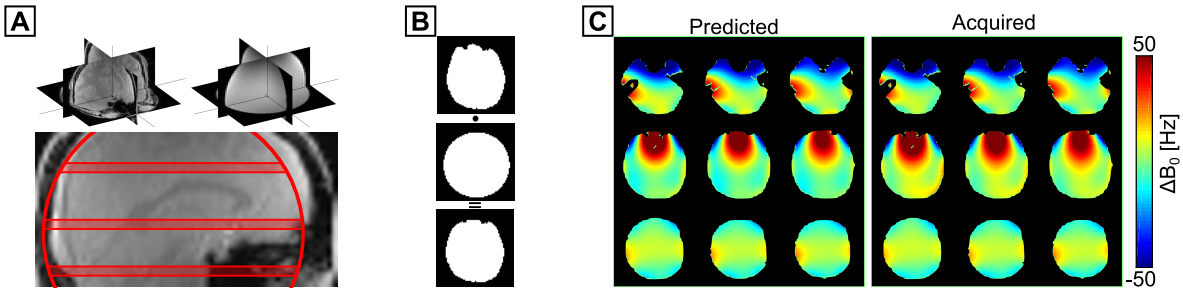

Figure 6.7: Dynamic shimming phantom results [2]. **(A)** Dynamic shim currents were calculated from an in vivo dataset and applied in a measurement using a spherical water phantom. The magnitude images of both datasets show their volumetric overlap. **(B)** A common region-of-interest is generated from both datasets and used to mask the in vivo and phantom images for better comparison. **(C)** Examples of three representative neighboring slices from the three different brain regions, which are marked on the sagittal magnitude image, show the match between the predicted shim field for the brain slices and the real shim fields as measured in the phantom.

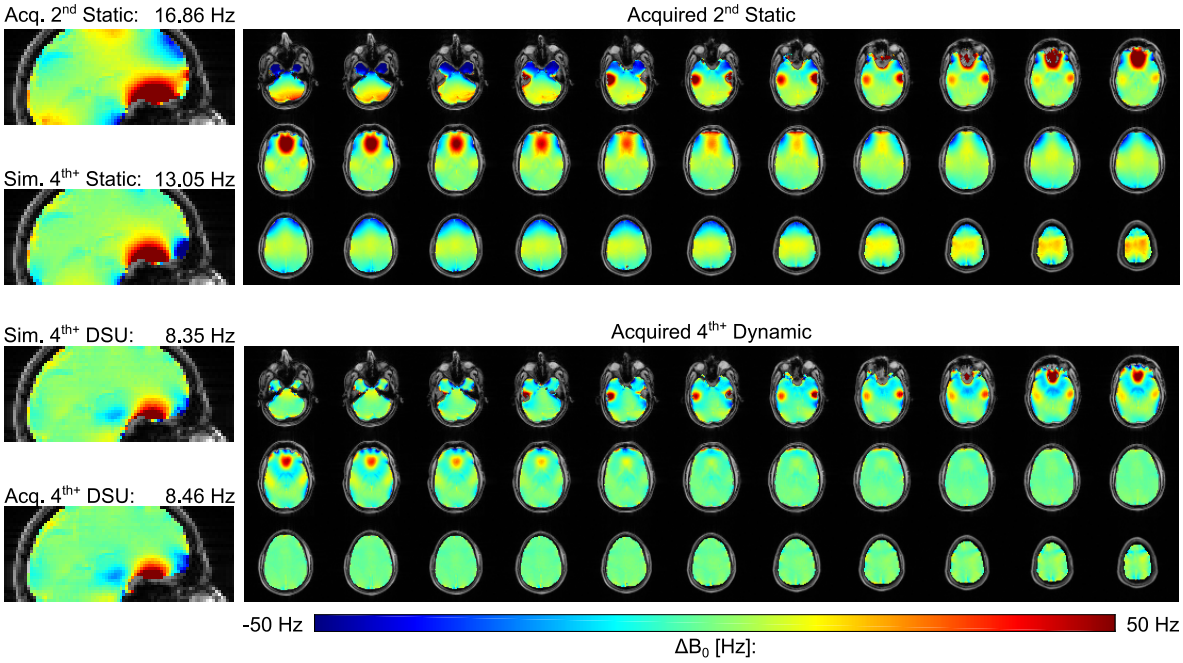

Figure 6.8: High-order dynamic in vivo shimming [2]. The sagittal views show the B_0 inhomogeneity distribution after measured static 2^{nd} order shimming and simulated static 4^{th+} order shimming. Moreover, the match between the simulated and the acquired high-order dynamic shimming field maps can be seen from the sagittal views. The homogeneity improvements when switching the high order shims dynamically can be seen from the comparison between the acquired 2^{nd} order static and the acquired 4^{th+} order dynamic axial field map slices.

parts of the brain and a strong reduction of the most prominent offsets in the prefrontal cortex area. A simulated 4^{th+} static shim solution is shown for comparison, allowing to estimate the gain provided by switching the shim set dynamically instead of statically.
Dynamic shimming results from all three subjects are summarized in Fig. 6.9. The slice-wise standard deviation of the residual B_0 inhomogeneity is plotted for the static and the dynamic field mapping results and is in agreement with the simulations from Section 6.4.2 using the same regularization parameters. To further quantitatively demonstrate that the number of high-offset voxels can be reduced through the addition of dynamic shimming, the 90^{th}-percentile-range plots

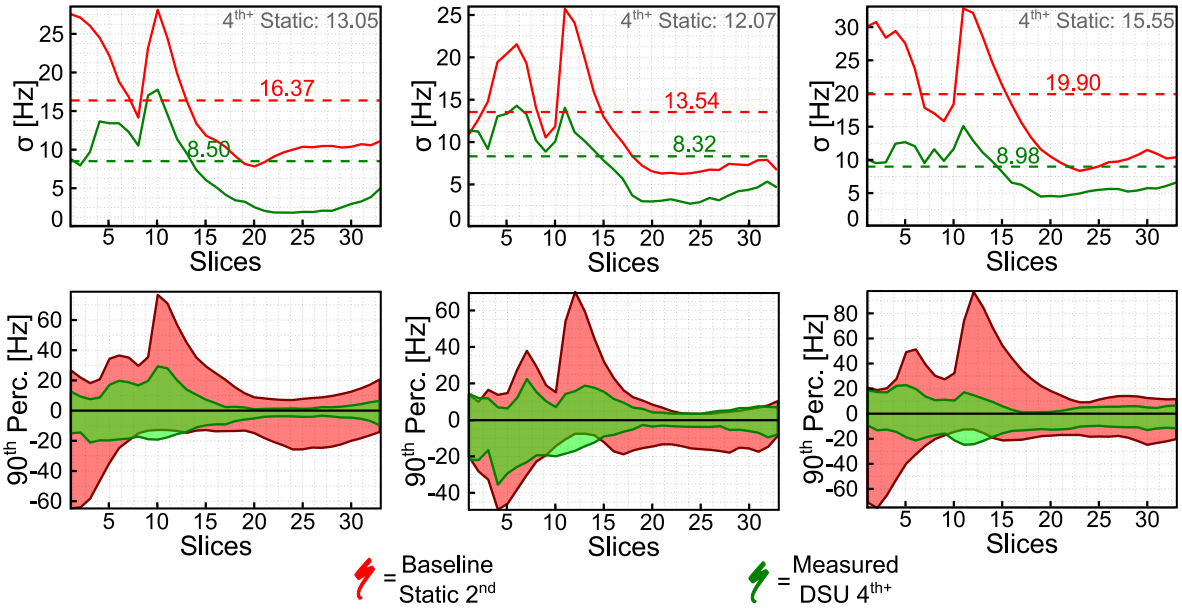

Figure 6.9: Dynamic shimming results from three subjects [2]. For each dataset, the slice-wise residual standard deviation is given alongside with the whole-brain standard deviation for the acquired 2nd order static, the acquired 4th+ order dynamic and a simulated 4th+ order static shim. The 90th percentile range plots delineate the frequency range that 90% of all field map voxels lie within and proves that the number of very high offset voxels can be substantially reduced with added high-order dynamic shimming.

indicate for each slice the frequency offset range that 90% of all voxels lie within.
To demonstrate the improved homogeneity in all brain regions, a full dataset from one subject is depicted in Fig. 6.10 and shows a comparison between the acquired 2nd order static and 4th+ order dynamic field maps.

6.4.5 Extension to other acquisition strategies

The analyses so far assumed sequential acquisition strategies. Many multi-slice MR imaging applications, however, employ different slice-ordering schemes, such as slice-interleaving or simultaneous multi-slice imaging. Slice-interleaving increases the distance between consecutively fitted slices and introduces a discontinuity between the last odd and the first even slice. Simultaneous multi-slice imaging requires sets of distant slices to be jointly optimized. Since the acquisition order is critical for the proposed inter-slice current constraints, both scenarios were evaluated in simulations.
For a comprehensive comparison, four acquisition strategies for spherical harmonic B_0 shimming were analyzed: Dynamic shimming for sequential acquisition modes was simulated for increasing spherical harmonic shim orders. Additionally, 4th+ order results for slice-interleaved dynamic shimming acquisitions and for simultaneous multi-slice acquisitions with acceleration factors 2, 3, 4 and 6 were simulated. To be able to set all results into context with the achievable B_0 homogeneity for conventional B_0 shimming, 2nd, 3rd and 4th+ order static shim solutions were calculated. In Fig. 6.11, the average whole-brain standard deviations from three subjects for each of these acquisition strategies are displayed.
The static and sequential dynamic shimming results show an expected B_0 homogeneity improvement when including higher shim orders. The altered slice acquisition orders for the interleaved

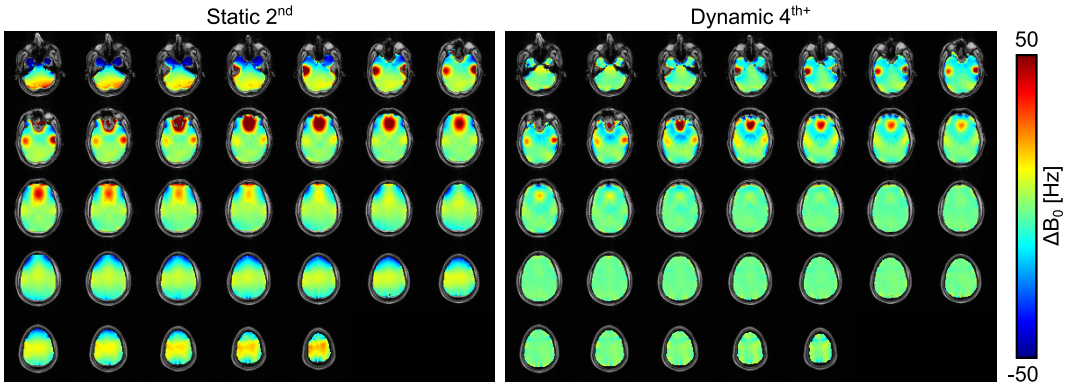

Figure 6.10: Static vs. dynamic B_0 field maps of all slices from one subject. The maps show the benefits and the limitations of the high order dynamic shim approach. Irrespective of the applied regularization, the full potential of the high-order shim set could be exploited to significantly improve the data quality when being compared to the static equivalent. Residual inhomogeneities in most parts of the brain could be eliminated or suppressed to a level that is sufficient for most MR applications. However, although the characteristic inhomogeneities in the frontal and temporal lobes could be reduced, they could not be eliminated.

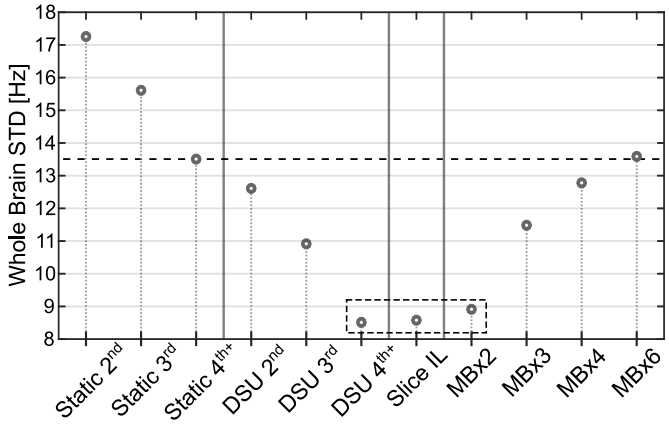

Figure 6.11: Comparison of the effectiveness of spherical harmonic shimming applied to different acquisition schemes [2]. The plot shows the simulated whole-brain standard deviation averaged over three subjects when applying static, sequential dynamic, interleaved dynamic or simultaneous multi-slice dynamic shimming. Conventional static whole-brain shimming improves according to expectations with the order of the included spherical harmonics. The same holds true for dynamic shimming in sequential slice acquisition mode. Furthermore, the plot indicates that the proposed algorithm can equally well be applied to slice interleaved acquisitions (Slice-IL). The simultaneous multi-slice dynamic shim setting for a two-fold acceleration is comparable to the single-slice dynamic shim solution and converges towards the static solution of the applied shim set for increasing accelerations. The dashed line indicates the achievable whole brain standard deviation when using the 4^{th+} order shim set in static mode. The dashed box highlights the comparable B_0 homogenization performance for sequential, slice-interleaved and simultaneous multi-slice acquisitions of equal shim order.

and for the multiband acquisition schemes entail an increase in achievable B_0 homogeneity of 0.07 Hz (interleaved) and 0.40 Hz (simultaneous multi-slice), respectively. Merely when increasing the multiband acceleration, the degradation in achievable B_0 homogeneity becomes more noticeable and converges towards a corresponding static solution. However, this degradation in shim quality is attributed to the requirement to optimize the shim over more regions simultaneously, rather than the applied current constraints.

6.5 Discussion and conclusions

In this work, high-order dynamic shimming hardware was installed and calibrated and the required acquisition and processing software was implemented. Resulting B_0 shimming improvements were analyzed in simulations and validated in phantom and in vivo measurements. The novel shim optimization framework has proven to substantially reduce the shim amplitudes and their temporal variation, and thus provides the means for better control over shim induced eddy currents. The simulations for the slice-interleaved and the simultaneous multi-slice acquisition schemes indicate that an extension to these more prevalent acquisition types is possible and introduces no significant loss in achievable B_0 homogeneity. Both, the simulated and acquired results for the sequential acquisitions strategies as well as the simulated results for these alternative acquisition strategies are in accordance with simulated dynamic shimming performance reported in the literature [40] and show an approximate two-fold homogeneity gain, as compared to standard static 2^{nd} order spherical harmonic shimming. It is shown that the loss in achievable B_0 homogeneity, as introduced by the applied constraints and regularization terms, is negligibly small and outweighed by the benefits of superior eddy current handling, lower dynamic shimming hardware requirements and an increased accuracy of the shim simulations. As a result, the addition of dynamic shimming capabilities to existing static shimming routines is facilitated and has the potential to make its application in 2D multi-slice or 3D slab acquisitions more readily available.

Since the dynamic shimming-specific problems are coupled and additive, the benefits of the proposed solution are manifold and have a cascading effect. The average six- to 23-fold reduction of the maximally occurring shim steps, as induced by the three different regularization weightings chosen in this work, directly translates into a reduction of the maximum eddy currents by the same amount. Additionally, in all the dynamic shimming volumes for which the regularization parameter ϵ is chosen too conservatively, the added box constraints will still guarantee that the current steps do not exceed the user-selected inter-slice current limit. As a result of both eddy current handling strategies, the number of channels that still require a pre-emphasis correction can be potentially decreased and counteract the projected eddy current compensation calibration effort for very high order dynamic shimming systems [103]. When shim current steps were limited to 0.5 A in magnitude, the shim system used in this work required a pre-emphasis correction for only five channels. Furthermore, since the maximum occurring current steps are dictated by the applied box constraints, and are consequently known beforehand, saving large parts of the dynamic range of the power supply for arbitrarily large pre-emphasis overshoots is no longer required. Moreover, because residual eddy currents after pre-emphasis correction scale with the applied shim step, it follows that when targeting equal eddy current suppression levels as in standard dynamic shim updating implementations, the pre-emphasis adjustments are more robust to calibration inaccuracies.

By additionally regularizing the amplitudes of the absolute shim currents and controlling their impact by the parameter λ, the ill-posedness of the optimization problem is intrinsically addressed in a similar way as shown in [89]. Furthermore, a shim degeneracy analysis [74] or the exclusion of certain spherical harmonic shim terms [101] is no longer needed. In contrast to the notion that optimal B_0 homogeneity for dynamically shimmed multi-slice applications can only be achieved by high-power shim supplies [176], the presented results indicate that an equally good shim performance can be achieved at substantially lower current amplitudes. Another direct effect is that the calculated currents will be closer to the current regime that can be covered in the static shim calibration procedure, thus making the simulations more accurate. Also, it is to be

noted that high current amplitudes are only penalized and not suppressed. This assures that the valuable shim currents that contribute significantly to canceling residual inhomogeneities are accepted and only those with marginal improvements are omitted.
In addition to the implementation of data sharing between adjacent dynamic shim volumes, which is achieved by fitting stacks of three slices in a moving boxcar mode, the use of previous slice-solutions as an initial guess for current iterations supports the regularization terms and helps the algorithm in finding solutions with smooth current variations. This is also true at the transition between the end-slices, and despite the application of a joint optimization framework to calculate the solutions for these slices simultaneously, no noticeable degradation in the achievable shim quality was found.
The high order shim insert used in this work is of a smaller diameter than the scanner shim coils and thus has a larger distance to the cryoshield and other eddy currents surfaces of the MR scanner. It is to be expected that this setup is, therefore, intrinsically less prone to generating eddy currents than the scanner's in-built shim coils. However, it can be stated that when switching the larger host shims dynamically, the proposed routine is likely to be even more beneficial.
For the proof-of-principle and the results obtained for this work, no regularization parameter optimization of λ and ϵ was performed and this leaves room for improvements. Moreover, since the higher order spherical harmonic shim coils become increasingly less efficient, the regularization weighting can be individually adapted for each channel. The same holds true for the maximum inter-slice shim current steps, which can be less restrictive for the higher order terms. In general, the regularization terms and the constraints can be re-formulated to be based on the given coil efficiencies, rather than on the applied currents. Furthermore, it can be investigated to what extent similar results with respect to the shim current reduction can be achieved when optimizing all slice solutions simultaneously and including the current variation into the optimization problem as a further parameter to be minimized.
In summary, it can be stated that dynamic shimming for 2D multi-slice applications makes optimal use of the available shim hardware. The added benefits of the proposed optimization framework facilitates its successful implementation and allows its incorporation into future studies. It was shown that the remaining inhomogeneities are not caused by the introduced constraints and regularization terms, but rather they are beyond the field shaping capabilities of the shim set. To date, none of the existing shimming techniques can fully mitigate all B_0 inhomogeneities. This is true for 2D approaches, and even more so for 3D and multi-band applications. Consequently, future work will concentrate on further hardware developments that are capable of more accurately approximating the complex B_0 inhomogeneities induced by the subject-dependent susceptibility distributions.

7

Generalized dynamic shim current optimization

In Chapter 4, the implementation of a conventional static B_0 shimming framework was described and results from simulations as well as phantom and in vivo experiments were presented. Based on this, an improved B_0 shim performance was demonstrated to be achievable with the dynamic shimming routine presented in Chapter 6. The required eddy current compensation techniques, which enable the transition from the static to the dynamic shim adjustments, were detailed in Chapter 5.

A key finding of this work was, that the dynamic shim current amplitudes and their temporal variation can be reduced compared to those derived from standard dynamic shim optimizations, while negligibly compromising B_0 homogenization performance. This has multiple implications, including lower hardware demands and more accurate shim simulations. Most importantly, however, it intrinsically reduces potential shim-induced eddy currents.

The previously introduced inter-slice shim current change constraining algorithm is based on a conventional dynamic shim optimization, in which the individual volumes are processed consecutively and independently from each other. The added functionality provides means to regularize the optimization and to dynamically adjust the optimization constraints. That way, the resultant shim amplitudes and their temporal variations are reduced and in extreme cases limited to a user-defined threshold.

In this chapter, the idea of reducing the inter-slice shim current changes is being generalized and formulated as a dedicated minimization problem. In terms of the objective and the results it is, therefore, similar to the routine presented in the previous chapter. However, the maximum shim current amplitude variations are more effectively reduced. Moreover, the optimization function is more elegantly formulated, easier to implement and dependencies on regularization parameter optimizations are largely removed.

Thus, this chapter completes the methodological developments of this thesis by taking up and optimizing the successful concept of calculating shim currents which not only effectively homogenize the static magnetic field, but which also have additional desired properties. Simulations are shown, which demonstrate the applicability of this generalized framework for dynamically shimmed whole-brain MR applications.

7.1 Introduction

Dynamic shimming makes the most efficient use of an available B_0 shim set on a given MR system. Guided by a certain data acquisition mode, the B_0 field homogeneity is individually optimized over multiple sub-volumes and the associated shim settings are effectuated at sequence runtime. The dynamic shim current optimizations are almost exclusively implemented such as to provide for the best possible B_0 field homogeneity within a specified target volume. B_0 field inhomogeneity in remote regions is sometimes also considered, for example in order to control the maximum field variation in regions adjacent to the target volume [92]. In this context, a multitude of B_0 shim optimization techniques and algorithms have been developed using a variety of robust and fast solvers [95]. However, the resultant current amplitudes are always entirely driven by the input B_0 field map data.
For static shim approaches, regularizations [89] and constraints [88] have been suggested to reduce the absolute shim current amplitudes. Apart from the inclusion of hardware limitations, similar implementations have not been suggested for dynamic shim optimization routines. This is in large parts due to the widely held belief, that strong shim power supplies and their full usage are indispensable for efficient dynamic shimming, at least when using spherical harmonic shim systems [176]. Therefore, within the optimization space dictated by the power supply specifications, dynamic B_0 shim optimization algorithms are virtually unconstrained and entirely driven by the acquired data. However, it can be shown, that significantly different solutions in terms of the individual shim current amplitudes can be determined, while having marginal impact on the resultant optimal B_0 field distribution. This insight opens up new possibilities in the design of shim current optimization routines and allows to impose desired properties on the solutions.
In the work presented in the previous chapter, this was exploited to limit the dynamic shim current amplitudes and their temporal variation. Starting from a solution for a given 2D slice, the shim currents for all other slices were sequentially calculated using dynamically adapted optimization constraints. This enables the calculation of solutions with significantly lower current demands at almost no losses in achievable B_0 homogeneity.
In this chapter, the idea of the inter-slice shim current change constrained optimization has been generalized and re-written into a comprehensive optimization framework. The objective function of the optimization has been formulated, such as to directly minimize the current changes. Thus, compared to conventional shim optimizations, which optimize the field and eventually include current constraints in a side condition, the shim current amplitudes are now directly subjected to the minimization. Using a set of in vivo B_0 field maps, it is shown in simulations that this achieves a significant shim current change reduction.

7.2 Theory

Conventional dynamic shim optimizations determine optimal shim settings by processing a number of N_{Vol} sub-volumes consecutively and independently from each other. In this context, let $\mathbf{b}_k$ denote the field map data in the region-of-interest of sub-volume k. Moreover, let $\mathbf{A}_k$ denote the spherical harmonic system matrix describing the shim fields of all N_{SH} included shim channels at the corresponding coordinates. A conventional shim optimization algorithm then seeks to find an optimal parameter vector, $\mathbf{x}_k$, for all $k \in \{1, \ldots, N_{\mathrm{Vol}}\}$, which corresponds to the best possible shim setting in the respective sub-volume.
Thus, when writing all system matrices as a block-diagonal matrix $\mathbf{A} = \mathrm{diag}(\mathbf{A}_1, \mathbf{A}_2, \ldots, \mathbf{A}_{N_{\mathrm{Vol}}})$ and the shim solution as well as the field map data of each sub-volume as $\mathbf{x} = [\mathbf{x}_1; \mathbf{x}_2; \ldots; \mathbf{x}_{N_{\mathrm{Vol}}}]$ and $\mathbf{b} = [\mathbf{b}_1; \mathbf{b}_2; \ldots; \mathbf{b}_{N_{\mathrm{Vol}}}]$, respectively, it is the objective to minimize $\|\mathbf{A}\mathbf{x} - \mathbf{b}\|^2$. Despite this unified problem formulation, the solution of each processed slice is decoupled and, thus, a desired reduction of the inter-slice shim current differences is not achieved in this standard form. However, by extending the objective function, the individual solutions can be coupled and the temporal variation of the shim current amplitudes can be minimized.
Let $N_{\mathrm{D}} = N_{\mathrm{Vol}} \cdot N_{\mathrm{SH}}$ denote the number of shim current differences between the shim values of all adjacent sub-volumes and all employed shim channels, i.e. the total number of shim changes that occur during the acquisition of the entire volume. Moreover, let $\mathbf{C}$ denote a matrix of size $N_{\mathrm{D}} \times N_{\mathrm{D}}$, which yields these differences via multiplication with $\mathbf{x}$. The unified and extended optimization problem given by

$$\min_{\mathrm{x}} \quad \left\| \begin{pmatrix} \mathbf{A} \\ \lambda \mathbf{C} \end{pmatrix} \mathbf{x} - \begin{pmatrix} \mathbf{b} \\ \mathbf{0} \end{pmatrix} \right\|^2 \tag{7.1}$$

is suited to calculate optimal shim currents for each sub-volume while simultaneously minimizing the temporal variation of the shim current amplitudes. The regularization parameter, λ, is required to weight the field approximation against the amount of current change reduction.
It follows that too large values for λ overemphasize the current change reductions and lead to an unsatisfactory B_0 field homogenization performance. On the other side, too small values for λ fail in achieving a desired reduction of the shim current variation. To avoid an associated regularization parameter optimization, an iterative approach based on Bregman-updates [170] was employed in this work to dynamically balance the data and the current-limiting terms. The exact implementation is described in the following.

7.3 Methods

The main functionality of the implemented dynamic shim current optimization is described in Algorithm 1 below. Besides the objective function given by Eq. 7.1, two further side conditions are included in the minimization. Similarly as described in Chapter 6, an optional maximum permitted change in shim current amplitude is implemented. This enables the inclusion of threshold values, for which a previously performed eddy current compensation implementation was considered effective. These hard constraints are described by the column-vector $\mathbf{\Delta} \in \mathbb{R}^{2N_D \times 1}$. Moreover, the maximum power supply output currents are acknowledged via the lower and upper current amplitude constraints $\mathbf{lb}, \mathbf{ub} \in \mathbb{R}^{N_D \times 1}$.
Through choice of an excessively high value for λ, it is ascertained, that the current amplitude reductions are initially overemphasized. The application of the given update condition of the data vector is then used to iteratively increase the impact of the data term. Thus, in the sequence of the update iterations, a balance between the data fidelity and the side conditions is gradually achieved. During each iteration, the predicted standard deviation of the residual B_0 field inhomogeneities is calculated for each sub-volume and compared to the standard deviations derived from a conventional dynamic shim current optimization. The difference between the standard deviation values for the current iteration and those of the conventional routine serves as a quality measure, $\Delta\sigma^{(k)}$, which indicates whether or not the current regularized solution is close to the optimal solution. If the difference in standard deviation in all sub-volumes falls below a certain threshold (σ_{min}), or if a maximum number of iterations (k_{max}) has been reached, the algorithm stops and outputs the current solution for $\mathbf{x}$. This shim current optimization was implemented in Matlab using *CVX*, a package for specifying and solving convex programs [177].

Data: Field map data $\mathbf{b}$, system matrix $\mathbf{A}$, max. permitted inter-slice shim difference $\mathbf{\Delta}$, power supply limits $\mathbf{lb}$ and $\mathbf{ub}$, data fidelity σ_{min}, regularization parameter λ and max. number of iterations k_{max}
Result: Slice-optimized dynamic shim currents $\mathbf{x}$
Initialize: $k = 0, \mathbf{b}^{(k)} = \mathbf{b}$
while $k < k_{max}$ **do**

$$\min_{\mathbf{x}} \quad \left\| \begin{pmatrix} \mathbf{A} \\ \lambda\mathbf{C} \end{pmatrix} \mathbf{x}^{(k)} - \begin{pmatrix} \mathbf{b}^{(k)} \\ \mathbf{0} \end{pmatrix} \right\|^2$$

$$\text{s.t.} \quad \begin{pmatrix} \mathbf{C} \\ -\mathbf{C} \end{pmatrix} \mathbf{x}^{(k)} \leq \mathbf{\Delta}$$

$$\mathbf{lb} \leq \mathbf{x}^{(k)} \leq \mathbf{ub}.$$

Compute $\Delta\sigma^{(k)}$
if $\Delta\sigma^{(k)} < \sigma_{min}$ **then**
Exit
else
$\mathbf{b}^{(k+1)} = \mathbf{b}^{(k)} - \left(\mathbf{A}\mathbf{x}^{(k)} - \mathbf{b}\right)$
end
end

Algorithm 1: Shim current optimization algorithm used to minimize the temporal variation of the dynamic shim current amplitudes.

7.4 Results

The acquired in vivo datasets of the dynamic B_0 shimming measurements described in Chapter 6 were re-processed using the previously described optimization algorithm. In order to retain comparability, the same hardware setup was simulated by using identical shim calibration result matrices. The slice-wise standard deviation threshold value in Algorithm 1 was chosen as $\sigma_{\text{min}} = 1\,\text{Hz}$ and the maximum number of Bregman-updates was set to $k_{\text{max}} = 4$. The regularization parameter value was set to $\lambda = 0.25$ and the maximum permitted inter-slice shim current difference was clipped at $\boldsymbol{\Delta} = 0.3$ A for all channels of the shim coil insert. The 1^{st} order terms of the 3 T host scanner system were virtually unconstrained due to their strong power supplies and the active shielding.

The achievable whole-brain standard deviation, averaged over all processed datasets, is shown in Fig. 7.1 A. The baseline homogeneity of the 2^{nd} order static shim solution was 17.27 ± 2.62 Hz and is given as a reference. An unconstrained shim optimization achieves an optimal whole-brain homogeneity of 7.98 ± 0.75 Hz. In contrast, the application of the optimization algorithm detailed in the previous chapter results into a homogeneity of 8.63 ± 0.85 Hz as compared to 8.55 ± 0.81 Hz using the joint minimization proposed in this work. In all cases, the dynamic shim optimization was performed by fitting the data in a moving boxcar mode over a stack of three slices. In terms of the B_0 shim performance, it is found that all three dynamic shim solutions produce near-identical results, for which the remaining differences are negligibly small.

This is confirmed by the predicted dynamically shimmed B_0 field map data shown in Fig. 7.1 B. For each of the three subjects, a representative field map slice is shown and depicts the B_0 field distribution for three different shim conditions. It demonstrates the homogeneity gains in an inferior, a central and a superior slice. In all cases, the expected improve in B_0 field homogeneity is seen for the high-order dynamic versus the 2^{nd} order static case. Amongst the individual dynamic shim solutions, only minor differences can be seen, thus confirming the aforementioned whole-brain standard deviation results.

While the dynamic shim optimizations are equally effective in their B_0 field homogenization performance, there are major differences in terms of the shim current amplitudes and their temporal variation. Fig. 7.2 illustrates the mean and the maximum dynamic shim current changes for all employed channels of the very high-order shim insert. The values are averaged over all datasets and, thus, correspond to shim current plots that are also shown in Fig. 6.5 in the previous chapter. Therefore, the excessively high current amplitude changes for the unconstrained case are not shown again, which better emphasizes the differences between both current-limiting approaches. It can be seen, that the application of both algorithms reduce the mean shim current changes equally effective. The direct minimization proposed in this chapter merely results into minor improvements. However, the average maximum shim current changes are further reduced, resulting into an overall improvement by a factor of two. Moreover, the algorithm still performed well using the user-defined maximum permitted inter-slice shim current difference of 0.3 A, whereas the constrained algorithm in the previous work required a more relaxed constraint of 0.5 A. The maximum shim current change was even below that limit and occurred in the Z2C2-shim with a value of only 0.21 A.

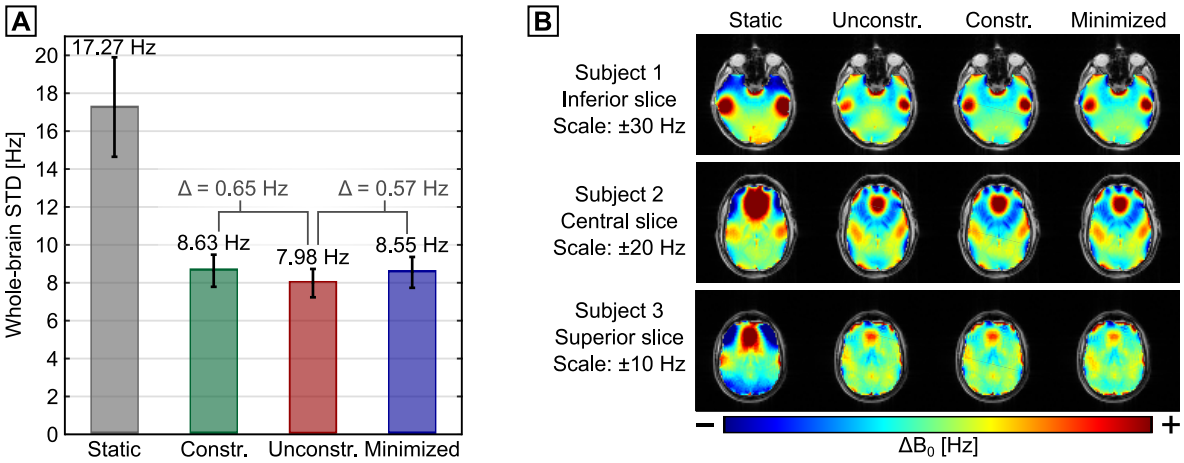

Figure 7.1: Static and dynamic shim simulation results. **(A)** The average whole-brain standard deviation values demonstrate the performance gains of a conventional very high-order dynamic shim solution (Unconstr.) over the 2^{nd} order static baseline case. The constrained algorithm detailed in the previous chapter (Constr.) as well as the algorithm which directly minimizes the temporal shim current variation (Minimized) achieve near-identical B_0 homogeneites. This is confirmed by the B_0 field map data shown in **(B)**. Representative slices from three different brain regions demonstrate the achievable B_0 homogeneity improvements and the negligible losses induced by the current-limiting operations. Note that the scaling of the images was adapted to better illustrate the homogeneity improvements in the different brain regions.

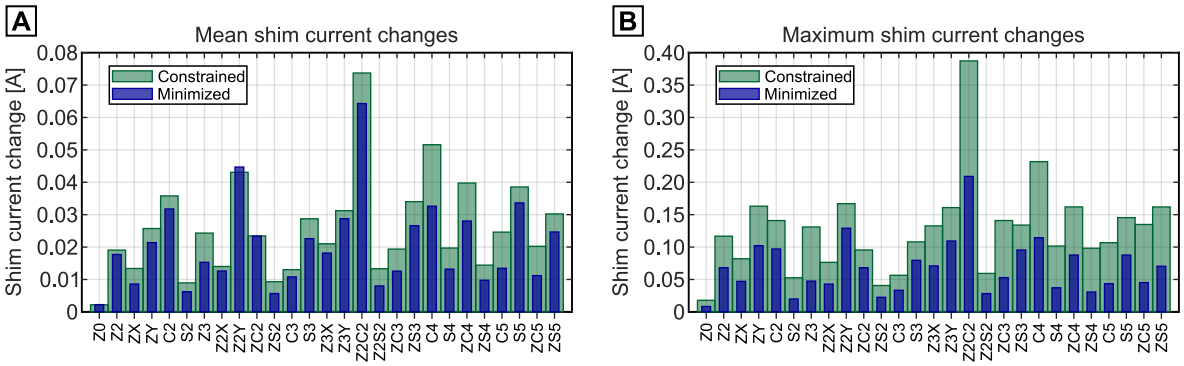

Figure 7.2: Shim current amplitude evaluation for simulated solutions obtained from and averaged over three in vivo datasets. **(A)** The mean shim current changes correspond to only a tiny fraction of what would theoretically be possible using the given ±5 A shim power supply. The values indicate that overall, both algorithm work equally well. **(B)** The associated maximum shim current changes can more effectively be reduced using the minimization technique presented in this work. An average two-fold decrease in the maximum shim current change corresponds theoretically to a reduction of any uncompensated eddy current term by the same amount.
For both measures, the values are significantly lower than for solutions obtained using an unconstrained algorithm. For better readability, these solutions are not plotted again, but can be seen in Fig. 6.5.

7.5 Discussion and conclusions

The improvement of dynamic shim optimization techniques was a central part of this thesis. The focus was on the determination of well-suited shim fields, while simultaneously optimizing the shim current amplitudes with respect to certain desired properties. In conclusion, both projects that were conducted in that regard within the scope of this work demonstrate, that still a near-optimal B_0 field homogeneity can be established when using a current-change limiting approach instead of a conventional optimization routine. Consequently, highly favorable results in terms of the shim power supply workload can be determined, simply by imposing these properties on the solution in a suitable numerical optimization framework. The most important advantage is a significant reduction of potential shim-induced eddy currents.

Both presented shim current optimization algorithms pursue different current-limiting approaches. Whereas the method presented in Chapter 6 reduces the shim current variation via side conditions, the present technique generalizes this idea and minimizes this measure directly. This has multiple advantages for both, the implementation of the algorithm as well as the associated shim current results.

In general, the implementation overhead for the algorithm presented in this chapter is significantly lower than for the constrained algorithm. For example, the shim optimization is no longer divided into three consecutive processing steps. Instead, the shim values are simultaneously optimized for all sub-volumes at once. Thus, in contrast to the previous constrained algorithm, an initial step in which the shim solutions for the end-slices are jointly calculated is no longer required. Consequently, the shim constraining *envelope* of lower and upper current constraints, which is for example visualized in Fig. 6.2, becomes obsolete. This implicates, that the sub-volumes have equal degrees-of-freedom for the calculation of the individual slice solutions and the final result corresponds to a best possible compromise between all of them. As a result, the maximum shim current changes are further decreased, resulting into an average two-fold reduction for the channels of the high-order shim insert.

Whereas the previous constrained algorithm required the adjustment of two regularization parameters, the direct minimization is merely based on one parameter, which balances the data and the regularization terms. Moreover, the choice of a solution approach which is based on Bregman-updates is less sensitive to an exact tuning of that variable parameter. The choice of the optimization variables given in Section 7.4 were found to robustly converge to the desired shim solutions while effectively reducing the temporal shim current variations.

In conclusion, the extension of the objective function to additionally optimize certain desired properties of the shim solution is very well-suited to improve dynamic shimming implementations. The negligibly small losses in achievable B_0 field homogeneity are outweighed by the added benefits of significantly reduced dynamic shim variations. Consequently, the proposed method facilitates dynamic shimming implementations and reduces the vulnerability to introducing temporal shim instabilities.

8

Summary and outlook

The Larmor equation describes the dependency of the frequency content of an MR signal on the strength of the underlying magnetic field and is a fundamental principle of any MR application. It forms the basis for the en- and decoding of the information that is accessible to MR and, thus, emphasizes the crucial importance of the application of well-defined magnetic fields. Especially when varying in space, deviations of the effectively applied from the nominally prescribed field can introduce severe artifacts in the data. Even though they can be caused by different sources, it is predominantly the homogeneity of the static magnetic field, B_0, which is critical in this regard. Unfortunately, due to the presence of steep magnetic susceptibility gradients and a high inter-subject variability with respect to this property, strong field inhomogeneities with complex spatial patterns are prevalent in many human MR applications. As a result, the data quality is often impaired or even insufficient for measurements that are highly sensitive to variations in B_0. It follows that there is an unmet demand for improved *shimming* strategies, which aim at homogenizing the magnetic field. Motivated by this, novel and efficient techniques for static and dynamic B_0 shimming were developed and implemented within the scope of this dissertation.

For this purpose, a dedicated B_0 shimming framework was first implemented, which constitutes the current state of the art in static magnetic field homogenization based on spherical harmonic shim coils. An important feature of any B_0 shim routine is a non-iterative establishment of the best possible magnetic field homogeneity at short processing times. These requirements were met by performing accurate shim system characterizations and by including the gained information into custom-written shim software. By this means, an accurate control over conventional 2^{nd} order shim systems was demonstrated and served as a starting point for the development of more effective non-standard shim techniques. For this, a dedicated shim insert and the associated control hardware were employed, by means of which the shim order was increased up to the full 4^{th} and partial 5^{th} and 6^{th} order. The required communication protocols were added to the software and an improvement in shim performance was demonstrated. In general, an upscaling of the shim order increases the field shaping capabilities so as to more accurately approximate the complex target fields encountered in many MR applications. However, due to the competition with other hardware elements for the available bore space and considering limited coil efficiencies, it is valid to state that static spherical harmonic shimming cannot be extended so as to entirely suppress all inhomogeneities to an acceptable level. This applies equally to the emerging multi-coil techniques, which employ arrays of small shim-loops, and which have so far failed in proving to be a suitable alternative for static shimming over extended volumes. For MR applications targeting the human brain, it is especially the frontal and temporal lobes that suffer from strong inhomogeneities which exceed the correction potential of currently available static shim technology.

Given these natural limitations of static B_0 shimming over extended volumes, the field homogeneity can be improved in many MR applications by dynamically updating the shim setting during the data acquisition. This technique exploits the potential of a given shim system most efficiently and, thus, was the key topic of this work. However, the assumption is widespread, that dynamic shimming is difficult to implement and limited in its efficiency when being scaled to higher-order spherical harmonic shim coils. This is due to the fact that, in general, dynamic shimming may require excessively high shim current amplitudes. Moreover, their rapid temporal variation can induce eddy currents and necessitates the implementation of *pre-emphasis* corrections. The strongest reservations pertinent to this technique, therefore, relate to a disproportionate effort required for a comprehensive eddy current compensation [103] and excessive technological demands on the shim power supplies [176]. Both arguments could, however, be invalidated by the work that was performed within the scope of this thesis.
The former issue was addressed by developing a novel and efficient eddy current characterization framework. For this, an MR image-based measurement sequence was implemented, which samples the distortion fields that are generated by the eddy currents more efficiently than an existing alternative approach [168]. Combined with a proposed model-based spherical harmonic fitting of the spatio-temporal field evolution, a robust pre-emphasis parameter reconstruction was demonstrated on the basis of both simulated as well as acquired data. Using this framework, even low-amplitude eddy currents were proven to be correctly detected in the presence of high noise levels. Ultimately, an appropriate adjustment of the eddy current compensation modules of a dynamic shimming unit was shown and enabled a pre-emphasized dynamic operation of the shim insert coils. Requiring approximately 10 minutes of acquisition time per shim channel, this technique cannot compete with the temporal sampling efficiency provided by NMR field probes [81]. However, because shim pre-emphasis adjustments typically have to be made only once, the resultant calibration times for an entire shim system are still within an acceptable range. Moreover, no additional measurement hardware is required.
The latter issue was handled by optimizing the dynamic shim current calculations such as to intrinsically reduce the temporal variation of the shim current amplitudes. The approach is based on the fact that the B_0 field inhomogeneities vary smoothly over volumetric discretization steps that are typically employed in MR acquisitions. Consequently, it is feasible to determine shim correction fields and associated shim current amplitudes, which reveal the same smooth variation over time. A first proof-of-principle of this concept was delivered by implementing this feature into a conventional shim optimization via a dynamic adaption of the lower and upper shim current constraints. The advantages were quantified in extensive simulations and the applicability was demonstrated in conducted in vivo measurements. Based on this, the constrained dynamic shim calculations were streamlined and further improved by re-formulating the objective function so as to optimally homogenize B_0, while *directly* minimizing the shim current variation at the same time. Overall, a more than 20-fold reduction of the average maximum shim current change was demonstrated to be achievable at negligibly small losses in the achievable B_0 homogeneity.
Both the determination of optimal pre-emphasis parameters as well as the regularization of the temporal dynamic shim current variation facilitate the implementation of dynamic B_0 shimming. The significant increase in the achievable B_0 field homogeneity can be exploited in measurements, for which the acquisition volume is partitioned *per se*. For example, the B_0 homogeneity during whole-brain multi-slice acquisitions is improved by a factor of two, when using the proposed high-order dynamic B_0 shimming routine instead of a conventional 2^{nd} order static shim. The homogeneity improvements are comparable to those of dynamic multi-coil approaches [40] and constitute the best-possible B_0 shim results that is achievable with currently available hardware.

Despite the homogeneity gains provided by dynamically shimming sequentially acquired sub-volumes, however, it is to be noted that the inhomogeneity in regions that are close to strong magnetic susceptibility gradients is reduced, but not eliminated. Moreover, dynamic shimming is not applicable to 3D acquisitions or multi-band acquisitions with accelerations above a factor of two or three. Thus, given that today's magnetic field homogenization technology cannot fully compensate for the apparent inhomogeneities in these widespread applications, further developments for a more effective B_0 shimming over extended volumes is required. The recent implementation of a ultra-high static magnetic field system operating at 10.5 T [178] and the advent of human MR systems with even higher field strengths [179] further emphasize this urgent need. Moreover, the compensation of dynamic field fluctuations in real-time gains more and more importance at these field strengths and should be considered in the design of novel B_0 shim technologies. In this context, also subject motion and the associated changes in susceptibility-induced field inhomogeneities must be addressed.
Consequently, an optimal B_0 field homogenization and stabilization framework must include an efficient and versatile possibility to sufficiently compensate for all B_0 inhomogeneities by means of an initial static shim setting. During the data acquisition, a field-monitoring approach can then be employed to acquire information about the dynamic field evolution. In this context, it is conceivable to also track potential subject-movements and to extrapolate the associated magnetic field distortions from the motion parameters. A compensation of the dynamic B_0 field fluctuations can then be effectuated via a feedback-loop using dynamic shim updates [114]. Thus, the establishment of an optimal static shim and a subsequently performed comprehensive monitoring and prospective correction of the measurement conditions should be the long-term goal of B_0 shimming developments.

Bibliography

1. M. Schwerter, C. H. Moon, H. P. Hetherington, J. W. Pan, L. Tellmann, J. Felder, and N. J. Shah, "Interslice current constrained B0 shim optimization for high order dynamic shim updating with strongly reduced eddy currents," in *Proc. Intl. Soc. Mag. Reson. Med.*, p. 836, 2018.

2. M. Schwerter, H. P. Hetherington, C. H. Moon, J. W. Pan, J. Felder, L. Tellmann, and N. J. Shah, "Interslice current change constrained B0 shim optimization for accurate high-order dynamic shim updating with strongly reduced eddy currents," *Magnetic Resonance in Medicine*, vol. 82, no. 1, pp. 263–275, 2019.

3. M. Schwerter, M. Zimmermann, and N. J. Shah, "Fast 4d model based eddy current characterization for shim pre-emphasis calibrations," in *Proc. Intl. Soc. Mag. Reson. Med.*, p. 444, 2019.

4. M. Schwerter, M. Zimmermann, and N. J. Shah, "2d image-based eddy current characterization using a model-based pre-emphasis parameter estimation." In preparation.

5. M. Schwerter, M. Zimmermann, and N. J. Shah, "Generalized dynamic shim optimization for optimal B0 homogeneity at low current amplitudes." In preparation.

6. I. I. Rabi, J. R. Zacharias, S. Millman, and P. Kusch, "A New Method of Measuring Nuclear Magnetic Moment," *Physical Review*, vol. 53, pp. 318–318, Feb. 1938.

7. E. M. Purcell, H. C. Torrey, and R. V. Pound, "Resonance Absorption by Nuclear Magnetic Moments in a Solid," *Physical Review*, vol. 69, pp. 37–38, Dec. 1945.

8. F. Bloch, W. W. Hansen, and M. Packard, "Nuclear Induction," *Physical Review*, vol. 69, pp. 127–127, Jan. 1946.

9. E. Odeblad and G. Lindstroem, "Some preliminary observations on the proton magnetic resonance in biologic samples," *Acta Radiologica*, vol. 43, pp. 469–476, June 1955.

10. R. Damadian, "Apparatus and method for detecting cancer in tissue." U.S. Patent No. 3,789,832, Feb. 1974.

11. P. C. Lauterbur, "Image Formation by Induced Local Interactions: Examples Employing Nuclear Magnetic Resonance," *Nature*, vol. 242, pp. 190–191, Mar. 1973.

12. A. Kumar, D. Welti, and R. R. Ernst, "NMR Fourier Zeugmatography," *Journal of Magnetic Resonance*, vol. 18, pp. 69–83, 1975.

13. P. Mansfield, "Multi-planar image formation using NMR spin echoes," *Journal of Physics C: Solid State Physics*, vol. 10, pp. L55–L58, Feb. 1977.

14. R. W. Brown, E. M. Haacke, Y.-C. N. Cheng, M. R. Thompson, and R. Venkatesan, *Magnetic Resonance Imaging: Physical Principles and Sequence Design*. John Wiley & Sons, 2 ed., June 2014.

15. M. H. Levitt, *Spin Dynamics: Basics of Nuclear Magnetic Resonance*. John Wiley & Sons, Nov. 2001.

16. A. Webb, ed., *Magnetic Resonance Technology - Hardware and System Component Design*. The Royal Society of Chemistry, May 2016.

17. M. A. Bernstein, K. F. King, and X. J. Zhou, *Handbook of MRI Pulse Sequences*. Elsevier, Sept. 2004.

18. L. G. Hanson, "Is quantum mechanics necessary for understanding magnetic resonance?," *Concepts in Magnetic Resonance Part A*, vol. 32A, pp. 329–340, Sept. 2008.

19. Z.-P. Liang and P. C. Lauterbur, *Principles of Magnetic Resonance Imaging - A Signal Processing Perspective*. SPIE Optical Engineering Press, 2000.

20. D. A. Yablonskiy, "Quantitation of intrinsic magnetic susceptibility-related effects in a tissue matrix. Phantom study," *Magnetic Resonance in Medicine*, vol. 39, pp. 417–428, Mar. 1998.

21. S. Ljunggren, "A simple graphical representation of fourier-based imaging methods," *Journal of Magnetic Resonance (1969)*, vol. 54, pp. 338–343, Sept. 1983.

22. J. Fessler, "Electrical Engineering and Computer Sciences Course 516." Lecture Notes: https://web.eecs.umich.edu/~fessler/course/516/l/, 2009.

23. Y. Lvovsky, E. W. Stautner, and T. Zhang, "Novel technologies and configurations of superconducting magnets for MRI," *Superconductor Science and Technology*, vol. 26, p. 093001, Sept. 2013.

24. R. Warner, "Ultra-high field magnets for whole-body MRI," *Superconductor Science and Technology*, vol. 29, p. 094006, Sept. 2016.

25. R. Turner, "Gradient coil design: A review of methods," *Magnetic Resonance Imaging*, vol. 11, pp. 903–920, Jan. 1993.

26. M. S. Poole, P. T. While, H. S. Lopez, and S. Crozier, "Minimax current density gradient coils: Analysis of coil performance and heating," *Magnetic Resonance in Medicine*, vol. 68, pp. 639–648, Aug. 2012.

27. M. Davids, B. Guerin, A. v. Endt, L. R. Schad, and L. L. Wald, "Prediction of peripheral nerve stimulation thresholds of MRI gradient coils using coupled electromagnetic and neurodynamic simulations," *Magnetic Resonance in Medicine*, vol. 81, no. 1, pp. 686–701, 2019.

28. J. Mispelter, M. Lupu, and A. Briguet, *NMR Probeheads for Biophysical and Biomedical Experiments: Theoretical Principles & Practical Guidelines*. Imperial College Press, 2006.

29. P. B. Roemer, W. A. Edelstein, C. E. Hayes, S. P. Souza, and O. M. Mueller, "The NMR phased array," *Magnetic Resonance in Medicine*, vol. 16, no. 2, pp. 192–225, 1990.

30. R. M. Heidemann, ï. ï¿½zsarlak, P. M. Parizel, J. Michiels, B. Kiefer, V. Jellus, M. Mï¿½ller, F. Breuer, M. Blaimer, M. A. Griswold, and P. M. Jakob, "A brief review of parallel magnetic resonance imaging," *European Radiology*, vol. 13, pp. 2323–2337, Oct. 2003.

31. R. A. De Graaf, "Chapter 10: Hardware," in *In Vivo NMR Spectroscopy*, pp. 479–548, John Wiley & Sons, 2013.

32. R. Turner, "A Target Field Approach to Optimal Coil Design," *Journal of Physics D: Applied Physics*, vol. 19, pp. L147–L151, Aug. 1986.

33. M. J. E. Golay, "Field Homogenizing Coils for Nuclear Spin Resonance Instrumentation," *Review of Scientific Instruments*, vol. 29, no. 4, pp. 313–315, 1958.

34. W. A. Anderson, "Electrical Current Shims for Correcting Magnetic Fields," *Review of Scientific Instruments*, vol. 32, no. 3, pp. 241–250, 1961.

35. F. Romeo and D. I. Hoult, "Magnet field profiling: Analysis and correcting coil design," *Magnetic Resonance in Medicine*, vol. 1, pp. 44–65, Mar. 1984.

36. C. Juchem, T. W. Nixon, S. McIntyre, D. L. Rothman, and R. A. d. Graaf, "Magnetic field modeling with a set of individual localized coils," *Journal of Magnetic Resonance*, vol. 204, pp. 281–289, June 2010.

37. K. M. Koch, D. L. Rothman, and R. A. de Graaf, "Optimization of Static Magnetic Field Homogeneity in the Human and Animal Brain In Vivo," *Progress in Nuclear Magnetic Resonance Spectroscopy*, vol. 54, pp. 69–96, Feb. 2009.

38. K. Wachowicz, "Evaluation of Active and Passive Shimming in Magnetic Resonance Imaging," *Research and Reports in Nuclear Medicine*, Oct. 2014.

39. C. Juchem and R. A. de Graaf, "B0 magnetic field homogeneity and shimming for in vivo magnetic resonance spectroscopy," *Analytical Biochemistry*, vol. 529, pp. 17–29, July 2017.

40. J. P. Stockmann and L. L. Wald, "In vivo B0 field shimming methods for MRI at 7 T," *NeuroImage*, vol. 168, pp. 71–87, Mar. 2018.

41. R. A. de Graaf and C. Juchem, "Chapter 4: B0 Shimming Technology," in *Magnetic Resonance Technology* (A. G. Webb, ed.), pp. 166–207, The Royal Society of Chemistry, 2016.

42. J. Finsterbusch, "Chapter 2: B0 Inhomogeneity and Shimming," in *Quantitative MRI of the Spinal Cord* (J. Cohen-Adad and C. A. M. Wheeler-Kingshott, eds.), pp. 68–90, Elsevier, 2014.

43. R. Warner and S. Pittard, "Chapter 2: Magnets," in *Magnetic Resonance Technology* (A. G. Webb, ed.), pp. 48–80, The Royal Society of Chemistry, 2016.

44. G. N. Chmurny and D. I. Hoult, "The Ancient and Honourable Art of Shimming," *Concepts in Magnetic Resonance*, vol. 2, pp. 131–149, July 1990.

45. J. Liu, J. A. de Zwart, P. van Gelderen, J. Murphy-Boesch, and J. H. Duyn, "Effect of Head Motion on MRI B0 Field Distribution," *Magnetic Resonance in Medicine*, May 2018.

46. J. Maclaren, M. Herbst, O. Speck, and M. Zaitsev, "Prospective motion correction in brain imaging: A review," *Magnetic Resonance in Medicine*, vol. 69, pp. 621–636, Mar. 2013.

47. F. Godenschweger, U. Kaegebein, D. Stucht, U. Yarach, A. Sciarra, R. Yakupov, F. Luesebrink, P. Schulze, and O. Speck, "Motion correction in MRI of the brain," *Physics in Medicine and Biology*, vol. 61, pp. R32–R56, Mar. 2016.

48. P.-F. Van de Moortele, J. Pfeuffer, G. H. Glover, K. Ugurbil, and X. Hu, "Respiration-Induced B0 Fluctuations and Their Spatial Distribution in the Human Brain at 7 Tesla," *Magnetic Resonance in Medicine*, vol. 47, pp. 888–895, May 2002.

49. R. R. Ernst, "Measurement and Control of Magnetic Field Homogeneity," *Review of Scientific Instruments*, vol. 39, pp. 998–1012, July 1968.

50. W. W. Conover, "Practical Guide to Shimming Superconducting NMR Magnets," in *Topics in Carbon-13 NMR Spectroscopy* (G. C. Levy, ed.), vol. 4, pp. 37–51, John Wiley & Sons, 1984.

51. D. Hoult, "Shimming on Spatially Localized Signals," *Journal of Magnetic Resonance*, vol. 73, pp. 174–177, June 1987.

52. D. Holz, D. Jensen, R. Proksa, M. Tochtrop, and W. Vollmann, "Automatic Shimming for Localized Spectroscopy," *Medical Physics*, vol. 15, pp. 898–903, Nov. 1988.

53. T. R. Brown, B. M. Kincaid, and K. Ugurbil, "NMR chemical shift imaging in three dimensions," *Proceedings of the National Academy of Sciences*, vol. 79, pp. 3523–3526, June 1982.

54. A. A. Maudsley, A. Oppelt, and A. Ganssen, "Rapid Measurement of Magnetic Field Distributions Using Nuclear Magnetic Resonance," *Siemens Forschungs- und Entwicklungsberichte/Siemens Research and Development Reports*, vol. 8, pp. 326–331, Dec. 1979.

55. A. A. Maudsley, H. E. Simon, and S. K. Hilal, "Magnetic Field Measurement by NMR Imaging," *Journal of Physics E: Scientific Instruments*, vol. 17, pp. 216–220, Mar. 1984.

56. J. Tropp, K. A. Derby, and C. Hawryszko, "Automated shimming of B0 for spectroscopic imaging," *Journal of Magnetic Resonance*, vol. 85, pp. 244–254, Nov. 1989.

57. J. Wilkins and S. Miller, "The Use of Adaptive Algorithms for Obtaining Optimal Electrical Shimming in Magnetic Resonance Imaging (MRI)," *IEEE Transactions on Biomedical Engineering*, vol. 36, pp. 202–210, Feb. 1989.

58. J. Frahm, K.-D. Merboldt, and W. Haenicke, "Localized proton spectroscopy using stimulated echoes," *Journal of Magnetic Resonance (1969)*, vol. 72, pp. 502–508, May 1987.

59. I. S. Mackenzie, E. M. Robinson, A. N. Wells, and B. Wood, "A simple field map for shimming," *Magnetic Resonance in Medicine*, vol. 5, pp. 262–268, Sept. 1987.

60. K. Sekihara, S. Matsui, and H. Kohno, "A New Method of Measuring Static Field Distribution Using Modified Fourier NMR Imaging," *Journal of Physics E: Scientific Instruments*, vol. 18, pp. 224–227, Mar. 1985.

61. M. G. Prammer, J. C. Haselgrove, M. Shinnar, and J. S. Leigh, "A New Approach to Automatic Shimming," *Journal of Magnetic Resonance*, vol. 77, pp. 40–52, Mar. 1988.

62. E. Schneider and G. Glover, "Rapid In Vivo Proton Shimming," *Magnetic Resonance in Medicine*, vol. 18, pp. 335–347, Apr. 1991.

63. P. Webb and A. Macovski, "Rapid, Fully Automatic, Arbitrary-Volume In Vivo Shimming," *Magnetic Resonance in Medicine*, vol. 20, pp. 113–122, July 1991.

64. S. Kanayama, S. Kuhara, and K. Satoh, "In Vivo Rapid Magnetic Field Measurement and Shimming Using Single Scan Differential Phase Mapping," *Magnetic Resonance in Medicine*, vol. 36, pp. 637–642, Oct. 1996.

65. T. G. Reese, T. L. Davis, and R. M. Weisskoff, "Automated Shimming at 1.5 T Using Echo-Planar Image Frequency Maps," *Journal of Magnetic Resonance Imaging*, vol. 5, pp. 739–745, Nov. 1995.

66. C. Windischberger, S. Robinson, A. Rauscher, M. Barth, and E. Moser, "Robust field map generation using a triple-echo acquisition," *Journal of Magnetic Resonance Imaging*, vol. 20, no. 4, pp. 730–734, 2004.

67. L. M. Klassen and R. S. Menon, "Robust Automated Shimming Technique Using Arbitrary Mapping Acquisition Parameters (RASTAMAP)," *Magnetic Resonance in Medicine*, vol. 51, pp. 881–887, May 2004.

68. R. Gruetter and C. Boesch, "Fast, Noniterative Shimming of Spatially Localized Signals. In Vivo Analysis of the Magnetic Field Along Axes," *Journal of Magnetic Resonance*, vol. 96, pp. 323–334, Feb. 1992.

69. R. Gruetter, "Automatic, Localized In Vivo Adjustment of All First- and Second-Order Shim Coils," *Magnetic Resonance in Medicine*, vol. 29, pp. 804–811, June 1993.

70. J. Shen, R. E. Rycyna, and D. L. Rothman, "Improvements on an In Vivo Automatic Shimming Method (FASTERMAP)," *Magnetic Resonance in Medicine*, vol. 38, pp. 834–839, Nov. 1997.

71. R. Gruetter and I. Tkac, "Field Mapping Without Reference Scan Using Asymmetric Echo-Planar Techniques," *Magnetic Resonance in Medicine*, vol. 43, pp. 319–323, Feb. 2000.

72. O. Reynaud, D. Gallichan, B. Schaller, and R. Gruetter, "Fast low-specific absorption rate B0-mapping along projections at high field using two-dimensional radiofrequency pulses," *Magnetic Resonance in Medicine*, vol. 73, pp. 901–908, Mar. 2015.

73. J. Shen, D. L. Rothman, H. P. Hetherington, and J. W. Pan, "Linear Projection Method for Automatic Slice Shimming," *Magnetic Resonance in Medicine*, vol. 42, pp. 1082–1088, Dec. 1999.

74. J. Shen, "Effect of Degenerate Spherical Harmonics and a Method for Automatic Shimming of Oblique Slices," *NMR in Biomedicine*, vol. 14, pp. 177–183, May 2001.

75. Y. Zhang, S. Li, and J. Shen, "Automatic high-order shimming using parallel columns mapping (PACMAP)," *Magnetic Resonance in Medicine*, vol. 62, pp. 1073–1079, Oct. 2009.

76. D. N. Splitthoff, F. Testud, J. Henning, O. Speck, and M. Zaitsev, "Real-time prospective shim correction using self-referencing navigators," in *Proc. Intl. Soc. Mag. Reson. Med.*, p. 985, 2007.

77. H. A. Ward, S. J. Riederer, and C. R. Jack, "Real-Time Autoshimming for Echo Planar Timecourse Imaging," *Magnetic Resonance in Medicine*, vol. 48, pp. 771–780, Nov. 2002.

78. L. Brateman, T. T. Bowman, S. Doenstrup, and K. N. Scott, "Magnetic field shimming by fourier analysis," *Magnetic Resonance in Medicine*, vol. 6, pp. 459–473, Apr. 1988.

79. D. Hoult, R. Richards, and P. Styles, "A novel field-frequency lock for a superconducting spectrometer," *Journal of Magnetic Resonance (1969)*, vol. 30, pp. 351–365, May 1978.

80. N. D. Zanche, C. Barmet, J. A. Nordmeyer-Massner, and K. P. Pruessmann, "NMR probes for measuring magnetic fields and field dynamics in MR systems," *Magnetic Resonance in Medicine*, vol. 60, pp. 176–186, July 2008.

81. C. Barmet, N. D. Zanche, and K. P. Pruessmann, "Spatiotemporal Magnetic Field Monitoring for MR," *Magnetic Resonance in Medicine*, vol. 60, pp. 187–197, July 2008.

82. C. Barmet, N. De Zanche, B. J. Wilm, and K. P. Pruessmann, "A transmit/receive system for magnetic field monitoring of in vivo MRI," *Magnetic Resonance in Medicine*, vol. 62, pp. 269–276, July 2009.

83. C. Barmet, B. J. Wilm, M. Pavan, G. Katsikatsos, J. Keupp, G. Mens, and K. P. Pruessmann, "Concurrent higher-order field monitoring for routine head MRI: an integrated heteronuclear setup," in *Proc. Intl. Soc. Mag. Reson. Med.*, p. 216, 2010.

84. M. Andersen, L. G. Hanson, K. H. Madsen, J. Wezel, V. Boer, T. van der Velden, M. J. van Osch, D. Klomp, A. G. Webb, and M. J. Versluis, "Measuring motion-induced B0-fluctuations in the brain using field probes," *Magnetic Resonance in Medicine*, vol. 75, pp. 2020–2030, May 2016.

85. S. J. Vannesjo, B. J. Wilm, Y. Duerst, S. Gross, D. O. Brunner, B. E. Dietrich, T. Schmid, C. Barmet, and K. P. Pruessmann, "Retrospective correction of physiological field fluctuations in high-field brain MRI using concurrent field monitoring," *Magnetic Resonance in Medicine*, vol. 73, pp. 1833–1843, May 2015.

86. C. N. Chen and D. I. Hoult, "Chapter 3: Magnets and Magnetic Fields," in *Biomedical Magnetic Resonance Technology* (R. F. Mould, ed.), pp. 76–116, IOP Publishing Ltd, 1989.

87. D. I. Hoult and D. Lee, "Shimming a superconducting nuclear-magnetic-resonance imaging magnet with steel," *Review of Scientific Instruments*, vol. 56, no. 1, pp. 131–135, 1985.

88. H. Wen and F. A. Jaffer, "An In Vivo Automated Shimming Method Taking Into Account Shim Current Constraints," *Magnetic Resonance in Medicine*, vol. 34, pp. 898–904, Dec. 1995.

89. D.-H. Kim, E. Adalsteinsson, G. H. Glover, and D. M. Spielman, "Regularized Higher-Order In Vivo Shimming," *Magnetic Resonance in Medicine*, vol. 48, pp. 715–722, Oct. 2002.

90. J. Lee, M. Lustig, D.-h. Kim, and J. M. Pauly, "Improved Shim Method Based on the Minimization of the Maximum Off-Resonance Frequency for Balanced Steady-State Free Precession (bSSFP)," *Magnetic Resonance in Medicine*, vol. 61, pp. 1500–1506, June 2009.

91. V. O. Boer, J. C. W. Siero, H. Hoogduin, J. S. v. Gorp, P. R. Luijten, and D. W. J. Klomp, "High-field MRS of the human brain at short TE and TR," *NMR in Biomedicine*, vol. 24, pp. 1081–1088, Nov. 2011.

92. A. Fillmer, T. Kirchner, D. Cameron, and A. Henning, "Constrained Image-Based B0 Shimming Accounting for "local minimum traps" in the Optimization and Field Inhomogeneities Outside the Region of Interest," *Magnetic Resonance in Medicine*, vol. 73, pp. 1370–1380, Apr. 2015.

93. J. L. Wilson, M. Jenkinson, I. de Araujo, M. L. Kringelbach, E. T. Rolls, and P. Jezzard, "Fast, Fully Automated Global and Local Magnetic Field Optimization for fMRI of the Human Brain," *NeuroImage*, vol. 17, pp. 967–976, Oct. 2002.

94. H. P. Hetherington, W.-J. Chu, O. Gonen, and J. W. Pan, "Robust Fully Automated Shimming of the Human Brain for High-Field 1h Spectroscopic Imaging," *Magnetic Resonance in Medicine*, vol. 56, pp. 26–33, July 2006.

95. S. Nassirpour, P. Chang, A. Fillmer, and A. Henning, "A Comparison of Optimization Algorithms for Localized In Vivo B0 Shimming," *Magnetic Resonance in Medicine*, vol. 79, pp. 1145–1156, Feb. 2018.

96. Y. Zhao, A. W. Anderson, and J. C. Gore, "Computer Simulation Studies of the Effects of Dynamic Shimming on Susceptibility Artifacts in EPI at High Field," *Journal of Magnetic Resonance*, vol. 173, pp. 10–22, Mar. 2005.

97. A. M. Blamire, D. L. Rothman, and T. Nixon, "Dynamic Shim Updating: A New Approach Towards Optimized Whole Brain Shimming," *Magnetic Resonance in Medicine*, vol. 36, pp. 159–165, July 1996.

98. G. Morrell and D. Spielman, "Dynamic Shimming for Multi-Slice Magnetic Resonance Imaging," *Magnetic Resonance in Medicine*, vol. 38, pp. 477–483, Sept. 1997.

99. R. A. de Graaf, P. B. Brown, S. McIntyre, D. L. Rothman, and T. W. Nixon, "Dynamic shim updating (DSU) for multislice signal acquisition," *Magnetic Resonance in Medicine*, vol. 49, pp. 409–416, Mar. 2003.

100. M. A. Morich, D. A. Lampman, W. R. Dannels, and F. T. D. Goldie, "Exact temporal eddy current compensation in magnetic resonance imaging systems," *IEEE Transactions on Medical Imaging*, vol. 7, pp. 247–254, Sept. 1988.

101. K. M. Koch, S. McIntyre, T. W. Nixon, D. L. Rothmann, and R. A. de Graaf, "Dynamic Shim Updating on the Human Brain," *Journal of Magnetic Resonance*, vol. 180, pp. 286–296, June 2006.

102. S. Sengupta, E. B. Welch, Y. Zhao, D. Foxall, P. Starewicz, A. W. Anderson, J. C. Gore, and M. J. Avison, "Dynamic B0 Shimming at 7 T," *Magnetic Resonance Imaging*, vol. 29, pp. 483–496, May 2011.

103. C. Juchem, T. W. Nixon, P. Diduch, D. L. Rothman, P. Starewicz, and R. A. De Graaf, "Dynamic Shimming of the Human Brain at 7 T," *Concepts in Magnetic Resonance Part B: Magnetic Resonance Engineering*, vol. 37B, pp. 116–128, July 2010.

104. M. Poole and R. Bowtell, "Volume Parcellation for Improved Dynamic Shimming," *Magnetic Resonance Materials in Physics, Biology and Medicine*, vol. 21, pp. 31–40, Mar. 2008.

105. V. O. Boer, D. W. J. Klomp, C. Juchem, P. R. Luijten, and R. A. de Graaf, "Multislice 1h MRSI of the Human Brain at 7 T Using Dynamic B0 and B1 Shimming," *Magnetic Resonance in Medicine*, vol. 68, pp. 662–670, Sept. 2012.

106. A. Fillmer, S. J. Vannesjo, M. Pavan, M. Scheidegger, K. P. Pruessmann, and A. Henning, "Fast Iterative Pre-Emphasis Calibration Method Enabling Third-Order Dynamic Shim Updated fMRI," *Magnetic Resonance in Medicine*, vol. 75, pp. 1119–1131, Mar. 2016.

107. K. M. Koch, L. I. Sacolick, T. W. Nixon, S. McIntyre, D. L. Rothman, and R. A. de Graaf, "Dynamically Shimmed Multivoxel 1h Magnetic Resonance Spectroscopy and Multislice Magnetic Resonance Spectroscopic Imaging of the Human Brain," *Magnetic Resonance in Medicine*, vol. 57, pp. 587–591, Mar. 2007.

108. S. Sengupta, M. J. Avison, J. C. Gore, and E. Brian Welch, "Software compensation of Eddy current fields in multislice high order dynamic shimming," *Journal of Magnetic Resonance*, vol. 210, pp. 218–227, June 2011.

109. A. J. van der Kouwe, T. Benner, and A. M. Dale, "Real-Time Rigid Body Motion Correction and Shimming Using Cloverleaf Navigators," *Magnetic Resonance in Medicine*, vol. 56, pp. 1019–1032, Nov. 2006.

110. B. Keating and T. Ernst, "Real-time Dynamic Frequency and Shim Correction for Single-Voxel Magnetic Resonance Spectroscopy," *Magnetic Resonance in Medicine*, vol. 68, pp. 1339–1345, Nov. 2012.

111. A. T. Hess, M. Dylan Tisdall, O. C. Andronesi, E. M. Meintjes, and A. J. W. van der Kouwe, "Real-time motion and B0 corrected single voxel spectroscopy using volumetric navigators," *Magnetic Resonance in Medicine*, vol. 66, pp. 314–323, Aug. 2011.

112. P. van Gelderen, J. de Zwart, P. Starewicz, R. Hinks, and J. Duyn, "Real-Time Shimming to Compensate for Respiration-Induced B0 Fluctuations," *Magnetic Resonance in Medicine*, vol. 57, pp. 362–368, Feb. 2007.

113. V. O. Boer, B. L. vd Bank, G. van Vliet, P. R. Luijten, and D. W. J. Klomp, "Direct B0 field monitoring and real-time B0 field updating in the human breast at 7 tesla," *Magnetic Resonance in Medicine*, vol. 67, pp. 586–591, Feb. 2012.

114. Y. Duerst, B. J. Wilm, B. E. Dietrich, S. J. Vannesjo, C. Barmet, T. Schmid, D. O. Brunner, and K. P. Pruessmann, "Real-Time Feedback for Spatiotemporal Field Stabilization in MR Systems," *Magnetic Resonance in Medicine*, vol. 73, pp. 884–893, Feb. 2015.

115. B. J. Wilm, Y. Duerst, B. E. Dietrich, M. Wyss, S. J. Vannesjo, T. Schmid, D. O. Brunner, C. Barmet, and K. P. Pruessmann, "Feedback field control improves linewidths in in vivo magnetic resonance spectroscopy," *Magnetic Resonance in Medicine*, vol. 71, pp. 1657–1662, May 2014.

116. Y. Duerst, B. J. Wilm, M. Wyss, B. E. Dietrich, S. Gross, T. Schmid, D. O. Brunner, and K. P. Pruessmann, "Utility of real-time field control in T2*-Weighted head MRI at 7t," *Magnetic Resonance in Medicine*, vol. 76, pp. 430–439, Aug. 2016.

117. M. Wyss, Y. Duerst, D. Nanz, L. Kasper, B. J. Wilm, B. E. Dietrich, S. Gross, T. Schmid, D. O. Brunner, and K. P. Pruessmann, "Feedback field control improves the precision of T2* quantification at 7 T," *NMR in Biomedicine*, vol. 30, Oct. 2017.

118. P. S. Oezbay, Y. Duerst, B. J. Wilm, K. P. Pruessmann, and D. Nanz, "Enhanced quantitative susceptibility mapping (QSM) using real-time field control," *Magnetic Resonance in Medicine*, vol. 79, pp. 770–778, Feb. 2018.

119. D. F. Hillenbrand, K. M. Lo, W. F. B. Punchard, T. G. Reese, and P. M. Starewicz, "High-Order MR Shimming: A Simulation Study of the Effectiveness of Competing Methods, Using an Established Susceptibility Model of the Human Head," *Applied Magnetic Resonance*, vol. 29, pp. 39–64, Mar. 2005.

120. D. M. Spielman, E. Adalsteinsson, and K. O. Lim, "Quantitative assessment of improved homogeneity using higher-order shims for spectroscopic imaging of the brain," *Magnetic Resonance in Medicine*, vol. 40, pp. 376–382, Sept. 1998.

121. J. W. Pan, K.-M. Lo, and H. P. Hetherington, "Role of Very High Order and Degree B0 Shimming for Spectroscopic Imaging of the Human Brain at 7 Tesla," *Magnetic Resonance in Medicine*, vol. 68, pp. 1007–1017, Oct. 2012.

122. T. Kim, Y. Lee, T. Zhao, H. P. Hetherington, and J. W. Pan, "Gradient-Echo EPI Using a High-Degree Shim Insert Coil at 7 T: Implications for BOLD fMRI," *Magnetic Resonance in Medicine*, vol. 78, pp. 1734–1745, Nov. 2017.

123. A. Jesmanowicz, J. S. Hyde, W. F. B. Punchard, and P. M. Starewicz, "Method for shimming a static magnetic field in a local MRI coil." U.S. Patent No. 6,294,972, Sept. 2001.

124. K. M. Koch, P. B. Brown, D. L. Rothman, and R. A. de Graaf, "Sample-specific diamagnetic and paramagnetic passive shimming," *Journal of Magnetic Resonance*, vol. 182, pp. 66–74, Sept. 2006.

125. S. Yang, H. Kim, M.-O. Ghim, B.-U. Lee, and D.-H. Kim, "Local In Vivo Shimming Using Adaptive Passive Shim Positioning," *Magnetic Resonance Imaging*, vol. 29, pp. 401–407, Apr. 2011.

126. J. L. Wilson, M. Jenkinson, and P. Jezzard, "Optimization of static field homogeneity in human brain using diamagnetic passive shims," *Magnetic Resonance in Medicine*, vol. 48, pp. 906–914, Nov. 2002.

127. J. L. Wilson, M. Jenkinson, and P. Jezzard, "Protocol to determine the optimal intraoral passive shim for minimisation of susceptibility artifact in human inferior frontal cortex," *NeuroImage*, vol. 19, pp. 1802–1811, Aug. 2003.

128. J. L. Wilson and P. Jezzard, "Utilization of an intra-oral diamagnetic passive shim in functional MRI of the inferior frontal cortex," *Magnetic Resonance in Medicine*, vol. 50, pp. 1089–1094, Nov. 2003.

129. R. Cusack, B. Russell, S. M. Cox, C. De Panfilis, C. Schwarzbauer, and R. Ansorge, "An evaluation of the use of passive shimming to improve frontal sensitivity in fMRI," *NeuroImage*, vol. 24, pp. 82–91, Jan. 2005.

130. R. A. Oesterbauer, J. L. Wilson, G. A. Calvert, and P. Jezzard, "Physical and physiological consequences of passive intra-oral shimming," *NeuroImage*, vol. 29, pp. 245–253, Jan. 2006.

131. J.-J. Hsu and G. H. Glover, "Mitigation of susceptibility-induced signal loss in neuroimaging using localized shim coils," *Magnetic Resonance in Medicine*, vol. 53, pp. 243–248, Feb. 2005.

132. C. Juchem, T. W. Nixon, S. McIntyre, D. L. Rothman, and R. A. de Graaf, "Magnetic Field Homogenization of the Human Prefrontal Cortex With a Set of Localized Electrical Coils," *Magnetic Resonance in Medicine*, pp. NA–NA, 2009.

133. E. C. Wong, "Why Should Shim Coils be Orthogonal?," in *Proc. SMR*, vol. 3, p. 313, 1995.

134. C. Juchem, D. Green, and R. A. de Graaf, "Multi-coil magnetic field modeling," *Journal of Magnetic Resonance*, vol. 236, pp. 95–104, Nov. 2013.

135. C. Juchem, P. B. Brown, T. W. Nixon, S. McIntyre, D. L. Rothman, and R. A. de Graaf, "Multicoil shimming of the mouse brain," *Magnetic Resonance in Medicine*, vol. 66, pp. 893–900, Sept. 2011.

136. C. Juchem, P. Herman, B. G. Sanganahalli, P. B. Brown, S. McIntyre, T. W. Nixon, D. Green, F. Hyder, and R. A. d. Graaf, "DYNAmic Multi-Coll TEchnique (DYNAMITE) shimming of the rat brain at 11.7 T," *NMR in Biomedicine*, vol. 27, pp. 897–906, Aug. 2014.

137. C. Juchem, T. W. Nixon, S. McIntyre, V. O. Boer, D. L. Rothman, and R. A. de Graaf, "Dynamic multi-coil shimming of the human brain at 7t," *Journal of Magnetic Resonance*, vol. 212, pp. 280–288, Oct. 2011.

138. C. Juchem, S. Umesh Rudrapatna, T. W. Nixon, and R. A. de Graaf, "Dynamic multi-coil technique (DYNAMITE) shimming for echo-planar imaging of the human brain at 7 Tesla," *NeuroImage*, vol. 105, pp. 462–472, Jan. 2015.

139. H. Han, A. W. Song, and T.-K. Truong, "Integrated parallel reception, excitation, and shimming (iPRES)," *Magnetic Resonance in Medicine*, vol. 70, pp. 241–247, July 2013.

140. J. P. Stockmann, T. Witzel, B. Keil, J. R. Polimeni, A. Mareyam, C. LaPierre, K. Setsompop, and L. L. Wald, "A 32-Channel Combined RF and B0 Shim Array for 3t Brain Imaging," *Magnetic Resonance in Medicine*, vol. 75, pp. 441–451, Jan. 2016.

141. T.-K. Truong, D. Darnell, and A. W. Song, "Integrated RF/shim coil array for parallel reception and localized B 0 shimming in the human brain," *NeuroImage*, vol. 103, pp. 235–240, Dec. 2014.

142. D. Darnell, T.-K. Truong, and A. W. Song, "Integrated Parallel Reception, Excitation, and Shimming (iPRES) With Multiple Shim Loops per Radio-Frequency Coil Element for Improved B0 Shimming," *Magnetic Resonance in Medicine*, vol. 77, pp. 2077–2086, May 2017.

143. D. Darnell, Y. Ma, H. Wang, F. Robb, A. W. Song, and T.-K. Truong, "Adaptive integrated parallel reception, excitation, and shimming (iPRES-A) with microelectromechanical systems switches: Adaptive iPRES," *Magnetic Resonance in Medicine*, vol. 80, pp. 371–379, July 2018.

144. P. T. While and J. G. Korvink, "Designing MR Shim Arrays With Irregular Coil Geometry: Theoretical Considerations," *IEEE Transactions on Biomedical Engineering*, vol. 61, pp. 1614–1620, June 2014.

145. A. Aghaeifar, C. Mirkes, J. Bause, T. Steffen, N. Avdievitch, A. Henning, and K. Scheffler, "Dynamic B0 Shimming of the Human Brain at 9.4 T With a 16-Channel Multi-Coil Shim Setup," *Magnetic Resonance in Medicine*, vol. 80, pp. 1714–1725, Oct. 2018.

146. E. Adalsteinsson, S. M. Conolly, H. Xu, and D. M. Spielman, "Design of Dedicated Shim Fields," in *Proc. Intl. Soc. Mag. Reson. Med.*, p. 477, 1999.

147. C. T. Harris, W. B. Handler, and B. A. Chronik, "A New Approach to Shimming: The Dynamically Controlled Adaptive Current Network," *Magnetic Resonance in Medicine*, vol. 71, pp. 859–869, Feb. 2014.

148. I. Zivkovic, C. Mirkes, and K. Scheffler, "B0 shimming at 9.4t using a multicoil approach - coil design with genetic algorithm," in *Proc. Intl. Soc. Mag. Reson. Med.*, p. 1152, 2016.

149. C. Juchem and R. A. de Graaf, "The Public Multi-Coil Information (PUMCIN) Policy," *Magnetic Resonance in Medicine*, vol. 78, pp. 2042–2047, Nov. 2017.

150. F. H. Lin, "Calculating magnetic field distributions using the Biot-Savart's law." URL: https://maki.bme.ntu.edu.tw/tools/190-2/, 2018.

151. J. Frahm, K.-D. Merboldt, and W. Haenicke, "Direct FLASH MR imaging of magnetic field inhomogeneities by gradient compensation," *Magnetic Resonance in Medicine*, vol. 6, pp. 474–480, Apr. 1988.

152. R. Constable and D. Spencer, "Composite image formation in z-shimmed functional MR imaging," *Magnetic Resonance in Medicine*, vol. 42, pp. 110–117, July 1999.

153. Q. X. Yang, G. D. Williams, R. J. Demeure, T. J. Mosher, and M. B. Smith, "Removal of local field gradient artifacts in T2*-weighted images at high fields by gradient-echo slice excitation profile imaging," *Magnetic Resonance in Medicine*, vol. 39, pp. 402–409, Mar. 1998.

154. R. T. Constable, "Functional MR imaging using gradient-echo echo-planar imaging in the presence of large static field inhomogeneities," *Journal of Magnetic Resonance Imaging*, vol. 5, pp. 746–752, Nov. 1995.

155. Q. X. Yang, B. J. Dardzinski, S. Li, P. J. Eslinger, and M. B. Smith, "Multi-gradient echo with susceptibility inhomogeneity compensation (MGESIC): Demonstration of fMRI in the olfactory cortex at 3.0 T," *Magnetic Resonance in Medicine*, vol. 37, pp. 331–335, Mar. 1997.

156. P. Jezzard and R. S. Balaban, "Correction for geometric distortion in echo planar images from B0 field variations," *Magnetic Resonance in Medicine*, vol. 34, no. 1, pp. 65–73, 1995.

157. J. L. R. Andersson, S. Skare, and J. Ashburner, "How to correct susceptibility distortions in spin-echo echo-planar images: application to diffusion tensor imaging," *NeuroImage*, vol. 20, pp. 870–888, Oct. 2003.

158. P. Chang, S. Nassirpour, and A. Henning, "Modeling Real Shim Fields For Very High Degree (and Order) B0 Shimming of the Human Brain at 9.4 T," *Magnetic Resonance in Medicine*, vol. 79, pp. 529–540, Jan. 2018.

159. S. Robinson, G. Grabner, S. Witoszynskyj, and S. Trattnig, "Combining phase images from multi-channel RF coils using 3d phase offset maps derived from a dual-echo scan," *Magnetic Resonance in Medicine*, vol. 65, pp. 1638–1648, June 2011.

160. J. Lindemeyer, *Optimisation of Phase Data Processing for Susceptibility Reconstruction in Magnetic Resonance Imaging*. PhD thesis, RWTH Aachen University, 2015.

161. M. Poole, *Improved Equipment and Techniques for Dynamic Shimming in High Field MRI*. PhD Thesis, University of Nottingham, 2007.

162. S. M. Smith, "Fast robust automated brain extraction," *Human Brain Mapping*, vol. 17, no. 3, pp. 143–155, 2002.

163. M. Jenkinson, "Fast, automated,N-dimensional phase-unwrapping algorithm," *Magnetic Resonance in Medicine*, vol. 49, pp. 193–197, Jan. 2003.

164. S. D. Robinson, K. Bredies, D. Khabipova, B. Dymerska, J. P. Marques, and F. Schweser, "An illustrated comparison of processing methods for MR phase imaging and QSM: combining array coil signals and phase unwrapping," *NMR in Biomedicine*, vol. 30, p. e3601, Apr. 2017.

165. J. Van Vaals and A. Bergman, "Optimization of eddy-current compensation," *Journal of Magnetic Resonance*, vol. 90, pp. 52–70, Oct. 1990.

166. S. J. Vannesjo, Y. Duerst, L. Vionnet, B. E. Dietrich, M. Pavan, S. Gross, C. Barmet, and K. P. Pruessmann, "Gradient and shim pre-emphasis by inversion of a linear time-invariant system model," *Magnetic Resonance in Medicine*, vol. 78, pp. 1607–1622, Oct. 2017.

167. M. Terpstra, P. Andersen, and R. Gruetter, "Localized Eddy Current Compensation Using Quantitative Field Mapping," *Journal of Magnetic Resonance*, vol. 131, pp. 139–143, Mar. 1998.

168. A. Bhogal, M. Versluis, J. Koonen, J. C. Siero, V. O. Boer, D. Klomp, P. R. Luijten, and H. Hoogduin, "Image-Based Method to Measure and Characterize Shim-Induced Eddy Current Fields," *Concepts in Magnetic Resonance Part A*, vol. 42, pp. 245–260, Nov. 2013.

169. E. J. Candes and B. Recht, "Exact Matrix Completion via Convex Optimization," *Foundations of Computational Mathematics*, vol. 9, pp. 717–772, Dec. 2009.

170. T. Goldstein and S. Osher, "The Split Bregman Method for L1-Regularized Problems," *SIAM Journal on Imaging Sciences*, Apr. 2009.

171. S. Boyd, "Distributed Optimization and Statistical Learning via the Alternating Direction Method of Multipliers," *Foundations and Trends in Machine Learning*, vol. 3, no. 1, pp. 1–122, 2010.

172. M. Fazel, T. K. Pong, D. Sun, and P. Tseng, "Hankel Matrix Rank Minimization with Applications to System Identification and Realization," *SIAM Journal on Matrix Analysis and Applications*, vol. 34, pp. 946–977, Jan. 2013.

173. M. Zimmermann, Z. Abbas, K. Dzieciol, and N. J. Shah, "Accelerated Parameter Mapping of Multiple-Echo Gradient-Echo Data Using Model-Based Iterative Reconstruction," *IEEE Transactions on Medical Imaging*, vol. 37, pp. 626–637, Feb. 2018.

174. S. A. Winkler, F. Schmitt, H. Landes, J. de Bever, T. Wade, A. Alejski, and B. K. Rutt, "Gradient and shim technologies for ultra high field MRI," *NeuroImage*, vol. 168, pp. 59–70, Mar. 2018.

175. P. Jehenson, M. Westphal, and N. Schuff, "Analytical Method for the Compensation of Eddy-Current Effects Induced by Pulsed Magnetic Field Gradients in NMR Systems," *Journal of Magnetic Resonance*, vol. 90, pp. 264–278, Nov. 1990.

176. A. Fillmer and A. Henning, "Expected Homogeneity Gain and Hardware Requirements for Slice-Wise 3rd Order Dynamic Shim Updating for fMRI," in *Proc. Intl. Soc. Mag. Reson. Med.*, p. 3211, 2015.

177. M. Grant and S. Boyd, "CVX: Matlab Software for Disciplined Convex Programming, version 2.1." URL: http://cvxr.com/cvx, Mar. 2014.

178. M. A. Ertuerk, X. Wu, Y. Eryaman, P.-F. V. d. Moortele, E. J. Auerbach, R. L. Lagore, L. DelaBarre, J. T. Vaughan, K. Ugurbil, G. Adriany, and G. J. Metzger, "Toward imaging the body at 10.5 tesla," *Magnetic Resonance in Medicine*, vol. 77, no. 1, pp. 434–443, 2017.

179. T. F. Budinger, M. D. Bird, L. Frydman, J. R. Long, T. H. Mareci, W. D. Rooney, B. Rosen, J. F. Schenck, V. D. Schepkin, A. D. Sherry, D. K. Sodickson, C. S. Springer, K. R. Thulborn, K. Ugurbil, and L. L. Wald, "Toward 20 T magnetic resonance for human brain studies: opportunities for discovery and neuroscience rationale," *Magnetic Resonance Materials in Physics, Biology and Medicine*, vol. 29, pp. 617–639, June 2016.

Acknowledgments

I would like to express my gratitude to Prof. Dr. N. Jon Shah for giving me the opportunity to work on my PhD project at the INM-4 and for supporting and advising me continuously during this time. I had the freedom to realize my own ideas, to work with high-end equipment and to travel the world to attend workshops and conferences or to meet our collaboration partners. This was very important to me and I am grateful for that.

I am also very much obliged to Prof. Dr. Achim Stahl for his time and willingness to review this thesis.

During my PhD project, I benefited greatly from the expertise of Dr. Hoby Hetherington, Dr. Jullie Pan and Dr. Chan Hong Moon from the MR Research Center at the University of Pittsburgh. Our scientific relationship evolved from a hands-on training on the B_0 shimming hard- and software to a fruitful collaboration between our institutes. I am very grateful for the hospitality and the valuable experiences that I gained in Pittsburgh.

Without good colleagues, I certainly would not have been able to complete this project successfully. I would like to thank all former and current members of the INM-4 for their helpfulness on various theoretical and practical issues, for proof-reading my work and in general for the working atmosphere in our institute.

I have the great fortune to find support and distraction in two wonderful circles of friends, who accompany me since my childhood in Lüdinghausen and my move to my home away from home in Düsseldorf. To escape for a little while from the struggles of a PhD project is essential for a successful completion of the thesis and allows one to address problems with new energy. I thank you for always having given me this opportunity and to have supported me on my journey.

The greatest support I have always found in my parents Marianne and Uli, my sister Eva and my wonderful girlfriend Johanna. Ein besonderer Dank gebührt auch meiner Großmutter Anni, die sich immer sehr für meinen Werdegang interessiert und mich unterstützt hat. Being able to count on you all always strengthened me in moments of doubt.